FINITE-CONTROL-SET MODEL PREDICTIVE CONTROL OF AXIALLY LAMINATED FLUX-SWITCHING PERMANENT MAGNET MACHINE WITH EXTENDED VOLTAGE SPACE VECTORS

by

Tianshi WANG, M.Eng. (Elec.)

Submitted for the Degree of Doctor of Philosophy

at

University of Technology Sydney

2018

CERTIFICATE OF AUTHORSHIP/ORIGINALITY

I certify that the work in this thesis has not previously been submitted for a degree nor has it been submitted as part of requirements for a degree except as fully acknowledged within the text.

I also certify that the thesis has been written by me. Any help that I have received in my research work and the preparation of the thesis itself has been acknowledged. In addition, I certify that all information sources and literature used are indicated in the thesis.

This research is supported by the Australian Government Research Training Program.

Signature of Student

ACKNOWLEDGEMENTS

This work was carried out at the School of Electrical and Data Engineering, Faculty of Engineering and Information Technology, University of Technology Sydney.

I would like to express my sincerest appreciation to my supervisor, Prof. Jianguo Zhu Head of Discipline - SEDE Electrical Power and Energy System, for his invaluable expert technical guidance and advice throughout my research and my life.

I would like to express my appreciation to my co-supervisor Dr. Gang Lei for his expert advice. Great gratitude also goes to Dr. Youguang Guo for his suggestion and kind help. Special gratitude goes to Mr. Jiang Chen for his technical support.

Acknowledgments go to Prof. Wei Xu for his idea of ALFSPMM, Prof. Youchang Zhang for his help on MPC, and Dr. Chengcheng Liu for his contribution to the FEM analysis.

I also would like to thank all my colleagues and friends including, Dr. Mohammad Jafari, Ms. Zahra Malekjamshidi, Mr. Lingfeng Zheng, Mr. Jianwei Zhang, Ms. Tingting He, Mr. Bo Ma and Mr. Nian Li.

Finally, I would like to express my deepest gratitude to my wife Shuyang Liu, my father Yanqing Wang and my mother Xiaoyun Jiang for their love and support during my study. I also dedicate this thesis to my lovely son Lucas Wang. I appreciate your patience and support during dad’s thesis writing.

TABLE OF CONTENTS

LIST OF SYMBOLS

$*$	Reference value
$\alpha\beta$	Stationary stator reference frame axes
dq	Rotary rotor reference frame axes
f	Frequency (Hz)
$\psi_a,\ \psi_b,\ \psi_c$	Three-phase flux linkages (Wb)
ψ_α, ψ_β	α- and β- axis stator flux linkages (Wb)
ψ_d, ψ_q	d- and q-axis stator flux linkages (Wb)
θ_r	Angle between two stator reference frame and rotor reference frame
L_d, L_q	d- and q-axis inductance (H)
ψ_f	Flux linkage generated by the rotor permanent magnet (Wb)
p	Number of the machine pole pairs
u_a, u_b, u_c	Stator voltages (V)
u_α, u_β	α- and β- axis stator voltages (V)
u_s, u_d, u_q	stator voltage vector, d- axis and q-axis stator voltage (V)
i_a, i_b, i_c	Stator currents (A)
i_α, i_β	α- and β- axis stator currents (A)
i_d, i_q	d- and q-axis stator currents (A)
R_s	Per-phase stator winding resistance (Ω)
T_e	Electromagnetic torque (Nm)
T_L	Load torque applied on the rotor shaft
$u_0 \cdots u_6$	Space voltage vectors produced by the two level inverter (V)
P_{in}	Total input power of a motor (W)
P_{em}	Electromagnetic power obtained by subtracting the mechanical loss from the input power (W)

ω_r	Rotor mechanical speed
ω_e	Electrical speed
u_s^k, u_d^k, u_q^k, i_d^k, i_q^k	Stator voltage vector, *d*- axis and *q*-axis stator voltage, *d*- axis and *q*-axis stator current at *(k)th* sampling instant
T_e^{k+1}, ψ_s^{k+1}, i_d^{k+1}, i_q^{k+1}	Predicted value of torque, flux, *d*- axis and *q*-axis stator current at *(k+1)th* sampling instant
k_1	Weighting factor
T_s	Sampling period (s)
η_{sys}	Efficiency of the drive system
P_{dc}	Power output of DC power supply (W)

LIST OF FIGURES

LIST OF TABLES

ABSTRACT

The Flux-switching permanent magnet machine (FSPMM) has recently attracted considerable interest for high performance drive applications due to their high torque and high power density features. The laminations of traditional FSPMMs are radially laminated, i.e. steel sheets are laminated perpendicular to the shaft axis. Due to the nonlinear magnetic path, the radial laminations can have serious partial magnetic saturation at the edges/tips of stator teeth or rotor poles. The rated frequency of FSPMMs is usually much higher than traditional rotor-inserted PM machines at a given speed. In this case, the core loss of FSPMMs becomes evident especially beyond the rated speed, which leads to decrease of output power, torque/power density and efficiency.

The reluctance motor with axially laminated rotor has received growing interest in recent years. This type of motor can achieve a higher torque density compared with segmented rotors and flux-barrier rotors. In this thesis, an axially laminated flux-switching permanent magnet machine (ALFSPMM) with HiB grain oriented silicon steel stator and rotor cores is proposed. The HiB silicon steel features high permeability and low specific core loss, and as a result, the total power loss of proposed motor is much lower than the conventional FSPMMs. The detailed fabrication procedures are presented. The theoretical characteristics of ALFSPMM are calculated by 2D finite element method (FEM). Experimental measurements of the prototype machine are presented to validate the FEM calculation.

On the machine control side, the direct torque control (DTC) is one of the most popular control algorithms. It features simple structure and fast dynamic response. However, the performance of DTC in terms of torque and flux ripples and drive system efficiency is unsatisfactory since the voltage space vector (VSV) is selected heuristically. Recently, the finite-control-set model predictive direct torque control (FCS-MPDTC) has been developed as a simple and promising control technique to overcome these problems.

The FCS-MPDTC still suffers from relatively high torque and flux ripples due to the limited number of VSVs.

This thesis proposes a novel FCS-MPDTC with an extended set of twenty modulated VSVs, which are formed by eight basic VSVs and twelve extended VSVs by modulating eight basic VSVs with fixed duty ratio. To mitigate the computational burden caused by the increased number of VSVs, a pre-selective scheme is designed for the proposed FCS-MPDTC to filter out the impractical VSVs. The drive system efficiency is also investigated. The theory and simulation are validated by experimental results on the ALFSPMM prototype.

CHAPTER 1

INTRODUCTION

1.1 Background and Significance

With the increasing concern on energy diversification, energy efficiency, and environmental protection, electric vehicles (EVs) are becoming more attractive and may be the most practical way for road transportation.

Motor drive system is the core technology for EVs that converts the on-board electrical energy to the desired mechanical motion and the electric machine is the key element of motor drive system. The ideal electric machine for EVs application should feature high efficiency, high torque/power density, wide speed range, low acoustic noise, reasonable cost and high reliability for vehicular environment. Various types of electric machine had been applied to EVs, such as DC machine (DCM), induction machine (IM), switch reluctance machine (SRM) and permanent magnet synchronous machine (PMSM). DCM possesses excellent controllability and low torque ripples. However the reliability is low, due to the usage of brushes and commutators. IM has robust rotor structures and low manufacturing costs, but the efficiency and power/torque density are low. SRM presents outstanding flux weakening ability and the drawbacks are low power density, large torque ripples and large acoustic noise. PMSM features high torque/power density and high efficiency. The major weaknesses are high cost, delicate rotor structure, poor heat dissipation and narrow speed range.

Recently, Flux-switching permanent magnet machine (FSPMM) has been proposed to overcome above problems for EV drive applications and various novel topologies based on the principle of flux-switching have been proposed in the last decade [1.1]-[1.6]. The laminations of traditional FSPMMs are radially laminated, i.e. steel sheets are laminated perpendicular to the shaft axis. Due to the nonlinear magnetic path, the radial laminations can have serious partial magnetic saturation and the maximal flux density is usually more than 2.0 T at the edges/tips of stator teeth or rotor poles. The pole pairs in

FSPMMs are equal to the number of rotor poles. As a result, the rated frequency of FSPMMs is usually much higher than that of the traditional rotor-inserted PM machines at a given speed. In this case, the core loss of FSPMMs becomes evident especially beyond the rated speed, which leads to decrease of output power, torque/power density and efficiency.

The reluctance motor with axially laminated rotor has received growing interest in recent years. It is increasingly used in servo drive applications, even though its industrial manufacturing process has not been well established yet [1.7]. This type of motor can achieve a higher torque density compared with segmented rotors [1.9]], [1.10] and flux-barrier rotors [1.11]. In this thesis, an axially laminated flux-switching permanent magnet machine (ALFSPMM) with HiB grain oriented silicon steel stator and rotor cores is proposed. The HiB silicon steel features high permeability and low specific core loss [1.12]. As a result, the total power loss of proposed motor is much lower than the conventional FSPMMs.

On the machine control side, the typical PMSM control methods are six-step control, field oriented control/vector control (FOC/VC) and direct torque control (DTC). The implantation of six-step control is simple and cost effective. However it is unable to deliver high accuracy torque/speed control. FOC/VC features excellent steady-state and dynamic performance and has been widely used in servo system. However FOC/VC requires constant precise angular position measurement to perform complex coordinate transformation [1.13]. The direct torque control (DTC) is one of the most popular control algorithms. It features simple structure and fast dynamic response. However, the performance of DTC in terms of torque and flux ripples and drive system efficiency is unsatisfactory since the voltage space vector (VSV) is selected heuristically [1.14]. Recently, the finite-control-set model predictive direct torque control (FCS-MPDTC) has been developed as a simple and promising control technique to overcome these problems [1.15]. The FCS-MPDTC still suffers from relatively high torque and flux ripples due to the limited number of VSVs. High sampling frequency of the control system is required to improve the performance. This would result in a high computational burden on the microprocessor hardware as well as high switching loss, which are undesirable in the real-time implementation.

This thesis proposes a novel FCS-MPDTC with an extended set of twenty modulated VSVs, which are formed by eight basic VSVs and twelve extended VSVs by modulating eight basic VSVs with fixed duty ratio. By evaluating all twenty VSVs, the concept of duty ratio control is naturally integrated into the proposed algorithm. Compared to conventional FCS-MPDTC, the proposed FCS-MPDTC requires less computing time and features lower torque and flux ripples, lower phase current THD and higher system efficiency.

The major objectives of this thesis project are:

- To conduct a comprehensive literature survey of the developmental history of EVs and EV drives
- To propose a novel FSPM machine for EV application.
- To propose a novel FCS-MPDTC control scheme for the purposes of torque/flux ripples reduction and drive system efficiency increase.
- To perform both simulation and experimental tests based on the proposed drive system and compare the test results to other conventional control schemes.

1.2 Thesis Outline

This thesis is organised in seven chapters, including this one as an introduction to the background and structure of the whole thesis.

Chapter 2 presents a comprehensive literature survey of the developmental history of EVs and the state of the art of permanent magnet synchronous machines (PMSMs). Various topologies of PMSMs and classifications are introduced. A literature review of all the major machine control methods is presented.

Chapter 3 proposes a novel FSPM machine for EV application. The design process and detailed fabrication procedures are presented. The theoretical characteristics of ALFSPMM, such as back-EMF, self/mutual inductance and cogging torque are

calculated by 2D finite element method (FEM). Experimental measurements of the prototype machine are presented to validate the FEM calculation.

Chapter 4 proposes a novel FCS-MPDTC with an extended set of twenty modulated VSVs, which are formed by eight basic VSVs (used in the conventional DTC) and twelve extended VSVs by modulating eight basic VSVs with fixed duty ratio.

In Chapter 5, numerical simulation and experimental tests of the proposed FCS-MPDTC are performed on the novel FSPM machine. The quantitative analysis in terms of torque/flux ripples and drive system efficiencies are also presented.

Chapter 6 presents the numerical simulation and experimental tests results of the proposed FCS-MPDTC based on a surface mounted PMSM. In addition, the drive system performance and efficiency are studied under the similar inverter switching frequency.

Chapter 7 draws conclusions from this thesis and proposes possible future works.

Lists of related references are attached at the end of each chapter.

REFERENCES

[1.1] I. A. A. Afinowi, Z. Q. Zhu, Y. Guan, J. C. Mipo and P. Farah, 'A Novel Brushless AC Doubly Salient Stator Slot Permanent Magnet Machine', *in IEEE Transactions on Energy Conversion*, vol. 31, no. 1, pp. 283-292, March 2016.

[1.2] M. He, W. Xu and C. Ye, 'Novel Single-Phase Doubly Salient Permanent Magnet Machine With Asymmetric Stator Poles'*, in IEEE Transactions on Magnetics*, vol. 53, no. 6, pp. 1-5, June 2017.

[1.3] E. Hoang, M. Lecrivain, et al., 'A new structure of a switching flux synchronous polyphased machine with hybrid excitation', *in Power Electronics and Applications, European Conference on*, pp. 1-8. 2007.

[1.4] R. L. Owen, Z. Q. Zhu, et al., 'Fault-Tolerant Flux-Switching Permanent Magnet Brushless AC Machines'*, in Industry Applications Society Annual Meeting*, pp. 1-8. 2008.

[1.5] Z. Q. Zhu, J. T. Chen, et al., 'Analysis of a Novel Multi-Tooth Flux-Switching PM Brushless AC Machine for High Torque Direct-Drive Applications', *Magnetics, IEEE Transactions on*, vol. 44, pp. 4313-4316, 2008.

[1.6] Z. Xiang, L. Quan and X. Zhu, 'A New Partitioned-Rotor Flux-Switching Permanent Magnet Motor With High Torque Density and Improved Magnet Utilization', in IEEE Transactions on Applied Superconductivity, vol. 26, no. 4, pp. 1-5, June 2016.

[1.7] N. Bianchi and B. J. Chalmers, "Axially laminated reluctance motor: analytical and finite-element methods for magnetic analysis," *IEEE Trans. Magn.*, vol. 38, no. 1, pp. 239-245, Jan. 2002.

[1.8] A. J. O. Cruickshank, R.W. Menzies, and A. F. Anderson, "Axially laminated anisotropic rotors for reluctance motors," in Proc. Inst. Elec. Eng. Electr. Power Appl., vol. 113, no. 12, pp. 2058–2060, Dec. 1966.

[1.9] P. J. Lawrenson and L. A. Agu, "Theory and performance of polyphase reluctance machine," in Proc. Inst. Elec. *Eng. Electr. Power Appl*., vol. 111, no. 8, pp. 1435–1445, Aug. 1964.

[1.10] P. J. Lawrenson and L. A. Agu, "Low-inertia reluctance machines," in Proc. Inst.

Elec. Eng. Electr. Power Appl., vol. 111, no. 12, pp. 2017-2025, Dec. 1964.

[1.11] J. K. Kostko, “Polyphase reaction synchronous motors,” J. Amer. Inst. Elect. Eng., vol. 42, no. 11, pp. 1162–1168, Nov. 1923.

[1.12] H. Hagihara, Y. Takahashi, K. Fujiwara, Y. Ishihara, and T. Masuda, “Magnetic properties evaluation of grain-oriented electrical steel sheets under bending stress,” IEEE Trans. Magn., vol. 50, no. 4, Art.ID 2002104, Apr. 2014.

[1.13] P. Vas, Vector Control of AC Machines, Clarendon Press, pp. 264, 1990.

[1.14] Takahashi and T. Noguchi, ‘A New Quick-Response and High-Efficiency Control Strategy of an Induction Motor’, Industry Applications, IEEE Transactions on, vol. IA-22, pp. 820-827, 1986.

[1.15] S. Kouro, P. Cortes, et al., ‘Model Predictive Control: A Simple and Powerful Method to Control Power Converters’, Industrial Electronics, IEEE Transactions on, vol. 56, pp. 1826-1838, 2009.

CHAPTER 2

A LITERATURE SURVEY ON ELECTRIC VEHICLES AND MOTOR DRIVES

2.1 Introduction

The development of internal combustion engine (ICE) vehicles is one of the greatest achievements of modern technology. Automobiles have made great contributions to the growth of modern society by satisfying many of the needs for mobility in the everyday life. The rapid development of the automotive industry, unlike that of any other industry, has helped human beings to progress from a primitive state to a highly developed industrial society.

However, the large number of automobiles in use around the world has caused and continues to cause serious problems to the environment and human life. Air pollution, global warming, and the rapid depletion of the Earth's petroleum resources are now problems of paramount concern.

Air pollution

At present, all vehicles rely on the combustion of hydrocarbon (HC) fuels to derive the energy which is necessary for their propulsion [2.1]. HC is a chemical compound with molecules made up of carbon and hydrogen atoms. Ideally, the combustion of HC yields only carbon dioxide and water, which is not harmful for the environment. Indeed, green plants 'digest' carbon dioxide by photosynthesis. However, the combustion of HC fuel in combustion engines is never ideal. Besides carbon dioxide and water, the combustion products contain a certain amount of nitrogen oxides (NO_x), carbon monoxides (CO), and unburned HCs, all of which are toxic to human health.

- Nitrogen Oxides: The most commonly found nitrogen oxide is nitric oxide (NO). Once released into the atmosphere, NO reacts with the oxygen to form NO_2. This is later decomposed by the Sun's

ultraviolet radiation back to NO and highly reactive oxygen atoms that attack the membranes of living cells.

Nitrogen dioxide is partly responsible for the smog. It reacts with the atmospheric water to form 'acid rains' and is responsible for the destruction of forests in industrialised countries. Acid rains also contribute to the degradation of historical monuments made of marble.

- Carbon Monoxide: It is a poison to human beings and animals who inhale/breathe it. Dizziness is the first symptom of carbon monoxide poisoning, which can rapidly lead to death.
- Unburned HCs: Unburned HCs may be harmful to living beings. Some of these unburned HCs may be direct poisons or carcinogenic chemicals [2.2] [2.3].

  Unburned HCs are also responsible for the smog.
- Other Pollutants: Impurities in fuels result in the emission of pollutants. The major impurity is sulphur. Sulphur dioxide (SO_2) is the major product of the combustion, which is a major component of acid rains [2.1].

Global warming

Global warming is a result of the 'greenhouse effect' induced by the presence of carbon dioxide and other gases, such as Nitrogen Oxides and methane, in the atmosphere. These gases trap the Sun's infrared radiation reflected by the ground, thus they retain the energy in the atmosphere and increase the temperature. Increased earth temperature results in major ecological damage and in many natural disasters that affect human populations. Fig 2.1.1 shows the distribution of global greenhouse gas emissions. The transportation sector is now one of the major contributors to the greenhouse gas emissions.

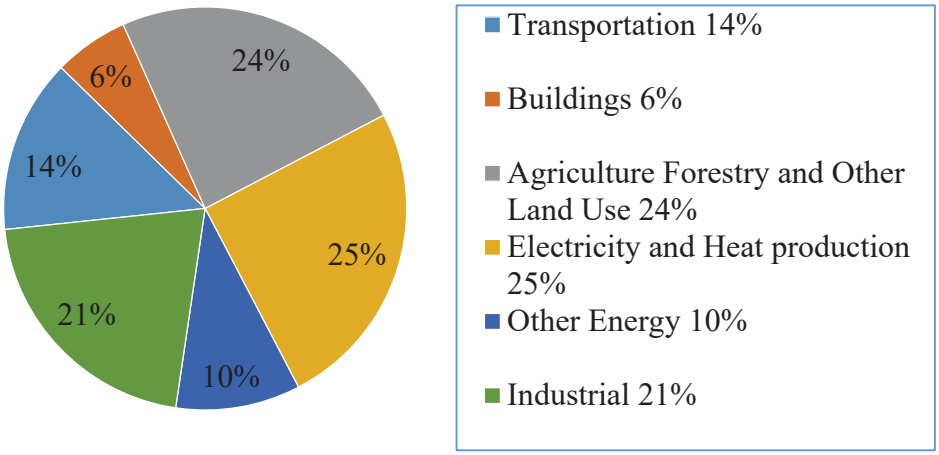

Fig. 2.1.1 Global greenhouse gas emissions, from IPCC 2014

Petroleum resources

The majority of fuels for transportation are liquid fuels originating from the petroleum. The number of years that petroleum resources on earth can support our consumption depends on the discovery of petroleum reserves and cumulative oil production (as well as cumulative oil consumption). Historical data shows that the discovery of petroleum reserves is growing slowly. On the other hand, the consumption remains at a high growth rate, as shown in Fig. 2.1.2. If the petroleum discovery and consumption follow the current trends, world petroleum resource will deplete by 2038 [2.4] [2.5].

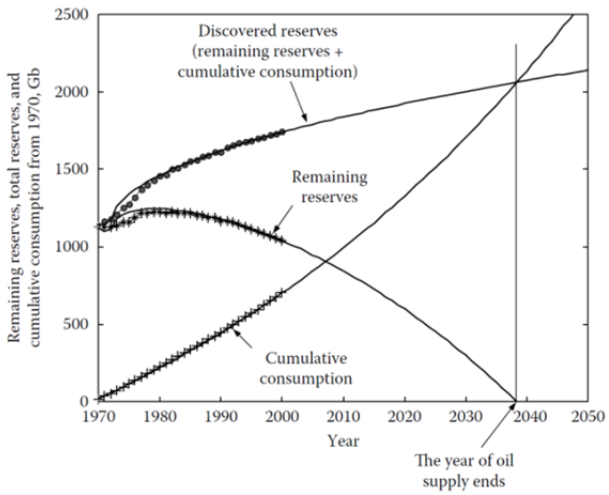

Fig.2.1.2 World petroleum discovery, remaining reserves and cumulative consumption (from [4])

Owing to the concerns about fast decreasing oil reserves and increasing environmental pollution and its effect on public health, the electric vehicle (EV) technology has aroused great interests all over the world. In recent decades, extensive research has been focused on the development of EV technologies, in particular, EV motors and their drives.

The developmental history of EVs is introduced in Section 2.2. The technical requirements of EV Motor drives are discussed in Section 2.3. Various types of electric machines and their applications in EVs are introduced in Section 2.3. Section 2.4 focuses on the state of art of permanent magnet synchronous machines. The machine control techniques are discussed in Section 2.5. Finally, the conclusion is drawn in Section 2.6.

2.2 Developmental History of EVs

The development of electricity storage technology, e.g. batteries, is playing the most important role in the developmental history of EVs. The EV was firstly invented in the late 19th century, which was a pure battery electric vehicle (BEV) fed by the lead-acid battery [6]. As the gasoline automobiles became more powerful and more flexible, the development of EVs was depressed. It is only until the recent few decades, the reduction of fuel consumption has become a new goal for the automobile industry and high energy density batteries (nickel–cadmium, nickel–metal hydride, and lithium-ion batteries) are available. As a result, modern hybrid electric vehicles (HEVs) were proposed and became commercialised in the late 20th century [2.6]. With the development of lithium-ion batteries and the pursuing of lower fuel consumption, the plug-in hybrid electric vehicles (PHEVs) were developed in the early 21th century [2.6]. As the lithium-ion batteries became more reliable and lower cost, BEVs have become a new trend of the automobiles industry.

In this section, the developmental history of EVs is staged as early BEVs, HEVs, PHEVs and modern BEVs.

2.2.1 Early battery electric vehicles

BEVs rely only on electricity from energy storage systems, e.g. batteries. Most of the early BEVs used lead-acid battery, whose typical energy density is only approximately 30-40 Wh/kg. The major advantages of lead-acid battery are low cost, high technological maturity, relatively high power capability and reasonably high number of lifetime cycles. The major disadvantages, on the other hand, are low energy density, mostly due to the high molecular weight of lead, and poor temperature characteristics. When the temperature drops below 10°C, its specific power and specific energy are greatly reduced [2.7-2.9]. This aspect severely limits the EV application of lead-acid batteries in cold climates.

The world's first BEV was built by Frenchman Gustave Trouvé in 1881. It was a tricycle powered by a 0.1 hp DC motor fed by lead-acid batteries. The whole vehicle and its driver weighed approximately 160 kg. A vehicle similar to this was built in 1883 by two British professors [2.6]. These early BEVs did not attract much attention from the public. The technology was not matured enough to compete with the horse carriages because the speeds of 15 km/h and a range of 16 km were nothing exciting for the potential customers [2.10].

The first commercial EV was the Morris and Salom's Electroboat. This vehicle was operated as a taxi in the New York City by a company created by its inventors. The Electroboat was proven to be more profitable than the horse cabs despite a higher purchase price (around $3000 vs. $1200). It could be used for three shifts of 4 hours with 90-min recharging periods in between. It was powered by two 1.5 hp motors that allowed a maximum speed of 32 km/h for a range of 40 km [2.6].

The most significant technical advance of that era was the invention of regenerative braking by Frenchman M. A. Darracq on his 1897 coupe. This method allows recycling the vehicle's kinetic energy through recharging the batteries, and thus can greatly enhance the driving range [2.6]. It is one of the most significant contributions to the BEV and HEV technologies as it contributes to energy efficiency more than anything else in urban driving. In addition, among the most significant EVs of that era was the

first vehicle ever to reach a range of 100 km. It was 'La Jamais Contente' built by Frenchman Camille Jenatzy [2.6].

The following 20 years were an era during which EVs competed with their gasoline counterparts. This was particularly true in America, where there were not many paved roads outside the cities. The limited range of EVs was not a big problem. However, the gasoline vehicles are favoured in Europe as the rapidly increasing paved roads called for extended ranges [2.11].

As ICEs became more powerful, more flexible and easier to control, EVs started to disappear. The high cost, limited driving range and performance impaired early EVs versus their gasoline counterparts. The last commercially significant EVs were released around 1905. In the next nearly 60 years, the only EVs sold were common golf carts and delivery vehicles [2.10].

During the 1960s to 1970s, concerns about the environment triggered some research on EVs. However, despite some new achievements in the battery technology and power electronics, their range and performance were still major obstacles.

The modern EV era began during the 1980s and early 1990s with the release of a few realistic vehicles such as the EV1 of GM [2.12-2.13] and the 106 Electrique of Peugeot Société Anonyme (PSA) [2.14]. Although these vehicles represented a real achievement, especially when compared with early EVs, it became clear during the early 1990s that EVs could never compete with ICE vehicles for range and performance [2.11]. The reason is simply because in batteries the energy is stored in the metal of the electrodes, which weigh far heavier than the gasoline for the same amount of energy. The automotive industry abandoned the EV to conduct research on hybrid electric vehicles. After a few years of development, these are far closer to the assembly line for mass production than EVs have ever been.

In the development of EVs, the battery technology is always the weakest point which greatly affects the usability of EVs for general customers. Great effort and investment have been put into the battery research to improve the performance. Unfortunately, the progress is limited and the performance is still far behind the requirement, especially in

terms of the energy storage capacity per unit weight and volume. This limits EVs to only some specific applications, such as at airports, railroad stations, mail delivery routes, and golf courses, etc. In fact, basic study shows that the EVs will never be able to challenge the ICE vehicles, even with the optimistic value of battery capacity [2.10]. From 1980s to early 2000s, advanced vehicle technology research has turned to HEVs and PHEVs.

2.2.2 Hybrid electric vehicles

Actually, the concept of HEV is almost as old as the automobile itself. The primary purpose of this design was not to lower the fuel consumption but rather to assist the ICE to provide an acceptable level of performance. The reason is that the ICEs were less advanced than electric machines in the early years [2.15].

The HEV possess the advantages of both ICEs and electrical machines. In general, the ICE functions to drive the electric generator which supplies the electric motor for driving the car and charges the battery. Since the ICE is operated at its highest efficiency region most of the time, the overall energy efficiency of a HEV can be significantly higher than that of a traditional ICE driven vehicle. There are three types of powertrain configurations for HEVs, namely series, parallel and hybrid, as shown in Fig. 2.2.1. The series configuration (Fig. 2.2.1(a)) may be the simplest, but the efficiency is the lowest because of the two stage energy conversion: the mechanical energy from the ICE is firstly converted to electrical energy by the generator, and then the electrical energy is converted to the mechanical energy to drive the vehicle by the electric motor. The parallel configuration (Fig. 2.2.1(b)) connects the ICE and the electric motor in parallel and either one can directly drive the vehicle. The hybrid series-parallel configuration (Fig. 2.2.1(c)) combines the merits of both the series and parallel ones and thus yields the highest overall performance with high efficiency and compact volume.

In the early stage, most of the HEVs were powered by the lead-acid battery. The Nickel-metal hydride (Ni-MH) battery has been on the market since 1989 [2.16]. The major advantages are high energy density (60-120 Wh/kg), environmental friendliness, flat discharge profile and rapid recharge capability. However, this battery still suffers from

high initial cost and memory effect [2.17-2.19]. A number of battery manufacturers, such as GM Ovonic, GP, GS, Panasonic, SAFT, VARTA and YUASA, have actively engaged in the development of this battery technology and applied it in modern HEVs.

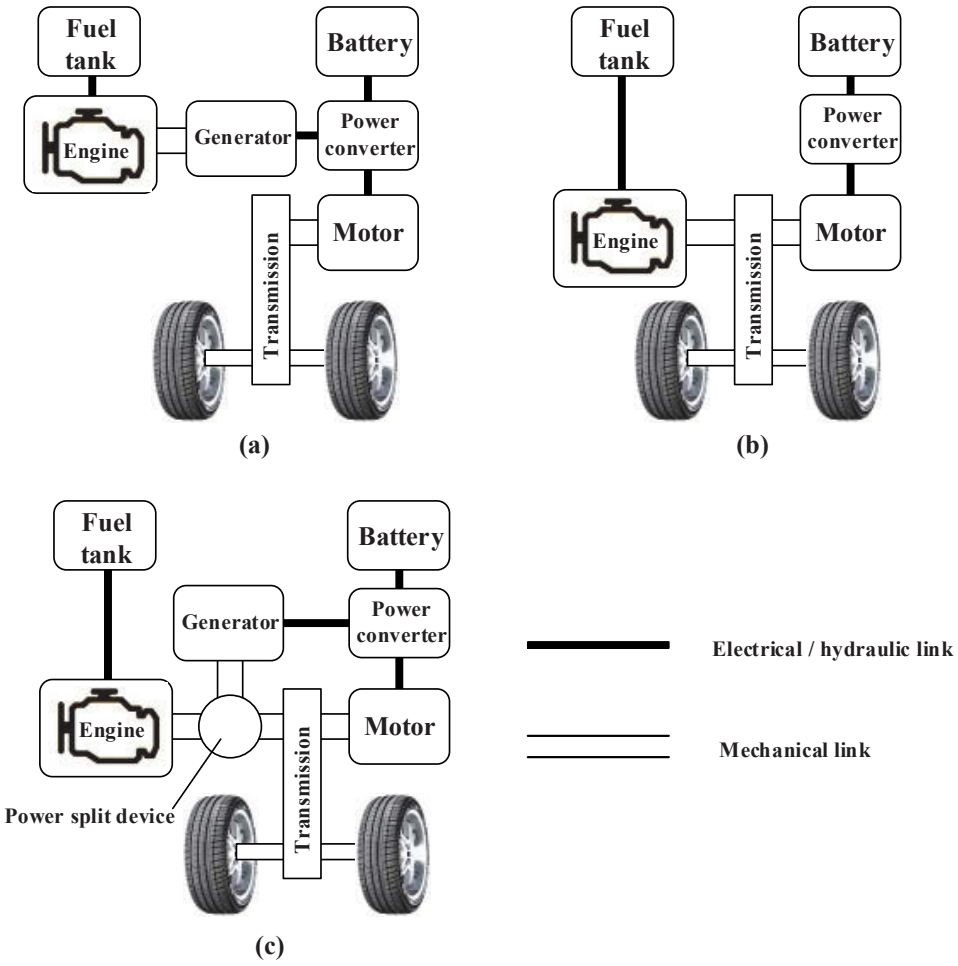

Fig. 2.2.1 HEV drive system configuration, (a) series configuration, (b) parallel configuration and (c) hybrid series-parallel configuration

The first HEV reported were shown at the Paris Salon of 1899 [2.15]. These were built by the Pieper establishments of Liège, Belgium and by the Vendovelli and Priestly Electric Carriage Company, France. The Pieper vehicle was a parallel hybrid with a small air-cooled gasoline engine assisted by an electric motor and lead-acid batteries. The batteries were charged by the engine when coasting or at standstill. When greater driving power was required than the engine rating, the electric motor provided additional power.

The other HEV introduced at the Paris Salon of 1899 was the first series HEV and was derived from a pure EV commercially built by the French firm Vendovelli and Priestly

[2.15]. This vehicle was a tricycle and the two rear wheels were powered by two independent motors. An additional 0.75 hp gasoline engine coupled to a 1.1 kW generator was mounted on a trailer towed behind the vehicle to extend the range by recharging the batteries. In this case, the hybrid design was used to extend the range of the EV only.

In 1903, Frenchman Camille Jenatzy presented a parallel powertrain HEV at the Paris Salon. This vehicle combined a 6 hp gasoline engine with a 14 hp electric machine that could either be driven by the ICE to charge the batteries or assist the ICE. Another Frenchman, H. Krieger, built the second reported series hybrid vehicle in 1902. His design used two independent DC motors driving the front wheels. They drew their energy from 44 lead-acid cells that were recharged by a 4.5 hp alcohol spark-ignited ICE coupled to a shunt DC generator [2.15].

Other HEVs, both the parallel and series powertrain types, were built during a period ranging from 1899 to 1914. Although electric braking has been used in these early designs, there is no mention of regenerative braking. Most of the designs used dynamic braking by short circuiting or adding a resistance to the armature circuit of the motors. The Lohner-Porsche vehicle of 1903 is a typical example of this approach [2.15].

Early HEVs were built in order to assist the weak ICEs or to improve the range of EVs. They made use of the basic electric technologies which were available at that time. Great creativity can be found in these designs. However these early HEVs could no longer compete with the greatly improved ICEs that came into use. After the World War I, the ICEs made tremendous improvements in terms of power density, size and efficiency. Electric motors were no longer needed to assist the ICEs. The additional cost of electric motors and the hazards associated with the lead-acid batteries were key factors in the disappearance of HEVs from the market after World War I. Another problem that these early designs had to cope with was the difficulty of controlling the electric machines. Power electronics were not available until the mid-1960s. Early electric motors were controlled by mechanical switches and resistors and they had a limited operating range incompatible with efficient operation [2.10].

Despite the two oil crises in 1973 and 1977 and growing environmental concerns, no HEV made it to the market during the 1980s. The possible reason is the lack of practical power electronics, modern electric motor and battery technologies. The HEV concept drew great interest during the 1990s when it became clear that EVs would never achieve the objective of energy saving. The Ford Motor Corporation initiated the Ford Hybrid Electric Vehicle Challenge, which drew efforts from universities to develop hybrid versions of production automobiles. Automobile manufacturers around the world built prototypes that achieved tremendous improvements in fuel economy over their ICE-powered counterparts [2.10]. In the United States, Dodge built the Intrepid ESX 1, 2, and 3. The ESX-1was a series hybrid vehicle, powered by a small turbocharged three-cylinder diesel engine and a battery pack. Two 100 hp electric motors were located in the rear wheels [2.20]. Efforts in Europe are represented by the French Renault Next, a small parallel powertrain hybrid vehicle using a 0.75 litre spark-ignited engine and two electric motors [2.21]. Volkswagen also built a prototype named Chico which was a small EV with a nickel-metal hydride battery pack and a three-phase induction motor [2.22].

The most significant effort in the development and commercialisation of HEVs was made by Japanese manufacturers. In 1997, Toyota released the Prius sedan in Japan and it achieved excellent figures in terms of fuel consumption [2.23-2.24]. Toyota's Prius has historical value in that it is the first hybrid vehicle commercialised in the modern era which can respond to the problem of personal vehicle fuel consumption [2.10].

2.2.3 Plug-in hybrid electric vehicle

Lithium-ion batteries are widely known via their use in laptops, mobile phones and consumer electronics. The traditional lithium-ion chemistry involves a lithium cobalt oxide cathode and a graphite anode. This yields cells with an impressive energy density of over 200 Wh/kg and 80 to 90% charge/discharge efficiency [2.25-2.27]. The downsides of traditional lithium-ion batteries include short cycle lives (hundreds to a few thousand charge cycles) and significant degradation with age. The cathode is also somewhat toxic. In addition, traditional lithium-ion batteries can pose a fire safety risk if punctured or charged improperly [2.28].

With the recent breakthrough of lithium-ion chemistry, new variations became available which sacrifice some of the energy and power density to provide fire resistance, environmental friendliness, rapid charges and long lifespans. It becomes possible to increase the capacity of electrical drive to achieve much higher energy efficiency than the HEV, whereas a small capacity ICE is employed to provide extra torque when there is a need and to generate electricity to extend the drive distance. Since the battery bank is mainly charged from the main power supply from the grid, this type of HEV is known as the plug-in hybrid electric vehicle (PHEV). In some literatures, it is also classified as 'gridable HEV' [2.29]. The PHEV can be considered as an extension of conventional HEV, which shares the characteristics both of a conventional HEV (having an electric motor and an ICE) and of a BEV (having a plug to connect to the electrical grid).

The electrical machine in the PHEVs plays the primary role while the ICE just acts as the auxiliary unit which only works in initial starting, acceleration, hill-climbing, and other urgent situations. In theory, the PHEV can bring about zero carbon dioxide emission if it is charged by green sources such as wind, solar, methane (from landfills), hydro, and diesels powered from synthetic fuel. These sources constitute green generation being interconnected with the utility at the distribution level.

One typical PHEV drive system configuration is presented in Fig. 2.2.2. It features a strong energy storage unit combining high capacity batteries with the supercapacitors. The batteries can store the energy by charging from the grid and can then power the drive system in normal driving. In addition, the supercapacitors can store the regenerative energy during braking or down hilling.

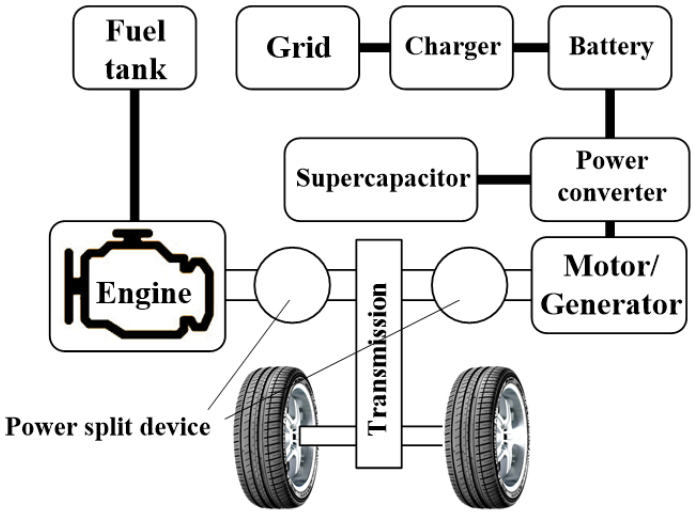

Fig. 2.2.2 PHEV drive system configuration

2.2.4 Modern battery electric vehicle

In the last decade, BEVs began to reappear in the market as the lithium-ion batteries became cheaper and more reliable. However, the travel range of BEVs is still less than that of ICE vehicles at the present status of battery technology. Typically, for a passenger car under urban driving with air-conditioning, a BEV can travel about 160-250 km per charge [2.30], whereas an ICE vehicle can offer about 500 km per refuel. It should be noted that some BEV models, such as Tesla Model S and X [2.31], purposely install three to four times the battery capacity to extend their driving range comparable with that of ICE vehicles. However, these BEV models will be much more expensive than general BEVs, which are actually not targeted for general buyers.

At the present time, the cost of lithium-ion battery accounts for 30–40% of the overall BEV cost. Moreover, the battery life can generally last for about 1500 cycles, which is equivalent to about 4–5 years of vehicle operation, indicating that all batteries of the BEV need to be renewed in the midway of the vehicle life. Thus, the long-term cost of the BEV is further higher than the initial cost.

In addition, the BEV takes time for battery charging. The charging period normally ranges from 5 to 8 hours based on a battery charger with the specifications of 110–240V, 13–40 A and 2–4kW, which may be too long for the BEV to provide continuous operation. When adopting the fast charging technique, it takes about 20–30 minutes to

charge the batteries up to 80% capacity based on a battery charger with the specifications of 200–400V, 100–200 A and 50kW [2.29]. Although this charging period may be acceptable for continuous operation, the installation and establishment of these fast charging stations are often costly.

2.2.5 PHEVs and BEVs in microgrids

The use of PHEVs and BEVs will provide a significant reduction of oil consumption and play an important role in decarbonising road transport. However, this could lead to a noticeable effect on future grid performances and load demands. Electricity suppliers will be needed to respond to this emerging trend, both in the electricity network and associated EV charging infrastructure. As the number of PHEVs and BEVs is increasing, this new type of electricity load will need to be carefully managed in order to minimise the impact on peak electricity demand [2.32].

The Smart Grid and Microgrid

The smart grid uses advanced information and communications technologies to improve the reliability, security, and efficiency of the electricity system from power plants, through to the delivery systems to electricity consumers as well as a number of distributed generation and energy storage resources. The idea of smart grid is to make lower voltage networks more visible and to enable the participation of electricity consumers in the operation of the power system through smart meters and smart homes.

A microgrid is defined by the U.S. Department of Energy as ‘a group of interconnected loads and DERs within clearly defined electrical boundaries that act as a single controllable entity with respect to the grid. A microgrid can connect and disconnect from the grid to enable it to operate in both grid-connected and island-mode’. In other words, microgrids are ‘the building blocks of smart grids’, which consist of several basic technologies for operation such as distributed generation, distributed storage, interconnection switches, and control systems, as shown in Fig. 2.2.3. Distributed generation (DG) units are small sources of energy located at or near the point of use. DG technologies typically include photovoltaic (PV), wind, fuel cells, microturbines, and ICEs with generators. Distributed storage (DS) technologies are used in microgrid

applications where the generation and loads of the microgrid cannot be exactly matched. The interconnection switch is the point of connection between the microgrid and the rest of the distribution system or the smart grid. The control system of the microgrid is designed to safely operate the system in grid-parallel and stand-alone modes.

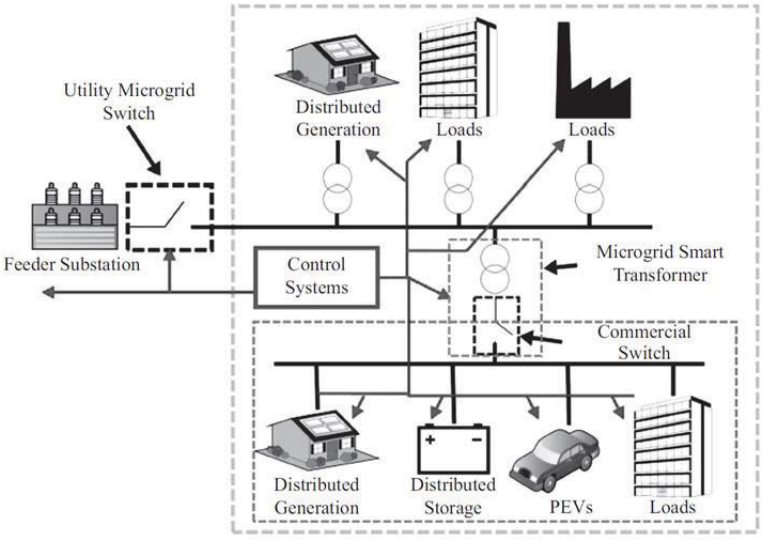

Fig. 2.2.3 Basic concept of the microgrid introduced in IEEE 1547.4 Standard (from [2.35])

Vehicle-To-Grid Technology

The PHEVs and BEVs possess dual dynamic characteristics as a load while in grid-to-vehicle (G2V) mode and as a generator while in vehicle-to-grid (V2G) mode. The integration of the smart grid and microgrid with V2G technology can enable PHEVs and BEVs can be used as distributed electricity storage devices and sending electricity back into the grid when needed. It can also enable the PHEVs and BEVs' charging load to be shifted to off-peak periods, flattening the daily load curve and reducing both generation and network investment needs. In this way, PHEVs and BEVs can help to reduce electricity system costs by offering a cost-effective means of providing regulation services, spinning reserves, and peak shaving capacity. However, there are still a number of technical, practical, and economic limitations to this new technology. A number of papers have discussed several topologies and control methods that can perform bidirectional power transfer using PHEVs and BEVs as the distributed energy resources [2.32-2.40].

2.3 Technical Requirements of EV Motor Drive

Motor drive is the core technology for EVs that converts the on-board electrical energy to the desired mechanical motion. Meanwhile, the electric machine is the key element of motor drive system. The requirements of electric machines for EVs are stricter than that for industrial applications due to the safety issue and space/weight limitation. The desired torque-speed and power-speed curves is shown in Fig. 2.3.1.

The ideal electric machine for EVs should possess the following features [2.41-2.45]:

- High torque density and high power density
- Wide speed range
- High efficiency over wide torque and speed ranges
- Low acoustic noise
- Reasonable cost
- High intermittent overload capability for acceleration and overtaking
- High reliability and robustness for vehicular environment
- High efficiency power generation over a wide speed range

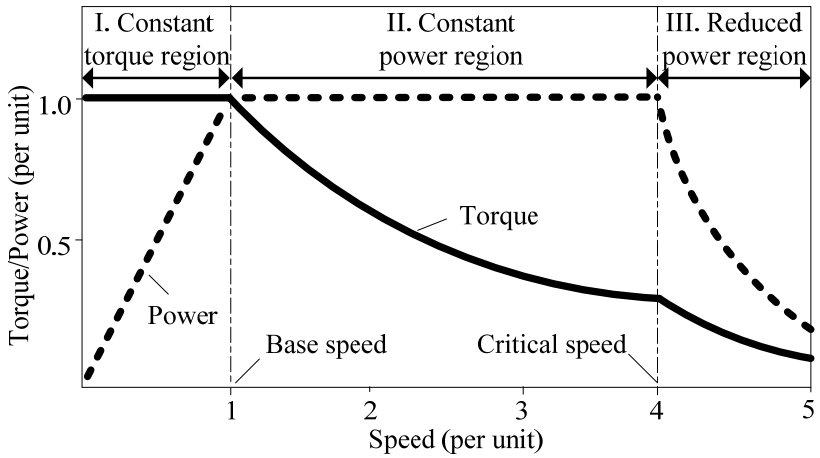

Fig. 2.3.1. Desired torque-speed and power-speed curves

2.4 Electric Machines for EV Drives

2.4.1 DC machines

In early days, DC machine drives were widely used for EV propulsion because of their merits such as technological maturity and control simplicity. However, they generally suffer from problems such as lower efficiency and lower power density compared to AC machine drives, and the need for regular maintenance of the carbon brushes and commutators. Consequently, aside from small or off-road EVs, DC machine drives have been superseded by AC or brushless DC machine drives for EV propulsion.

DC machines were invented by the British scientist William Sturgeon in 1832 and have been in service for more than a century [2.46]. Since the advent of AC machines, the role of DC machines for electric propulsion has been phased out. Nevertheless, some low-end or off-road EVs still adopt DC machines mainly for the sake of simplicity.

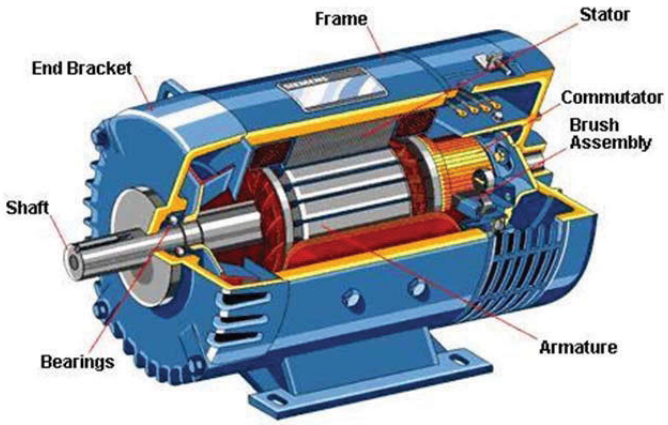

Fig. 2.4.1 DC machine exploded diagram (from [2.47])

Figure 2.4.1 shows the basic structure of a DC machine which mainly consists of a stator, a rotor, and a commutator with brushes. The stator is the field circuit that incorporates the field winding or permanent magnets (PMs) to produce a magnetic field, and the rotor is the armature circuit that installs the armature winding where the armature current is bidirectional and switched by the commutator via carbon brushes [2.48].

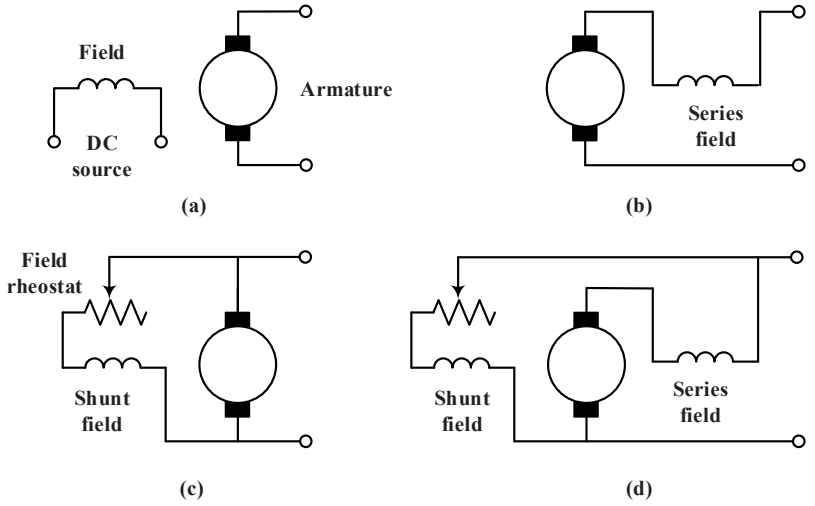

Fig. 2.4.2 DC machine excitation arrangements, (a) separate excitation, (b) series excitation,
(c) shunt excitation and (d) compound excitation

Different arrangements of the field and armature circuits create different types of DC machines, hence providing different torque-speed characteristics. As shown in Figure 2.4.2, the field excitation arrangement of a DC machine can be classified as separate, series, shunt, and compound excitations. In the separately excited DC machine, the field and armature circuits are separately fed by different voltage sources so that their currents are controlled independently. In the shunt DC machine, the field and armature circuits are connected in parallel and fed by the same source so that their currents are controlled simultaneously. In the series DC machine, the field circuit is connected in series with the armature circuit so that the field and armature currents are the same and controlled simultaneously. In the compound DC machine, there are two field circuits, where one is connected in series and the other in shunt with the armature circuit.

DC machines suffer from a fundamental problem because of the use of the commutator and carbon brushes. The commutator causes torque ripples and limits the operating speed, while the carbon brushes are responsible for the friction and radio-frequency interference. Moreover, due to wear and tear, it is necessary to regularly maintain the commutator and carbon brushes. These drawbacks make the DC machines less reliable and unsuitable for maintenance-free operation, hence limiting their application in modern EVs.

Applications:

In 1975, Dr. Victor Wouk along with his colleagues built a parallel hybrid version of a Buick Skylark, as shown in Fig. 2.4.3. The vehicle was powered by a Mazda rotary engine coupled with manual transmission. It was assisted by a 15 hp separately excited DC machine located in front of the transmission. The energy storage system was made of eight 12 V automotive batteries. The vehicle has a top speed of 129 km/h and it can hit 96 km/h from standstill in 16 s [2.49].

Fig. 2.4.3 Victor Wouk with his 1974 hybrid Buick Skylark.

The two-seat Fiat Panda Elettra was developed in 1990. It was a full-electric power-train version of Fiat Panda, as shown in Fig. 2.4.4. Batteries replaced the rear seats and occupied some of the engine bay where a 14 kW DC motor was fitted. The motor drives the car through the normal clutch and gearbox. This increases the weight of the car significantly. Panda Elettra weighted 1,150 kg which was 450 kg heavier than the standard Panda. 1992 revisions to the Elettra improved the power which increased to 17.7 kW. Further, the weight was reduced. However, the Elettra remained significantly heavier and much more expensive than the standard Panda (three times the price of the base model), which made it a commercial failure. The Panda Elettra was discontinued in 1998 [2.50-2.51].

Fig. 2.4.4 Fiat Panda Elettra (from [2.51])

Fig. 2.4.5 The battery pack of Fiat Panda Elettra (from [2.51])

2.4.2 Induction machines

At present, induction motor (IM) drives are the most matured technology among various commutatorless motor drives. There are two types of IMs: the wound-rotor and squirrel-cage rotor IMs. Because of the high cost, need for maintenance, and lack of sturdiness, the wound-rotor IM is less attractive than the squirrel-cage counterpart, especially for EV propulsion. In addition to the common advantages of commutatorless motor drives, the IM drives possess the advantages of low cost and ruggedness. These advantages can generally outweigh the major disadvantage of control complexity and can facilitate IM drives being widely adopted for EVs [2.48].

The most common type of IMs is the squirrel-cage IM. As shown in Fig. 2.4.6, it consists of a stator incorporated with three-phase armature windings, a rotor

incorporated with cage bars that are short-circuited by two end-rings, which can also be moulded with fan blades to cool the machine during rotation, two end-bearings to support the rotor and a machine frame with two end-bells to house the machine.

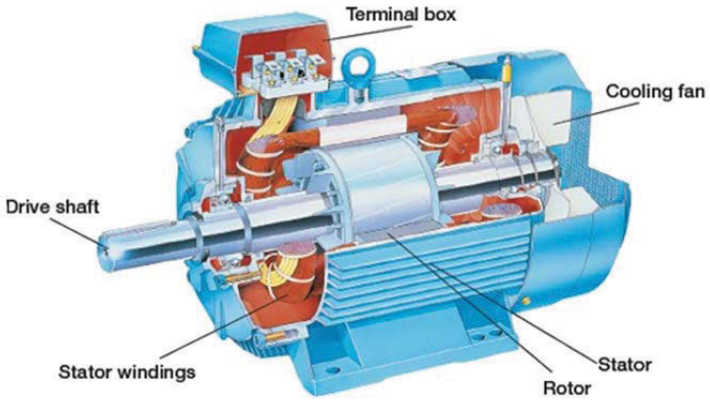

Fig. 2.4.6 Induction machine exploded diagram (from [2.52])

Fig. 2.4.7 shows schematically the cross section of a basic three-phase two-pole IM in which the stator is installed with three-phase windings and the rotor is inserted with squirrel-cage bars. The stator windings are distributed in such a way that the winding current produces a sinusoidally distributed flux in the air-gap. All cage bars are short-circuited together by the front and rear end-rings so that the rotor circuit can be induced to produce the same number of poles as the stator.

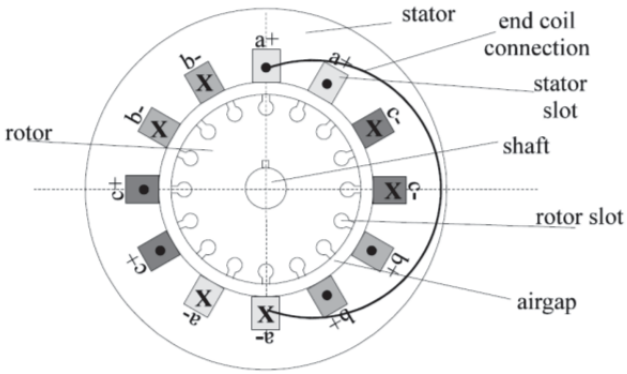

Fig. 2.4.7 Basic induction machine topology (from [2.48])

IMs were used in EVs very early because of their light weight, small volume, simple structure, high efficiency, low price, reliable operation, well established manufacturing and mature control technique. Good starting performance can be obtained for inverter fed IMs by applying suitable voltage and frequency. Good dynamic torque control

performance can be achieved by using either field oriented/vector control or direct torque control. The major disadvantage of IMs is the narrow constant power speed range, which is only 2-3 times the base speed. Although it can be extended to 4-5 times the base speed, a more complicated design should be applied in that case [45] [53-55].

Applications:

In 1945, three researchers at Bell Laboratories invented the transistor, a device which has revolutionised the world of electronics and electricity. The transistor enabled the regulation of the power to be fed to an electric motor without inefficient rheostats and allowed the driving of AC motors at variable frequencies [2.56]. In 1966, General Motors (GM) built the Electrovan, which was propelled by IMs fed by inverters as shown in Fig. 2.4.8 [2.57].

During the 1960s and 1970s, concerns about the environment triggered some research on EVs. However, despite new achievements in energy storage technology and power electronics, their range and performance were still limited.

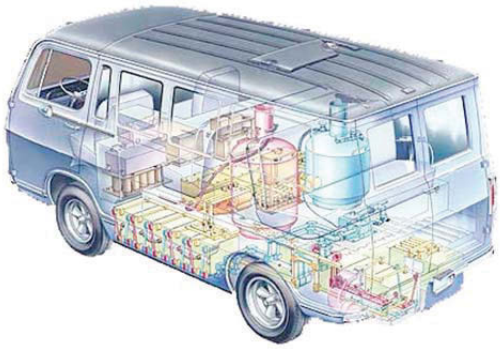

Fig. 2.4.8 General Motors Electrovan (from[57])

In 1992, Volkswagen built a prototype EV named ‘Chico’, as shown in Fig. 2.4.9. It was equipped with a nickel-metal hydride battery pack and a three-phase IM. A 34 hp two-cylinder petrol engine was used to recharge the batteries and provide additional power for high-speed cruising [2.22]. Renault presented a prototype parallel hybrid vehicle named ‘Next’ in 1995, which used a 750 cc three-cylinder engine and two IMs, as shown in Fig. 2.4.10. It achieved a fuel consumption of 3.4 L/100km and a maximum speed of 165 km/h [2.21].

Fig. 2.4.9 Volkswagen Chico

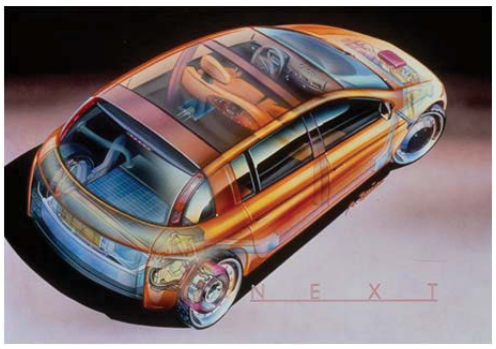

Fig. 2.4.10 Renault Next

In 1996, GM released the EV1 with a 102 kW 3-phase IM, as shown in Fig. 2.4.11. It was the first mass-produced and purpose-designed EV from a major automobile manufacturer [2.58]. The EV1 was made available through limited lease-only agreements and it was not available for purchase. While the customer reaction to the EV1 was positive, GM believed that electric cars occupied an unprofitable niche of the automobile market and ended up recalling all their electric cars, regardless of the protesting customers. The EV1 program was subsequently discontinued in 2002 and all cars produced by GM were repossessed [2.59].

Fig. 2.4.11 General Motors EV1

In 2008, Tesla Motors (now Tesla, Inc.) produced the Tesla Roadster, which is a plug-in EV (PEV) sports car with a 3-phase 4-pole IM (185 kW, 270 Nm). The Roadster was the first highway legal serial production PEV to use lithium-ion battery cells. According to the US Environmental Protection Agency (EPA), the Roadster can travel 393 km on a single charge and can accelerate from 0 to 97 km/h in 3.7 or 3.9 seconds depending on the model [2.60]. From 2008 to 2012, Tesla sold about 2,450 Roadsters in over 30 countries [2.61].

Fig. 2.4.12 Tesla Motors Roadster

In June 2012, Tesla Inc. announced the Tesla Model S, which is a full-sized five-door luxury PEV. The Model S base model has a three phase, four pole IM (285 kW, 430 Nm) rear-mounted with copper rotor. It has a top speed of 180 km/h and it accelerates from 0 to 97 km/h in 6.5 seconds. The powertrain also provides regenerative braking power of more than 60 kW which reduces both energy consumption and improves brake lifetime [2.62].

Fig. 2.4.13 Tesla Model S and its powertrain

2.4.3 Switched reluctance machines

The modern switched reluctance machine (SRM) drives are becoming attractive for EV propulsion because of their low system cost, robust structure, reliable converter topology, control simplicity, and high efficiency. On the other hand, they suffer from the drawbacks of large torque ripple, high machine nonlinearities and annoying acoustic noise [2.41].

The SRM has salient poles on both the stator and rotor as shown in Fig. 2.4.12. It has installed multiphase concentrated windings in the stator, but with no copper winding or PM piece in the rotor. There are many possible topological structures for the SRM, depending mainly on the number of phases and the numbers of stator and rotor poles.

Fig. 2.4.12 Switched reluctance machine exploded diagram

Fig. 2.4.13 shows two basic SRM topologies: the three-phase 6/4-pole topology, which has six stator poles and four rotor poles and the four-phase 8/6-pole topology, which has eight stator poles and six rotor poles. The three-phase 6/4-pole SRM has the advantages of lower cost and better phase-advancing capability for high-speed operation. However, it suffers from higher torque ripple and acoustic noise. On the other hand, the four-phase 8/6-pole SRM has better starting torque and lower torque ripple, but requires more power devices and involves higher converter cost [2.29].

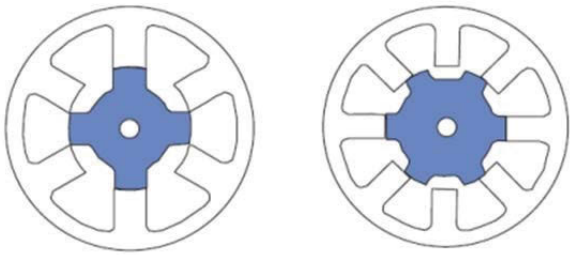

(a) (b)

Fig. 2.4.13 Basic switched reluctance machine topologies:
(a) three-phase 6/4-pole and (b) four-phase 8/6-pole (from [2.29])

SRM works by the reluctance torque. While the concentrated multiphase windings are mounted on the stator, the rotor of an SRM has simple salient poles of either solid mild steel or SiFe laminations. When a stator phase winding is energised, the adjacent rotor poles are attracted to align with stator poles to minimise the reluctance, then the reluctance torque is produced. The SRM has a simple, rugged, and low-cost structure. It has no PM or winding on the rotor. This structure not only reduces the cost of the SRM but also offers high-speed operation capability for this motor. Meanwhile, it is also very suitable for in-wheel drive due to its high mechanical integrity. Unlike the induction and permanent magnet machines, the SRM is capable of high-speed operation without the concern for mechanical failures resulting from the high-level centrifugal force. In addition, the inverter of the SRM drive has a reliable topology. The stator windings are connected in series with the upper and lower switches of the inverter. This topology can prevent the shoot-through fault that exists in the induction and permanent motor drive inverter. Moreover, high efficiency over a wide speed range and control simplicity are known merits of the SRM drive. However, the major problems concerning SRMs are low power density, significant torque ripples, and an excessive amount of acoustic noise [2.63]-[2.67].

Applications:

In 2000, the Commonwealth Scientific and Industrial Research Organisation (CSIRO) and GM Holden developed the Holden ECOmmodore. This hybrid concept car is based on Holden VT Commodore and it was powered by a 2.0-litre four-cylinder petrol engine combined with SRMs. To eliminate the requirement of the expensive DC/DC converter, a dual electrical storage system consisting of lead-acid batteries and super

capacitors was developed. The peak power of two SRMs are 32 kW (powered by super capacitors) and 10 kW (powered by batteries), respectively [2.68]. It was first unveiled at the Melbourne International Motor Show in May 2000, and in 2001 it made appearances at the North American International Auto Show in Detroit and the Hannover Trade Fair. It was further used as the VIP car during the 2000 Summer Olympics Torch Relay held in Sydney [2.69].

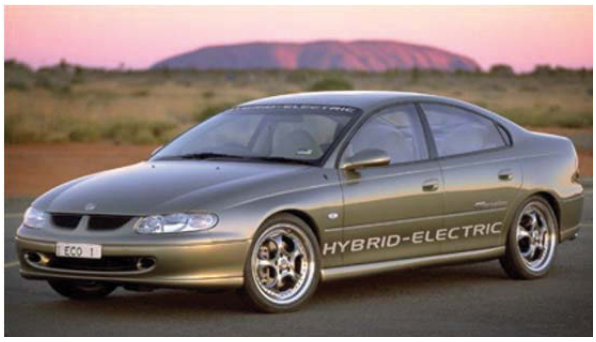

(a)

(b)

Fig. 2.4.14 (a) Holden ECOmmodore and (b) Cutaway view of the motor/generator (in the blue casing, between the engine and the transmission, from [2.69])

At the 2013 Geneva Motor Show, Land Rover unveiled a range of new electric Defender vehicles which are powered by a SRM drive system which was developed and built by Nidec SR Drives Ltd, as shown in Fig. 2.4.15. The standard diesel engine and gearbox of the Land Rover 110 Defender has been replaced by an 70kW SRM, twinned with a 300V 27kWh lithium-ion battery pack, giving a range of more than 80 km. It has a top speed of 112 km/h and can run for up to eight hours before recharging in typical low speed off-road use [2.70].

Fig. 2.4.15 New Land Rover electric Defender (from [2.70])

2.4.4 Permanent magnet machines

Among various types of machine drives, PM machine drives, especially the permanent magnet synchronous machine (PMSM) drive, are currently the most attractive machine drives for EV propulsion. Their key features are high power density and high efficiency. PM machines are becoming dominant in the market share of EV motor drives. However, these PM machine drives still have some shortcomings such as high cost and thermal instability of the PM material [2.71]-[2.82].

By replacing the field winding of the wound rotor synchronous machine with PM poles, the PMSM can be generated, as shown in Fig. 2.4.16. Like the conventional synchronous machine, the stator has the three-phase distributed armature winding in the stator. When the armature winding is fed with three-phase sinusoidal currents, a synchronously rotating sinusoidal air-gap flux is created. Hence, the PM rotor with the same number of poles as the rotating air-gap flux always rotates in synchronism, which depends on the applied frequency.

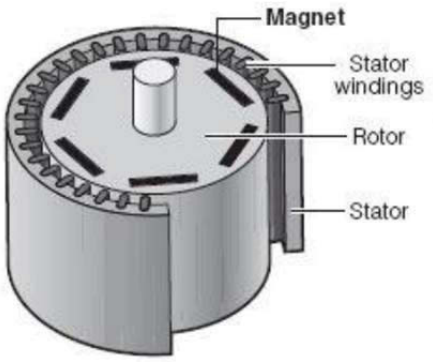

Fig. 2.4.16 Permanent magnet machine exploded diagram (from [2.74])

The major advantages of PM machines include [2.71]-[2.82]:

- High efficiency: PM machines are the most efficient of all electric motors. This is due to the use of PMs for rotor field excitation, which consumes no power.
- Compactness: The introduction of rare-earth magnets makes it possible to achieve high torque density, which allows making the motor small and light for the same power requirement.

- Ease of cooling: There is no current circulation in the rotor. Therefore, the rotor of a PM motor does not heat up. The only heat production is on the stator, which is easier to cool than the rotor because it is static and on the periphery of the motor.
- Low maintenance, great longevity and reliability: The absence of brushes and mechanical commutators suppresses regular maintenance work. The longevity is therefore only a function of the winding insulation, bearings, and magnet life-length.
- Low noise emissions: There is no acoustic noise associated with the commutation because it is electronic and not mechanical. The driving converter switching frequency is high enough so that the harmonics are not audible.

However, the PM machine drives also suffer from some disadvantages such as:

- Cost: Rare-earth magnets are much more expensive than other magnets and result in an increase in the manufacturing cost.
- Limited speed range: Due to the poor flux-weakening ability, the speed range of PM motors is quite limited.
- Safety: In case of a vehicle accident, if the wheel is spinning freely, the motor is still excited by its magnets and generating high voltage on the motor terminals that could possibly endanger the passengers.
- Magnet demagnetisation: Magnets can be demagnetised by large opposing MMFs and high temperature. Great care must be exercised when cooling the motor, especially when the motor has been built compactly.
- High-speed capability: The surface mounted PM motors cannot reach high speeds due to the limited restraint strength between the rotor body and the magnets.

Applications:

The Toyota Prius first went on sale in Japan in 1997 [2.24], making it the first mass-produced hybrid vehicle. The Prius is sold in almost 80 countries and regions. Global cumulative Prius sales reached the milestone of 1 million vehicles mark in May 2008, 2 million in September 2010, and it passed the 3 million mark in June 2013 [2.83]. The

first generation of Prius (1997–2003) uses a 1.5 L gasoline engine and a 30 kW PM motor. The second generation (2003–2009) is powered by a 1.5 L gasoline engine with a 50 kW PM motor. The third generation (2009–2015) is equipped with a 1.8 L gasoline engine and a 60 kW PM motor [2.84]. The latest generation (2015 - present) is propelled by a 1.8 L gasoline engine and a 53 kW PM motor, as shown in Fig. 2.4.17 [2.85].

Fig. 2.4.17 Toyota Prius of latest generation (from [2.85])

The Honda Insight is a hybrid vehicle which was first released in 2000 [2.86], as shown in Fig. 2.4.18. It combines a conventional petrol-driven engine with an additional motor driven by a battery. The Insight employs a system named Integrated Motor Assist (IMA) system, which integrates a 10 kW PM motor into the petrol engine. The PM motor is about 6 cm thick, located between the engine and the gearbox, and directly connected to the crankshaft. The Insight, marketed as the least expensive petrol-electric hybrid, ranked as the top-selling vehicle in Japan for the month of April 2009, a first for a hybrid model.

Fig. 2.4.18 Honda Insight (from [2.86])

In 2009, Ford Motor Company launched the Fusion Hybrid, which is a petrol-electric hybrid powered version of the mid-size Ford Fusion sedan, as shown in Fig. 2.4.19. The vehicle was powered by a 2.5L 116 kW Atkinson cycle petrol engine and a 79 kW PM motor. Fusion Hybrid can achieve a fuel consumption of 5.7L/100 km in the city and 6.5L/100 km on the highway [2.87].

Fig. 2.4.19 Ford Fusion Hybrid (from [89])

Mercedes-Benz at the 2009 New York International Auto Show released ML 450 Hybrid, as shown in Fig. 2.4.20. The new ML450 Hybrid powered by a 3.5-liter V6 petrol engine (working in Atkinson cycle) and two PM motors. Each motor serves a specific purpose. The motor on the transmission shaft outputs 60 kW and 260 Nm of torque and it is dedicated to pulling away the vehicle from standstill. The second motor is located closer to the petrol engine. It is set up specifically for acceleration and is rated at 62 kW and 234 Nm of torque [2.88].

Fig. 2.4.20 Mercedes-Benz ML 450 Hybrid (from [2.88])

The Nissan Leaf (Leading, Environmental friendly, Affordable, Family) car introduced in Japan and the United States in December 2010 is a five door hatchback EV as shown in Fig. 2.4.21. Currently, it has the largest market share of worldwide EVs sold since 2010. Using its on-board 24kWh lithium-ion battery, it can offer a driving range of 135

km per charge based on the US EPA profile. The drive system equipped with an 80 kW and 254Nm PM synchronous motor. With the single speed transmission, it can offer the top speed of over 150 km/h. Leaf battery packs can be charged from fully discharged to 80% capacity in about 30 minutes using DC fast charging [2.89].

Fig. 2.4.21 Nissan Leaf (from [2.89])

The BYD Qin is a plug-in hybrid compact sedan developed by BYD Auto with an all-electric range of 70 km and a hybrid electric powertrain that can extend the car's total range to a distance similar to that of a conventional gasoline powered vehicle, as shown in Fig. 2.4.22. The BYD Qin concept car was unveiled at the 2012 Beijing International Automotive Exhibition, and the car is named after China's first empire, the Qin Dynasty. An all-electric variant with a range of 300 km (190 mi), propelled with two 110kW PM motors. The Qin was the world's second best-selling plug-in hybrid car in 2015 after the Mitsubishi Outlander P-HEV, and also ranked the fifth in 2015 among the world's top selling plug-in electric cars [2.90].

Fig. 2.4.22 BYD Qin (from [2.90])

In 2016, Tesla revealed the Tesla Model 3, which is a mid-size all-electric four-door luxury sedan powered by a 3-phase permanent magnet motor (192kW, 430Nm). According to Tesla officials the standard Model 3 delivers an EPA rated all-electric range of 350 km and will be able to accelerate from 0 to 100 km/h in 5.8 seconds [2.91]. Within a week of the 2016 unveiling, Tesla said they had taken 325,000 Model 3 reservations. By August 2017, there were 455,000 net reservations and an average of 1,800 additional being added per day [2.92].

Fig. 2.4.23 Tesla Model 3 (from [2.91])

2.4.5 Comparison of electric machines

Overall, DC machines have excellent controllability and performance, such as linear torque/speed curve and low torque ripples, but because of the use of brushes and commutators, the reliability and power or torque density are low. IMs have robustness rotor structures and low manufacturing costs, but the efficiency and power/torque density are low. SRMs have very robust construction and outstanding flux weakening ability, but they have problems of low power density, large torque ripples and large acoustic noise, because of their salient structures. Most PM machines have excellent features like high power density, high efficiency, high controllability, and fast dynamic response. The major weaknesses are the delicate rotor structure because of the low mechanical strength of PMs and narrow speed range due to the difficulty to weaken the field of PMs.

A qualitative evaluation of the electric machines mentioned above is presented in this section. In Table 2-1, the characteristics of DC machines, induction machine, PM machine and SR machine are evaluated in seven aspects, such as power density,

efficiency, controllability, speed range, reliability, maturity and cost. Each aspect comes with a weighing factor for priorities and a review comment. The weighing factors are classified as 'very high=4', 'high=3', 'moderate=2' and 'low=1'. The review comments are classified as 'excellent=5', 'good=4', 'average=3', 'poor=2'and 'bad=1'. The score of review comments is multiplied by the weighing factors and added together. For example, the score of DC machine is 3*4+3*4+5*2+4*3+2*4+5*2+4*3=76. It is evident that the PM machine has the highest score (86 for PM located in rotor; 90 for PM located in stator), which makes it an ideal candidate for modern EV applications.

Table 2-1. Comparison of Electrical Machines

	DC Machine	*Induction Machine*	*PM Machine*	*SR Machine*
Power density *(Very high)*	Average	Average	Excellent	Average
Efficiency *(Very high)*	Average	Average	Excellent	Average
Controllability *(Moderate)*	Excellent	Good	Good	Average
Speed range *(High)*	Good	Average	Average	Excellent
Reliability *(Very high)*	Poor	Excellent	Average (PM in rotor)/Good (PM in stator)	Excellent
Maturity *(Moderate)*	Excellent	Excellent	Good	Average
Cost *(High)*	Good	Good	Average	Good
Total	76	83	86/90	83
Note: Excellent=5, Good=4, Average=3, Poor=2, Bad=1 Weighing factors of priorities: Very high=4, High=3, Moderate=2, Low=1				

An investigation of performance difference of surface mounted permanent magnet (SPM) motor, interior permanent magnet (IPM) motor, IM and SRM is found in [2.41]. All motors have the same axial active length, excitation current density and slot filling factor. The numerical calculation results are summarised in Table 2-2.

Table 2-2. Comparison of Performance

	SPM	***IPM***	***IM***	***SRM***
Rated Speed (rev/min)	1500	1500	1479	1500
Peak Phase Voltage (V)	150	152	125	100
Peak Current (A)	100	100	100	185
Average Torque (Nm)	126.53	130.47	95.00	91.85
Peak Torque (Nm)	16.36	18.71	10.00	41.35
Torque Ripple (%)	12.90	14.30	10.50	45.00
Power Factor	0.88	0.90	0.76	0.65

From the table, it can be found that the IPM motor produces the highest average torque and highest power factor, seconded by the SPM motor. In actual applications, SPM motor is usually built with a larger air-gap length than IPM motor due to the construction constraints. As a result, the torque production capability of SPM motor will be compromised. IM has the lowest torque ripple. However, it generates only 73% of the torque compared with IPM. SRM presents the lowest average torque and highest torque ripple of the four motors.

To evaluate the applicability in EV applications, nine performance indices are compared in Fig. 2.4.23, i.e. torque/power density, torque ripple, efficiency, power factor, field weakening ability, DC-link voltage utilisation, power converter requirement, noise/vibration, and fault tolerance. In addition to high torque/power density, high efficiency and good fault tolerance, power factor is a good indicator for the inverter size. Extended speed range can be evaluated according to DC-link voltage utilization and field weakening capability. Low noise emissions and torque ripples are crucial for comfort. Power converter requirement is directly related to the system cost.

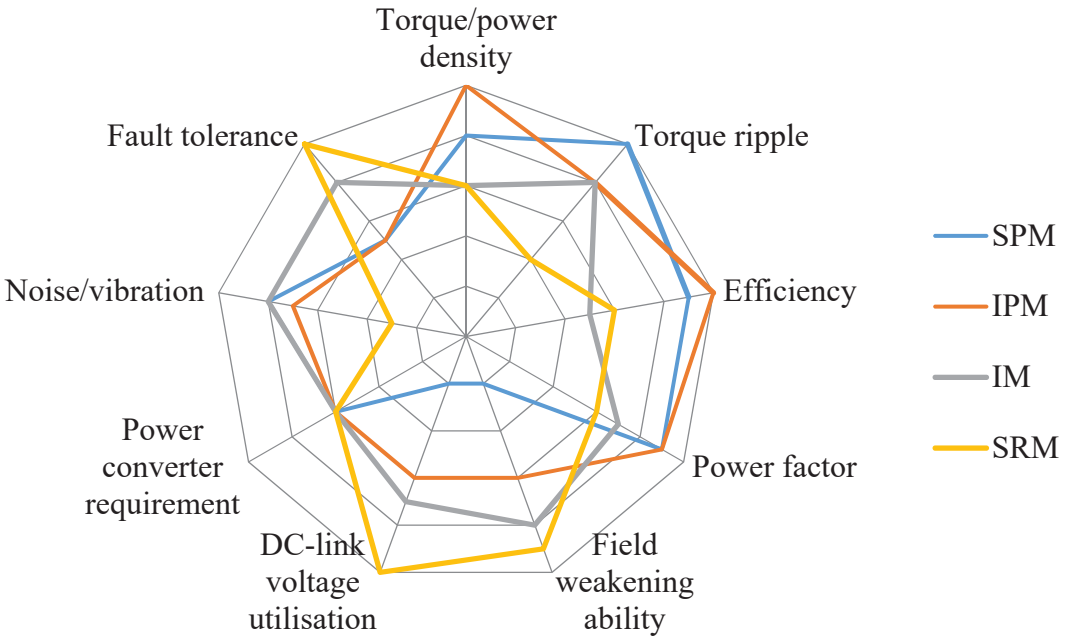

Fig. 2.4.23 Comparison according to the applicability in EV applications (derived from the analysis of [2.41])

Table 2-3 Electric Motors in Electric Vehicles (extracted from [2.30])

Vehicle	**Motor type**	**Rated Torque (Nm)**	**Rated Power (kW)**
Nissan Leaf	IPM	254	80
Mitsubishi i-MiEV	PMSM	196	49
Volkswagen e-Golf	PMSM	270	85
Honda FIT EV	PMSM	256	92
BMW i3	Hybrid PMSM	250	125
Ford Focus EV	PMSM	250	107
KIA Soul EI	IPM	285	81.4
Mercedes B-Class	IM	340	132
BYD e6	PMSM	450	90
Toyota RAV4 EV	IM	370	115
Tesla Model S 60	IM	430	283
Tesla Model 3	PMSM	430	192

From above qualitative evaluations, it can be found that PM machines are the ideal candidate for modern EV applications. This conclusion was also confirmed by recent developments in the EV industry. Table 2-3 summarises the electric motors used in popular EVs on the market [2.30]. The table reveals that almost the entire passenger EV industry has shifted to PM machines in order to meet the increasing power density and efficiency requirements.

2.5 The State of the Art of PMSMs

PM machines are the most efficient of all types of electrical machines due to the use of permanent magnets for rotor field excitation, which consumes no power in motor operation. Other merits of PM machines include simple control technique, high power density, and ease of cooling. However, PM machines also suffer from some disadvantages, such as narrow constant power speed range, possible demagnetization, and high cost.

The topologies of PM machines are various. According to the location of PMs, they can be divided into two categories: PMs on rotor and PMs on stator.

2.5.1 Permanent magnets on the rotor

Similar to the conventional synchronous machine, the stator has the three-phase distributed armature winding in the stator. When the armature winding is fed with three-phase sinusoidal currents, a synchronously rotating sinusoidal air-gap flux is created. Hence, the PM rotor with the same number of poles as the rotating air-gap flux always rotates in synchronism, which depends on the applied frequency.

This is a classical topology of PM machines, including the SPM machine and IPM machine. The IPM machine can be further classified as surface-inset, interior-radial, and interior-circumferential topologies as shown in Fig. 2.5.1.

- Fig. 2.5.1 (a): surface-mounted topology. The PMs are simply glued on the rotor surface, which offers the advantage of simplicity of manufacture. Since the permeability of PMs is near to that of the air, the effective air-gap is the sum of the actual air-gap length and the radial thickness of the PMs. The corresponding armature reaction field is small and the stator winding inductance is low. The d- and q-axis stator winding inductances are nearly the same. As a result, its reluctance torque is almost zero. In addition, there is a possibility that the PMs may fall off the rotor surface due to the centrifugal when operated at high-speeds.

- Fig. 2.5.1 (b): surface-inset topology. The PMs are inset into the rotor surface. The q-axis inductance becomes higher than the d-axis inductance, which produces an additional reluctance torque. Inserting the PMs in the rotor can offer better mechanical integrity than the one in Fig. 2.5.1 (a), and can stand higher centrifugal force at high-speeds.

- Fig. 2.5.1 (c): interior-radial topology. The PMs are radially buried inside the rotor. Compared with the one in Fig. 2.5.1 (b), this topology enables the PMs to be protected from flying apart and improve the mechanical integrity for high-

speed operation. Due to its *d–q* axis saliency, an additional reluctance torque can be generated.

- Fig. 2.5.1 (d) interior-circumferential topology. The PMs are circumferentially buried inside the rotor. It takes the definite advantage that the air-gap flux density can be higher than the PM remanence, i.e. flux-focusing or flux-concentration. It possesses the merits of both good mechanical integrity and additional reluctance torque. However, because of the significant flux leakage at the inner ends of PMs, a nonmagnetic shaft or collar is generally required, which may degrade the torsional stiffness of the rotor shaft.

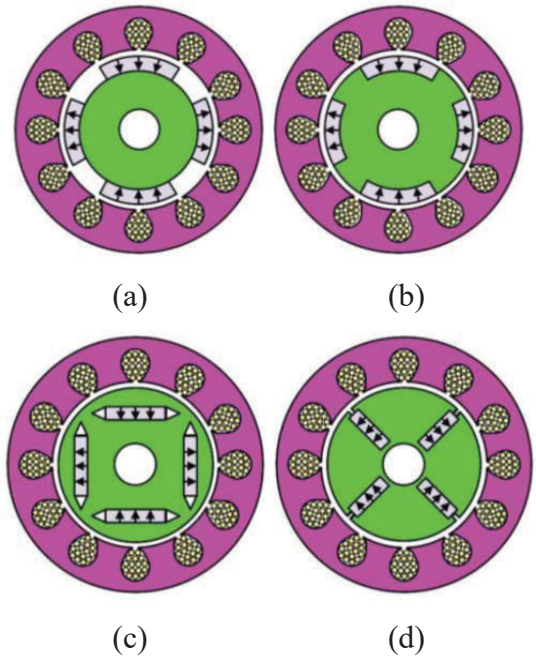

Fig. 2.5.1 PM synchronous machine topologies: (a) surface-mounted, (b) surface-inset, (c) interior-radial, and (d) interior-circumferential (from [29])

Numerous novel designs IPM machines have been proposed. In 1995, M. Azizur Rahman and Ruifeng Qin designed a PM hysteresis hybrid synchronous motor which is the combination of conventional stator and hybrid rotor, as shown in Fig. 2.5.2(a) [2.93]. On the rotor, PMs are inserted in the slots at the inner surface of the hysteresis material ring. The merit of this design is the high starting torque due to the magnet brake torque of a conventional PM motor compensated by the high eddy current and hysteresis torques. At the synchronous speed, the motor behaves as a permanent magnet motor due to the absence of eddy current torque.

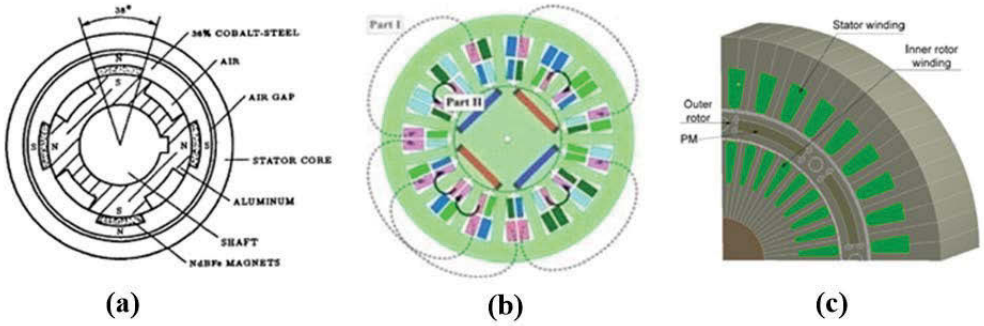

Fig. 2.5.2 Cross sectional view of (a) PM hysteresis hybrid machine (from [2.93]), (b) 4-layer hybrid winding machine (from [2.94]), and (c) double rotor synchronous PM machine (from [2.95])

In 2010, Won-ho Kim, and Jae-Nam Bae, *et al*., suggested a 4-layer hybrid winding (concentrated and distributed winding) layout designing to extend the operating range of IPMSM, shown in Fig. 2.5.2(b) [2.94]. This design has more sinusoidal air-gap flux density and higher power density.

Also in 2010, Peter Pisek, and Bojan Stumberger, *et al*., designed a double rotor synchronous PM machine which can be used in HEVs or EVs as a traction motor or generator, as shown in Fig. 2.5.2 (c). The merits of this design are high torque density and low torque ripples [2.95].

Rotor shaping methods can effectively minimise the torque ripple. However, the fundamental air-gap flux density and the torque density decrease as well. In 2014, K. Wang and Z. Q. Zhu, *et al*., proposed a rotor shaping technique with optimal third harmonic to enhance the average torque of IPM machines, as shown in Fig. 2.5.3 [2.96].

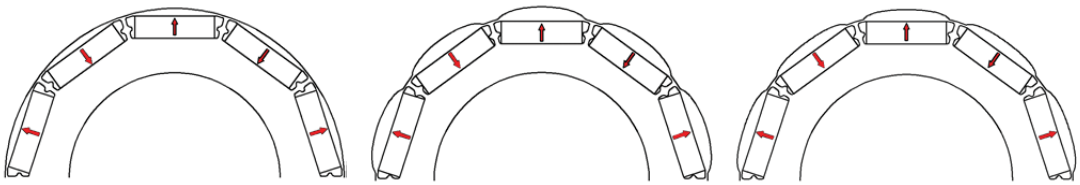

(a) (b) (c)

Fig. 2.5.3 IPM machines with different rotor structures: (a) conventional rotor, (b) inverse-cosine-shaped rotor, and (c) inverse-cosine-shaped with third harmonic rotor (from [2.96])

In 2017, Nan Zhao and Nigel Schofield proposed the pole shoe rotor topology as shown in Fig. 2.5.4. Compared to the conventional IPM machines, rotor poles of the pole shoe machines are shaped to achieve a more sinusoidal airgap flux distribution, which can reduce the machine phase back electromotive force (back *emf*) harmonics and on-load torque ripples [2.97].

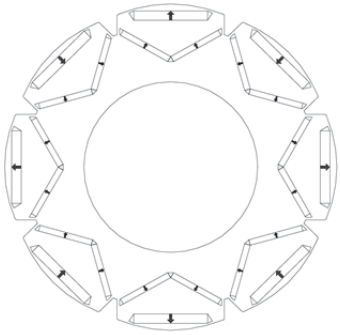

Fig. 2.5.4 Proposed pole-shoe rotor (from [2.97])

2.5.2 Permanent magnets on the stator

When the permanent magnets are located on the stator, the rotor must have salient pole geometry, making it similar to a SRM. This topology has inherently the advantages of a simple and rugged structure, high speed operation and good heat dissipation. Some machines have PMs located in the stator back-iron, which are named doubly salient permanent magnet (DSPM) machines, and others have PMs fitted in the stator teeth, known as flux switching permanent magnet (FSPM) machines.

Doubly Salient Permanent Magnet Machines

The DSPM was first proposed by Yuefeng Liao and Feng Liang in 1992 [2.98], which is an evolution of the doubly salient homopolar inductor machine. In a DSPM, the field excitation is supplied by the PMs which are planted in the stator or rotor. The torque is produced by both PMs' flux and current excitation flux in the windings. The basic structure of DSPM is similar to that of SRM as shown in Fig. 2.5.5 (a). The major advantages of the DSPM are high torque density, high efficiency, simple and rugged structure, high speed capability, small VA rating of the power converter and fast response times. The drawbacks of DSPM are poor torque quality and limited speed range which is critical for EVs.

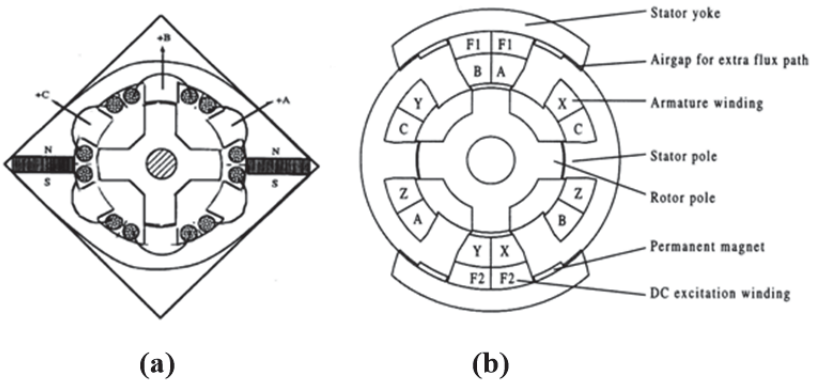

Fig. 2.5.5 Cross sectional view of (a) the first proposed DSPM, and (b) stator doubly fed DSPM (from [[2.98]])

In recent years, to extend the speed range and improve the efficiency of DSPM for EV applications, numerous novel designs have been proposed. In 2003, K.T. Chau suggested a stator doubly fed DSPM, which consists of two types of stator windings, a three-phase armature winding and a DC field winding as shown in Fig. 2.5.5 (b) [2.99]. The three-phase armature winding operates like that in the conventional DSPM, whereas the DC field winding works as a tool for flux weakening or flux strengthening. Moreover, an extra flux path is added in this topology to reinforce the effect of flux weakening and flux strengthening. With the help of these artful designs, the constant power operation range can be extended to four times that of the base speed which is suitable for EV applications. The efficiency on the flux weakening operation is also improved.

In 2005, Xiaoyong Zhu and Ming Cheng proposed a stator hybrid excited doubly salient permanent magnet (SHEDS-PM) brushless machine with a magnetic bridge as shown in Fig. 2.5.6, which is a similar approach to that suggested by K.T. Chau in 2003 [2.100]. The magnetic bridge could maintain the entirety of the stator lamination as well as amplify the effect of DC excitation flux on PM flux.

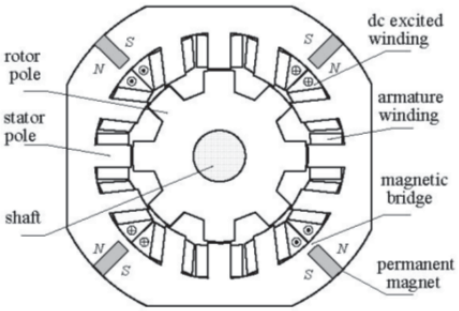

Fig. 2.5.6 Structure of SHEDS-PM (from [[2.100]])

In 2016, Ibrahim. Afinowi and Z. Q. Zhu designed a novel DSPM machine with 12/10 stator/rotor poles, as shown in Fig. 2.5.7. This machine features lower torque ripple, lower acoustic noise/vibration, negligible cogging torque and fail-safe capability [2.101].

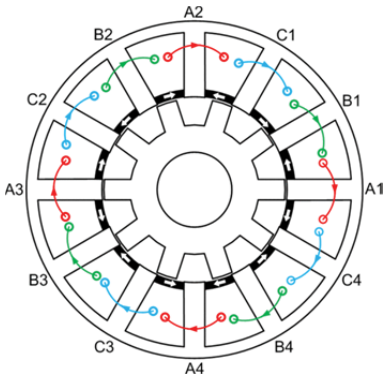

Fig. 2.5.7 DSPM machine with 12/10 stator/rotor poles (from [2.101])

In 2017, Mingjie He, Wei Xu and Caiyong Ye proposed a 4/6 single-phase DSPM machine with asymmetric stator poles, as shown in Fig. 2.5.8. The authors claims that the output torque and PM cost based on the new machine can be improved 11% and reduced 6% in comparison with those of the traditional DSPM [2.102].

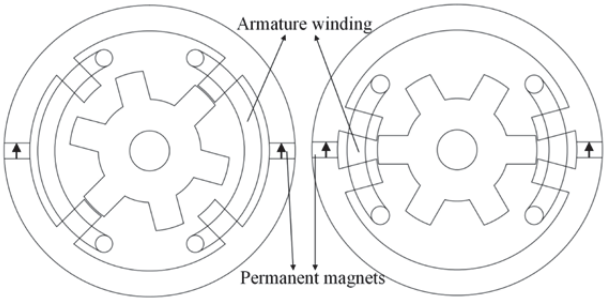

Fig. 2.5.8 Topologies of DSPM machine: (a) Traditional and (b) Proposed (from [2.102])

Flux Switching Permanent Magnet Machines

The concept of FSPM was firstly proposed by S.E. Rauch and L.J. Johnson in 1955 and was used in 4/2 pole and 4/6 pole flux-switch alternators which are designed for missiles as shown in Fig. 2.5.9 (a) and (b) [2.103].

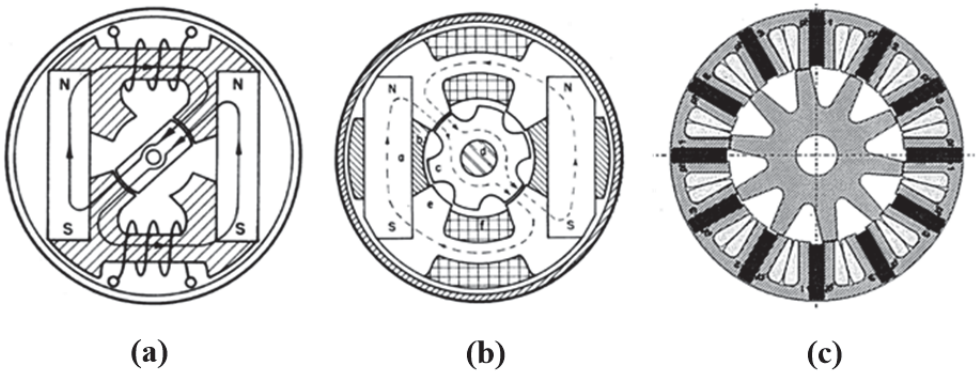

Fig. 2.5.9 Structure of (a) 4/2 pole flux-switch alternator (from [2.102]),
(b) 4/6 pole flux-switch (from [2.103]) alternator, and
(c) FSPM proposed by E. Hoang in 1997 (from [2.104])

In 1997, E. Hoang presented a new structure of FSPM with PMs inserted in the stator teeth and full pitch concentrated stator winding which can be considered as the modern conventional FSPM [2.104]. As shown in Fig. 2.5.9 (c), due to the air gap flux being a compound of the PM flux and the winding excitation flux, in theory, the capability of flux weakening is infinite. Besides the inherent merits of the SRM and PM machine, the most prominent advantage of the proposed design is its wide operating speed range. Although the structure of FSPM is similar to that of SRM, the acoustic noise of FSPM is lower than that of SRM by the help of a different flux control method.

In the last decade, numerous novel FSPM topologies have been developed for various applications as shown in Fig. 2.5.10. The fault-tolerant design proposed by R.L. Owen and Z.Q. Zhu in 2008, is achieved by employing an alternate pole and wound windings topology, as shown in Fig. 2.5.10 (b) [2.105]. However, the conventional FSPM machine has the demerit of high magnet volume, which can be improved by replacing the stator pole without armature winding with a simple stator tooth, as shown in Fig. 2.5.10 (c) E-core FSPM [2.106]. Moreover, the simple stator tooth can be removed to enlarge the slot area, and consequently the C-core FSPM is produced as presented in Fig.

2.5.10 (d). As shown, the rotor pole number is twice of the stator pole number in the E- and C-core FSPM designs, whilst they are equal in the conventional FSPM. In order to improve the torque density, in 2008, Z.Q. Zhu, and J.T. Chen, *et al*., presented a multi-tooth FSPM topology as shown in Fig. 2.5.10 (e). However, as the magnetic circuit becomes saturated more quickly as the current is increased, its torque capability becomes inferior to that of a conventional FSPM machine, due to the higher armature reaction.

In 2012, A. Zulu suggested a novel FSPM design with segmental rotor, as shown in Fig. 2.5.10 (f) [2.107]. The idea of this design is to provide a defined magnetic path for conveying the field flux to adjacent stator armature coils as the rotor rotates, in order to shorten the end-winding and improve the overall efficiency. However, further study should be carried out, due to the normal experimental performance compared with the conventional FSPM. Also, the hybrid excited FSPM evolved from the conventional FSPM was proposed in 2007 by E. Hoang and M. Lecrivain as shown in Fig. 2.5.10 (g). A DC excitation winding was added in the back of the PMs, in order to modulate the excitation of the permanent magnets. In this way, both the flux weakening and flux strengthening effect can be achieved for a wide speed range in a constant power region and high torque at starting period. A partitioned-rotor FSPM was designed by Zixuan Xiang, Li Quan and Xiaoyong Zhu in 2016 [2.108]. The authors claim that the proposed motor not only can retain the high torque density and efficiency but also can avoid the stator flux leakage and improve the PM utilization significantly, as shown in Fig. 2.5.10 (h). In 2016, T.S. Wang and J.G. Zhu, *et al*. proposed an axially laminated FSPM (ALFSPM) machine, as shown in Fig. 2.5.10 (i) [2.109][2.110]. The windings and magnets of this machine are located in the stator, while the rotor is passive with great mechanical robustness. Inheriting the merits of both switched reluctance machine and traditional rotor-PM machine, it has good attributes of high torque/power density, high efficiency, excellent flux-weakening capability, strong robustness, and convenience of cooling.

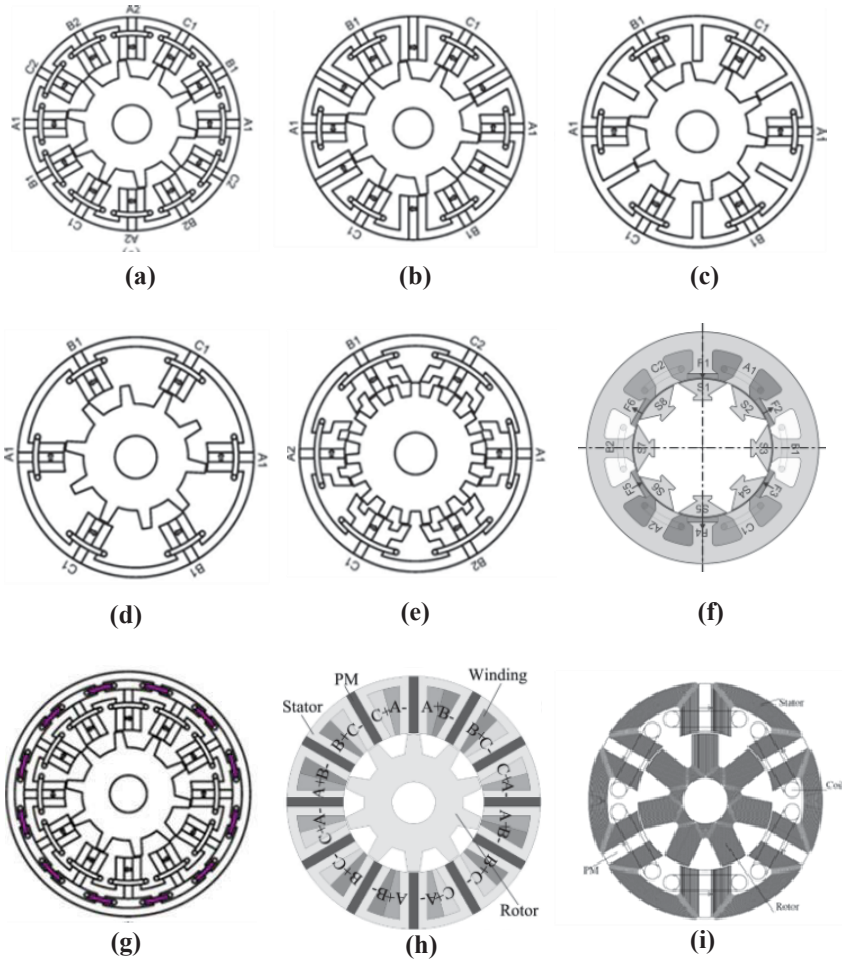

Fig. 2.5.10 Topologies of modern FSPM, (a) conventional FSPM, (b) fault-tolerant FSPM (from [2.105]), (c) E-core FSPM (from [2.106]), (d) C-core FSPM(from [2.106]), (e) multi-tooth FSPM(from [2.106]), (f) segmental rotor FSPM(from [2.107]), (g) hybrid excited FSPM(from [2.104]), (h) partitioned-rotor FSPM (from [2.108]), and (i) axial laminated structure FSPM (from [2.110]),

2.6 Electric Motor Control Techniques

2.6.1 Six-step control

The conventional DC machines feature high performance and high efficiency. However, the major drawback is that they need a commutator and brushes which are subject to wear and require maintenance. The development of solid-state switches enabled the realization of maintenance-free machines which are known as electronically commutated motors (ECMs) [2.111] or brushless DC (BLDC) motors [2.112][2.113]. The BLDC motor was first developed in 1964 by the National Aeronautics and Space

Administration (NASA) [2.114].

The basic principle of BLDC motors and conventional DC motors are almost the same. The primary difference is the inverse relationship of rotating and stationary components. The conventional DC motors have a stationary magnetic field and rotating armature, while the BLDC motors have a rotating PM rotor and stationary armature windings. In the six-step control method, the solid-state switches function as the commutators and brushes, in order to commutate the stator current [2.115].

The PM BLDC motors are different from PMSMs in that the former's back *emf* waveform is rectangular or trapezoidal, whereas the latter is sinusoidal, as shown in Fig. 2.6.1. The electrical cycle of the BLDC rotor is divided into six sectors, and the control method of BLDC motors, known as the six-step method, can be implemented by detecting the rotor position to generate the gating signals to control the six solid state switches of the three phase inverter. The most common position sensor used in BLDC motors is the Hall element, or switching Hall sensor. The installation position of the sensors is shown in Fig. 2.6.2. Compared with the other rotating position sensors, such as encoder, resolver or linear Hall sensors, the Hall elements are cheaper and more robust. However, they can only produce low resolution feedbacks as shown in Fig. 2.6.3.

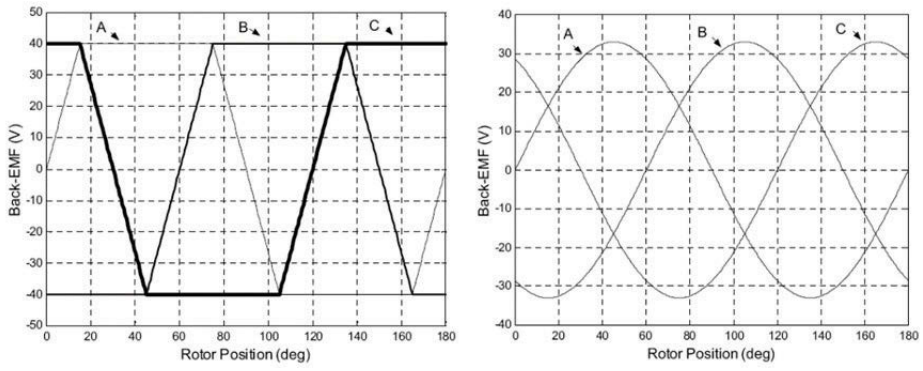

(a) (b)

Fig. 2.6.1 Back *emf* waveform of BLDC and PMSM: (a) Trapezoidal back *emf* of BLDC motor, and (b) Sinusoidal back *emf* of PMSM.

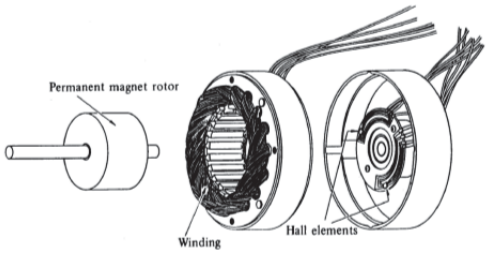

Fig. 2.6.2 Disassembled view of a BLDC motor: PM rotor, winding and Hall elements (from [2.116])

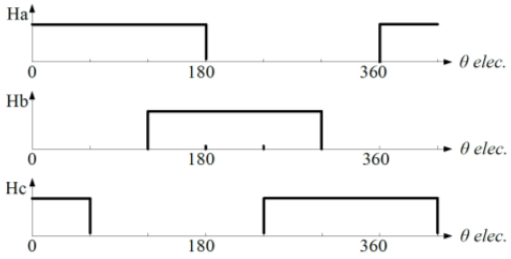

Fig. 2.6.3 Feedback signals generated by Hall elements

The six-step control methods for BLDC motors can be classified into 120° and 180° conduction modes [2.117]. In the 120° conduction mode, known as the two-phase feeding mode [2.118], only two switches are turned on at a time and the electronic commutation takes place every 60 electrical degrees. The inverter operates as a commutator feeding the DC current into two phases of the motor. The third phase can be considered as open circuit. The rotating magnetic field is created by commutating the DC current from phase to phase at intervals equivalent to 60 electrical degrees. The commutation is synchronized to the rotor position sensor signals. Under this mode, each inverter switch works for 120 electrical degrees in every cycle.

Under the 180° conduction mode, the electronic commutation interval is still 60 electrical degrees but three switches are turned on at one time. All inverter switches conduct for 180° in one cycle. The 120° conduction method is more popular in the controller design and applications (as will be explained below). The inverter status in these conduction modes are shown in Fig. 2.6.4.

For a star connected BLDC motor, the overall torque generation depends on the conduction modes. For example, when the DC bus current fed to the armature windings is constant and the switches T1 and T2 are turned on in the 120° conduction mode, the

currents in phase *A* and *C* have the same magnitude but different direction. The total electromagnetic torque is equal to $\sqrt{3}T_a$, which can be obtained by the arithmetic sum as shown in Fig. 2.6.5 (a), where T_a is the electromagnetic torque produced by phase *a* current. In 180° conduction mode, inverter T1, T2, and T6 are turned on and the total electromagnetic torque is only 1.5 T_a, as shown in Fig. 2.6.5 (b).

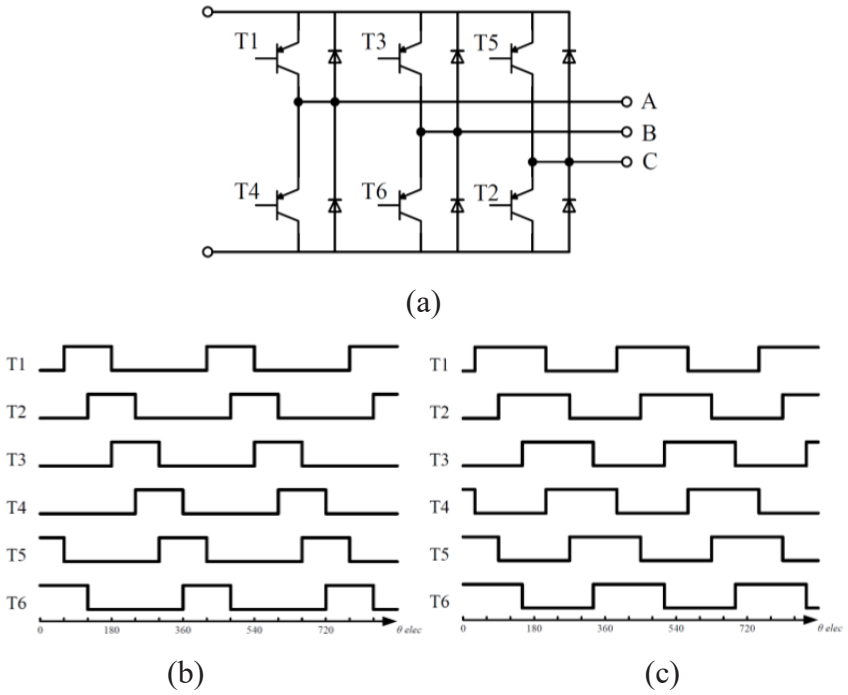

Fig. 2.6.4 Inverter diagram and conduction modes for six-step control: (a) Inverter structure, (b) Switch status at 120° conduction mode, and (c) Switch status at 180° conduction mode

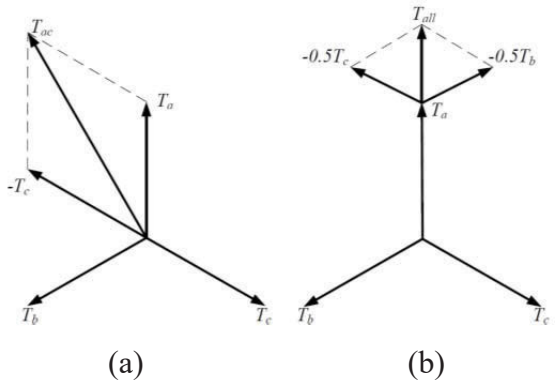

Fig. 2.6.5 Torque generation under different conduction modes: (a) Torque composition in 120° conduction mode, and (b) Torque composition in 180° conduction mode

2.6.2 Field oriented/vector control

In the 1990s, with the availability of high energy permanent magnet materials and fast switching power electronic devices, much progress has been achieved for PMSM drives. However, the nonlinear characteristics and inherent coupling problem of the PMSM make the torque control difficult. Fortunately, field oriented or vector controlled PMSM drives play an important role in providing good performance characteristics similar to or even better than those of DC motors.

The vector control (VC) or field oriented control (FOC) scheme was proposed in the 1970s by Blaschke [2.119]. It is a fundamental method for controlling AC machines by essentially transforming their dynamic structure into that of DC machines. The VC method was developed based on the Park transform, which was proposed to model the synchronous machines [2.120][2.121]. The control objective is to decouple the stator current i_s, into its flux producing and torque producing components, i_d and i_q, respectively. This method enables independent control of the field and torque of the machine by manipulating the corresponding field-oriented quantities. This system adapts to any load disturbances and/or set-point variation as fast as a DC motor can operate.

The VC controller for PMSMs was proposed based on the original FOC concepts, transferring the electrical excitation field to a permanent magnet based field [2.122]. Striving for a sinusoidal *emf* of the motor, the power and the torque transmitted are independent of time and rotor angle. The stator current can be subdivided into its *d*- and *q*-axis components, i_d and i_q, respectively. Only the component i_q develops the torque for non-salient pole rotor machines, whereas i_d influences the magnitude of the air-gap field. In order to develop the required torque at minimum current, the phase angle of the current is chosen in a way such that no i_d component exists. The desired locus of stator current spatial vector is that of a round circle. Fig. 2.6.6 shows the diagram of the classical VC scheme for PMSMs.

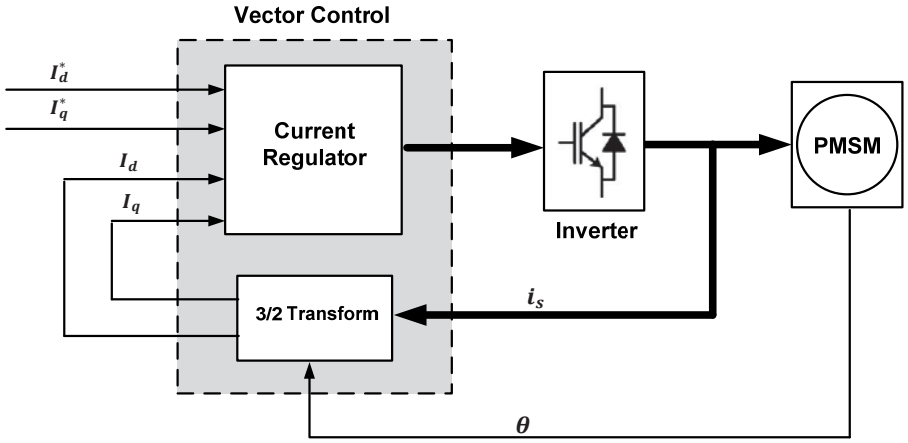

Fig. 2.6.6 Diagram of vector control drive system

Based on the VC scheme, the motor currents and voltages are manipulated in the *dq* reference frame. This means that the measured motor currents must be mathematically transformed from the three phase static reference frame of the stator windings to the rotor *dq* reference frame, prior to being processed by the PI controller. Later, the voltages have to be transformed from the *dq* frame to the *abc* reference frame for the PWM output. For these transformations, the fast and intensive calculation capability of a high performance microprocessor or digital signal processor (DSP) is necessary. The powerful microprocessors or DSP have presented an effective solution to the high performance digital PMSM controllers. Additionally, the availability of the unexpected computation of microprocessors or DSPs has also made the current controller possible.

In 1986, a digital-based speed loop was reported with an analogue internal current controller [2.123]. In 1988, a DSP vector controller was reported, but the detailed implementation was not proposed [2.124]. The theoretical background to the digital implementation of vector and current control was proposed in [2.125], which makes a fully operational digital implementation of the vector/current controllers available and reliable. Based on the previous research, in [2.126], Allen applied a dual digital signal processor board for the control of PMSMs. As system reliability and cost reduction can be achieved by the full digital solution, a digital VC scheme has been developed with a space voltage modulation algorithm by Boldea and Nasar [2.127].

In 1992, Cecati presented the fully digital implementation of a classical rotor flux orientation (RFO) VC scheme for a PMSM drive [2.128]. Based on the cascade control,

the whole system is composed of two loops. The well-known principle of rotor flux oriented control is applied in the current control loop as the inner control loop, and the outer loop is for speed control, which is realized by PI controllers.

With the application of fast digital signal processors, the space vector modulation technique has been digitally implemented together with the VC scheme. In 1993, a new VC drive scheme was presented with an application specific integrated circuit for pulse width modulation (PWM) [2.129].

In 2002, Bolognani and Zigliotto designed a novel vector control scheme whereby the current space vector in the synchronous *d-q* reference frame is controlled [2.130]. The best voltage vector is applied in order to reduce the mean prediction based on motor equations, which somewhat recalls the direct torque control (DTC) methodology. The proposed algorithm is a hysteresis control on both current vector amplitude and torque angle. Simulation and experiment have confirmed the validity and simplicity of the method, which is particularly suited for low-cost and full-digital DSP based applications. In addition, the switching count is impressively reduced.

2.6.3 Direct torque control

In a VC based PMSM drive system, the output torque is controlled indirectly by regulating the stator current, meaning the efforts to improve the system's performance are mainly focused on estimating accurate machine feedback and developing an effective current controller, which will unfortunately increase the computation load, and slow down the system's dynamic response.

Another drive method for PMSMs was then proposed as DTC, which regulates the generated torque and air-gap flux directly. The DTC scheme was developed firstly for induction machines, by Takahashi as the DTC [2.131] and by Depenbrock as the direct self-control (DSC) [2.132]. The basic idea of DTC for the induction motor is to control the torque and flux linkage by selecting the voltage space vectors properly, which is based on the relationship between the slip frequency and torque [2.133]. It has been proven that DTC could be used for PMSM drives although there is little difference from that of induction motors. Fig. 2.6.7 shows a typical structure of the DTC system. The

current controller followed by a PWM comparator is not used in DTC systems, and the parameters of the motor are also not used, except the stator resistance [2.134]. Therefore, the DTC possesses advantages such as less parameter dependence and faster torque response when compared with the torque control via VC based current control. The switching state of the inverter is updated once only in every sampling interval and it does not change until the output of the hysteresis controller change states. Therefore, the ripples in torque and flux are relatively high when compared with those of the vector control drive system. Although a smaller hysteresis bandwidth may result in less torque ripples, the switching loss of the inverter will dramatically increase. Furthermore, the switching frequency of the inverter is not constant. The switching action only depends on the observed torque and flux linkage values. Therefore, the inverter switching frequency varies against the rotor speed, load torque and the bandwidth of the two hysteresis controllers [2.135][2.136].

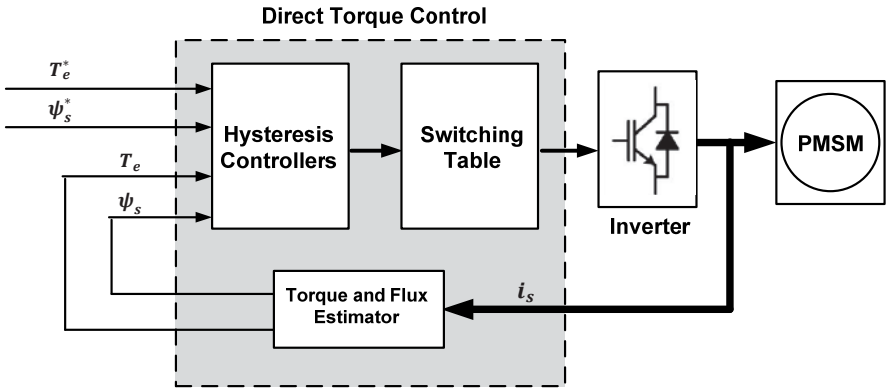

Fig. 2.6.7 Diagram of direct torque control drive system

Many schemes have been proposed to improve the DTC scheme to achieve better performance and they are summarized in Fig. 2.6.8. In [2.137]-[2.139], the hysteresis controllers are replaced by a fuzzy logic controller, which considers not only the sign of the error, but also the amplitude. In [2.140], neural network is used to select the vector. In [2.141]-[2.143], Output space regulation (OSR) is used to select the vector. The proposed strategies focus on a direct regulation of two outputs, namely torque and flux amplitude. These strategies are based on the minimization of a weighted function of quadratic or absolute value functions of the output errors. The classic DTC is considered as a special case of OSR and it belongs to the class of strategies based on a quadratic criterion. In [2.144], a 3-level inverter fed DTC scheme with modified

switching table is proposed to improve performance at low speed. However, it failed to consider other problems, such as neutral point balance and voltage jump. In [2.145], the duration time, i.e. duty ratio of the selected vector is obtained by solving the optimal value which will lead to minimum torque ripple RMS during one period. In [2.146], the duty of the active vector in one period can also be obtained from a fuzzy logic controller. However, the performance improvement is quite limited. In [2.147], a band-constrained technique is proposed, which aims at limiting the torque ripple to the hysteresis band, not the minimal RMS of torque ripple. A completely different approach to achieve better performance has been proposed in [2.148] and [2.149], which consists of replacing the hysteresis torque and flux controllers with proportional–integral (PI) regulators and voltage modulators. However, it reduces the simplicity of the classic DTC scheme.

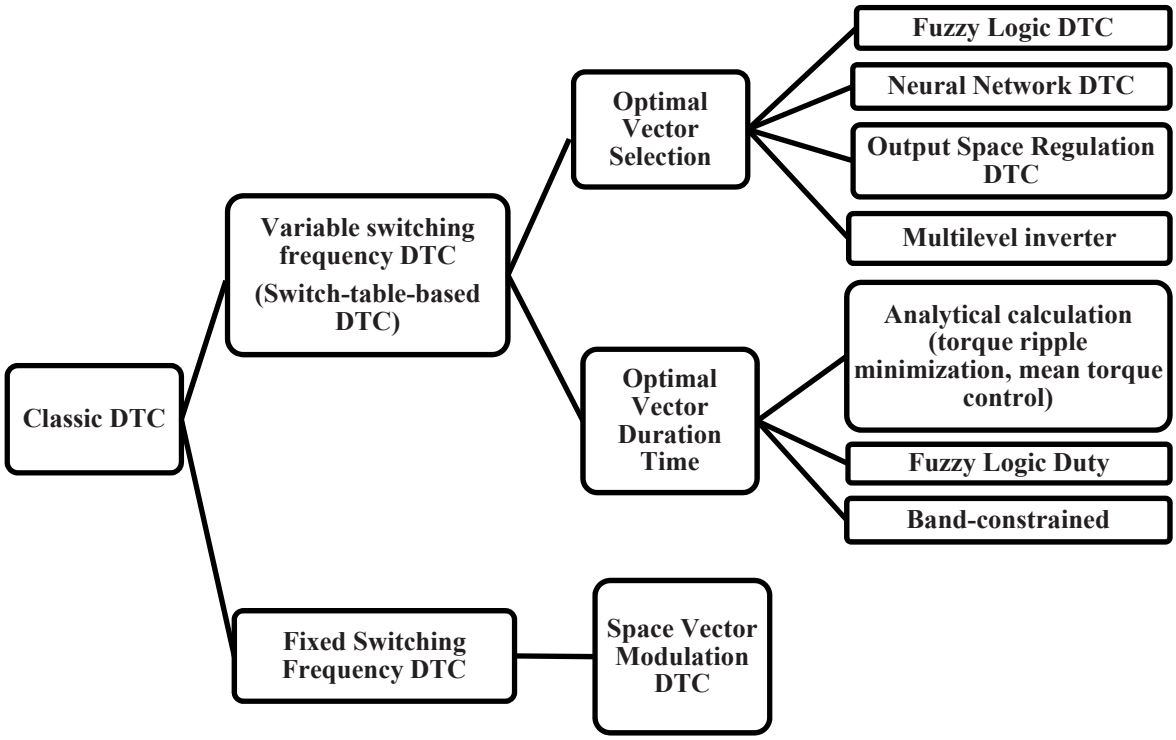

Fig. 2.6.8 Development of DTC scheme

2.6.4 Model predictive control

The linear PID-controllers used in electrical drive system were widely built with analogue operational amplifiers and used the control deviation to generate the commanding signal [2.150]. This type of controller does not include any knowledge of the plant and this knowledge is only required for designing the controller. With the availability of inexpensive microcomputers and digital control techniques in drive system, the idea to pre-calculate the plant's behaviour via a mathematic model and to determine the optimum values for the actuating variables from these pre-calculated values, i.e. predictive control, was born.

In terms of the functional principles of the different predictive control algorithms, they can be classified into three main groups: hysteresis-based, trajectory-based, and model-based strategies.

The basic principle of hysteresis-based control strategies is to keep the value of the controlled variable within a tolerance band or a tolerance area, i.e. the so-called hysteresis. The simple form of such a controller is the well-known hysteresis or bang-bang controller. Hysteresis-based strategies have the advantage that precise knowledge of the drive system is not required. Even with possible model divergences the control error can be kept within the specified limit band by the hysteresis controller. To achieve this, it must always be ensured that the hysteresis controller reacts very quickly if the actual value has gone outside of the hysteresis band. This is a major problem if the hysteresis-based predictive controller is implemented in a digital processor, as the detection of the reference signal crossing the hysteresis band will be done only during the next sampling instant. At this time, it may happen that the error has grown to a large value. Hence, the hysteresis-based predictive control is more suitable when the realization is done using analogue operational amplifiers rather than microprocessor controllers.

The trajectory-based control methods are based on the principle to force the system onto pre-calculated system trajectories. Once the system has been pushed onto one of these trajectories, it remains there because of its own properties until a change is enforced form outside. The trajectory-based control is based on a very precise prediction of the

future control system behaviour. Hence, in contrast to hysteresis controllers, controllers of this type require an exact model of the system to be controlled. Because of the quite complex pre-calculation of the system trajectories, these methods are better suited for implementations in the form of digital controllers on microprocessors.

Both hysteresis and trajectory-based predictive controllers use the current system state to pre-calculate the value of the controlled variable for the next sampling cycle. The past is not explicitly taken into consideration as it is hidden in the actual system state. Although there is a relationship between hysteresis and trajectory-based predictive control algorithms, model-based strategies are based on completely different ideas. Model-based predictive control methods are able to consider the past and to optimize the future values of the actuating variables, not only for the next sampling cycle, but also up to a specified future cost or control horizon.

The model predictive control (MPC) is derived from a rather old approach whose first ideas were published more than 20 years ago [2.151][2.152]. Its strategies are based on an explicit and identifiable model of the controlled system, which is used to pre-calculate the behaviour of the plant and to choose an optimal value of the control variables. Because of the great computational power required by MPC, its implementation has been formerly limited to slowly varying systems, such as chemical processes, in which the time interval is long enough to process the complete control algorithm. As the performance of the available computing hardware has rapidly increased and new faster algorithms have been developed, it is now possible to implement MPC for fast systems using shorter time steps.

MPC makes explicit use of the system mathematical model to predict the future behaviour of the system. An optimal aim is defined and solved in MPC to obtain the most appropriate control input. Similar to the nature of FOC and DTC, MPC can also be classified into two categories: continuous MPC [2.153], [2.154] and finite control set MPC (FCSMPC) [2.155], [2.156]. Like FOC, the continuous MPC also requires the use of PWM or the concept of duty cycle, which fails to consider the discrete nature of the converter. In contrast, FCSMPC evaluates the effects of each possible voltage vector and the one that minimizes the error between the reference value and the feedback value is selected. FCSMPC is similar to DTC in that they both directly select one and only

one voltage vector during one control period. Due to its intuitive concept and simple principle, FCSMPC has been widely studied and applied to the control of power converters and motor drives. FCSMPC can be categorized into two groups according to the predictive horizon N [2.156] [2.157]. With a short predictive horizon of N = 1, the calculation burden is relatively small and can be easily implemented in modern DSPs. With a longer predictive horizon of N > 1, it is possible to obtain a better control performance. In [2.157], for a three-level inverter-fed DTC motor drive, a predictive horizon greater than one is employed to obtain reduced switching frequency whilst keeping the torque, flux, and neutral point potential within their respective hysteresis bands.

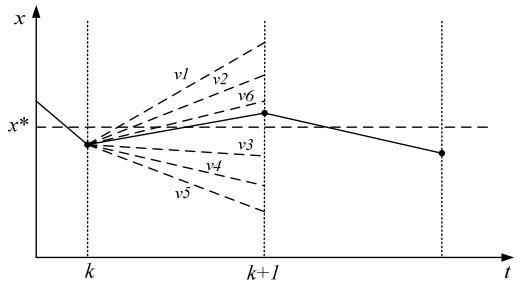

Fig. 2.6.9 Finite control set MPC scheme

Delay compensation is an important issue in the implementation of FCSMPC [2.158][2.159]. It is widely recognized that there is a one-step delay between the commanding voltage and the applied voltage, which means that the commanding voltage obtained at any current time instant will not be applied until the next time instant. This delay is usually caused by the update mechanism in DSP. The influence of one-step delay is especially serious when the sampling frequency is low. As MPC uses the internal model to predict the future behaviour of the system, it is natural to further use the predictive results to eliminate the one-step delay, which is called a two-step prediction in [2.160].

For power converters and inverter-fed drives, it is desirable to reduce the switching frequency to obtain reduced switching loss and higher efficiency [2.157][2.158][2.161]. However, so far the incorporation of switching frequency reduction in MPC for motor drives is very rare. In [2.160], the application of MPC for the torque and flux control of an induction motor drive is investigated, but the switching frequency reduction is not

addressed. Reference [2.159] considered the switching frequency reduction in a three-level inverter fed induction motor drive by using hysteresis controllers. The implementation is complex and requires the use of ASIC to accomplish the fast computation requirement [2.162].

A cost function suitable for electrical machine drive systems was proposed by Kouro and Cortes [2.163]. The cost function evaluates all predictions and the one with the minimum cost is chosen. Then future control actions are implemented. In addition to the torque and stator flux, other control variables, such as switching frequency, efficiency and spectrum shaping can also be included in the cost function. The priority of each control variable is adjusted by weighting factors. This paper presents great ideas on implementation of MPC. However, it lacks experimental results to verify the effectiveness of the proposed method.

In [2.164], a guideline of the weighting factor design is presented, but it does not mention any analytical or numerical solution. The weighting factors are still determined by empirical methods.

In [2.165], T. Wang and C. Liu, *et al*., proposed a novel finite-control-set model predictive direct torque control with extended set of twenty modulated voltage space vectors. To mitigate the computational burden caused by the increased number of voltage space vectors, a pre-selective scheme is designed for the proposed FCS-MPDTC to filter out the impractical voltage vectors instead of evaluating all twenty voltage space vectors. The drive system efficiency of the conventional direct torque control, the conventional FCS-MPDTC, and the proposed method are investigated. The theory and simulation are validated by experimental results on a PMSM prototype.

2.6.5 Qualitative comparison of control methods

In general, the classic VC method can bring good performance to PMSM drive systems. However, in order to control the drive system in real time, a high computational power microprocessor is needed to perform complicated coordinate transformations. The classical DTC method works with hysteresis controllers and a switching table to achieve rapid response times. However, it is insensitive to machine parameter variations, and its

steady state performance is poor. In contrast, the MPC features both good dynamic and steady state performance. The most attractive feature of the MPC is the great flexibility of the cost function, i.e. the controllable variables such as torque ripple, switching frequency, and power loss can be included in the cost function.

The details of each control method are compared in Table 2-4.

Table 2-4 Qualitative comparison of control methods

	Classic FOC	**Classic DTC**	**MPC**
Speed Estimation	Encoder output	Encoder output	Encoder output
Speed Controller	PI controller	PI controller	Cost function definition
Flux-linkage Estimation	N/A	*abc*-to- *αβ* transformation with Integration	*abc*-to-*dq* transformation
Flux-linkage Controller	N/A	Hysteresis controller	Cost function definition
Current/Torque Estimation	*abc*-to-*dq* transformation	Calculation from flux linkage and currents	*abc*-to-*dq* transformation
Current/Torque Controller	PI controller	Hysteresis controller	Cost function definition
Inverter Control	PWM	Look-up table	Cost function definition

2.7 Summary

In this chapter, a thorough literature survey on the development of EVs, electric motors used in EVs and machine control strategies has been conducted. In Section 2.2-2.4, the fundamentals and key features of DC machine, IM, SRM and PMSM are presented. With a detailed comparison of the above machines, PMSM appears to be an ideal

candidate for EV applications. This conclusion is also confirmed by the recent development in electric vehicle industry. Almost the entire light-duty hybrid electric vehicle industry has shifted to PMSMs in order to meet the increasing power density and efficiency requirements. In Section 2.5, the state of the art of PMSMs is introduced. In Section 2.6, various machine control techniques are reviewed and compared qualitatively.

REFERENCES

[2.1] C. R. Ferguson and A. T. Kirkpatrick, Internal Combustion Engines - *Applied Thermo-Sciences*, Second Edition, John Wiley & Sons, New York, 2001.

[2.2] 'Automobile emissions: An overview', U.S. *Environmental Protection Agency (EPA)*, EPA 400-F-92-007, Fact Sheet OMS-5, August 1994.

[2.3] 'Automobiles and ozone', *U.S. Environmental Protection Agency (EPA),* EPA 400-F-92-006, Fact Sheet OMS-4, January 1993.

[2.4] M. Ehsani, D. Hoelscher, N. Shidore, and P. Asadi, 'Impact of hybrid electric vehicles on the world's petroleum consumption and supply,' *Society of Automotive Engineers (SAE) Future Transportation Technology Conference*, Paper No. 2003-01 2310, 2003.

[2.5] J. E. Hake, 'International energy outlook—2000 with projection to 2020', http://tonto.eia.doe.gov/FTPROOT/presentations/ieo2000/sld008.htm, accessed 15 April 2016

[2.6] E. H.Wakefield, 'History of the Electric Automobile: Battery-only Powered Cars', *Society of Automotive Engineers (SAE)*, ISBN: 1-56091-299-5, Warrendale, PA, 1994.

[2.7] C. Ivan, 'All about Batteries, Part 3: Lead-Acid Batteries', *UBM Canon*, accessed 3 November 2015.

[2.8] L. David and B. Thomas, *Handbook of Batteries (3rd edition),* New York: McGraw-Hill. p. 23.5. ISBN 0-07-135978-8. 2002.

[2.9] C. Thomas Roy, *Battery Reference Book*, Newnes, 2000.

[2.10] M. Ehsani, Y. Gao and A. Emadi, *Modern Electric, Hybrid Electric, and Fuel Cell*

Vehicles: Fundamentals, Theory, and Design, Second Edition, ISBN 9781420053982, 21 September 2009.

[2.11] Y. Gao and M. Ehsani, 'An investigation of battery technologies for the Army's hybrid vehicle application', *in Proceedings of the IEEE 56th Vehicular Technology Conference*, Vancouver, British Columbia, Canada, September 2002.

[2.12] EV1 White Paper, https://web.archive.org/web/20090726034344/http://www.cleanup-gm.com/ev1.html, accessed 14 November 2017.

[2.13] F. Jamerson, 'EV1 Timeline', https://web.archive.org/web/20071216090230/http://www.evworld.com/article.cfm?storyid=1053, accessed 14 November 2017.

[2.14] T. Blade, 'Peugeot offers new small car in Europe', https://news.google.com/newspapers?id=hxEwAAAAIBAJ&sjid=RQMEAAAAIBAJ&pg=4874,1270397&dq=peugeot-106&hl=en, accessed 14 November 2017.

[2.15] E. H. Wakefield, 'History of the Electric Automobile: Hybrid Electric Vehicles', *Society of Automotive Engineers (SAE)*, ISBN: 0-7680-0125-0, Warrendale, PA, 1998.

[2.16] 'In search of the perfect battery', *The Economist*, 6 March 2008.

[2.17] Nickel Metal Hydride Handbook (PDF) (NiMH02.01 ed.). Energizer Battery Manufacturing.

[2.18] 'Nickel–Metal Hydride (NiMH) Battery Charger and Battery Pack. User's Manual', *Sea-Bird Electronics, Inc.,* accessed 14 November 2017.

[2.19] 'Charge Methods for Nickel Metal Hydride Batteries', *Nickel Metal Hydride Handbook*. Panasonic, accessed 14 November 2017.

[2.20] 'Chrysler Hybrid-Electric Cars of the 1990s: Dodge Intrepid ESX', *Allpar.com*. accessed 14 November 2017.

[2.21] 'Back on Next Concept-Car Story', *group.renault.com*, Chrono 115, Episode 5, accessed 14 November 2017.

[2.22] 'From Beetle to Up!: A Brief History of Volkswagen's Entry-Level Cars', *Car and Driver.* 1 September 2011.

[2.23] 'Toyota Prius Family', Toyota Motor Corporation, accessed 14 November 2017.

[2.24] 'Toyota Passenger Car Chronology', Toyota Motor Corporation,

http://toyotanews.pressroom.toyota.com, accessed 14 November 2017.

[2.25] 'NCR18650B Specifications', http://www.batteryspace.com, accessed 14 November 2017.

[2.26] 'NCR18650GA Specifications', http://www.batteryspace.com, accessed 14 November 2017.

[2.27] 'Rechargeable Li-Ion OEM Battery Products', *Panasonic.com*, accessed 14 November 2017.

[2.28] S. S. Williamson, A. K. Rathore and F. Musavi, 'Industrial Electronics for Electric Transportation: Current State-of-the-Art and Future Challenges', *in IEEE Transactions on Industrial Electronics*, vol. 62, no. 5, pp. 3021-3032, May 2015.

[2.29] K. T. Chau, *Electric Vehicle Machines and Drives: Design, Analysis and Application*, ISBN: 978-1-118-75252-4, May 2015.

[2.30] E. A. Grunditz and T. Thiringer, 'Performance Analysis of Current BEVs Based on a Comprehensive Review of Specifications', *in IEEE Transactions on Transportation Electrification*, vol. 2, no. 3, pp. 270-289, Sept. 2016.

[2.31] Tesla Official Website, *https://www.tesla.com/*, accessed 14 November 2017.

[2.32] J. Lu and J. Hossain, *Vehicle-to-Grid: Linking electric vehicles to the smart grid*, IET Digital Library, 2015.

[2.33] J. Ekanayake, K. Liyanage, J. Wu, A. Yokoyama, and N. Jenkins, *Smart Grid – Technology and Application*, John Wiley & Sons, 2012.

[2.34] P. Asmus, ''Why microgrids are moving into the mainstream', *IEEE Electrification Magazine,* March, 2014

[2.35] 'IEEE guide for design, operation, and integration of distributed resource island systems with electric power systems', *IEEE Standards Coordinating Committee 21,*IEEE Std 1547.4TM-2011, July 20, 2011

[2.36] W. Su, H. Rahimi-Eichi, W. Zeng and M. Chow, 'A survey on the electrification of transportation in a smart grid environment', *IEEE Transaction on Industrial Informatics,* Vol. 8, No. 1, February 2012.

[2.37] C. Pang, P. Dutta and M. Kezunovic, 'BEVs/PHEVs as dispersed energy storage for V2B uses in the smart grid', *IEEE Transaction on Smart Grid*, Vol. 3, No. 1,

March 2012.

[2.38] M. C. Kisacikoglu, B. Ozpineci and L. M. Tolbert, 'EV/PHEV bidirectional charger assessment for V2G reactive power operation', *IEEE Transaction on Power Electronics*, Vol. 28, No. 12, December 2013.

[2.39] F. Ahourai and M. A. Al Faruque, 'Grid impact analysis of a residential microgrid under various EV penetration rates', *Technical Report 13-08*, July 30, 2013.

[2.40] Q. Wu, *Grid Integration of Electric Vehicles in Open Electricity Market*, Wiley, 2013.

[2.41] E. Bostanci, M. Moallem, A. Parsapour and B. Fahimi, 'Opportunities and Challenges of Switched Reluctance Motor Drives for Electric Propulsion: A Comparative Study', *in IEEE Transactions on Transportation Electrification*, vol. 3, no. 1, pp. 58-75, March 2017.

[2.42] X. Shi and M. Krishnamurthy, 'Survivable Operation of Induction Machine Drives With Smooth Transition Strategy for EV Applications', *in IEEE Journal of Emerging and Selected Topics in Power Electronics*, vol. 2, no. 3, pp. 609-617, Sept. 2014.

[2.43] M. Jafari, A. Gauchia, K. Zhang and L. Gauchia, 'Simulation and Analysis of the Effect of Real-World Driving Styles in an EV Battery Performance and Aging', *in IEEE Transactions on Transportation Electrification*, vol. 1, no. 4, pp. 391-401, Dec. 2015.

[2.44] C. Dépature, W. Lhomme, A. Bouscayrol, L. Boulon, P. Sicard and T. Jokela, 'Characterisation of the electric drive of EV: on-road versus off-road method', *in IET Electrical Systems in Transportation*, vol. 7, no. 3, pp. 215-222, 9 2017.

[2.45] Z. Yang, F. Shang, I. P. Brown and M. Krishnamurthy, 'Comparative Study of Interior Permanent Magnet, Induction, and Switched Reluctance Motor Drives for EV and HEV Applications', *in IEEE Transactions on Transportation Electrification*, vol. 1, no. 3, pp. 245-254, Oct. 2015.

[2.46] Al-Khalili, Jim. 'The Birth of the Electric Machines: A Commentary on Faraday 'Experimental Researches in Electricity'', *Philosophical Transactions. Series A, Mathematical, Physical And Engineering Sciences,* PMC.

[2.47] 'Classification of Electric Motors', *ElectricalKnowhow, http://www.electrical-*

knowhow.com, accessed 14 November 2017.

[2.48] I. Boldea and S. A. Nasar*, Electric Drives, Third Edition*, June 30, 2016 by CRC Press

[2.49] G. Judith, 'Godfather of the Hybrid', *Engineering & Science. California Institute of Technology,* ISSN 0013-7812. 2012

[2.50] 'Toen al groen: Fiat Panda Elettra' (in Dutch). *FIATblog.nl,* accessed 14 November 2017.

[2.51] 'eBay watch: historic Fiat Panda electric car for sale', *greencarreports.com*, accessed 14 November 2017.

[2.52] 'Three Phase Induction Motor', *http://www.mytech-info.com,* accessed 14 November 2017.

[2.53] G. Pellegrino, A. Vagati, B. Boazzo and P. Guglielmi, 'Comparison of Induction and PM Synchronous Motor Drives for EV Application Including Design Examples', *in IEEE Transactions on Industry Applications*, vol. 48, no. 6, pp. 2322-2332, Nov.-Dec. 2012.

[2.54] E. Dehghan-Azad, S. Gadoue, D. Atkinson, H. Slater, P. Barrass and F. Blaabjerg, 'Sensorless Control of IM for Limp-Home Mode EV Applications', *in IEEE Transactions on Power Electronics,* vol. 32, no. 9, pp. 7140-7150, Sept. 2017.

[2.55] W. Li, J. Cao and X. Zhang, 'Electrothermal Analysis of Induction Motor With Compound Cage Rotor Used for PHEV', *in IEEE Transactions on Industrial Electronics*, vol. 57, no. 2, pp. 660-668, Feb. 2010.

[2.56] R.G. Arns, 'The other transistor: early history of the metal–oxide–semiconductor field-effect transistor', Engineering Science and Education Journal. 7 (5): 233–240, accessed 14 November 2017.

[2.57] B. Bowman, '1966 GM Electrovan', GM Heritage Center https://history.gmheritagecenter.com, accessed 14 November 2017.

[2.58] T. Quiroga, 'Driving the Future', Car and Driver, p. 52. August 2009.

[2.59] '20 Truths about the GM EV1 Electric Car', *GreenCar.com, http://www.greencar.com/features/gm-ev1/,* accessed 14 November 2017.

[2.60] 'Performance Specs', *Tesla Motors. https://www.tesla.com/*, accessed 14

November 2017.

[2.61] 'SEC Form 10-K for Fiscal Year Ended Dec 31, 2012, Commission File Number: 001-34756, Tesla Motors, Inc'. *SEC. 2016-02-06,* accessed 14 November 2017.

[2.62] 'Model S Specs and Standard features', *Tesla Motors. https://www.tesla.com/*, accessed 14 November 2017.

[2.63] T. Guo, N. Schofield and A. Emadi, 'Double Segmented Rotor Switched Reluctance Machine With Shared Stator Back-Iron for Magnetic Flux Passage', *in IEEE Transactions on Energy Conversion,* vol. 31, no. 4, pp. 1278-1286, Dec. 2016.

[2.64] W. Ding, S. Yang, Y. Hu, S. Li, T. Wang and Z. Yin, 'Design Consideration and Evaluation of a 12/8 High-Torque Modular-Stator Hybrid Excitation Switched Reluctance Machine for EV Applications', *in IEEE Transactions on Industrial Electronics,* vol. 64, no. 12, pp. 9221-9232, Dec. 2017.

[2.65] Y. Hu, W. Ding, T. Wang, S. Li, S. Yang and Z. Yin, 'Investigation on a Multimode Switched Reluctance Motor: Design, Optimization, Electromagnetic Analysis, and Experiment', *in IEEE Transactions on Industrial Electronics*, vol. 64, no. 12, pp. 9886-9895, Dec. 2017.

[2.66] J. Zhu, K. W. E. Cheng, X. Xue and Y. Zou, 'Design of a New Enhanced Torque In-Wheel Switched Reluctance Motor With Divided Teeth for Electric Vehicles', *in IEEE Transactions on Magnetics*, vol. 53, no. 11, pp. 1-4, Nov. 2017.

[2.67] M. Asgar, E. Afjei and H. Torkaman, 'A New Strategy for Design and Analysis of a Double-Stator Switched Reluctance Motor: Electromagnetics, FEM, and Experiment', *in IEEE Transactions on Magnetics*, vol. 51, no. 12, pp. 1-8, Dec. 2015.

[2.68] W. Wu, H. C. Lovatt and J. B. Dunlop, 'Optimisation of switched reluctance motors for hybrid electric vehicles', *2002 International Conference on Power Electronics, Machines and Drives*, pp. 177-182, 2002.

[2.69] 'Low emission vehicles', *CSIRO Pedia, https://csiropedia.csiro.au/low-emission-vehicles/*, accessed 14 November 2017.

[2.70] 'Nidec SR Drive Motors Power New Land Rover', *Nidec SR Drives Ltd*, *http://www.srdrives.com/land-rover.shtml*, accessed 14 November 2017.

[2.71] J. F. Gieras, *Permanent Magnet Motor Technology: Design and Applications, Third Edition*, 26 August 2009.

[2.72] M. P. Kazmierkowski, 'Handbook of Automotive Power Electronics and Motor Drives', *in IEEE Industrial Electronics Magazine*, vol. 2, no. 2, pp. 46-47, June 2008.

[2.73] B. K. Bose, *Modern Power Electronics and AC Drives*, Prentice Hall PTR, 2002

[2.74] 'The Best Electric Vehicle Motor', *New Energy and Fuel, http://newenergyandfuel.com/,* accessed 14 November 2017.

[2.75] T. A. Huynh and M. F. Hsieh, 'Comparative Study of PM-Assisted SynRM and IPMSM on Constant Power Speed Range for EV Applications', *in IEEE Transactions on Magnetics,* vol. 53, no. 11, pp. 1-6, Nov. 2017.

[2.76] L. Zhang, Y. Fan, R. D. Lorenz, R. Cui, C. Li and M. Cheng, 'Design and Analysis of a New Five-Phase Brushless Hybrid-Excitation Fault-Tolerant Motor for Electric Vehicles', *in IEEE Transactions on Industry Applications*, vol. 53, no. 4, pp. 3428-3437, July-Aug. 2017.

[2.77] C. Lu, S. Ferrari and G. Pellegrino, 'Two Design Procedures for PM Synchronous Machines for Electric Powertrains', *in IEEE Transactions on Transportation Electrification*, vol. 3, no. 1, pp. 98-107, March 2017.

[2.78] W. Zhang, X. Liang, M. Lin, L. Hao and N. Li, 'Design and Analysis of Novel Hybrid-Excited Axial Field Flux-Switching Permanent Magnet Machines', *in IEEE Transactions on Applied Superconductivity*, vol. 26, no. 4, pp. 1-5, June 2016.

[2.79] K. M. Rahman, S. Jurkovic, C. Stancu, J. Morgante and P. J. Savagian, 'Design and Performance of Electrical Propulsion System of Extended Range Electric Vehicle (EREV) Chevrolet Volt'*, in IEEE Transactions on Industry Applications*, vol. 51, no. 3, pp. 2479-2488, May-June 2015.

[2.80] Y. Shi, L. Jian, J. Wei, Z. Deng and Z. Ling, 'Electromagnetic Design and Analysis of a Novel Transmission System Supporting Multi-Path Power Flows for Electric Vehicles', *in IEEE Transactions on Magnetics*, vol. 53, no. 11, pp. 1-7, Nov. 2017.

[2.81] G. Zhang, W. Hua and M. Cheng, 'Rediscovery of permanent magnet flux-

switching machines applied in EV/HEVs: Summary of new topologies and control strategies', *in Chinese Journal of Electrical Engineering*, vol. 2, no. 2, pp. 31-42, Dec. 2016.

[2.82] J. M. Mun, G. J. Park, S. Seo, D. W. kim, Y. J. Kim and S. Y. Jung, 'Design Characteristics of IPMSM With Wide Constant Power Speed Range for EV Traction', *in IEEE Transactions on Magnetics*, vol. 53, no. 6, pp. 1-4, June 2017.

[2.83] 'Worldwide Sales of Toyota Hybrids Surpass 10 Million Units', *Toyota Global Newsroom, http://newsroom.toyota.co.jp/en/,* accessed 14 November 2017.

[2.84] 'History of the Toyota Prius', *THE OFFICIAL BLOG OF TOYOTA GB, log.toyota.co.uk/history-toyota-prius,* accessed 14 November 2017.

[2.85] 'Toyota Specs', *Official Toyota.website. https://www.toyota.com,* accessed 14 November 2017.

[2.86] 'Honda Insight Concept Hybrid Vehicle to Debut at Paris International Auto Show', *Honda Corporate Press Release*. accessed 14 November 2017.

[2.87] 'Ford Fusion Hybrid', *Hybrid Cars*, *http://www.hybridcars.com /vehicle/ford-fusion-hybrid.html,* accessed 14 November 2017.

[2.88] 'ML 450 Hybrid to Debut at New York Show', *Automoblog.net,* accessed 14 November 2017.

[2.89] 'Nissan Leaf Specs', *official Nissan website, https://www.nissanusa.com*, accessed 14 November 2017.

[2.90] J. Lundblad, 'BYD's New Plug-In Hybrid; More Details Emerging', *China Car Times*, accessed 14 November 2017.

[2.91] 'Tesla Model 3 Specs', *official Tesla web site, https://www.tesla.com/*, accessed 14 November 2017.

[2.92] J. Crosbie, 'Elon Musk Finally Reveals the Number of Tesla Model 3 Reservations', *inverse.com,* accessed 14 November 2017.

[2.93] M. A. Rahman and Q. Ruifeng, 'A permanent magnet hysteresis hybrid synchronous motor for electric vehicles', *Industrial Electronics, IEEE Transactions on,* vol. 44, pp. 46-53, 1997.

[2.94] W. H. Kim, J. N. Bae, et al., 'A study on 4-layer hybrid winding layout of the

IPMSM and location of the permanent magnets', *in Electromagnetic Field Computation (CEFC), 2010 14th Biennial IEEE Conference on*, 2010, pp. 1-1.

[2.95] P. Pisek, B. Stumberger, et al., 'Design and FE analysis of a double rotor synchronous PM machine', *in Electromagnetic Field Computation (CEFC), 2010 14th Biennial IEEE Conference on*, 2010, pp. 1-1.

[2.96] K. Wang, Z. Q. Zhu, G. Ombach and W. Chlebosz, 'Average Torque Improvement of Interior Permanent-Magnet Machine Using Third Harmonic in Rotor Shape', *in IEEE Transactions on Industrial Electronics,* vol. 61, no. 9, pp. 5047-5057, Sept. 2014.

[2.97] N. Zhao and N. Schofield, 'Field-Weakening Capability of Interior Permanent-Magnet Machines With Salient Pole Shoe Rotors', *in IEEE Transactions on Magnetics,* vol. 53, no. 11, pp. 1-7, Nov. 2017

[2.98] Y. Liao, F. Liang, et al., 'A novel permanent magnet motor with doubly salient structure', *in Industry Applications Society Annual Meeting*, pp. 308-314 vol.1, 1992.

[2.99] K. T. Chau, J. Z. Jiang, et al., 'A novel stator doubly fed doubly salient permanent magnet brushless machine', *Magnetics, IEEE Transactions on*, vol. 39, pp. 3001-3003, 2003.

[2.100] X. Zhu and M. Cheng, 'A novel stator hybrid excited doubly salient permanent magnet brushless machine for electric vehicles', *International Conference Electrical Machines and Systems on*, pp. 412-415 Vol. 1. 2005.

[2.101] I. A. A. Afinowi, Z. Q. Zhu, Y. Guan, J. C. Mipo and P. Farah, 'A Novel Brushless AC Doubly Salient Stator Slot Permanent Magnet Machine', *in IEEE Transactions on Energy Conversion*, vol. 31, no. 1, pp. 283-292, March 2016.

[2.102] M. He, W. Xu and C. Ye, 'Novel Single-Phase Doubly Salient Permanent Magnet Machine With Asymmetric Stator Poles'*, in IEEE Transactions on Magnetics*, vol. 53, no. 6, pp. 1-5, June 2017.

[2.103] S. E. Rauch and L. J. Johnson, 'Design Principles of Flux-Switch Alternators', *Power Apparatus and Systems, Part III. Transactions of the American Institute of Electrical Engineers*, vol. 74, pp. 1261-1268, 1955.

[2.104] E. Hoang, M. Lecrivain, et al., 'A new structure of a switching flux synchronous

polyphased machine with hybrid excitation', *in Power Electronics and Applications, European Conference on*, pp. 1-8. 2007.

[2.105] R. L. Owen, Z. Q. Zhu, et al., 'Fault-Tolerant Flux-Switching Permanent Magnet Brushless AC Machines', *in Industry Applications Society Annual Meeting*, pp. 1-8. 2008.

[2.106] Z. Q. Zhu, J. T. Chen, et al., 'Analysis of a Novel Multi-Tooth Flux-Switching PM Brushless AC Machine for High Torque Direct-Drive Applications', *Magnetics, IEEE Transactions on*, vol. 44, pp. 4313-4316, 2008.

[2.107] A. Zulu, B. Mecrow, et al., 'A wound-field three-phase flux-switching synchronous motor with all excitation sources on the stator', *in Energy Conversion Congress and Exposition,* pp. 1502-1509, 2009.

[2.108] Z. Xiang, L. Quan and X. Zhu, 'A New Partitioned-Rotor Flux-Switching Permanent Magnet Motor With High Torque Density and Improved Magnet Utilization', *in IEEE Transactions on Applied Superconductivity*, vol. 26, no. 4, pp. 1-5, June 2016.

[2.109] W. Xu; J. Zhu; Y. Zhang; Y. Guo and G. Lei; , 'New Axial Laminated-Structure Flux-Switching Permanent Magnet Machine With 6/7 Poles', *Magnetics, IEEE Transactions on* , vol.47, no.10, pp.2823-2826, Oct. 2011

[2.110] T. Wang et al., 'Fabrication and Experimental Analysis of an Axially Laminated Flux-Switching Permanent-Magnet Machine', *in IEEE Transactions on Industrial Electronics,* vol. 64, no. 2, pp. 1081-1091, Feb. 2017.

[2.111] P. C. Krause, R. R. Nucera, R. J. Krefta, and O. Wasynczuk, 'Analysis of a Permanent Magnet Synchronous Machine Supplied from a 180° Inverter with Phase Control', *Energy Conversion, IEEE Transactions on*, vol. EC-2, no. 3, pp. 423-431, 1987.

[2.112] N. Sato, 'A Study of Commutatorless Motor', *Elec. Eng. Jap.,* vol. 84, pp. 42-51, 1964.

[2.113] A. H. Hoffmann, 'Brushless Synchronous Motors for Large Industrial Drives', *Industry and General Applications, IEEE Transactions on*, vol. IGA-5, no. 2, pp. 158-162, 1969.

[2.114] P. A. Studer, 'Development of Brushless DC Motors for Space Applications',

NASA TN-D-2108, Feb. 1964.

[2.115] S. Murugesan, 'An Overview of Electric Motors for Space Applications', Industrial Electronics and Control Instrumentation, *IEEE Transactions on,* vol. IECI-28, no. 4, pp. 260-265, 1981.

[2.116] J.G. Zhu, 'Chapter 12. Brushless Motors, Electromechanical Systems', University of Technology Sydney, Faculty of Engineering and Information Technologies

[2.117] S. D. Sudhoff and P. C. Krause, 'Average-value Model of the Brushless DC 120° inverter system', *Energy Conversion, IEEE Transactions on*, vol. 5, no. 3, pp. 553-557, 1990.

[2.118] H. Le-Huy, R. Perret, and R. Feuillet, 'Minimization of Torque Ripple in Brushless DC Motor Drives', Industry Applications, *IEEE Transactions on,* vol. IA-22, no. 4, pp. 748-755, 1986.

[2.119] F. Blaschke, 'Das Prizip der Feldorientierung, die Grundlage far die TRANSVEKTOR-Regerung von Drehfeldmaschinen', *Siemens-Zeitschrift*, vol. 45, pp. 757-760, Oct, 1971.

[2.120] R. H. Park, 'Definition of an Ideal Synchronous Machine and Formula for the Armature Flux Linkages', *General Electric Review*, vol. 31, p. 332, 1928.

[2.121] R. H. Park, 'Two-Reaction Theory of Synchronous Machines Generalized Method of Analysis: Part I', *American Institute of Electrical Engineers*, vol. 48, pp. 716-727, 1929.

[2.122] G. Pfaff, A. Weschta, et al., 'Design and Experimental Results of a Brushless AC Servo Drive', *Industry Applications, IEEE Transactions on*, vol. IA-20, pp. 814-821, 1984.

[2.123] M.F Rahman, T.S. Low and L.B. Wee, 'Development of a digitally controlled permanent magnet brushless DC drive system', *Proceedings of the IEEE Conference on Applied Control*, pp. 283-288. 1986.

[2.124] B.K. Bose, and P.M. Szczesny, 'A microcomputer-based control and simulation of an advanced IPM synchronous machine dreive system for electric vehicle propulsion', *IEEE Transactions on Industrial Electronics*, Vol. 35, No. 4, , pp. 547-559. Nov. 1988.

[2.125] N. Matsui and H. Ohashi, 'DSP-based adaptive control of a brushless motor', *Conference Record of the 1988 IEEE IAS Annual Meeting*, Vol. 1, Oct. 2-7, pp. 375-380. 1988.

[2.126] C. Allen and P. Pillay, 'TMS320 design for vector and current control of AC motor drives', *Electronics Letters*, Vol. 28, No. 23, pp. 2188-2190. 5 Nov. 5 1992.

[2.127] J. Boldea and A. Nasar, *Vector control of AC machines*, CRC Press, ISBN/ISSN 0849344085, 1992.

[2.128] C. Cecati, F. Parasiliti, and M. Tursini, 'Multicomputer-based speed control of permanent magnet synchronous motor drives', Proceedings of the 1992 *International Conference on Industrial Electronics, Control, Instrumentation, and Automation (Power Electronics and Motion Control)*, vol. 1,. pp. 101-106. Nov. 9-13, 1992.

[2.129] N. Bennett, J. Wang, D.W. Shimmin, and K.J. Binns, 'A new vector control scheme for an adjustable sped AC drive system utlising a high field permanent magnet synchronous machine', *Proceedings of the Sixth International Conference on Electrical Machines and Drives*, pp. 121-126. Sep. 8-10, 1993.

[2.130] Bolognani, S. and Zigliotto, M., 'A space-vector approach to the analysis and design of three-phase current controllers', *Industrial Electronics. Proceedings of the 2002 IEEE International Symposium on* , vol.2, no., pp. 645- 650 vol.2, 2002

[2.131] Takahashi and T. Noguchi, 'A New Quick-Response and High-Efficiency Control Strategy of an Induction Motor', *Industry Applications, IEEE Transactions on,* vol. IA-22, pp. 820-827, 1986.

[2.132] U. Baader, M. Depenbrock, et al., 'Direct self control (DSC) of inverter-fed induction machine: a basis for speed control without speed measurement', *Industry Applications, IEEE Transactions on*, vol. 28, pp. 581-588, 1992.

[2.133] C. French and P. Acarnley, 'Direct torque control of permanent magnet drives', Industry Applications, *IEEE Transactions on*, vol. 32, pp. 1080-1088, 1996.

[2.134] M. F. Rahman and L. Zhong, 'Comparison of torque responses of the interior permanent magnet motor under PWM current and direct torque controls', *in Industrial Electronics Society, The 25th Annual Conference of the IEEE*, pp. 1464-1470 vol.3. 1999.

[2.135] P. Vas, *Sensorless Vector and Direct Torque Control*, Oxford, UK: Oxford University Press, 1998.

[2.136] M. P. K. Tunia, *Automatic Control of Converter-fed Drives*, Amsterdam, the Netherlands: Elsevier, 1994.

[2.137] A. Bouafia, F. Krim, et al., 'Fuzzy-Logic-Based Switching State Selection for Direct Power Control of Three-Phase PWM Rectifier', *Industrial Electronics, IEEE Transactions on,* vol. 56, pp. 1984-1992, 2009.

[2.138] X. Yang and W. Oghanna, 'Fuzzy direct torque control of induction motor with stator flux estimation compensation', *in Industrial Electronics, Control and Instrumentation,* 23rd International Conference on, pp. 505-510 vol.2. 1997.

[2.139] S. A. Mir, M. E. Elbuluk, et al., 'Fuzzy implementation of direct self-control of induction machines', *Industry Applications, IEEE Transactions on*, vol. 30, pp. 729-735, 1994.

[2.140] L. A. Cabrera, M. E. Elbuluk, et al., 'Learning techniques to train neural networks as a state selector for inverter-fed induction machines using direct torque control', *Power Electronics, IEEE Transactions on*, vol. 12, pp. 788-799, 1997.

[2.141] G. Escobar, A. M. Stankovic, et al., 'A family of switching control strategies for the reduction of torque ripple in DTC', *Control Systems Technology, IEEE Transactions on*, vol. 11, pp. 933-939, 2003.

[2.142] R. Ortega, N. Barabanov, et al., 'Direct torque control of induction motors: stability analysis and performance improvement', *Automatic Control, IEEE Transactions on*, vol. 46, pp. 1209-1222, 2001.

[2.143] M. A. M. Prats, G. Escobar, et al., 'A switching control strategy based on output regulation subspaces for the control of induction motors using a three-level inverter'*, Power Electronics Letters, IEEE*, vol. 1, pp. 29-32, 2003.

[2.144] K. B. Lee, J. H. Song, et al., 'Improvement of low-speed operation performance of DTC for three-level inverter-fed induction motors', *Industrial Electronics, IEEE Transactions on,* vol. 48, pp. 1006-1014, 2001.

[2.145] Jun-Koo and S. Seung-Ki, 'New direct torque control of induction motor for minimum torque ripple and constant switching frequency', *Industry Applications, IEEE Transactions on*, vol. 35, pp. 1076-1082, 1999.

[2.146] L. Romeral, A. Arias, et al., 'Novel direct torque control (DTC) scheme with fuzzy adaptive torque-ripple reduction', *Industrial Electronics, IEEE Transactions on*, vol. 50, pp. 487-492, 2003.

[2.147] V. Ambrozic, G. S. Buja, et al., 'Band-constrained technique for direct torque control of induction motor', *Industrial Electronics, IEEE Transactions on,* vol. 51, pp. 776-784, 2004.

[2.148] C. Lascu and A. M. Trzynadlowski, 'Combining the principles of sliding mode, direct torque control, and space vector modulation in a high-performance sensorless AC drive', *in Industry Applications Conference*, *37th IAS Annual Meeting,* pp. 2073-2079 vol.3,.2002/=.

[2.149] Yen-Shin and C. Jian-Ho, 'A new approach to direct torque control of induction motor drives for constant inverter switching frequency and torque ripple reduction', *Energy Conversion, IEEE Transaction on*, vol. 16, pp. 220-227, 2001.

[2.150] R. K. A. Linder, R. Kennel and P. Stolze, *Model-Based Predictive Control of Electric Drives*, Germany: Cuvillier Verlag, 2010.

[2.151] D. W. Clarke, C. Mohtadi and P. S. Tuffs, 'Generalized predictive control – part I. the basic algorithm', *Automatica*, vol. 23, pp.137–148, 1987.

[2.152] C. E. Garcia, D. M. Prett and M. Morari, 'Model Predictive Control: Theory and practice – a survey', *Automatica*, vol. 25, pp. 335–348, 1989

[2.153] P. Cortes, M. Kazmierkowski, R. Kennel, D. Quevedo, and J. Rodriguez, 'Predictive control in power electronics and drives', *IEEE Trans. Ind. Electron.*, vol. 55, no. 12, pp. 4312 –4324, Dec. 2008.

[2.154] A. Beccuti, S. Mariethoz, S. Cliquennois, S. Wang, and M. Morari, 'Explicit model predictive control of dc-dc switched-mode power supplies with extended kalman filtering', *IEEE Trans. Ind. Electron.,* vol. 56, no. 6, pp. 1864 –1874, June 2009.

[2.155] S. Kouro, P. Cortes, R. Vargas, U. Ammann, and J. Rodriguez, 'Model predictive control—a simple and powerful method to control power converters', *IEEE Trans. Ind. Electron.*, vol. 56, no. 6, pp. 1826 –1838, June 2009.

[2.156] J. Rodriguez, R. M. Kennel, J. R. Espinoza, M. Trincado, C. A. Silva, and C. A. Rojas, 'High-performance control strategies for electrical drives: An experimental

assessment', *IEEE Trans. Ind. Electron*., vol. 59, no. 2, pp. 812–820, 2012.

[2.157] T. Geyer, G. Papafotiou, and M. Morari, 'Model predictive direct torque control - part I: Concept, algorithm, and analysis', *IEEE Trans. Ind. Electron*., vol. 56, no. 6, pp. 1894 –1905, june 2009.

[2.158] Y. Zhang, J. Zhu, and W. Xu, 'Predictive torque control of permanent magnet synchronous motor drive with reduced switching frequency', *in Proc. Int Electrical Machines and Systems,* pp. 798–803, 2010.

[2.159] P. Cortes, J. Rodriguez, C. Silva, and A. Flores, 'Delay compensation in model predictive current control of a three-phase inverter', *IEEE Trans. Ind. Electron.*, vol. 59, no. 2, pp. 1323–1325, 2012.

[2.160] H. Miranda, P. Cortes, J. Yuz, and J. Rodriguez, 'Predictive torque control of induction machines based on state-space models', *IEEE Trans. Ind. Electron*., vol. 56, no. 6, pp. 1916 –1924, June 2009.

[2.161] R. Vargas, P. Cortes, U. Ammann, J. Rodriguez, and J. Pontt, 'Predictive control of a three-phase neutral-point-clamped inverter', *IEEE Trans. Ind. Electron*., vol. 54, no. 5, pp. 2697 –2705, Oct. 2007.

[2.162] G. Papafotiou, J. Kley, K. Papadopoulos, P. Bohren, and M. Morari, 'Model predictive direct torque control-part II: Implementation and experimental evaluation', *IEEE Trans. Ind. Electron*., vol. 56, no. 6, pp. 1906 –1915, June 2009.

[2.163] S. Kouro, P. Cortes, et al., 'Model Predictive Control: A Simple and Powerful Method to Control Power Converters', *Industrial Electronics, IEEE Transactions on*, vol. 56, pp. 1826-1838, 2009.

[2.164] P. Cortes, S. Kouro, et al., 'Guidelines for weighting factors design in Model Predictive Control of power converters and drives', *in Industrial Technology, International Conference on,* pp. 1-7, 2009.

[2.165] T. Wang, C. Liu, G. Lei, Y. Guo and J. Zhu, 'Model predictive direct torque control of permanent magnet synchronous motors with extended set of voltage space vectors', *in IET Electric Power Applications*, vol. 11, no. 8, pp. 1376-1382, Sep 2017.

CHAPTER 3

ANALYSIS AND DESIGN OF AXIALLY LAMINATED FLUX SWITCHING PERMANENT MAGNET MACHINE

3.1 Introduction

A novel flux switching permanent magnet (FSPM) machine is proposed in this chapter. The design process is introduced in Section 3.2. The detailed fabrication procedures are presented in Section 3.3. In Section 3.4, the theoretical characteristics of axially laminated FSPM machine (ALFSPMM), such as back *emf*, self/mutual inductance and cogging torque are calculated by 2D finite element method (FEM). The influence of misalignment between the stator core and the rotor shaft (a common issue in motor manufacturing) is investigated by FEM. In Section 3.5, experimental measurements of the prototype machine are presented to validate the FEM calculation. The load tests are presented in Section 3.6. The influence of the bending processes on soft magnetic material is discussed in Section 3.7.

3.2 The Design of ALFSPMM

3.2.1 Comparison of different types of stator-PM machines

PM machines feature high power density, high efficiency, high controllability and fast dynamic response. The major weakness is the delicate rotor structure because of the low mechanical strength of PMs. Another issue is the narrow speed range due to the difficulty to weaken the field of PMs.

To overcome the weakness of rotor structure and retain the merits of the PM machines, several variations of the machine topology were proposed by placing the PMs on/in the stator and employing a solid salient rotor similar to that of the SRM [3.1]-[3.3]. Fig. 3.2.1 presents the recently proposed topologies in this category, such as the double salient permanent magnet machine (DSPMM), hybrid excited DSPMM (HEDSPMM), and FSPMM.

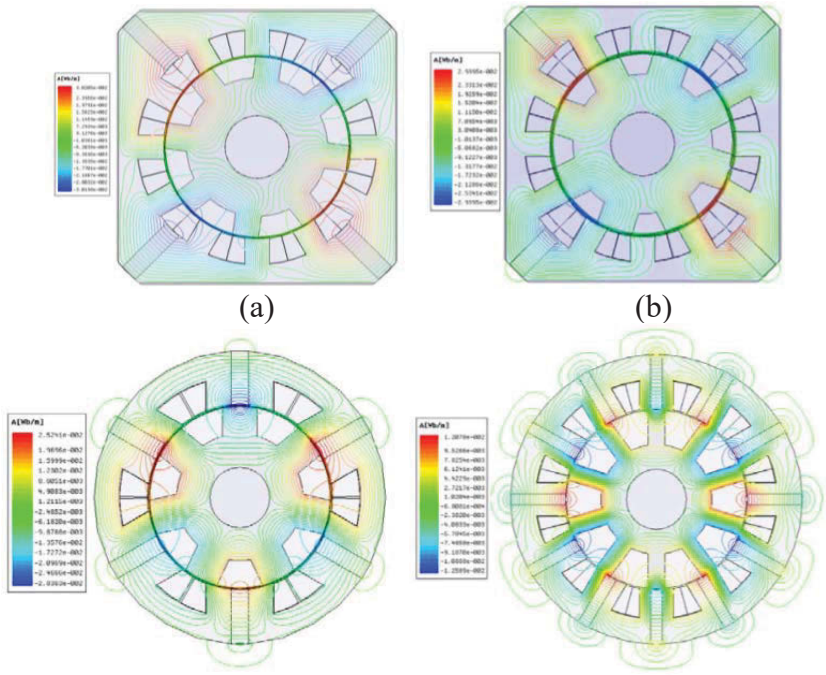

(a) (b)

(c) (d)

Fig.3.2.1 Flux distribution of four machines, (a) DSPMM with 12/8 poles, (b) HEDSPMM with 12/8 poles, (c) FSPMM with 6/7 poles and (d) FSPMM with 12/10 poles

From the structures and the PM flux distributions shown in Fig. 3.2.1, the key features of these machines can be summarised in contrast to the conventional PM machines as the following:

- Concentrated winding - The edge connection of stator winding is shorter than the distributed ones, which means less copper loss with the same amplitude of stator current.
- Strong thermal dissipation capability - As the PMs are located in the stator, they can have greater cross sectional area and are less likely to suffer the demagnetization problem. In continuous operation, the stator temperature can be maintained well below 125°C, which is in the range of H-grade insulation by water cooling.
- Strong structure robustness - Similar to SRMs, the rotor has no PMs and therefore is suitable for high speed operation. For a given power rating, as the rated speed increases, the machine volume can be reduced.
- High power/torque density - Same as the rotor mounted PM machines, PMs are

employed to generate the major air gap flux in the DSPMM, HEDSPMM and FSPMM.

- Great flux weakening ability - It is one of the key indices for EV applications. In general, the flux weakening ability (the ratio between the maximum and base speeds) of the conventional PM machines does not exceed 3. However, some recent studies [3.4]-[3.6] show that the flux weakening abilities of DSPMM, HEDSPMM, and FSPMM may reach 3, 4, and 4, respectively.
- Feasible control schemes - The back-*emf* of stator mounted PM machines could be optimized to close to sine waves by skewing the rotor, and the advanced control schemes for traditional machines, such as the vector control and direct torque control, can be readily applied to achieve excellent steady and dynamic state performances.

The drawbacks of the stator mounted PM machines include:

- There exist partial saturation phenomena in the stator and rotor components, such as the stator teeth and rotor poles;
- The back-*emf* waves contain harmonics, resulting in extra copper loss;
- The mutual inductances are nonlinear functions of the rotor position and stator currents, which causes difficulty to the advanced performance control;
- With the PMs inserted in the stator, the fabrication of the stator iron core is more complicated than that of traditional PM machines.

The performances of four types of machine are compared in this section. Table 3-1 lists the parameters of four machines. The FEM predicted flux linkage and torque curves of four machines are illustrated in Fig. 3.2.2.

The performances are summarised in Table 3-2, it is concluded that:

- Power density - the FSPMM with 6/7 poles has the highest power density of 1.93 kW/kg, followed by the FSPMM with 12/10 poles of 1.60 kW/kg. The main reason for the difference in power density between the two FSPMM is that the one with more poles has higher leakage inductance. The power densities of the DSPMM and HEDSPMM are significantly lower than those of the FSPMMs. This is mainly because less PM material is used in these machines in

order to achieve acceptable flux weakening ability.

- Torque - the FSPMM with 6/7 poles has the highest average torque and lowest torque ripple, followed by the FSPMM with 12/10 poles. The DSPMM and HEDSPMM have lower rated torque and their torque ripples are higher than those of the FSPMMs.
- Efficiency - In the calculation, it is assumed that the total of the frictional, windage and stray losses is up to 1.50 % of the output power. The core loss is calculated by summing up the core losses in each finite element, which is obtained by interpolating the silicon steel core loss curves according to the flux density in each element and the frequency. As shown in the table, the FSPMM with 6/7 poles presents the highest efficiency, while the HEDSPMM with 12/8 poles has the lowest efficiency because of the extra copper loss produced by the DC excitation current.

Table 3-1 Main Dimensions of Four Machines (length unit: mm)

	FSPMM (6/7)	**FSPMM (12/10)**	**DSPMM**	**HEDSPMM**
Outer radius	101.5	101.5	101.5	101.5
Stator York height	23	17.5	23.5	23.5
Number of pole	6	12	12	12
Pole width	46.8	23.4	16	16
Pole height	20.4	20.8	17.5	17.5
Number of turns per pole winding	13	9	8	8
PM Width	12	8	12	12
Height	36.3	18.1	40	34
Air gap length	0.5	0.5	0.5	0.5
Rotor Pole width	24	12	17	24
Pole height	24.6	24.2	14	14
York	17.5	17.5	25	25
Number of poles	7	10	8	8
Radius of shaft	21	21	21	21
Effective axial length	211	211	211	211

Table 3-2 Performance of Four Machines

	FSPMM (6/7)	**FSPMM (12/10)**	**DSPMM**	**HEDSPMM**
Power density	1.93	1.60	1.07	0.9
Average torque (Nm)	272.00	215.00	153.50	137.70
Torque ripple (%)	2.52	2.93	11.91	17.17
Efficiency	97.10	96.77	96.2	95.18

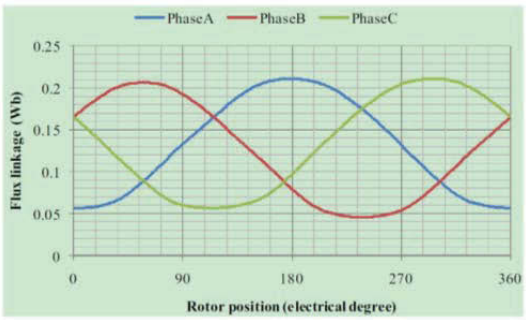

(a1) Flux linkage

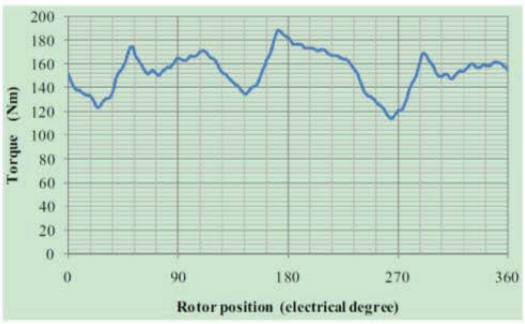

(a2) Torque (average: 153.50 Nm)

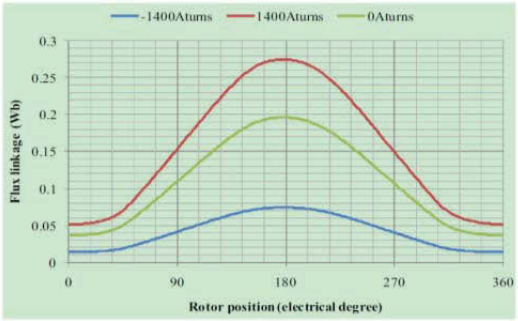

(b1) Flux linkage

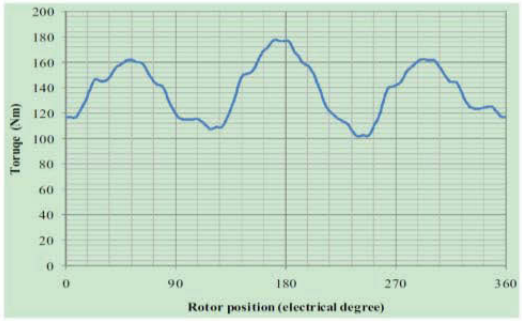

(b2) Torque (average: 137.60 Nm)

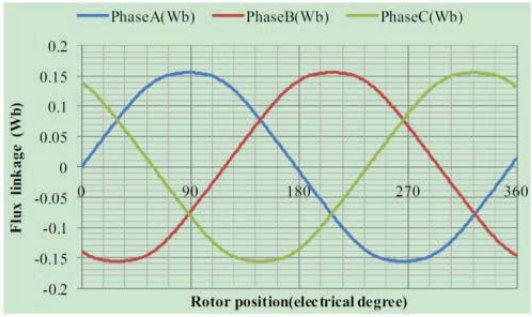

(c1) Flux linkage

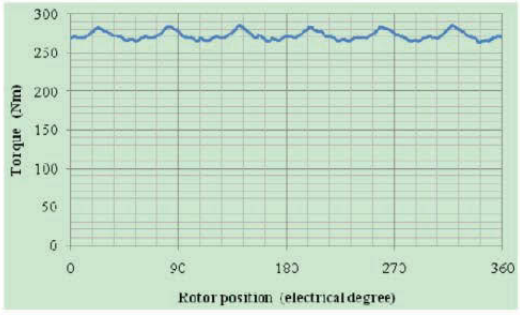

(c2) Torque (average: 272.00 Nm)

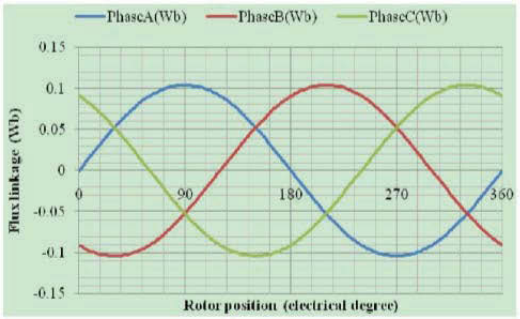

(d1) Flux linkage

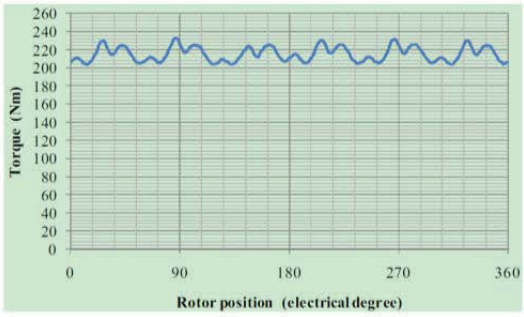

(d2) Torque (average: 215.00 Nm)

Fig. 3.2.2 FEM predicted flux linkage and torque, (a) DSPMM with 12/8 poles, (b) HEDSPMM with 12/8 poles, (c) FSPMM with 6/7 poles and (d) FSPMM with 12/10 poles

From above qualitative comparison, it is found that the FSPMM with 6/7 poles presents better performance than DSPMM, HEDSPMM and FSPMM with 12/10 poles in terms of power/torque density, torque output, torque ripple and efficiency.

3.2.2 The proposed ALFSPMM

FSPMMs have attracted considerable interest for high performance drive applications due to their features of high torque and power densities [3.1]-[3.14]. Many novel topologies based on the principle of flux-switching have been proposed in the last decade [3.15]-[3.22].

The laminations of traditional FSPMMs are radially laminated, i.e. steel sheets are laminated perpendicular to the shaft axis. Due to the nonlinear magnetic path, the radial laminations can have serious partial magnetic saturation and the maximal flux density is usually more than 2.0 T at the edges/tips of stator teeth or rotor poles. The pole pairs in FSPMMs are equal to the number of rotor poles. As a result, the rated frequency of FSPMMs is usually much higher than the traditional rotor-inserted PM machines at a given speed. In this case, the core loss of FSPMMs becomes evident especially beyond the rated speed, which leads to decrease of output power, torque/power density and efficiency.

The reluctance motor with axially laminated rotor has received growing interest in recent years. It is increasingly used in servo drive applications, even though its industrial manufacturing process has not well been established yet [3.23]. This type of motor was firstly proposed in 1966 [3.24] to achieve a higher torque density compared with segmented rotors [3.25], [3.26] and flux-barrier rotors [3.27]. The axially laminated rotor is fabricated by stacking steel sheets with nonmagnetic interlaminar insulation sheets and then nonmagnetic bolts and pole holders are used to fix the laminations. The typical topologies of axially laminated rotors are summarized in [3.28].

Based on the comparison in Section 3.2.1, an axially laminated 6/7 poles flux-switching permanent magnet machine (ALFSPMM) with high grain oriented silicon steel stator and rotor cores is proposed in this section. The cross sectional view and 3D-view of the proposed machine in presented in Figs. 3.2.3 – 3.2.4 and the parameters of the machine are shown in Table 3-3.

Table 3-3 Dimensions of FSPMM and ALFSPMM

Stator outer radius	54.6 mm
Yoke height	8.8mm
Number of stator poles	6
Stator pole width	23.6 mm
Stator pole height	13.8 mm
Turns per coil	78
Magnet dimension	W22 x H6 x L50 mm
Magnet relative permeability	1.03
Magnet remanence	1.19 T
Air gap length	0.6 mm
Rotor pole width	12.2 mm
Rotor pole height	14.6 mm
Rotor yoke height	6.1mm
Rotor poles	7
Radius of shaft	10.6mm
Effective axial length	49mm

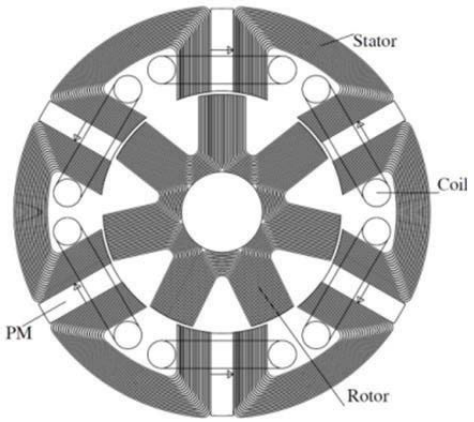

Fig. 3.2.3. Cross section view of ALFSPMM.

Fig. 3.2.4 3D-view of ALSFSPMM

The major difference between the traditional FSPMM and ALFSPMM is that the steel sheets of stator and rotor cores are laminated axially in perpendicular to the shaft axis in the traditional FSPMMs, while in ALFSPMM, they are laminated axially in parallel to the shaft. As seen from Figs. 3.2.3 – 3.2.4, the stator core has six separate lamination modules, while the rotor core has seven modules.

The 0.27 mm high grain oriented silicon steel sheets (HiB) are used in the construction of stator and rotor laminations. The HiB silicon sheet steel features high permeability (meaning low magnetisation current and thus low copper loss) and low specific core loss. As a result, the total power loss of proposed motor is much lower than the conventional motor, leading to higher efficiency under a given load. On the other hand, from the flux density contours of ALFSPMM and the conventional FSPM are shown in Fig. 3.2.3, it can be seen that the flux density in the stator teeth of ALFSPMM is higher than that of the conventional FSPM, and the flux density distribution in the stator teeth of ALFSPMM is more uniform than that of the conventional FSPM. Compared with the conventional FSPMM, ALFSPMM can have higher magnetic loading and thus the higher torque density.

The HiB steel sheet has a very thin surface insulation coating. Due to absence of interlaminar insulation sheets, the ALFSPMM can achieve a high lamination factor. Besides the nonmagnetic bolts and pole holders fixing, the steel sheets are bonded with high-strength heat-resistant glue in order to improve the mechanical strength.

3.2.2 Comparison of conventional FSPMM and ALFSPMM

This section compares the FEM predicted performances of the conventional FSPMM and ALFSPMM. Two machines have the same physical dimensions as shown in Table 3-3. The magnetic parameters and magnetic field of ALFSPMM are calculated with the 2D FEM. The nonlinear magnetic property and the grain orientation of the HiB steel sheets are considered to increase the accuracy of the calculation.

To accurately model the grain oriented effect of the HiB steel sheets, the stator and rotor are divided into several sections, and each section is set to have its own magnetic properties. As shown in Fig. 3.2.5, each piece of stator core is divided into three

sections and each piece of rotor core is divided into three sections as well. The anisotropic magnetic property of the HiB steel sheets is considered in the modelling of the stator teeth and the rotor teeth. To simplify the model, the anisotropic magnetic property of the stator and rotor yoke is not considered. The permeabilities of the stator and rotor teeth are specified as μ_x in the easy magnetization direction and μ_y in the hard magnetization direction. They can be expressed as

$$\mu_x = \nu\mu_{steelx} + (1-\nu)\mu_{\text{air}} \tag{3.1}$$

$$\mu_y = \nu\mu_{steelz} + (1-\nu)\mu_{\text{air}} \tag{3.2}$$

where ν is the stacking factor of the motor, μ_{air} the permeability of air, and μ_{steelx} and μ_{steelz} are the permeabilities of HiB steel in the x and z (perpendicular to the steel sheets) directions, respectively. The permeability of the stator and rotor yoke is isotropic, which equals μ_x. The magnetization curves of the steel sheet on the easy and hard axes are shown in Fig. 3.2.6.

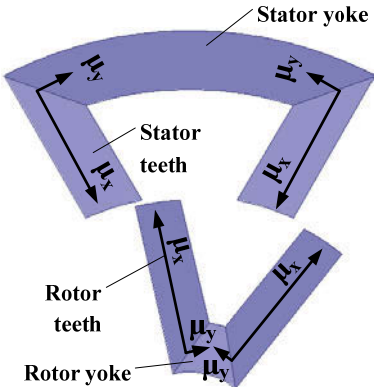

Fig. 3.2.5 Modelling of stator and rotor cores

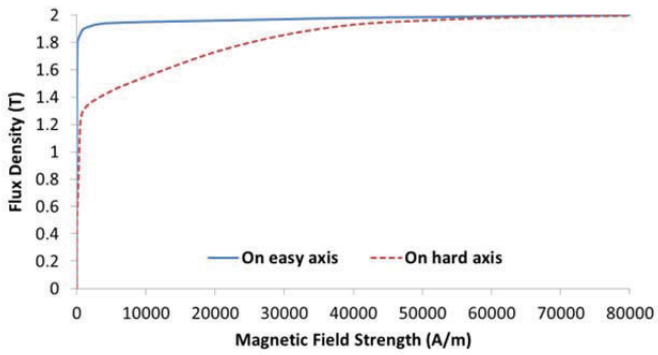

Fig. 3.2.6 The magnetization curves of the HiB steel sheet used in ALFSPMM

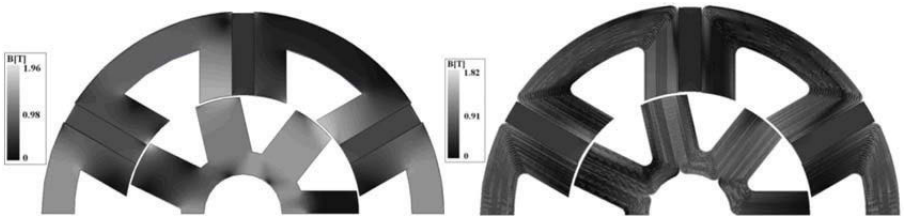

(a) (b)

Fig. 3.2.7 Flux density contour, (a) conventional FSPMM, and (b) ALSFSPMM

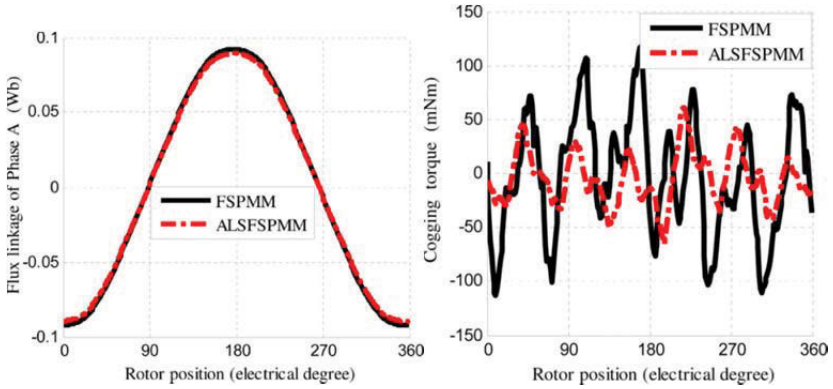

(a) (b)

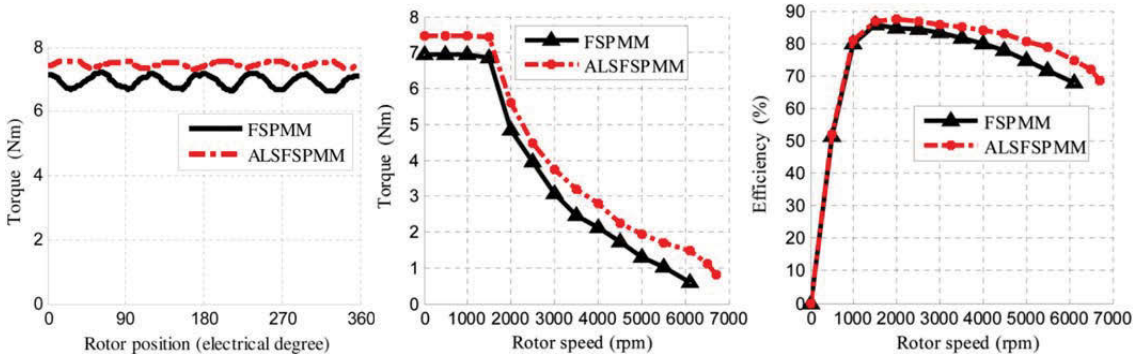

(c) (d) (e)

Fig. 3.2.8 FEM predicted performances of conventional FSPMM and ALFSPMM, (a) Flux linkage (Phase A), (b) Cogging torque, (c) Rated torque, (d) Torque versus speed, and (e) Efficiency versus speed

Comparisons are made on the typical performance criteria, such as flux density contour, PM flux linkage, cogging torque, rated torque and torque/efficiency in the whole operation range, as shown in Figs. 3.2.7 – 3.2.8. Based on the FEM predictions, it can be seen that

- Contour of flux density – as shown in Fig. 3.2.7 (a), a serious partial magnetic saturation can be seen in the conventional FSPMM with radial lamination. By employing the axial lamination, the partial magnetic saturation is reduced in ALSFSPMM at the edges/tips of stator teeth and rotor poles. Under the

excitation of the same-size PM, the maximal flux density in the conventional FSPMM is 1.96 T, which is greater than that of ALSFSPMM with 1.82 T.

- Flux linkage - as shown in Fig. 3.2.8 (a), the flux linkage is mostly sinusoidal. Due to the reason that the magnetic flux could go across different stator laminations, the average equivalent length of air gap along the flux path in ALSFSPMM is larger. As a result, the amplitude of the flux linkage of ALSFSPMM is 1.70% smaller than that of the conventional FSPMM.
- Cogging torque - as shown in Fig. 3.2.8 (b), the proposed ALSFSPMM presents smaller cogging torque than the conventional FSPMM. The cogging torque can cause negative influence to the stable operation of the drive system, which should be carefully considered in the process of optimal design. In general, it is closely relative to the magnetic reluctance which is affected by the machine topology, such as the widths of stator tooth and rotor pole, depth of stator slot, and thickness of PM, etc.
- Rated torque and torque ripple - as shown in Fig. 3.2.8 (c), thanks to the reduction of partial electromagnetic saturation and iron loss, the rated torque of ALSFSPMM is 4.80% higher than that of the conventional FSPMM. It is also seen that ALSFSPMM has smaller torque ripple than the conventional FSPMM.
- Operating range (torque verse speed) - two machines are excited with the same phase current (5A). As shown in Fig. 3.2.8 (d), the proposed ALSFSPMM presents higher maximum output torque and wider speed range than the conventional FSPMM.
- Efficiency - as shown in Fig. 3.2.8 (e), ALSFSPMM and the conventional FSPMM have the similar efficiency (86.9% and 85.6%) at the base speed. As the speed increases, ALSFSPMM presents higher efficiency than the conventional FSPMM. Due to the implement of axial lamination and HiB steel sheet, ALSFSPMM presents lower core loss than the conventional FSPMM, especially at high speeds.

From above analysis, it is found that the ALSFSPMM features higher torque/power density, wider speed range and higher efficiency than the conventional FSPMM and it can be an excellent candidate for EV application. The detailed fabrication process is presented in the following section.

3.3 Prototype Fabrication

The prototype of ALFSPMM was made at the mechanical workshop of University of Technology Sydney (UTS), Australia. The fabrication of ALFSPMM is a challenging and complicated job. Only a limited number of motors with axially laminated structures are found in the literatures and the construction procedures of this type of motor are rarely described. One key requirement is that the magnetic properties of HiB steel sheet should be well retained during the stator and rotor cores construction. The machining procedures of the sheets are carefully developed in order to minimize the damage to the coating and magnetic properties. The HiB steel sheets are bonded with Loctite 325, a typical glue used in electric motor assemblies. Loctite 325 can retain good bonding strength when exposed at high temperatures for a long period. According to the manufacture's manual, it has 75% and 25% of initial strength after 5000 hours exposure time at the temperature of 120 ^{o}C and 150 ^{o}C, respectively. The detailed fabrication procedures are presented in the sections below.

3.3.1 Rotor

The construction procedure of rotor is shown in Fig. 3.3.1, where (a) V shape dies made to press the steel sheets, (b) the HiB steel sheets being pressed individually with different shape of dies, Loctite spreading evenly among the sheets, the sheets put back into the die in order to squeeze out excess glue, and the glued sheets held in the die until the glue is fully cured, (c) seven pieces of laminated cores made to form the rotor, (d) the rotor shaft with fixing bolts used to mount the rotor laminations, and the shaft and bolts are made of non-magnetic stainless steel, (e) the heat resistant plastics shaped and inserted to the gaps between the rotor poles in order to reduce the wind resistance and increase the mechanical strength of the rotor, and (f) the rotor saliencies roughly cut out to form an approximate circle, then the rotor mounted to the lathe and the saliencies finely milled to the designated radius with a grinder.

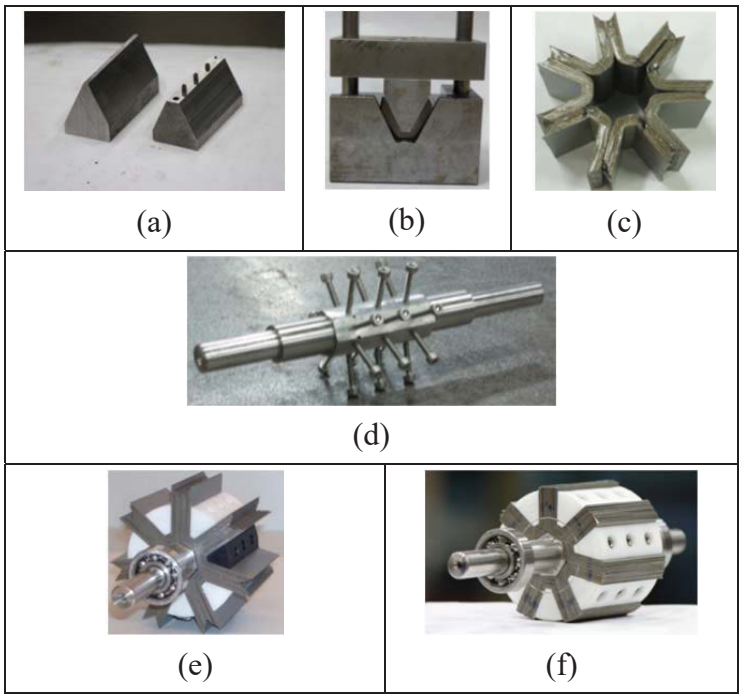

Fig. 3.3.1 Construction procedure of rotor.

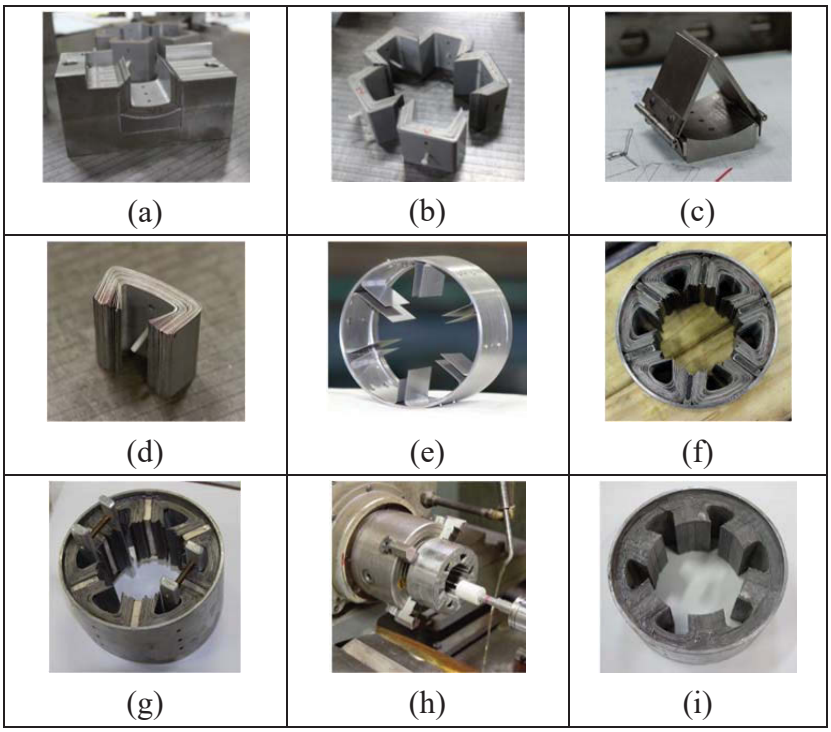

Fig. 3.3.2 Construction procedure of stator.

3.3.2 Stator

The stator laminated core is constructed in the following steps as shown in Fig. 3.3.2, where (a) a U shape die made to press the steel sheets, (b) laminations made with the die, (c) a specially made clamping device used to bend the laminations, (d) one bent stator lamination core, (e) the stator housing made of non-magnetic stainless steel for mounting the laminated stator cores, (f) the stator laminated cores and magnets fitted inside the stator housing, (g) the Loctite 325 applied between the loose space of the steel sheets, clamping plates used to squeeze out the unwanted Loctite and hold the steel sheets until the glue is cured, (h) removal of the unwanted stator laminations, and (i) the completed stator with clean surface and coating.

3.3.3 Stator windings

The construction of stator windings are shown in Fig. 3.3.3, where (a) enamelled copper wire wound on a heat resistant plastic holder and a counter used to count the turns, (b) a finished winding, (c) windings fitted to the stator core and the polarity verified with gauss meter, (d) windings grouped and labelled, and (e) the stator core fitted to the motor housing made of aluminum and wires tied up with cotton threads

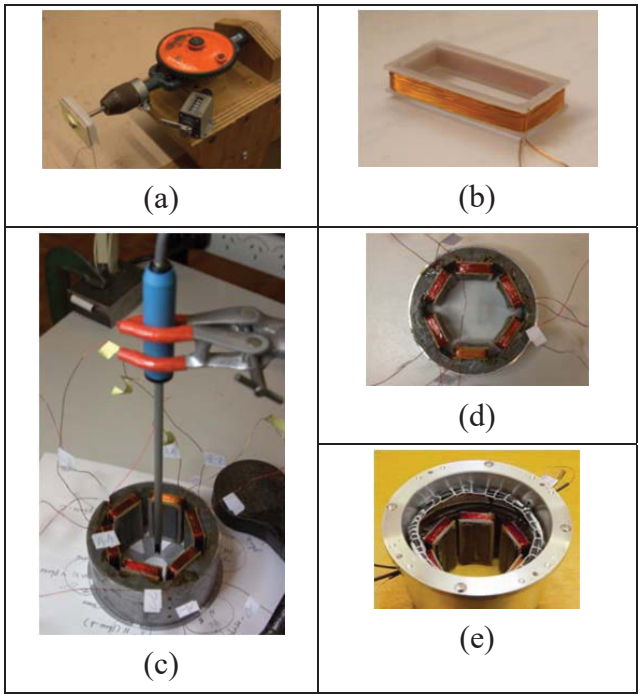

Fig. 3.3.3 Construction procedure of winding and final assembly

3.3.4 Final assembly

The final steps of ALFSPMM construction are presented in Fig. 3.3.4, where (a) clear coating applied to the windings and laminations for protection, (b) end brackets with bearings mounted to the motor housing, and (c) motor mounted to the testing bed and the shaft clamped with a three-jaw chuck.

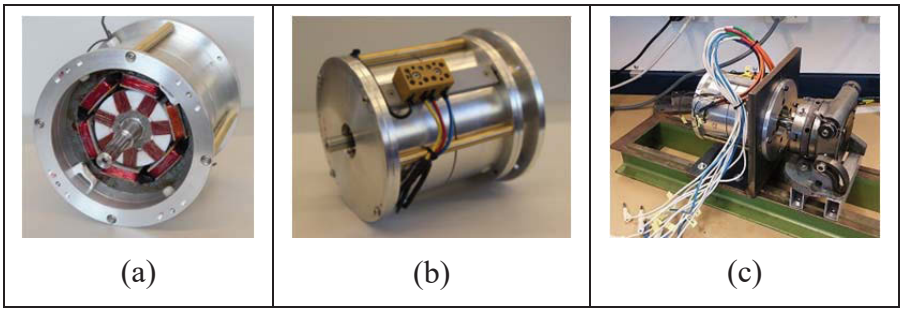

(a) (b) (c)

Fig. 3.3.4 Final assembly of ALFSPMM

3.4 Models of ALFSPMM

Due to the difficulties encountered in the complicated fabrication process, some of the parameters were changed in the final prototype. For example, the number of turns per coil is reduced by 6 turns. The stator width is increased by 0.4mm. The rotor width is reduced by 0.7mm, and the rotor height is increased by 0.5mm. The ALFSPMM is re-modelled in this section with different complexity and one misaligned FEM model is also presented to aid the analysis of the machine.

The final parameters of ALFSPMM are presented in Table 3-4.

Table 3-4 Final ALFSPMM Prototype Parameters

Number of phases	3
Stator outer radius	54.60 mm
Number of stator poles	6
Stator pole width	24.00 mm
Stator pole height	13.80 mm
Air gap length	0.60 mm
Turns per coil	72
Rated current	1.50 A
Axial length	50 mm
Rotor outer radius	31.50 mm
Rotor poles	7
Rotor pole width	11.50 mm
Rotor pole height	21.20 mm
Magnet dimension	W22 x H6 x L50 mm
Magnet remanence	1.20 T
Magnet relative permeability	1.05
Rated speed	1500 rpm
Rated torque	1 Nm
Stator resistance	3.66 Ω
d-axis inductance	9.54 mH
q-axis inductance	10.02 mH

3.4.1 The complete, reduced and simplified models

To reduce the calculation time and facilitate the future research of ALFSPMM, three ALFSPMM FEM models are proposed, as shown in Fig. 3.4.1. The first one is named the complete model which best reconstructs the actual mechanical structure of the motor as shown in Fig. 3.4.1 (a). In the complete model, each of the stator and rotor lamination consists of 32 and 21 layers of HiB steel sheets, respectively. Due to the high complexity, carrying out the 2D FEM calculation with the complete model is a very time-consuming process and it takes nearly seven hours to complete the calculation of each iteration. Completing the FEM analysis of one electrical cycle (equal to 51.40 degrees mechanical) requires 136 times of field calculation (0.38 mechanical degree per step).

The ‘reduced model’ with half the layers of the complete model is proposed as shown in Fig. 3.4.1 (b). Under the same system setup, the calculation time of the reduced model is approximately 21% of the complete model.

To further reduce the calculation time and acquire a rough but quick approximation in some cases, a 'simplified model' with only one equivalent layer is proposed as shown in Fig. 3.4.1 (c). It takes about 10 minutes for each calculation, which is 2.40% of the time using the complete model.

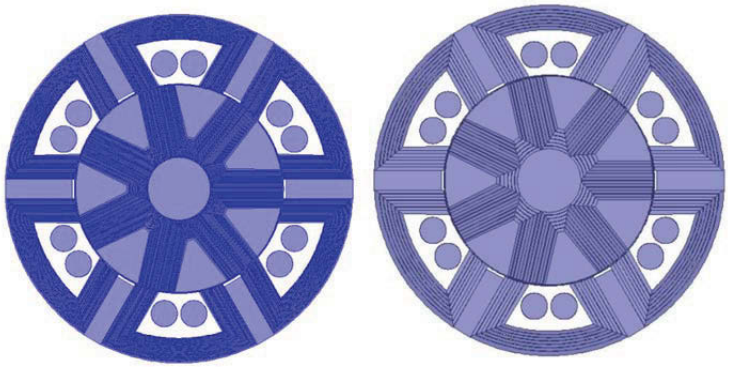

(a) (b)

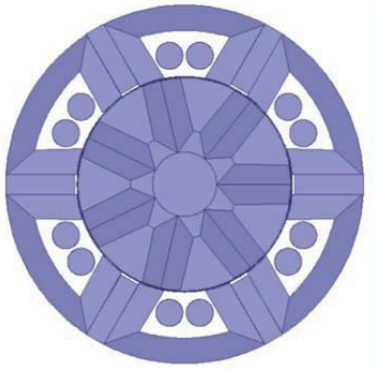

(c)

Fig. 3.4.1 FEM models of ALFSPMM, (a) complete model, (b) reduced model, and (c) simplified model.

3.4.2 Rotor lamination core misalignment model

Noticeable disagreements between the FEM predictions and experimental measurements are found in the data analysis after the fabrication of the motor and carrying out all the tests (detailed results to be presented in Section IV). The FEM predictions of ALFSPMM seem reasonable according to the past experience of FSPMM calculation. However, the experimental measurements of ALFSPMM do not match the expectation very well, especially the measurement of cogging torque. The waveform of cogging torque measurement is less periodic and symmetrical than the FEM predictions.

The motor is mostly hand-made at a university workshop rather than being manufactured in a motor factory. The manufacturing error of the motor is slightly high and it may bring out some issues, such as misalignment between the stator core and the rotor shaft, uneven weight distribution of the rotor, diversity and variations of magnetic properties of the permanent magnets and HiB sheets caused in the manufacturing and bending procedure.

Misalignment between the stator core and the rotor shaft is a common issue in the motor fabrication and it can cause asymmetrical air gap of the motor. The ALFSPMM is designed to have high flux concentrating effect and any slight asymmetry of the air gap could cause non-negligible impact on the magnetic performance. To further investigate the reason for the discrepancy between the FEM calculation and the measurements, a misaligned FEM model (based on the reduced model) is proposed as shown in Fig. 3.4.2. The misalignment L_{mis} is set to be half of the air gap (0.3mm).

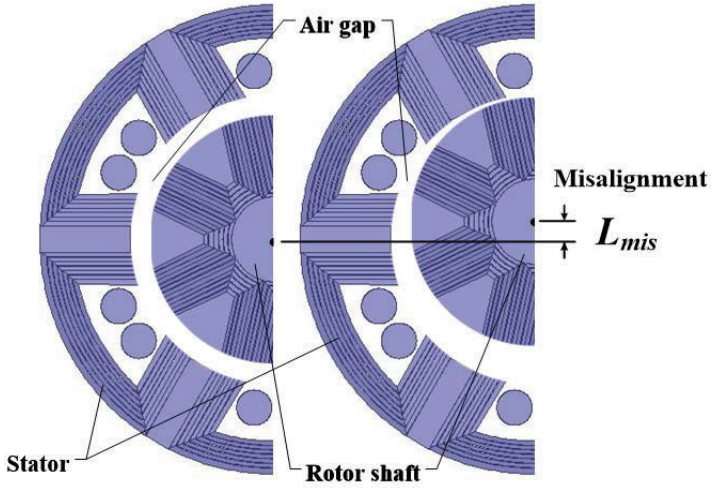

Fig. 3.4.2 ALFSPMM FEM model with misalignment

3.5 FEM Numerical Calculations and Experimental Measurements of ALFSPMM

3.5.1 Stator resistance

The stator resistance is measured by the volt/ampere method according to the Ohm's law. By averaging the resistances of three phases, the final stator resistance of the motor can be obtained. All tests are conducted under the temperature of 21.60 ℃.

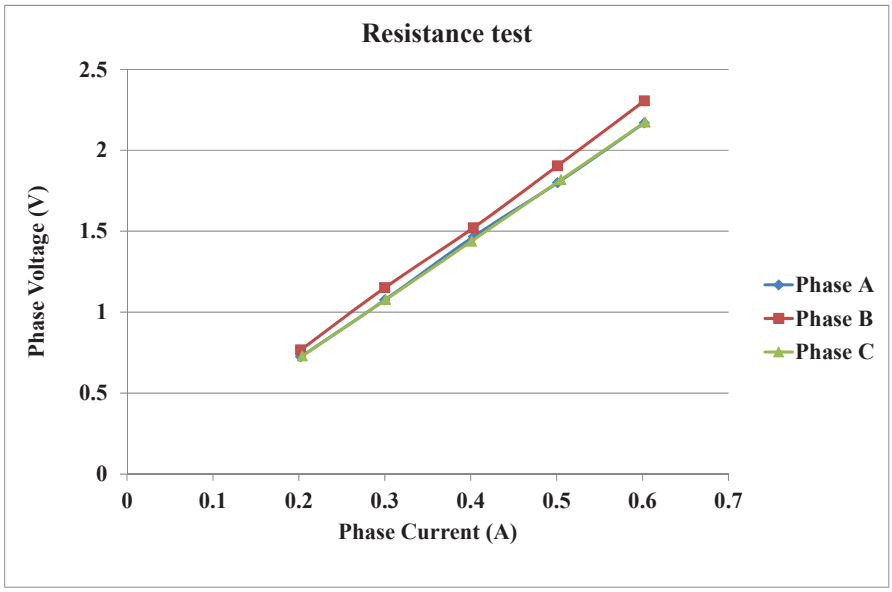

Fig. 3.5.1 Resistance test of ALSFSPMM

From above tests, the phase winding resistances are calculated by measured terminal voltage and current. The final stator resistance is obtained by

$$R_s = \frac{(R_a + R_b + R_c)}{3} \tag{3.3}$$

The resistances of three phase stator windings are 3.60Ω, 3.79 Ω and 3.59 Ω, respectively. The average resistance is 3.66 Ω.

Applying the temperature coefficient to the measured resistance value, one can deduce the resistance at a specific temperature by

$$R_0 = R_m + \alpha(T_0 - T_m) \tag{3.4}$$

where T_0 is a fixed reference temperature, R_0 the resistance at temperature T_0, T_m and R_m are measured value of temperature and resistance, respectively, and α is the temperature coefficient. The temperature coefficient of copper is 0.0038. The actual resistance value at the reference temperature (20°C) can thus be deduced as 3.66 Ω

3.5.2 Magnetic flux density distribution

Fig. 3.5.2 shows the no load magnetic flux density distribution of ALFSPMM. The maximum flux density of three models occurs at the corners of the stator teeth (around 1.90 T). It can be seen that the complete model and reduced model present similar magnetic flux density distribution as shown in Figs. 3.5.2 (a) and (b). In Fig. 3.5.2 (c), the simplified model can only provide a rough prediction of the magnetic flux density distribution due to the extremely rough approximation of the model.

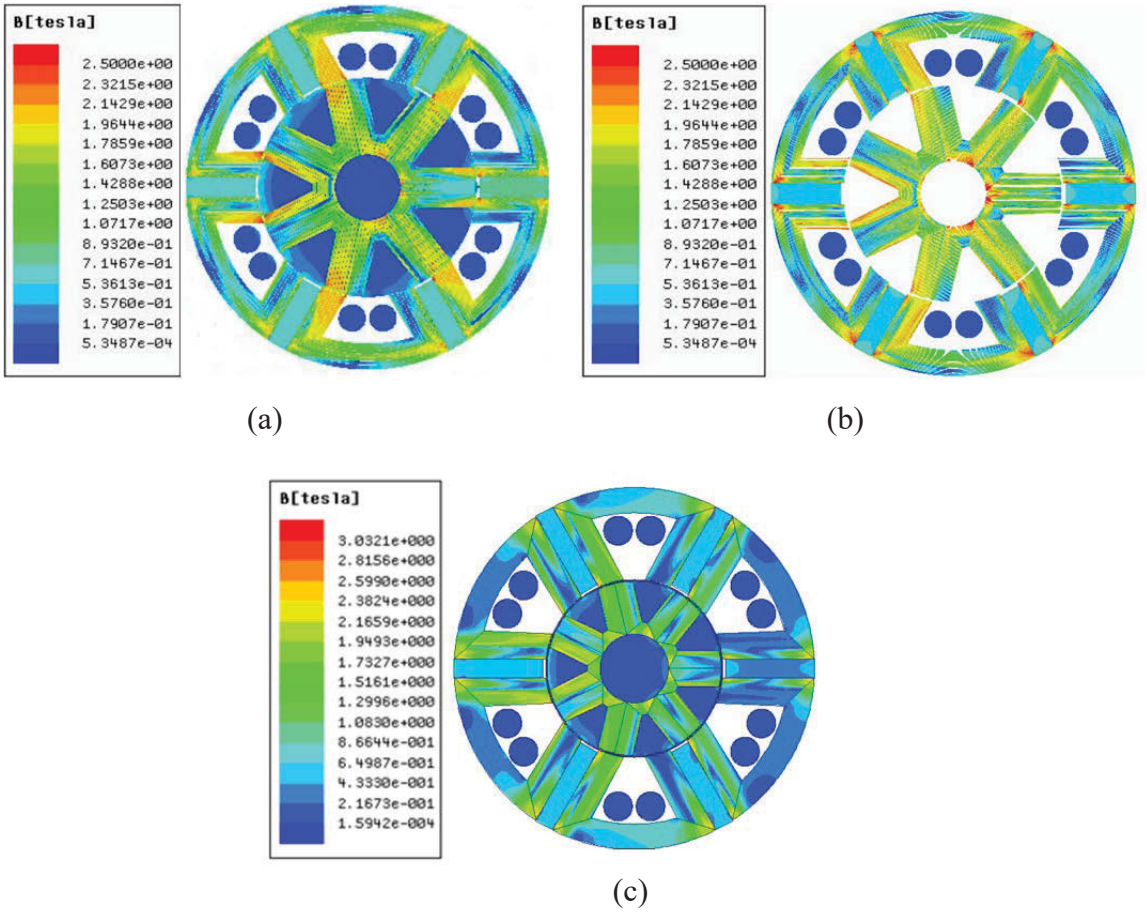

Fig. 3.5.2 Flux density contour of ALFSPMM, where (a) complete model, (b) reduced model, and (c) simplified model

3.5.3 Flux linkages

Fig. 3.5.3 shows the permanent magnet (PM) flux linkage per phased winding of the ALFSPMM. It can be seen that the simplified model presents the highest amplitude of PM flux and followed by the reduced model, misalignment model, and complete model (in descending order). The reason is that the complete model has more air gap layers in

the stator teeth than other models, i.e. the effective area for magnetic flux density of the complete model is the smallest.

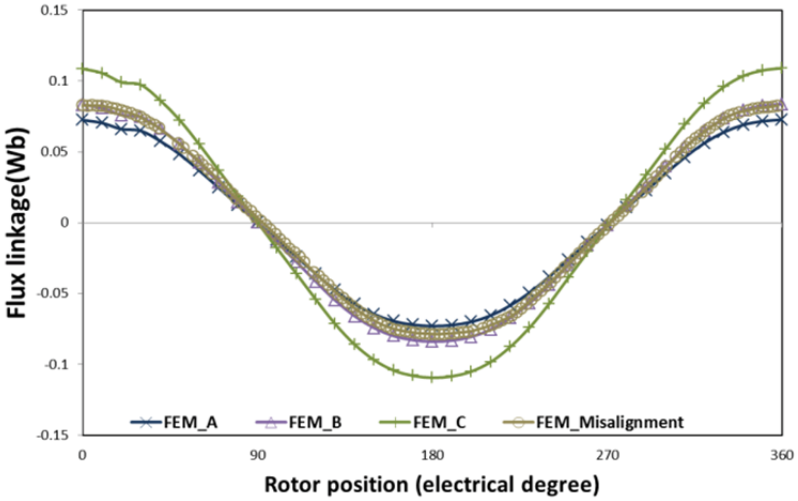

Fig. 3.5.3 Flux linkage of four models. In the figure, (FEM_A) presents the complete model, (FEM_B) the reduced model, (FEM_C) the simplified model and (FEM_Misalignment) the misalignment model.

3.5.4 Inductances

The block diagram of inductance measurement is illustrated in Fig. 3.5.4 and the test platform is shown in Fig. 3.5.5. There are three main components in this test system, which are the power source (function generator and power amplifier), signal measurement (three phase power analyzer) and the ALFSPMM with chuck. A 50 Hz sine wave is supplied by the function generator. The RMS value of the power amplifier output current is maintained at 0.2 ± 0.05 A. This RMS value of the current is determined by the method of trial and error and it is small enough to eliminate the influence of the AC signals to the total magnetic field produced by the permanent magnets. With this amount of current, an observable amount of voltage can be produced in the unexcited phases in the mutual-inductance measurement and the accuracy of measurement can be well guaranteed due to the limited small signal sensitivity of the instruments. A set of high voltage AC capacitors are connected to the power amplifier in series in order to eliminate the minor DC offset signal generated by the function generator. The stator windings of the ALFSPMM are star-connected. One phase (e.g. phase A) is excited by the power amplifier and the values of current, voltage and power

factor of this phase is measured by one channel of the power analyzer. The other two phases (i.e. phases B and C) are open circuited and the induced voltages are measured by the other two channels of the power analyzer.

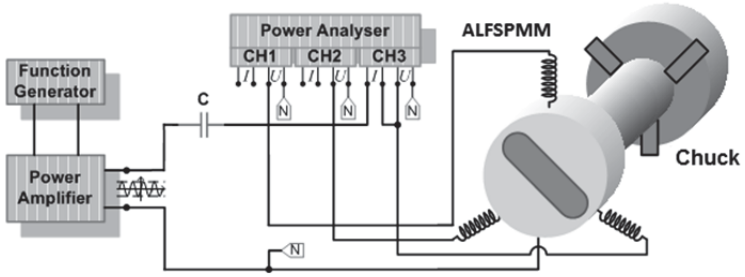

Fig.3.5.4 Block diagram of experimental ALFSPMM inductance measurement.

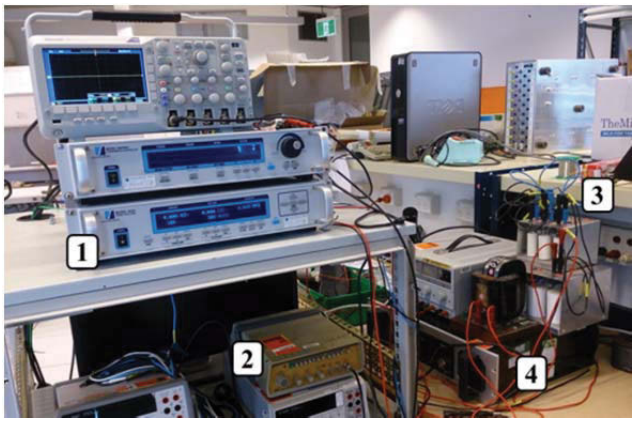

Fig. 3.5.5 Platform setup of experimental inductance measurement, where (1) power analyser, (2) function generator, (3) capacitors and (4) power amplifier.

The self and mutual-inductances are calculated by

$$L_s = \frac{|V_s|\sqrt{1-\cos\varphi^2}}{2\pi f |I_s|} \tag{3.5}$$

$$L_m = \frac{|V_m|}{2\pi f |I_s|} \tag{3.6}$$

where L_s is the self-inductance, L_m the mutual-inductance, V_s the voltage across the phase winding terminals, V_m the induced *emf* in the unexcited phase winding, cosφ the power factor, and I_s the phase current.

On the machine side, the shaft of the ALFSPMM is clamped by a three-jaw chuck. The

rotor position can be adjusted or locked by using the chuck and the resolution of the chuck is 1 mechanical degree per scale. The rotor position is adjusted between 0 and 52 mechanical degrees to obtain a whole electrical cycle. The voltage, current and power factor readings were taken in every two mechanical degrees.

The magneto-static module is utilized to calculate the inductance of ALFSPMM. Figs. 3.5.6 and 3.5.7 present the self- and mutual-inductances of the 2D FEM predictions and experimental measurements, respectively. In both figures, the self/mutual inductance curves of the complete, reduced, and simplified models are mostly overlapped because the FEM calculations from these three models are quite similar. Based on the calculations by using the reduced model, the FEM predicted average self- and mutual-inductances, d– and q–axis inductances are 6.17mH, 2.92mH, 8.63 mH and 9.76 mH, respectively. The experimentally measured average self- and mutual-inductances, d– and q–axis inductances are 6.95 mH, 2.76 mH, 9.54 mH and 10.02 mH, respectively.

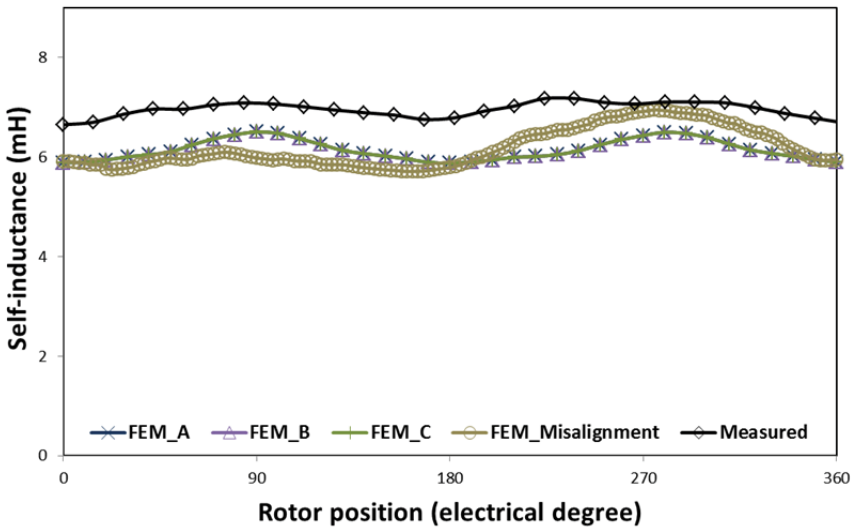

Fig. 3.5.6 FEM predicted and measured self-inductance of ALFSPMM, where (FEM_A) presents the complete model, (FEM_B) the reduced model, (FEM_C) the simplified model, (FEM_Misalignment) the misalignment model and (Measured) the experimental measurement.

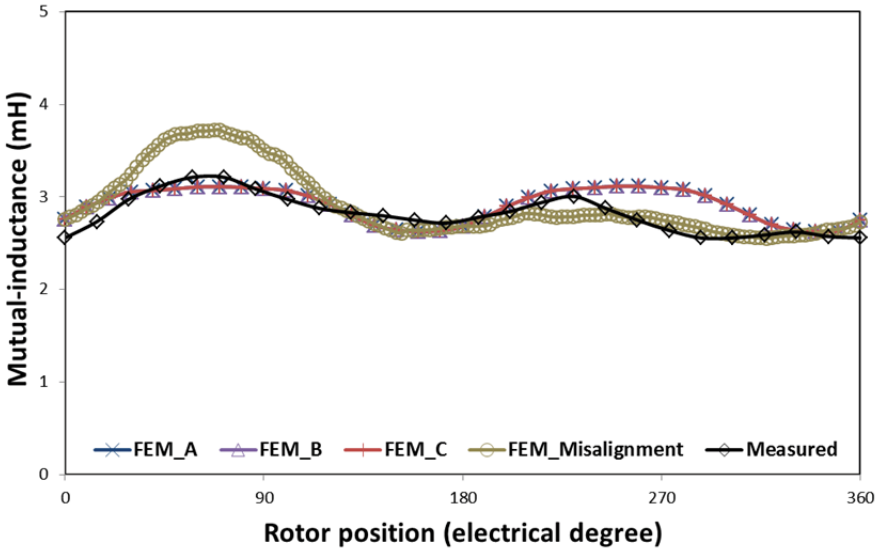

Fig. 3.5.7 FEM predicted and measured mutual-inductance of ALFSPMM, where (FEM_A) presents the complete model, (FEM_B) the reduced model, (FEM_C) the simplified model, (FEM_Misalignment) the misalignment model and (Measured) the experimental measurement.

In Fig. 3.5.6, it can be seen that the calculated self-inductances FEM_A, B and C are slightly lower than the measured self-inductance. In Fig. 3.5.7, it is found that the calculated mutual-inductances FEM_A, B and C are slightly higher than the measured mutual-inductance. The main reason could be attributed to that the measured inductances include magnetization inductance and the leakage inductance. However, the 2D FEM model only calculated the magnetization inductance while the leakage inductance is absent.

In Figs. 3.5.6 and 3.5.7, it can also be seen that the measured self- and mutual-inductances are asymmetrical. The possible reasons for the asymmetry were discussed previously in Section 3.4.2 and then the misaligned model was proposed for the verification. By comparing the calculations of misaligned model with the experimental measurements, similar trend of asymmetry can be found in In Figs. 3.5.6 and 3.5.7. Therefore, it can be concluded that the misaligned rotor shaft could be the major reason for the disagreement between the FEM calculations and experimental measurements.

3.5.5 Back-*emf*

The ALFSPMM is driven by a cordless hand drill at 680 rpm and the phase terminals of the ALFSPMM are connected to a digital oscilloscope. Fig. 3.5.8 shows the induced back-*emf* waveforms of the FEM predictions and experimental measurement.

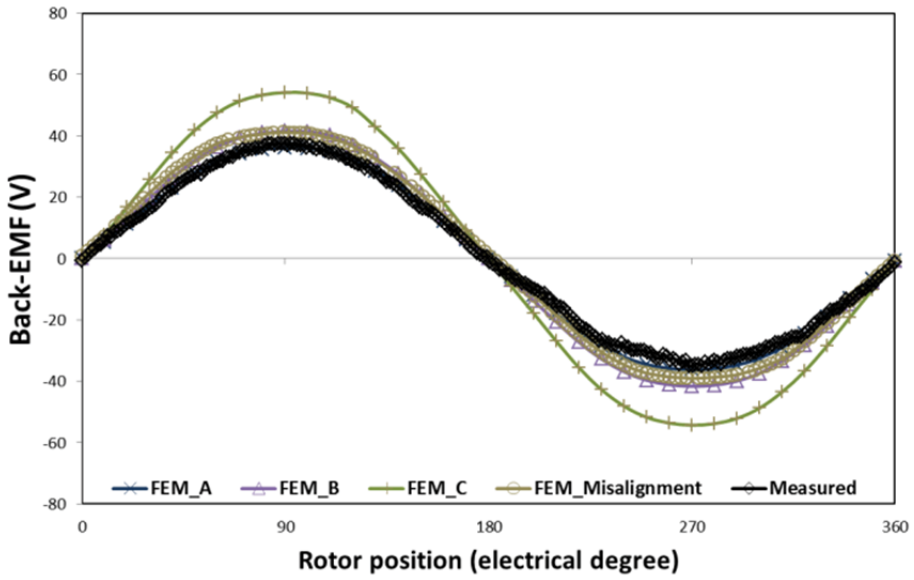

Fig. 3.5.8. FEM predicted and measured back-*emf* of ALFSPMM, where (FEM_A) presents the complete model, (FEM_B) the reduced model, (FEM_C) the simplified model, (FEM_Misalignment) the misalignment model and (Measured) the experimental measurement.

It can be seen that the simplified model presents the highest amplitude of back-*emf* and followed by the reduced model, misalignment model, experimental measurement and complete model (in descending order). It is noted that the waveform of the experimental measurement is asymmetrical as the area of the positive cycle is slightly larger than that of the negative cycle. The waveform of the misalignment model presents the similar trend of asymmetry. The maximum, minimum, average and root mean square (RMS) values of above back-*emf*s are presented in Table 3-5.

Table 3-5 Data Analysis of Back-*emf*s

	Max (V)	Min (V)	Avg (V)	RMS (V)
FEM_A	36.1	-36.2	-0.20	25.6
FEM_B	41.5	-41.6	-0.24	29.4
FEM_C	54.2	-54.3	-0.28	38.4
FEM_Misalignment	41.2	-39.0	-0.39	28.9
Measured	37.5	-35.0	+0.51	24.9

3.5.6 Cogging torque

Cogging torque is produced by the interaction of the magnets in the stator and the rotor teeth. It is a kind of pulsating torque and its average value is zero. Cogging torque does not contribute to the total torque output. However, it is a main reason for the speed/torque ripples and vibrations and accurate measurement of cogging torque is necessary for both machine design and machine control [3.29]-[3.31]. There are several common methods for cogging torque measurement, such as the conventional torque transducer, strain gauge bridge based on the reaction torque on the stator, torque observer based on the voltage and current measurements, and special cogging torque measurement transducer. The conventional torque transducers are usually used in the average electromagnetic torque measurement on load but they are not suitable for the measurement of pulsating torque with zero average value due to the limited accuracy. The special torque transducers for cogging torque measurement can be very accurate. However, they are usually expensive. The strain gauge bridge needs a special set-up to measure the reaction torque on the stator. The torque observer naturally can only present the theoretical calculations and cannot provide reliable cogging torque information.

In this section, a simple cogging torque measuring method is presented which is inspired by the method introduced in [3.32]. Fig. 3.5.9 is the schematic diagram of the proposed cogging torque measurement and Fig. 3.5.11 shows the platform setup. One end of the rotor shaft is coupled with an optical encoder (10000 pulses per turn) to accurately measure the rotor mechanical position. The other end of the rotor shaft is clamped by a three-jaw chuck. A balanced beam (length L=47.59cm) with a spirit level is fixed on the end bracket of ALFSPMM. There is a hole at the center of the beam. The rotor shaft passes through the hole and can spin freely as shown in Fig. 3.5.10. Two

rotatable steel stands are fitted to the beam with screws. One of the steel stands rests on the pan of a digital scale (capacity 8100g， readability 0.1 g). The digital scale is calibrated to zero once the beam is levelled. A pre-load weight is attached to the metal stand, in order to ensure the contact between the stand and the pan during the test, i.e. a positive DC offset to the cogging torque waveform.

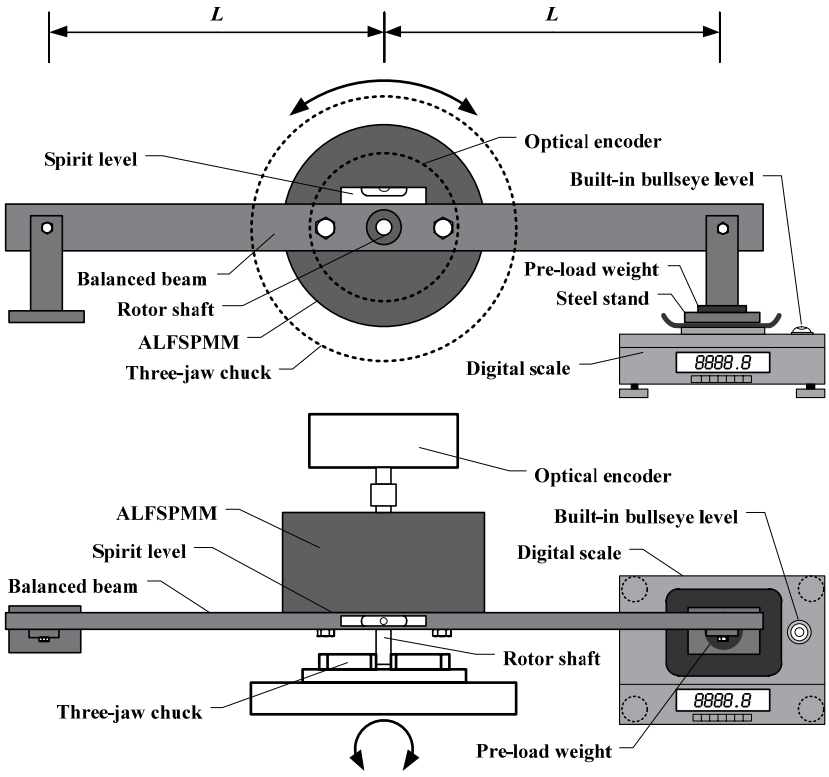

Fig. 3.5.9 Schematic diagram of cogging torque measurement.

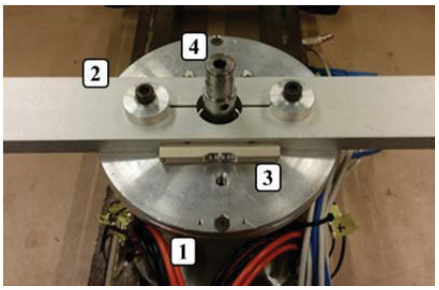

Fig. 3.5.10 Balanced beam fixed on the motor end bracket, where (1) ALFSPMM, (2) balanced beam, (3) spirit level, and (4) rotor shaft.

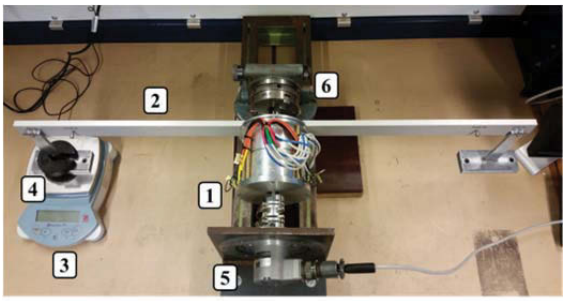

Fig. 3.5.11 Platform setup of cogging torque measurement, where (1) ALFSPMM, (2) balanced beam with two steel stands, (3) digital scale, (4) pre-load weight, (5) encoder and (6) three- jaw chuck.

In [3.32], the chuck clamps on the stator of the motor and the balanced beam are fixed on the rotor shaft. This method requires a lathe with a much larger chuck to clamp the stator rather than clamping the rotor shaft. In most cases, all the measurements need to be done within the mechanical workshop due to the usage of lathe. The method proposed in this paper only requires a small chunk to rotate the motor, and all the tests can be done on a small bench top.

To measure the cogging torque, the rotor position is varied by rotating the chuck in one direction. The step in the cogging torque measurement is set to be approximately 0.5 mechanical degree, i.e. 3.5 electrical degrees. The cogging torque is calculated by

$$T_{cogging} = L(M_{scale} - M_{pre-load}) \tag{3.7}$$

where $T_{cogging}$ is the cogging torque, M_{scale} the reading from the digital scale, $M_{pre\text{-}load}$ the weight of the pre-load, and L the length of the balanced beam.

For the accuracy of cogging torque measurement, the following requirements should be well met in the measuring procedure:

- The beam should be maintained at the horizontal position at all times, and the spirit level should be checked after each measurement;
- The beam should be well balanced, including the fittings, such as screws and washers, and the balancing weights should be fitted to the beam if necessary;
- The pre-load weight should be heavy enough in order to ensure that the reading of the digital scale remains positive at all times.

Fig. 3.5.12 presents the measured cogging torque waveforms of ALFSPMM in 360 mechanical degrees. Seven repeating mechanical cycles can be found as there are seven poles in the rotor. It is noted that the shape of seven mechanical cycles are slightly different. The reason may be attributed to that the motor is mostly hand-made in a university workshop rather than manufactured in a motor factory. The manufacturing error of the motor is slightly high, which leads to the inconsistency of the poles.

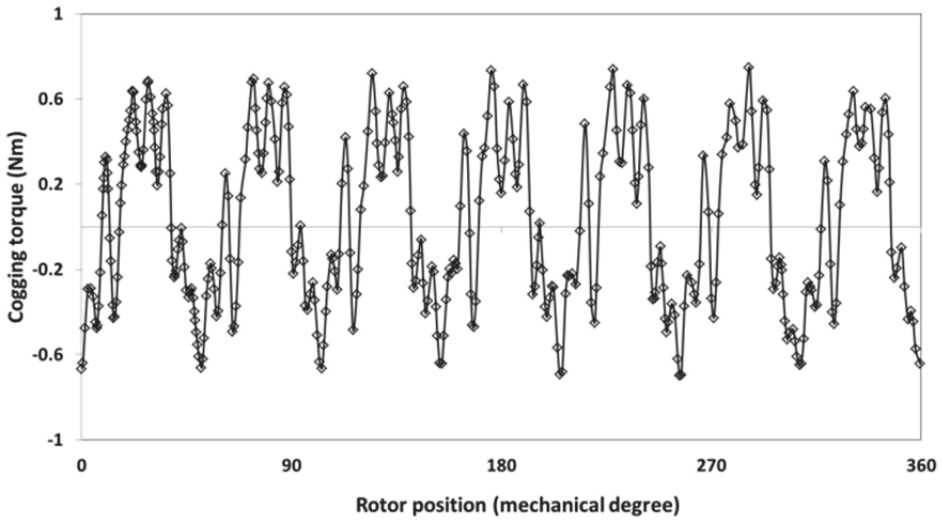

Fig. 3.5.12 Cogging torque measurement in 360 mechanical degrees.

The magneto-static module is applied in the cogging torque calculation of ALFSPMM. Fig. 3.5.13 presents the FEM calculations of the complete model, reduced model, and simplified model in one electrical cycle (51.4 mechanical degrees). It can be seen that the calculated cogging torque waveform by the simplified model is highly symmetrical. The waveform of reduced model presents some degrees of asymmetry in both the positive and negative cycles and noticeable asymmetry can be seen from the cogging torque waveform of the complete model.

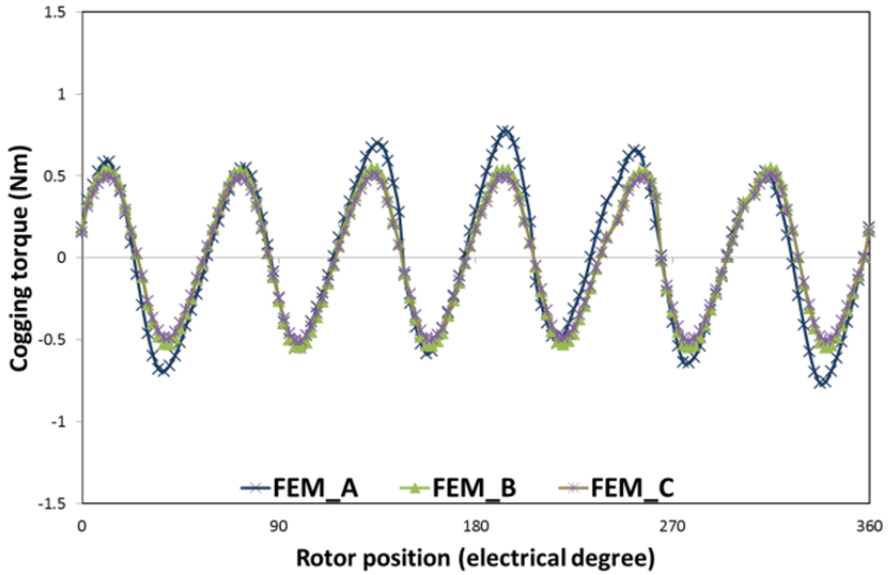

Fig. 3.5.13 FEM predicted cogging torque of ALFSPMM, where (FEM_A) presents the complete model, (FEM_B) the reduced model and
(FEM_C) the simplified model

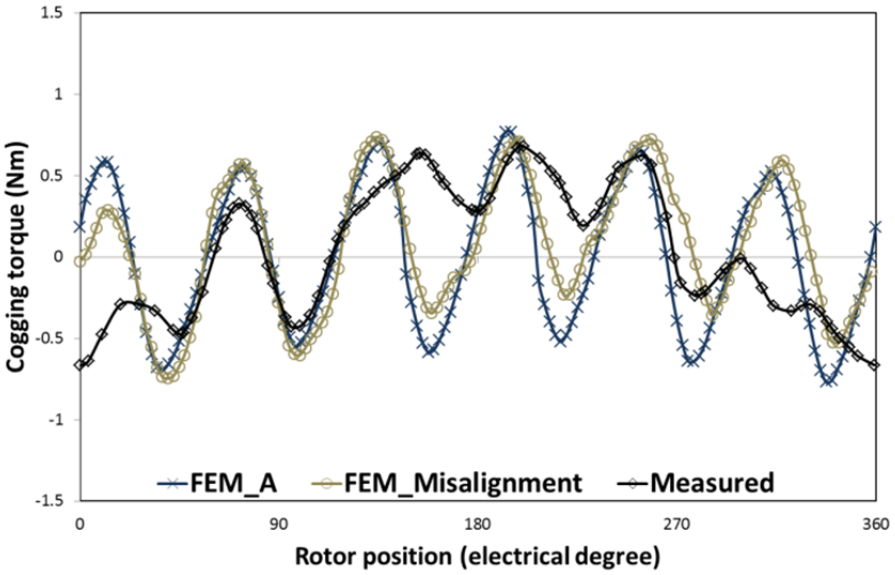

Fig. 3.5.14 Measured and FEM predicted (with misalignment) cogging torque of ALFSPMM, where (FEM_A) presents the complete model, (FEM_Misalignment) the misalignment model and
(Measured) the experimental measurement.

The measured cogging torque and FEM calculations of complete model and misaligned model are shown in Fig. 3.5.14. It can be noted that the waveform of the misaligned model presents a higher degree of asymmetry than the complete model. The waveform

of measured cogging torque seems highly asymmetrical and random. However, it still has a few sections which well overlap with the FEM calculations.

The reason for the discrepancy between the calculation and the measurement can be investigated from two aspects, one is the fabrication errors and the other is the inaccuracy of the FEM calculation. As the ALFSPMM is hand made in the university's workshop, many issues can cause the fabrication errors, such as misalignment between the stator core and the rotor shaft, uneven distribution of the stator/rotor lamination cores, inconsistency of the permanent magnets and the possible magnetic properties damage of the sheets caused in the bending procedure. In the FEM calculations, the rotor shaft misalignment is investigated in the misalignment model and the calculated cogging torque waveform develops a trend toward the measurement. Therefore, it can be concluded that misaligned rotor shaft is one possible reason for the disagreement. To improve the accuracy of the model, other issues in the motor fabrication as discussed above also need to be considered in the future research work. In addition, the FEM calculations in this paper are carried out in 2D. Due to the axially laminated structure of the motor, the 3D FEM could be more accurate. However, a more complex model and much more calculation time are needed for the 3D FEM [3.33]-[3.36].

3.6 Load Tests

The load tests of ALFSPMM are performed with a two-level inverter-fed motor drive system. A dSPACE DS1104 PPC/DSP control board is employed to implement the real-time algorithm coding using the C language. The external load is applied using a programmable dynamo-meter controller DSP6000. The motor speed is obtained by a 10000-pulse incremental encoder. All experimental results are recorded by the ControlDesk interfaced with DS1104 and PC at 10 kHz sampling frequency. The experimental setup is illustrated in Fig. 3.6.1. The FEM calculation and experimental measurements of load tests are shown in Fig. 3.6.2. The major reason for the discrepancy is that the friction in the bearings is ignored in the FEM calculation.

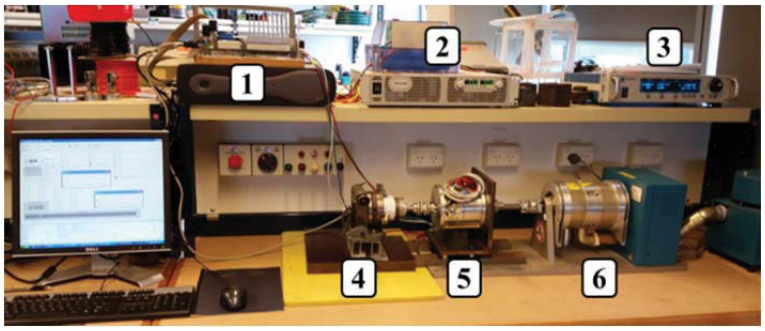

Fig. 3.6.1 Platform setup of load test, where (1) dSPACE control board, (2) DC power supply, (3) dynamometer controller, (4) encoder, (5) ALFSPMM, and (6) dynamometer.

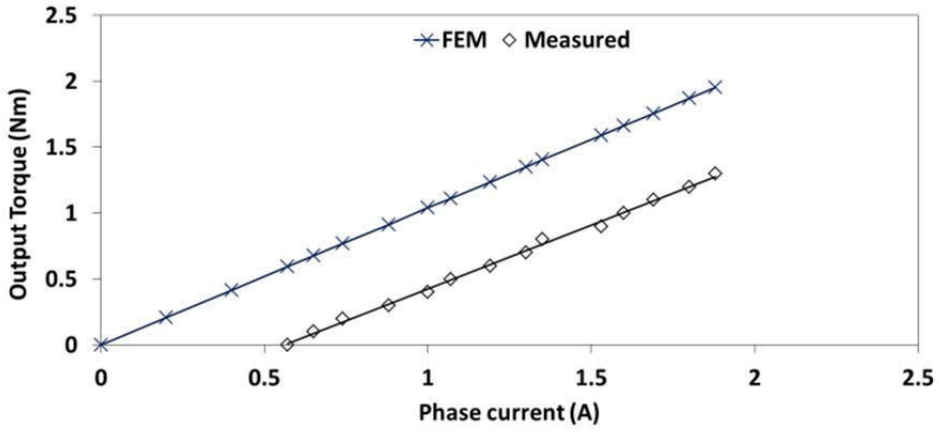

Fig. 3.6.2. Measured torque output versus phase current of ALFSPMM.

3.7 The Influence of the Bending Processes on Soft Magnetic Material

The fabrication of the laminated stator and rotor segments are complicated and sensitive to errors in particular with respect to the air gap error and the diversity of the soft magnetic characteristics of the permanent magnets and HiB steel sheets. The influence of the bending processes on soft magnetic material characteristics, mechanical tolerance and balance are discussed in this chapter.

- The influence on soft magnetic material characteristics

In 2014, Hiroto Hagihara, et al., investigated this issue and the authors conclude that the bending processes can cause some degree of deterioration in the magnetic properties of grain-oriented steel sheets [3.37]. However, the magnetic properties of the bended sheets can be partly or mostly recovered by annealing depending on the degree of the bending. The magnetisation properties of bended specimens before and after annealing

are presented in Fig. 3.7.1, where the numbers after letter "d" are the bending diameters in millimetres.

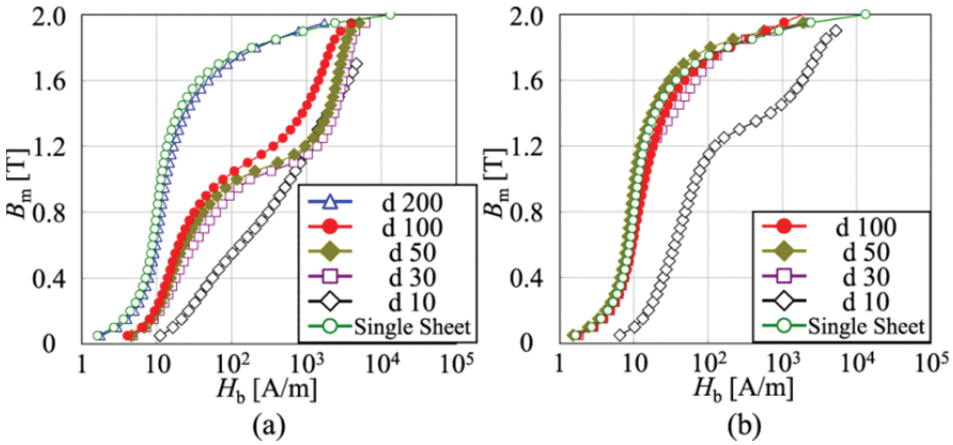

Fig. 3.7.1 Measured magnetization properties of bended specimens before and after annealing at 50 Hz [3.37], where (a) Before annealing, (b) After annealing.

In ALFSPMM, the bending diameters of the stator and rotor laminations are approximately 11mm and 15mm, respectively. Assuming that the magnetic properties of the sheets in [3.37] and ALFSPMM are similar, one can recover mostly the magnetic property deterioration caused by bending in ALFSPMM after annealing. However, the before/after-annealing magnetic properties of the bended steel sheets used in ALFSPMM are not studied yet. Another fact is that the steel sheets used in ALFSPMM are 24% thicker than those in [3.37] and there may be a possibility that thicker sheets can have better resistance to magnetic properties deterioration caused by bending. These open questions are very attractive to the authors and will be addressed in the future research work.

- The influence on mechanical tolerances

The mechanical tolerances in the complicated fabrication process of ALFSPMM could be a problem. Many methods are tried and some custom-made tools are used to facilitate the fabrication and reduce the mechanical tolerances as shown in Fig. 3.7.2.

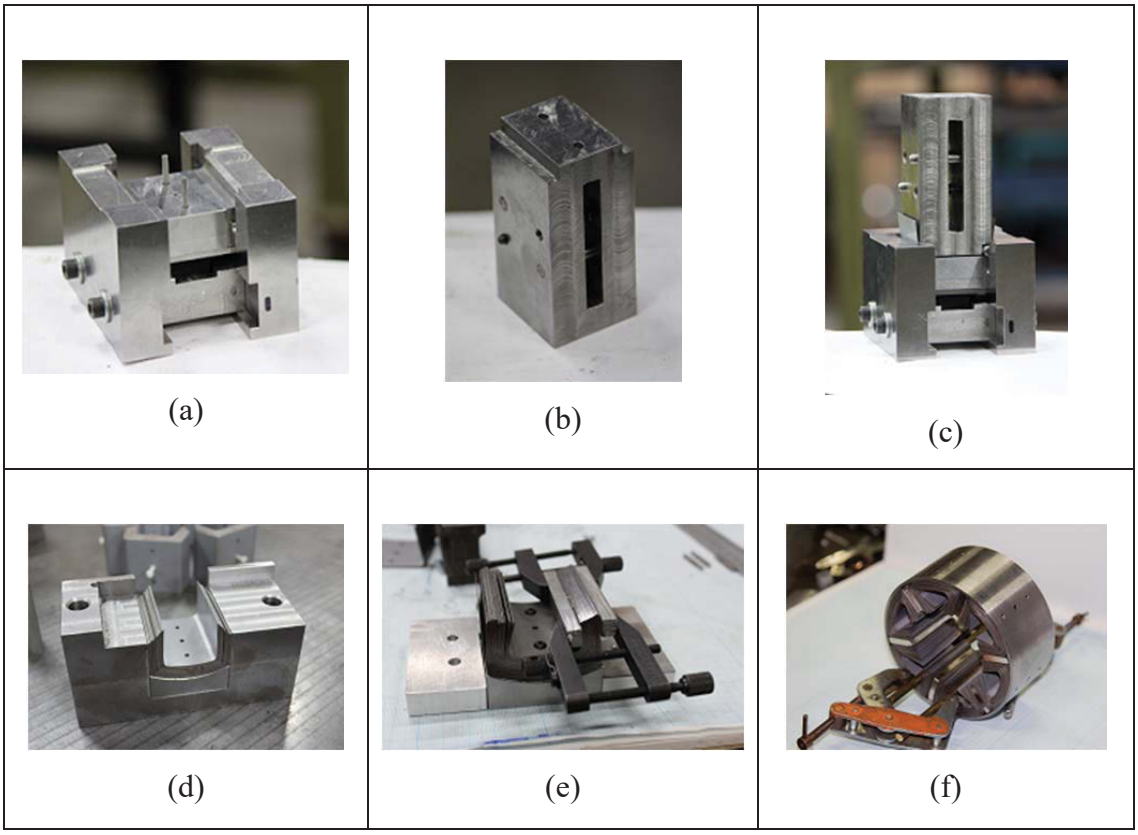

Fig. 3.7.2 Custom-made tools and methods used in fabrication of ALFSPMM, where (a)-(d) custom-made dies used in pressing the stator and rotor laminations, and (e) and (f) clamps used in squeezing out excess glue and insuring the thickness of the laminations.

In the fabrication of stator and rotor laminations, the HiB steel sheets are pressed individually with different shape of dies and then the Loctite is spread evenly among the sheets. The glued sheets are put back into the die or clamped with splints in order to squeeze out excess glue and hold the piece during curing. The designated total thickness of the laminations can also be guaranteed in this process. After the assembly of the stator/rotor laminations, they are mounted on the lathe and carefully milled with a grinder according to the designated stator/rotor poles height.

- The influence on balance

Due to the manual bending process and uneven distribution of the glue, the unbalances are theoretically existent and they are probably inevitable. By analysing the experimental measurements (inductances, back-*emf* and cogging torque), it can be found that the influence of the unbalances seems quite limited.

3.8 Summary

An axially laminated flux-switching permanent magnet machine with high grain oriented silicon steel is proposed. The fabrication procedures are presented in details. Compared with the traditional radially-laminated motors, the major difficulty is that the fabrication of ALFSPMM's stator/rotor laminations is more complicated and time consuming.

According to the study in [3.37] , the bending processes can cause some degree of deterioration in the magnetic properties of grain-oriented steel sheets. However, the magnetic properties deterioration in ALFSPMM could be mostly recovered after annealing, as the bending diameters of the stator and rotor laminations are approximately 11mm and 15mm, respectively.

To optimize and facilitate the industrial manufacturing, the following aspects should be considered in the future:

- Dies should be made of tool steel in order to improve the accuracy and durability;
- Multiple sets of dies and holding/clamping devices need to be made in order to fabricate multiple laminations in parallel;
- The lengths of the steel sheets in each layer should be individually calculated in order to save the material and reduce the grinding time;
- The stator/rotor laminations should be annealed in order to recover the magnetic property deterioration in bending process.

Three ALFSPMM models with different complexity are proposed to facilitate the 2D FEM calculation. The complete model can provide a more accurate prediction and the simplified model can greatly speed up the calculation. The reduced model is a trade-off between accuracy and time consumption. The issues in the motor fabrication are discussed and a model with rotor shaft misalignment is proposed. Based on the FEM calculations of the misaligned model, it can be concluded that the misaligned rotor shaft is a possible reason for the disagreement between the previous FEM calculations and

experimental measurements. To improve the accuracy of the FEM calculation, other issues in the motor fabrication as discussed above also need to be considered in the future research work. In addition, a simple low-cost method to accurately measure the cogging torque is presented.

REFERENCES

[3.1] W. Xu, J. G. Zhu, Y. C. Zhang, Y. G. Guo, and G. Lei, "New axial laminated-structure flux-switching permanent magnet machine with 6/7 poles," *IEEE Trans. Magn*., vol. 47, no. 10, pp. 2823-2826, Oct. 2011.

[3.2] W. Xu, G. Lei, T. S. Wang, X. H. Yu, J. G. Zhu, and Y. G. Guo, "Theoretical research on new laminated structure flux switching permanent magnet machine for novel topologic plug-in hybrid electrical vehicle," *IEEE Trans. Magn*., vol. 48, no. 11, pp. 4050-4053, Nov. 2012.

[3.3] Z.Q. Zhu, D. Howe, "Electrical Machines and Drives for Electric Hybrid and Fuel Cell Vehicles", Proceedings of the IEEE, vol. 95, no. 4, pp. 746-765, Apr. 2007.

[3.4] W.X. Zhao, "Analysis of fault-tolerant performance of a doubly salient permanent-magnet motor drive using transient cosimulation method", IEEE Trans. Ind. Electron., vol. 55, no. 4, pp. 1739-1748, Apr. 2008.

[3.5] X.Y. Zhu, "Design and analysis of a new hybrid excited doubly salient machine capable of field control", Proc. Industry Applications Conference, pp. 2382-2389, Oct. 2006.

[3.6] W. Hua, "Inductance characteristics of 3-phase flux-switching permanent magnet machine with doubly-salient structure", Trasactions of China Electrotechnical Society, vol. 22, pp. 25-32, Nov. 2007.

[3.7] W. Hua, G. Zhang, and M. Cheng, "Investigation and design of a high-power flux-switching permanent magnet machine for hybrid electric vehicles," IEEE Trans. Magn., vol. 51, no. 3, Art.ID: 8201805, Mar. 2015.

[3.8] L. Mo, L. Quan, X. Zhu, Y. Chen, H. Qiu, and, K.T. Chau, "Comparison and analysis of flux-switching permanent-magnet double-rotor machine with 4QT used for HEV," *IEEE Trans. Magn*, vol. 50, no. 11, Art.ID 8205804, Nov. 2014.

[3.9] F. Li, W. Hua, M.H. Tong, G.S. Zhao, and M. Cheng, "Nine-phase flux-switching permanent magnet brushless machine for low-speed and high-torque applications," *IEEE Trans. Magn*, vol. 51, no. 3, Art.ID 8700204, Mar. 2015.

[3.10] W. Z. Fei, P.C.K. Luk, J. X. Shen, Y. Wang, and M. J. Jin, "A novel permanent-magnet flux switching machine with an outer-rotor configuration for in-wheel light traction applications," *IEEE Trans. Ind. Appl.,* vol. 48, no. 5, pp. 1496-1506, Sep. 2012.

[3.11] J. T. Chen, Z.Q. Zhu, and D. Howe, "Stator and rotor pole combinations for multi-tooth flux-switching permanent-magnet brushless ac machines," *IEEE Trans. Magn*, vol. 44, no. 12, pp. 4659-4667, Dec. 2008.

[3.12] M. Cheng, W. Hua, J. Zhang , and W. Zhao, "Overview of stator permanent magnet brushless machines", *IEEE Trans. Ind. Electron*, vol. 58, no. 11, pp. 5087 -5101, Nov. 2011.

[3.13] M.O.E. Aboelhassan, T. Raminosoa, A. Goodman, L. de Lillo, and C Gerada, "Performance evaluation of a vector-control fault-tolerant flux-switching motor drive," *IEEE Trans. Ind. Electron*, vol. 60, no. 8, pp. 2997-3006, Aug. 2013.

[3.14] B. Gaussens, E. Hoang, M. Lecrivain, P. Manfe, and M. Gabsi, "A hybrid-excited flux-switching machine for high-speed DC-alternator applications," *IEEE Trans. Ind. Electron*., vol. 61, no. 6, pp. 2976-2989, Jun. 2014.

[3.15] Y. Wang, and Z. Deng, "Hybrid excitation topologies and control strategies of stator permanent magnet machines for DC power system," *IEEE Trans. Ind. Electron*., vol. 59, no. 12, pp. 4601-4616, Dec. 2012.

[3.16] G. Zhang, W. Hua, M. Cheng, and J. Liao, "Design and comparison of two six-phase hybrid-excited flux-switching machines for EV/HEV applications," *IEEE Trans. Ind. Electron*., vol. 63, no. 1, pp. 481-493, Jan. 2016.

[3.17] X. Xue, W. Zhao, J. Zhu, G. Liu, X. Zhu, and M. Cheng, "Design of five-phase modular flux-switching permanent-magnet machines for high reliability applications," *IEEE Trans. Magn*., vol. 49, no. 7, pp. 3941-3944, Jul. 2013.

[3.18] R.L. Owen, Z.Q. Zhu, and G.W. Jewell, "Hybrid excited flux switching permanent magnet machines with iron flux bridges," *IEEE Trans. Magn*., vol. 46, no. 6, pp. 1726-1729, Jun. 2010.

[3.19] B. Zhang, M. Cheng, J. Wang, and S. Zhu, "Optimization and analysis of a yokeless linear flux-switching permanent magnet machine with high thrust density," *IEEE Trans. Magn*., vol. 51, no. 11, Art.ID 8204804, Nov. 2015.

[3.20] Z.Q. Zhu and J.T. Chen, "Advanced flux-switching permanent magnet brushless machines," *IEEE Trans. Magn*., vol. 46, no. 6, pp. 1447-1453, Jun. 2010.

[3.21] W. Zhao, T.A. Lipo, and B. Kwon, "A novel dual-rotor axial field fault tolerant flux switching permanent magnet machine with high torque performance," *IEEE Trans. Magn*., vol. 51, no. 11, Art.ID 8112204, Nov. 2015.

[3.22] A. S. Thomas, Z. Q. Zhu, and L. J. Wu, "Novel modular rotor switched flux permanent magnet machines," *IEEE Trans. Ind. Appl.*, vol. 48, no. 6, pp. 2249-2258, Nov. 2012.

[3.23] N. Bianchi and B. J. Chalmers, "Axially laminated reluctance motor: analytical and finite-element methods for magnetic analysis," *IEEE Trans. Magn.*, vol. 38, no. 1, pp. 239-245, Jan. 2002.

[3.24] A. J. O. Cruickshank, R.W. Menzies, and A. F. Anderson, "Axially laminated anisotropic rotors for reluctance motors," *in Proc. Inst. Elec. Eng. Electr. Power Appl.*, vol. 113, no. 12, pp. 2058–2060, Dec. 1966.

[3.25] P. J. Lawrenson and L. A. Agu, "Theory and performance of polyphase reluctance machine," *in Proc. Inst. Elec. Eng. Electr. Power Appl*., vol. 111, no. 8, pp. 1435–1445, Aug. 1964.

[3.26] P. J. Lawrenson and L. A. Agu, "Low-inertia reluctance machines," *in Proc. Inst. Elec. Eng. Electr. Power Appl.*, vol. 111, no. 12, pp. 2017-2025, Dec. 1964.

[3.27] J. K. Kostko, "Polyphase reaction synchronous motors," *J. Amer. Inst. Elect. Eng.*, vol. 42, no. 11, pp. 1162–1168, Nov. 1923.

[3.28] Y. H. Kim, J. H. Lee, and J. K. Lee, "Optimum design of axially laminated anisotropic rotor synchronous reluctance motor for torque density and ripple improvement," *in Proc. IET Computation in Electromagnetics*, pp. 1-2. Mar. 2014.

[3.29] Z.Q. Zhu, A.S. Thomas, J.T. Chen, and G.W Jewell, "Cogging torque in flux-switching permanent magnet machines," *IEEE Trans. Magn*., vol. 45, no. 10, pp. 4708-4711, Oct. 2009.

[3.30] D. Wang, X. Wang, and S. Jung, "Reduction on cogging torque in flux-switching permanent magnet machine by teeth notching schemes," *IEEE Trans. Magn*., vol. 48, no. 11, pp. 4228-4231, Nov. 2012.

[3.31] J. Yan, H. Lin, Y. Feng, Z.Q. Zhu, P. Jin, and Y. Guo, "Cogging torque optimization of flux-switching transverse flux permanent magnet machine," *IEEE Trans. Magn*., vol. 49, no. 5, pp. 2169-2172, May 2013.

[3.32] Z. Q. Zhu, "A simple method for measuring cogging torque in permanent magnet machines," *in Proc. IEEE Power & Energy Society General Meeting*, pp. 1-4. Jul. 2009.

[3.33] H.J. Shin, J.Y. Choi, S.M. Jang, and K.Y. Lim, "Design and analysis of axial permanent magnet couplings based on 3D FEM," *IEEE Trans. Magn*., vol. 49, no. 7, pp. 3985-3988, Jul. 2013.

[3.34] T. D. Nguyen, K. J. Tseng, S. Zhang, and T. H. Nguyen, "A novel axial flux permanent-magnet machine for flywheel energy storage system: design and analysis," *IEEE Trans. Ind. Electron*, vol. 58, no. 9, pp. 3784-3794, Sep. 2011

[3.35] G. Lei, T. S. Wang, Y. G. Guo, J. G. Zhu, and S. H. Wang, "System-level design optimization methods for electrical drive systems: deterministic approach," *IEEE Trans. Ind. Electron*., vol. 61, no. 12, pp. 6591-6602, Dec. 2014.

[3.36] G. Lei, T. S. Wang, J. G. Zhu, Y. G. Guo, and S. H. Wang, "System-level design optimization method for electrical drive systems—robust approach," *IEEE Trans. Ind. Electron*., vol. 62, no. 8, pp. 4702-4713, Aug. 2015.

[3.37] H. Hagihara, Y. Takahashi, K. Fujiwara, Y. Ishihara, and T. Masuda, "Magnetic properties evaluation of grain-oriented electrical steel sheets under bending stress," *IEEE Trans. Magn*., vol. 50, no. 4, Art.ID 2002104, Apr. 2014.

CHAPTER 4

FINITE-CONTROL-SET MODEL PREDICTIVE DIRECT TORQUE CONTROL OF PERMANENT MAGNET SYNCHRONOUS MOTORS WITH EXTENDED SET OF VOLTAGE SPACE VECTORS

4.1 Introduction

Direct torque control (DTC) features simple structure and fast dynamic response. In DTC, the voltage space vector (VSV) is selected by using two hysteresis comparators and a pre-defined switching table. The performance of DTC in terms of torque and flux ripples and drive system efficiency is unsatisfactory since the VSV is selected heuristically [4.1]-[4.2]. Recently, the finite-control-set model predictive direct torque control (FCS-MPDTC) has been developed as a simple and promising control technique to overcome these problems [4.3]-[4.6]. Based on the system model, the FCS-MPDTC can predict the future behaviour of the controlled variables, such as torque, stator flux, and switching transitions, etc. Each possible VSV is evaluated by the cost function and the VSV with the minimum cost is chosen to apply for the next control period [4.3]. FCS-MPDTC has several advantages such as good dynamic response and great flexibility of incorporating various constraints. It has been applied to a variety of fields, such as total harmonic distortion (THD) reduction [4.7], loss minimisation [4.8], switching frequency reduction [4.9], and common-mode voltage suppression [4.10]. In [4.11], a novel model predictive control with extended VSVs and time-optimised control is proposed for ripple reduction. A high-bandwidth explicit mode-predictive controller in [4.12] is developed, exhibiting high dynamic performance at various operating points. In [4.13], an improved FCS-MPDTC with duty ratio control is investigated for the control of a three-level inverter-fed induction motor drive, reducing the average switching frequency up to 35% compared to that of conventional FCS-MPDTC. However, the FCS-MPDTC still suffers from relatively high torque and flux ripples due to the limited number of VSVs. High sampling frequency of the control system is required to improve the performance [4.14]. This would result in a high computational burden on the microprocessor hardware, which is undesirable in the real-time implementation.

In DTC, it is a common practice that the steady-state performance of torque and flux can be improved by applying duty cycle control [4.15]-[4.17] and this concept was recently introduced to FCS-MPDTC [4.18]-[4.22]. In [4.18], the principle of torque ripple minimization is introduced to calculate the optimal weighting factor and each sampling period is divided into two intervals to achieve further torque ripple reduction. The calculation of optimal weighting factor is complicated and parameter dependent. Similar method was proposed in [4.19], which also divides the control period into two intervals. In [4.20], the principle of torque ripple minimization is employed to calculate the duration of the active VSV and a fixed weighting factor is used. Compared with the conventional FCS-MPDTC, better steady-state performance can be obtained. However, in these methods, the best VSV and the duty ratio are decided in a cascaded manner which may not be able to achieve the best result from the system level.

This chapter proposes a novel FCS-MPDTC with an extended set of twenty modulated VSVs, which are formed by eight basic VSVs (used in the conventional DTC) and twelve extended VSVs by modulating eight basic VSVs with fixed duty ratio. By evaluating all twenty VSVs, the concept of duty ratio control is naturally integrated into the proposed algorithm. To mitigate the computational burden caused by the increased number of VSVs, a pre-selective scheme is designed for the proposed FCS-MPDTC to filter out the impractical VSVs instead of evaluating all twenty VSVs.

4.2 Model of Permanent Magnet Synchronous Motors

The mathematical model of a machine, in terms of controller design and performance analysis, is usually one or several equations, in which the relationship between the machine input and output variables is analytically expressed, most of the time, by using the machine parameters. This relationship could be generally classified as the electrical and the mechanical processes in the device.

The conventional permanent magnet synchronous motor (PMSM) model described in this sector was oriented for motors with sinusoidal back *emf*, which is widely used for development of the machine drive strategies. It was firstly derived in a stationary reference frame and then transformed to a rotating reference fame to achieve field

control. Linear assumptions were made to simplify the magnetic properties in the model and the nonlinear saturation effect is neglected.

For a PMSM, it is assumed that the three-phase stator windings are symmetrical and each phase has the same parameter. The electrical model of the device is similar to that of electrically excited synchronous machines (SM) and it is normally expressed by using the per phase voltage equation, in which the phase current is a function of the input voltage signal and the machine electrical parameters, i.e. resistance and inductance.

It is different from the electrically excited SM in that the *emf* in PMSM is induced by the permanent magnets fixed on the rotor and it is related to the magnet rotating speed. Therefore, the per phase flux linkage is always utilized to express the machine electrical equation. The voltage equation for the stator phase can be expressed as

$$u_s = R_s i_s + \frac{d\psi_s}{dt} \tag{4.1}$$

where u_s is the stator phase voltage, i_s the stator phase current, R_s the stator resistance, and ψ_s the phase flux linkage.

By assuming that the flux linkage is contributed by both the three-phase stator currents and the rotating magnet, the PMSM model in the stationary reference frame can be derived as

$$\begin{bmatrix} u_a \\ u_b \\ u_c \end{bmatrix} = R_s \begin{bmatrix} i_a \\ i_b \\ i_c \end{bmatrix} + \begin{bmatrix} L_{aa} & L_{ab} & L_{ac} \\ L_{ba} & L_{bb} & L_{bc} \\ L_{ca} & L_{bc} & L_{cc} \end{bmatrix} \frac{d}{dt} \begin{bmatrix} i_a \\ i_b \\ i_c \end{bmatrix} + \frac{\partial}{\partial \theta} \begin{bmatrix} \psi_a \\ \psi_b \\ \psi_c \end{bmatrix} \omega_e \tag{4.2}$$

where u_a, u_b and u_c are the three-phase voltage, i_a, i_b and i_c the three-phase current, ψ_a, ψ_b and ψ_c the three-phase flux linkage, respectively, and $\begin{bmatrix} L_{aa} & L_{ab} & L_{ac} \\ L_{ba} & L_{bb} & L_{bc} \\ L_{ca} & L_{bc} & L_{cc} \end{bmatrix}$ is the inductance matrix, including both the self- and mutual-inductances.

The last part in (4.2) is usually defined as the back *emf* of the machine and it can be found that the *emf* values are proportional to the rotating speed.

In order to decouple the control of flux and torque, the two-phase orthogonal reference frame in stationary and rotation are developed (*α-β* and *d-q* reference frames). Fig. 4.2.1 shows the spatial vector relationship between these reference-frames, where θ is defined as the angle between the stationary and rotating frames.

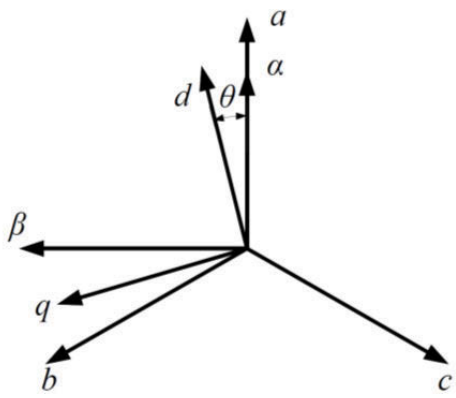

Fig. 4.2.1 Relationship between different reference frames

The Park and Clark transformations defined below are applied to convert the variables between these reference-frames:

$$\begin{bmatrix} \psi_a \\ \psi_\beta \end{bmatrix} = \sqrt{\frac{2}{3}} \begin{bmatrix} 1 & -\frac{1}{2} & -\frac{1}{2} \\ 0 & \frac{\sqrt{3}}{2} & -\frac{\sqrt{3}}{2} \end{bmatrix} \begin{bmatrix} \psi_a \\ \psi_b \\ \psi_c \end{bmatrix} \tag{4.3}$$

and

$$\begin{bmatrix} \psi_d \\ \psi_q \end{bmatrix} = \sqrt{\frac{2}{3}} \begin{bmatrix} \cos\theta & \cos\left(\theta - \frac{2}{3}\pi\right) & \cos\left(\theta + \frac{2}{3}\pi\right) \\ -\sin\theta & -\sin\left(\theta - \frac{2}{3}\pi\right) & -\sin\left(\theta + \frac{2}{3}\pi\right) \end{bmatrix} \begin{bmatrix} \psi_a \\ \psi_b \\ \psi_c \end{bmatrix} \tag{4.4}$$

Therefore, the machine electrical variables in the stationary frame could be expressed by using the *d*-*q* reference frame variables. The voltage, current and flux linkage of phase *a* could be expressed as

$$\begin{aligned} i_a &= \sqrt{\frac{2}{3}}\left(i_d \cos\theta - i_q \sin\theta\right) \\ u_a &= \sqrt{\frac{2}{3}}\left(u_d \cos\theta - u_q \sin\theta\right) \\ \psi_a &= \sqrt{\frac{2}{3}}\left(\psi_d \cos\theta - \psi_q \sin\theta\right) \end{aligned} \tag{4.5}$$

By substituting (4.5) into (4.1), a simplified expression can be obtained as the following

$$\left(\frac{d\psi_d}{dt} - \psi_q \frac{d\theta}{dt} + R_s i_d - u_d\right)\cos\theta + \left(-\frac{d\psi_q}{dt} - \psi_d \frac{d\theta}{dt} - R_s i_q + u_q\right)\sin\theta = 0 \tag{4.6}$$

Since this equation satisfies for any value of θ, the following *d*-*q* axes voltage equations are always valid.

$$\begin{aligned} u_d &= R_s i_d + \frac{d\psi_d}{dt} - \psi_q \frac{d\theta}{dt} \\ u_q &= R_s i_q + \frac{d\psi_q}{dt} + \psi_d \frac{d\theta}{dt} \end{aligned} \tag{4.7}$$

In the conventional machine model, the *d*- and *q*-axis flux linkages are usually defined as

$$\begin{aligned} \psi_d &= L_d i_d + \psi_f \\ \psi_q &= L_q i_q \end{aligned} \tag{4.8}$$

where L_d and L_q are the *d*- and *q*-axis inductances, respectively, and ψ_f is the flux linkage generated by the permanent magnet.

It can be found that the *q*-axis flux linkage is produced by the *q*-axis stator current only. Along the *d*-axis, the flux linkage is produced by both the *d*-axis stator current and the permanent magnet on the rotor. The electrical model in (4.7) can be rewritten as

$$\begin{aligned} u_d &= R_s i_d + L_d \frac{di_d}{dt} - \omega_e L_q i_q \\ u_q &= R_s i_q + L_q \frac{di_q}{dt} + \omega_e L_d i_d + \omega_e \psi_f \end{aligned} \tag{4.9}$$

Fig. 4.2.2 shows the equivalent circuit in the *d*-*q* reference frame.

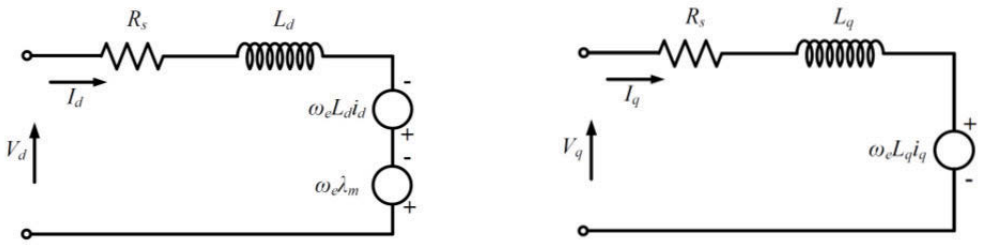

(a) (b)

Fig. 4.2.2 PMSM equivalent circuits in (a) *d*-, and (b) *q*-axes

When the machine is operated as a motor, the total input power of the device can be expressed by using the terminal voltages and currents of three-phase and *d*-*q* rotating reference frames as the following:

$$P_{in} = u_a i_a + u_b i_b + u_c i_c \tag{4.10}$$

and

$$P_{in} = \frac{3}{2}(u_d i_d + u_q i_q) \tag{4.11}$$

By substituting (4.9) in (4.11), the input total power can be expressed as

$$P_{in} = \frac{3}{2}\left[R_s(i_d^2 + i_q^2) + i_q \frac{d\psi_q}{dt} + i_d \frac{d\psi_d}{dt} + \omega_e(\psi_q i_q - \psi_d i_d) \right] \tag{4.12}$$

By eliminating the terms of the copper losses and the variation of magnetic energy, the electromechanical power becomes

$$P_{em} = \frac{3}{2}\frac{p\omega_r}{2}(\psi_q i_q - \psi_d i_d) \tag{4.13}$$

where ω_r is the rotor mechanical speed converted from the electrical speed

$$\omega_e = \frac{p}{2}\omega_r \tag{4.14}$$

and p is the number of poles.

The mechanical equation of the model can be written as

$$T_e = T_L + J\frac{d\omega_r}{dt} + F \cdot \omega_r \tag{4.15}$$

where T_L is the load torque applied on the rotor shaft, J the inertia of the motor, and F the shaft friction coefficient.

By dividing the electromagnetic power by the rotor mechanical speed, the electromagnetic torque, when the damping effects are ignored because there are no damping windings in the PMSMs, can be expressed as

$$T_e = \frac{3}{2} p\left(\psi_d i_q - \psi_q i_d\right) \tag{4.16}$$

Substituting (4.8) into (4.16), one obtains

$$\begin{aligned} T_e &= \frac{3}{2} p\left[\psi_f i_q + \left(L_d - L_q\right) i_d i_q\right] \\ &= \frac{3p|\psi_s|}{4L_d L_q}\left[2\psi_f L_q \sin\delta + |\psi_s|\left(L_d - L_q\right)\sin 2\delta\right] \end{aligned} \tag{4.17}$$

where δ is the electrical angle between the stator- and rotor-flux vectors.

As shown, the electromagnetic torque is composed of two parts: the permanent magnet torque and the reluctance torque caused by the rotor saliency.

For a surface-mounted PMSM without saliency, the *d*- and *q*-axis inductances are equal to the synchronous inductance, i.e. $L_d = L_q = L_s$. The torque does not include the reluctance torque and can be simplified as

$$T_e = \frac{3}{2} p\psi_f i_q = \frac{3}{2} p \frac{\psi_f |\psi_s|}{L_s} \sin\delta \tag{4.18}$$

The voltage and stator flux equations can also be simplified similarly.

In the stationary frame (the components indicated by $\alpha\beta$), they can be expressed using a complex vector as

$$u_s = R_s i_s + \frac{d\psi_s}{dt} \tag{4.19}$$

and

$$\psi_s = L_s i_s + \psi_r \tag{4.20}$$

where $\psi_r = \psi_f e^{j\theta_r}$ and the torque in the stationary frame is expressed as

$$T_e = \frac{3}{2} p\psi_s \times i_s = \frac{3}{2} p(\psi_\alpha i_\beta - \psi_\beta i_\alpha) \tag{4.21}$$

4.3 The Conventional DTC

Fig. 4.3.1 shows the implementation diagram of the classical DTC scheme for the PMSM drive. Two hysteresis controllers are applied to the flux linkage and torque control loops. The calculated flux linkage is also sent to the switching table to identify the current flux vector position. The switching table for controlling both the amplitude and rotating direction is shown in Table 4-1, and the inverter voltage vector and spatial sector definitions are illustrated in Fig. 4.3.2. The electromagnetic torque and flux linkage are calculated with (4.8) and (4.16).

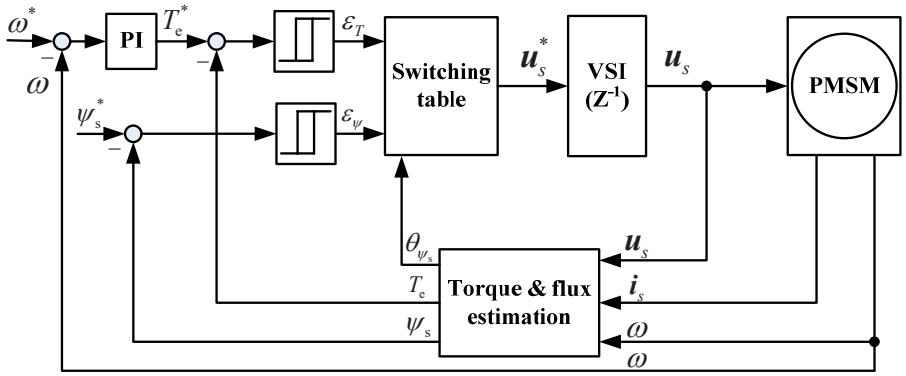

Fig. 4.3.1 Block diagram of PMSM DTC drive system

Table 4-1 Switching table of classic DTC scheme for PMSM drive

φ	T_e	θ					
		θ_1	θ_2	θ_3	θ_4	θ_5	θ_6
$\Delta\varphi = 1$	$\Delta T_e = 1$	$V_2(110)$	$V_3(010)$	$V_4(011)$	$V_5(001)$	$V_6(101)$	$V_1(100)$
	$\Delta T_e = 0$	$V_6(101)$	$V_1(100)$	$V_2(110)$	$V_3(010)$	$V_4(011)$	$V_5(001)$
$\Delta\varphi = 0$	$\Delta T_e = 1$	$V_3(010)$	$V_4(011)$	$V_5(001)$	$V_6(101)$	$V_1(100)$	$V_2(110)$
	$\Delta T_e = 0$	$V_5(001)$	$V_6(101)$	$V_1(100)$	$V_2(110)$	$V_3(010)$	$V_4(011)$

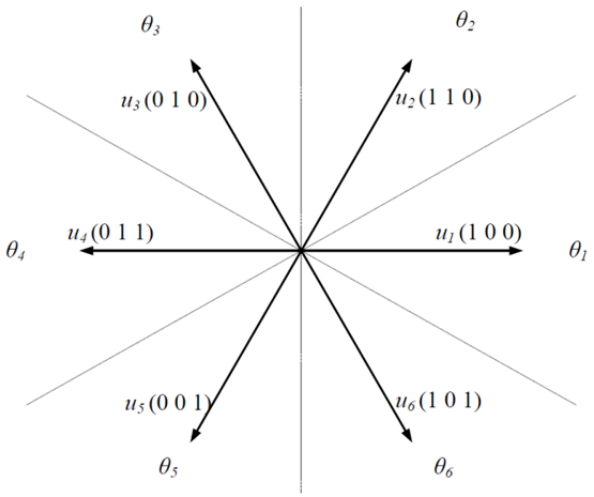

Fig. 4.3.2 Voltage vector and spatial sector definition

4.4 The Conventional FCS-MPDTC

The principle of model predictive control (MPC) was introduced for industrial control applications in the 1970s after the publication of this strategy in the 1960s. The MPC requires great computational effort and it has been formerly limited to slowly varying systems, e.g. chemical processes. With the availability of inexpensive high computing power microcomputers and modern digital control techniques, MPC is able to be applied to electrical drive systems.

Recently, MPC methods have been applied for torque control of PMSMs [4.23]-[4.26]. This approach is called the finite control set model predictive torque control (FCS-MPDTC) and is similar to the conventional direct torque control (DTC).

Apart from the employment of hysteresis comparators and the switching table in the conventional DTC, the principle of VSV selection in FCS-MPDTC is based on evaluating a defined cost function. The selected VSV from the conventional switching table in DTC may not necessarily be the best one for the purposes of torque and flux ripple reduction. Since there are limited discrete VSVs in the two-level inverter-fed PMSM drives, it is possible to evaluate the effects of each VSV and select the one minimizing the cost function.

The key technology of FCS-MPDTC lies in the definition of the cost function, which is related to the control objectives. The greatest concern of PMSM drive applications are the torque and stator flux, and thus, the cost function is defined in such a way that both the torque and stator flux at the end of control period are as close as possible to the reference values. In this thesis, the cost function is defined as

$$\min.\ G = \left|T_e^* - T_e^{k+1}\right| + k_1 \left\|\psi_s^*\right| - \left|\psi_s^{k+1}\right\| \tag{4.22}$$

$$s.t.\quad u_s^k \in \{V_0, V_1, \ldots V_6, V_7\}$$

where T_e^* and ψ_s^* are the reference values of torque and flux, T_e^{k+1} and ψ_s^{k+1} the predicted values of torque and flux, respectively, and k_1 is the weighting factor, introduced to unify the terms of torque and flux which are different in physical nature. In this thesis, k_1 is selected to be T_n / ψ_n, where T_n and ψ_n are the rated values of torque and stator flux, respectively. When a null VSV is selected, the specific state (V_0 or V_7) will be determined based on the principle of minimal switching commutations, which is related to the switching states of the old VSV.

From (4.9) in the last section, which is copied here for the convenience

$$\begin{aligned} u_d &= R_s i_d + L_d \frac{di_d}{dt} - \omega_e L_q i_q \\ u_q &= R_s i_q + L_q \frac{di_q}{dt} + \omega_e L_d i_d + \omega_e \psi_f \end{aligned} \tag{4.9}$$

the stator current in the *d-q* frame can be expressed in the form of state space equations as

$$\frac{di_d}{dt} = \frac{-R_s i_d + \omega L_q i_q + u_d}{L_d}$$
$$\frac{di_q}{dt} = \frac{-\omega L_d i_d - R_s i_q + u_q - \omega \psi_f}{L_q} \tag{4.23}$$

The stator current in *d-q* frame at $(k+1)th$ instant can be obtained by discretizing (4.23) as

$$i_d^{k+1} = i_d^k + \frac{1}{L_d}\left(-R_s i_d^k + \omega\ L_q i_q^k + u_d^k\right)T_s$$
$$i_q^{k+1} = i_q^k + \frac{1}{L_q}\left(-\omega\ L_d i_d^k - R_s i_q^k + u_q^k - \omega\ \psi_f\right)T_s \tag{4.24}$$

With the knowledge of future stator current, both the torque and flux at the $(k+1)th$ time instant can be calculated by (4.8) and (4.16). The block diagram of MPC is shown in Fig. 4.4.1. The inputs of the system are the reference and estimated values of torque and flux. By evaluating the effects of each VSV when applied to the machine, the VSV which minimizes the difference between the reference and predicted values is first selected, and then it is generated by the inverter.

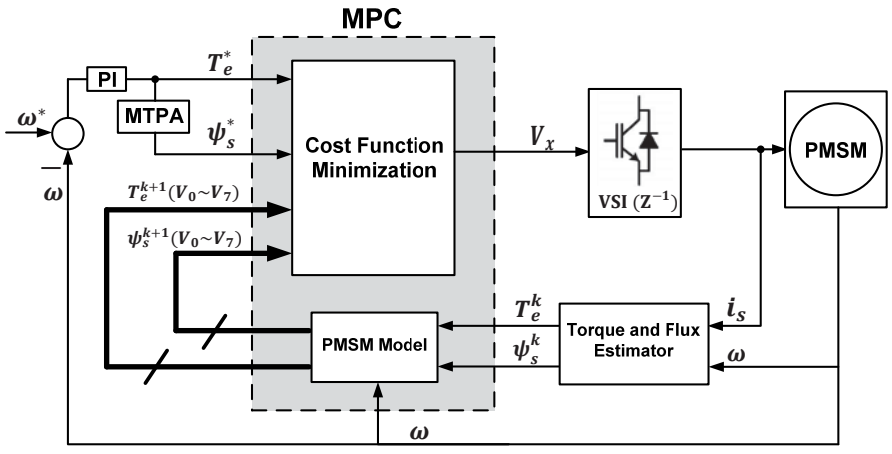

Fig. 4.4.1 Block diagram of MPC drive system

4.5 One-step delay compensation

4.5.1 FCS-MPDTC with one-step delay compensation

The cost function in (4.22) assumes that all calculations and judgments are implemented in the *kth* instant and the selected VSV will be applied immediately. However, in the practical digital implementation, this assumption is not true and the applied VSV is not applied until the (*k+1*)*th* instant.

In other words, for the duration between the *kth* and (*k+1*)*th* instants, the applied VSV u_s^k has been decided by the value in the (*k—1*)*th* instant and the evolutions of ψ_s and T_e for this duration are uncontrollable. What is left to be decided is actually the VSV u_s^{k+1}, which is applied at the beginning of the (*k+1*)*th* instant.

To eliminate the one-step delay, the two-step prediction is required which means the variables of ψ_s^{k+2} and T_e^{k+2} should be used rather than ψ_s^{k+1} and T_e^{k+1}. This fact is clearly illustrated in Fig. 4.4.2, where *x* indicates the state variables of a dynamic system and *u* is the input to be decided. For PMSM, *x* represents the torque or stator flux value.

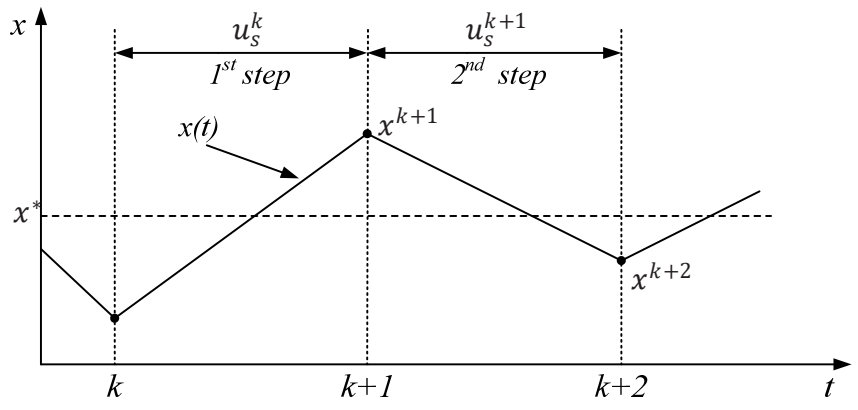

Fig. 4.4.2 One-step delay in digital control systems

The actual stator current in the *d-q* frame at the (*k+1*)*th* time instant I_d^{k+1} I_q^{k+1} are calculated by (4.24), and then the *d*- and *q*-axis stator currents at the (*k+2*)*th* time instant I_d^{k+2} I_q^{k+2} are calculated by (4.25). Finally, ψ_s^{k+2} and T_e^{k+2} can be obtained by

(4.8) and (4.17). It is noted that the meaning of u_s^k, u_d^k and u_q^k in different equations are different. In (4.24), their values are determined in the (*k—1*)*th* instant. Their values are based on eight possible VSVs in the equation below

$$i_d^{k+2} = i_d^{k+1} + \frac{1}{L_d}\left(-R_s i_d^{k+1} + \omega\ L_q i_q^{k+1} + u_d^k\right)T_s \tag{4.25}$$

$$i_q^{k+2} = i_q^{k+1} + \frac{1}{L_q}\left(-\omega\ L_d i_d^{k+1} - R_s i_q^k + u_q^k - \omega\ \psi_f\right)T_s$$

Accordingly, the cost function with one-step delay compensation is defined as

$$\min.\ G = \left|T_e^* - T_e^{k+2}\right| + k_1\left|\left|\psi_s^*\right| - \left|\psi_s^{k+2}\right|\right| \tag{4.26}$$

$$s.t.\quad u_s^k \in \{V_0, V_1, \ldots V_6, V_7\}$$

4.5.2 Conventional DTC with one-step delay compensation

To eliminate the one-step delay in DTC, the torque and flux at the (*k+1*)*th* instant should be employed to the switching table instead of the *kth*, i.e. T_e^{k+1} and ψ_s^{k+1} are used to select u_s^{k+1} instead of T_e^k and ψ_s^k. The model-based prediction is introduced to obtain the variables at the (*k+1*)*th* instant (same procedure used in Chapter 4.5.1). The stator current at the (*k+1*)*th* instant can be calculated by (4.24). Then, both torque and flux at the (*k+1*)*th* instant can be obtained by (4.8) and (4.16).

4.6 The Proposed FCS-MPDTC

4.6.1 Definition of extended VSVs

The extended VSVs are created by modulating two adjacent basic active VSVs or one basic active VSV and one zero VSV with a fixed duty ratio of 0.5. The extended VSVs are indexed in Table 4-2 and Fig. 4.6.1.

Table 4-2 Modulation of Extended VSVs

Vector	Modulated by	Gate signal (d=0.5)
V_7	V_1+V_{19}	d,0,0
V_8	V_2+V_{20}	1,1,d
V_9	V_3+V_{19}	0,d,0
V_{10}	V_4+V_{20}	d,1,1
V_{11}	V_5+V_{19}	0,0,d
V_{12}	V_6+V_{20}	1,d,1
V_{13}	V_1+V_2	1,d,0
V_{14}	V_2+V_3	d,1,0
V_{15}	V_3+V_4	0,1,d
V_{16}	V_4+V_5	0,d,1
V_{17}	V_5+V_6	d,0,1
V_{18}	V_1+V_6	1,0,d
V_{19}		0,0,0
V_{20}		1,1,1

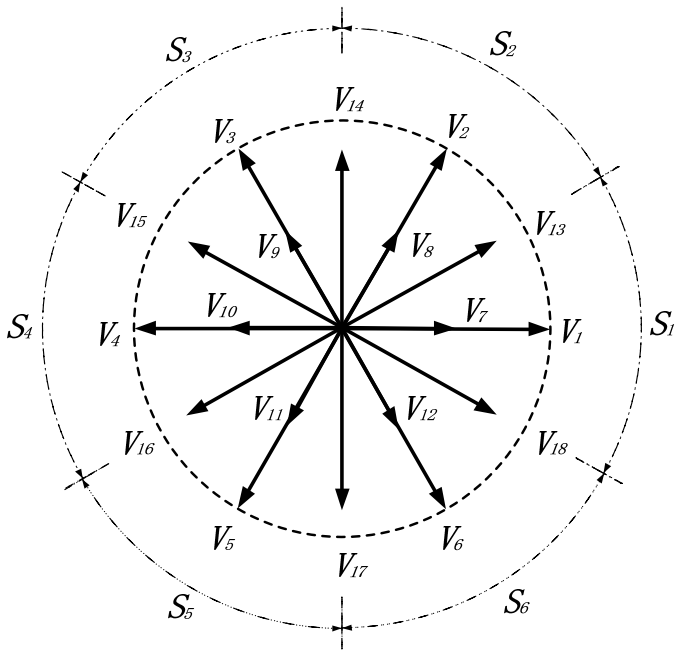

Fig. 4.6.1 Basic VSVs and extended VSVs.

4.6.2 The pre-selective scheme

To mitigate the computational burden caused by the increased number of VSVs, a pre-selective scheme is designed for the proposed FCS-MPDTC to filter out the impractical VSVs instead of evaluating all twenty VSVs as shown in Table 4-3. In the table, $\Delta\varphi$

represents the error between the actual and reference stator fluxes, ΔT_e the error between the actual and reference torques. For example, if the reference stator flux is greater than the actual stator flux, the reference torque is greater than the actual torque and the stator flux is located in space sector S_1. Only V_1, V_2, V_7, V_8, V_{13} and V_{14} are considered as the candidate VSVs, and then provided to the cost function for evaluation. This pre-selective scheme is inspired by the switching table used in the conventional DTC. With the help of the proposed scheme, the number of candidate VSVs is dropped from 20 to 6 and the proposed FCS-MPDTC even runs faster than the conventional FCS-MPDTC. To be more specific, the computing time of FCS-MPDTC with 20 VSVs and FCS-MPDTC with both 20 VSVs and pre-selective scheme are 201% and 93% of the conventional FCS-MPDTC.

Table 4-3 Pre-selective scheme

$\Delta\varphi$	ΔT_e	**Candidate VSVs in Corresponding Space Sector (S_x)**					
		S_1	S_2	S_3	S_4	S_5	S_6
1	1	$V_1V_2V_7$ $V_8V_{13}V_{14}$	$V_2V_3V_8$ $V_9V_{14}V_{15}$	$V_3V_4V_9$ $V_{10}V_{15}V_{16}$	$V_4V_5V_{10}$ $V_{11}V_{16}V_{17}$	$V_5V_6V_{11}$ $V_{12}V_{17}V_{18}$	$V_1V_6V_7$ $V_{12}V_{13}V_{18}$
	-1	$V_1V_6V_7$ $V_{12}V_{17}V_{18}$	$V_1V_2V_7$ $V_8V_{13}V_{18}$	$V_2V_3V_8$ $V_9V_{13}V_{14}$	$V_3V_4V_9$ $V_{10}V_{14}V_{15}$	$V_4V_5V_{10}$ $V_{11}V_{15}V_{16}$	$V_5V_6V_{11}$ $V_{12}V_{16}V_{17}$
-1	1	$V_3V_4V_9$ $V_{10}V_{14}V_{15}$	$V_4V_5V_{10}$ $V_{11}V_{15}V_{16}$	$V_5V_6V_{11}$ $V_{12}V_{16}V_{17}$	$V_1V_6V_7$ $V_{12}V_{17}V_{18}$	$V_1V_2V_7$ $V_8V_{13}V_{18}$	$V_2V_3V_8$ $V_9V_{13}V_{14}$
	-1	$V_4V_5V_{10}$ $V_{11}V_{16}V_{17}$	$V_5V_6V_{11}$ $V_{12}V_{17}V_{18}$	$V_1V_6V_7$ $V_{12}V_{13}V_{18}$	$V_1V_2V_7$ $V_8V_{13}V_{14}$	$V_2V_3V_8$ $V_9V_{14}V_{15}$	$V_3V_4V_9$ $V_{10}V_{15}V_{16}$

4.6.3 Principle of the Proposed FCS-MPDTC

The block diagram of the proposed FCS-MPDTC is illustrated in Fig. 4.6.2. Firstly, the candidate VSVs are chosen based on $\Delta\varphi$, ΔT_e and the location of stator flux. The VSV with the minimum cost will be generated by the inverter in the next sampling period.

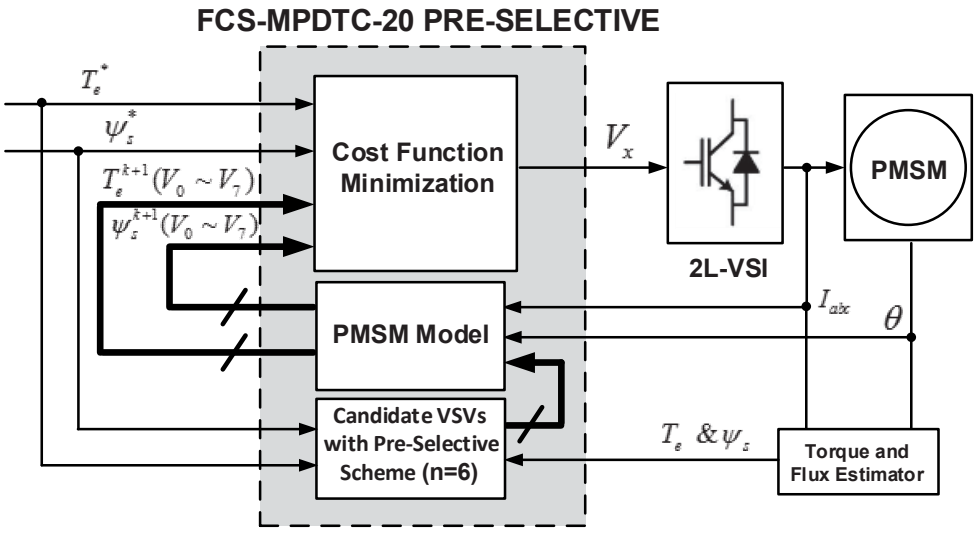

Fig. 4.6.2 Block diagram of proposed FCS-MPDTC drive system

In other algorithms with duty ratio control [18]-[20], the best active VSV is firstly selected based on the cost function minimization and the duty ratio is subsequently calculated. The former part of the algorithm utilizes the system model and the latter usually relies on numerical calculation according to the pre-defined principles. This complex cascaded processing manner can lead to relatively poor low-speed performance and it cannot ensure the global minimization of torque error as the selected VSV may not remain optimal if it is not applied for the whole sampling period.

In the proposed algorithm, the concept of duty ratio control is naturally integrated into the extended VSVs, i.e. the model-based VSV selection and duty ratio control are implemented simultaneously. In contrast to the cascaded duty ratio processing methods, the proposed algorithm presents less system complexity and can make better utilization of concept of model predictive control.

Fig. 4.6.3 illustrates the number of selected VSVs of three methods in MATLAB/Simulink. The conventional DTC, conventional FCS-MPDTC, and proposed FCS-MPDTC are abbreviated as DTC-8, MPDTC-8 and MPDTC-20, respectively. It can be observed that both the conventional DTC and conventional FCS-MPDTC are repeatedly jumping between an active VSV and a zero VSV or adjacent active VSV to follow the torque reference and meanwhile maintain the speed of the motor. The hesitation in the VSV selection of these two methods indicates that no VSV is found to best match the current situation and the control algorithm itself begins to “modulate”

new VSVs. However, this kind of "modulation" is ineffective and results in considerable torque and flux ripples. In the proposed FCS-MPDTC, new VSVs are inherently modulated and the choices of VSVs for the control algorithm are extended to twenty. As a result, the torque and flux ripples and the THD of phase current of the proposed method can be greatly reduced.

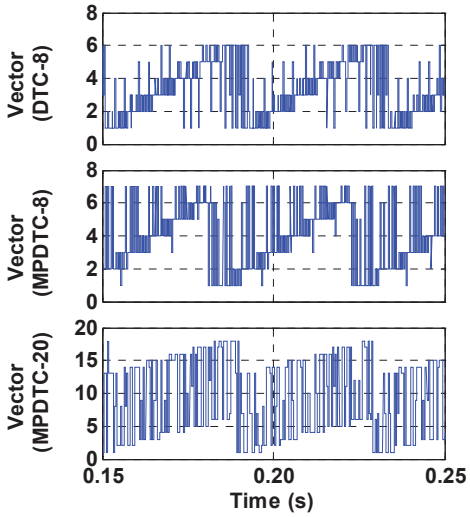

Fig. 4.6.3 The selection of VSVs at 1000 r/min (simulation).

4.7 Summary

This chapter proposes a FCS-MPDTC with an extended set of VSVs. Compared to the conventional DTC and conventional FCS-MPDTC, the choices of VSVs for the control algorithm are extended from eight to twenty by inherently modulating the basic VSVs. Compared to other cascaded duty ratio processing methods, the proposed algorithm can articulate the duty ratio control in the motor model and make better utilization of the concept of model predictive control. To mitigate the computational burden caused by the increased number of VSVs, a pre-selective scheme is designed to filter out the impractical VSVs instead of evaluating all twenty VSVs.

REFERENCES

[4.1] I. Takahashi, T. Noguchi, "A new quick-response and high efficiency control strategy of an induction motor", *IEEE Trans. on IA*, vol. 22, no. 5, pp. 820-827, Sep. 1986.

[4.2] M. Koc, T. Sun and J. Wang, "Performance improvement of direct torque controlled interior mounted permanent magnet drives by employing a linear combination of current and voltage based flux observers," *IET Power Electronics,* vol. 9, no. 10, pp. 2052-2059, Jul. 2016.

[4.3] S. Vazquez, J. Rodriguez, M. Rivera, L. G. Franquelo and M. Norambuena, "Model Predictive Control for Power Converters and Drives: Advances and Trends," *IEEE Trans. Ind. Electron*., vol. 64, no. 2, pp. 935-947, Feb. 2017.

[4.4] H. Yang, Y. Zhang, P. Walker, J. Liang, N. Zhang and B. Xia, "'Speed Sensorless Model Predictive Current Control with Ability to Start A Free Running Induction Motor", *IET Electric Power Applications,* DOI: 10.1049/iet-epa.2016.0481, Oct. 2016.

[4.5] S. Bayhan, H. Abu-Rub and O. Ellabban, "Sensorless model predictive control scheme of wind-driven doubly fed induction generator in dc microgrid," *IET Renewable Power Generation*, vol. 10, no. 4, pp. 514-521, Apr. 2016.

[4.6] L. Rovere, A. Formentini, A. Gaeta, P. Zanchetta and M. Marchesoni, "Sensorless Finite-Control Set Model Predictive Control for IPMSM Drives," *IEEE Trans. Ind. Electron*., vol. 63, no. 9, pp. 5921-5931, Sept. 2016.

[4.7] M. Uddin, S. Mekhilef and M. Rivera, "Experimental validation of minimum cost function-based model predictive converter control with efficient reference tracking," *IET Power Electronics*, vol. 8, no. 2, pp. 278-287, Feb. 2015.

[4.8] A. Parida and D. Chatterjee, "Model-based loss minimisation scheme for wind solar hybrid generation system using (grid-connected) doubly fed induction generator," *IET Electric Power Applications*, vol. 10, no. 6, pp. 548-559, Jul. 2016

[4.9] A. Dekka, B. Wu, V. Yaramasu and N. Zargari, "Integrated model predictive control with reduced switching frequency for modular multilevel converters", *IET Electric Power Applications*, DOI: 10.1049/iet-epa.2016.0454. Nov. 2016.

[4.10] L. Guo, X. Zhang, S. Yang, Z. Xie and R. Cao, "A Model Predictive Control-Based Common-Mode Voltage Suppression Strategy for Voltage-Source Inverter," *IEEE Trans. Ind. Electron*., vol. 63, no. 10, pp. 6115-6125, Oct. 2016.

[4.11] H. Fang, Z. Zhang, X. Feng and R. Kennel, "Ripple-reduced model predictive direct power control for active front-end power converters with extended switching vectors and time-optimised control," *IET Power Electronics*, vol. 9, no. 9, pp. 1914-1923, Jul. 2016.

[4.12] S. Mariethoz, A. Domahidi, and M. Morari, “High-bandwidth explicit model predictive control of electrical drives,” *IEEE Trans. Ind. Appl.*, vol. 48, no. 6, pp. 1980–1992, Nov./Dec. 2012.

[4.13] Y. Zhang, H. Yang and B. Xia, "Model predictive torque control of induction motor drives with reduced torque ripple," *IET Electric Power Applications*, vol. 9, no. 9, pp. 595-604, Nov. 2015.

[4.14] Y. Zhang and H.Yang, “Model predictive torque control of induction motor drives with optimal duty cycle control,” *IEEE Trans. Power Electron*., vol. 29, no. 12, pp. 6593–6603, Dec. 2014.

[4.15] S. A. Davari, D. A. Khaburi, and R. Kennel, “An improved FCS-MPC algorithm for an induction motor with an imposed optimized weighting factor,” *IEEE Trans. Power Electron*., vol. 27, no. 3, pp. 1540–1551, 2012.

[4.16] C. A. Rojas, J. Rodriguez, F. Villarroel, J. R. Espinoza, C. A. Silva, and M. Trincado, “Predictive torque and flux control without weighting factors,” *IEEE Trans. Ind. Electron*., vol. 60, no. 2, pp. 681–690, Feb. 2013.

[4.17] F. Wang, S. Li, X. Mei, W. Xie, J. Rodríguez and R. M. Kennel, "Model-Based Predictive Direct Control Strategies for Electrical Drives: An Experimental Evaluation of PTC and PCC Methods," in *IEEE Transactions on Industrial Informatics*, vol. 11, no. 3, pp. 671-681, June 2015.

[4.18] Y. Zhang and J. Zhu, “Direct torque control of permanent magnet synchronous motor with reduced torque ripple and commutation frequency,” *IEEE Trans. Power Electron*., vol. 26, no. 1, pp. 235–248, Jan. 2011.

[4.19] J.-K.Kang and S.-K. Sul, “New direct torque control of induction motor for minimum torque ripple and constant switching frequency,” *IEEE Trans. Ind. Appl*., vol. 35, no. 5, pp. 1076–1082, Sep./Oct. 1999.

[4.20] Y. Zhang and J. Zhu, "A novel duty cycle control strategy to reduce both torque and flux ripples for DTC of permanent magnet synchronous motor drives with switching frequency reduction," in *IEEE Transactions on Power Electronics*, vol. 26, no. 10, pp. 3055-3067, Oct. 2011.

[4.21] Y. Zhang and H.Yang, “Torque ripple reduction of model predictive torque control of induction motor drives,” *in Proc. IEEE Energy Convers. Congr. Expo*., 2013, pp. 1176–1183.

[4.22] Y. Zhang and H.Yang, “Generalized two-vector-based model-predictive torque control of induction motor drives,” *IEEE Trans. Power Electron*., vol. 30, no. 7, pp. 3818-3829, Jul. 2015.

[4.23] F. Wang, S. Li, X. Mei, W. Xie, J. Rodríguez, R. M. Kennel, "Model-based predictive direct control strategies for electrical drives: An experimental evaluation of PTC and PCC methods", IEEE Trans. Ind. Informat., vol. 11, no. 3, pp. 671-681, Jun. 2015.

[4.24] C. S. Lim, E. Levi, M. Jones, N. A. Rahim, W. P. Hew, "FCS-MPC-based current control of a five-phase induction motor and its comparison with PI-PWM control", IEEE Trans. Ind. Electron., vol. 61, no. 1, pp. 149-163, Jan. 2014.

[4.25] E. Fuentes, J. Rodriguez, C. Silva, S. Diaz, D. Quevedo, "Speed control of a permanent magnet synchronous motor using predictive current control", Proc. 6th IEEE Int. Power Electron. Motion Control Conf., pp. 390-395, May 2009

[4.26] A. A. Ahmed, "Fast-speed drives for permanent magnet synchronous motor based on model predictive control", Proc. IEEE Veh. Power Propulsion Conf., pp. 1–6, Oct. 2015

CHAPTER 5

NUMERICAL SIMULATION AND EXPERIMENTAL TESTS OF ALFSPMM

5.1 Introduction

The detailed numerical simulation and experimental tests of axially laminated flux switching permanent magnet motor (ALFSPMM) are presented in this chapter. Firstly, the model of ALFSPMM for model predictive control is derived in Section 5.2. In Section 5.3, the conventional DTC, conventional FCS-MPDTC and proposed FCS-MPDTC are simulated in the environment of Matlab/Simulink. In Section 5.4, above tests are experimentally repeated on a prototype ALFSPMM drive system controlled by a dSPACE. Finally, the quantitative analysis in terms of torque/flux ripples and drive system efficiencies are presented in Section 5.5.

5.2 Model of ALFSPMM

To simplify the theoretical analysis, the effects of magnetic saturation, eddy currents, and core losses are ignored in the analysis.

Based on these assumptions, the PM flux, self and mutual inductances are supposed ideally sinusoidal. The three-phase PM flux can then be expressed as

$$\begin{aligned}\psi_{pm,a} &= \psi_m \cos\theta \\ \psi_{pm,b} &= \psi_m \cos(\theta - \frac{2}{3}\pi) \\ \psi_{pm,c} &= \psi_m \cos(\theta + \frac{2}{3}\pi)\end{aligned} \tag{5.1}$$

where ψ_m is the amplitude of phase PM flux.

In addition, the inductance can be given by

$$\begin{aligned} L_a &= L_0 - L_m \cos(2\theta) \\ L_b &= L_0 - L_m \cos(2\theta + \frac{2}{3}\pi) \\ L_c &= L_0 - L_m \cos(2\theta - \frac{2}{3}\pi) \end{aligned} \tag{5.2}$$

where L_0 and L_m are the phase inductance initial value and amplitude, respectively. It is assumed that $\theta = 0$ as the position where the stator tooth is aligned centrally with the rotor slot. In many literatures, the mutual inductance is ignored, which could bring some defects to model accuracy. In this chapter, the mutual inductance of ALFSPMM is considered as

$$\begin{aligned} M_{ab} &= M_{ba} = M_0 - M_m \cos(2\theta - \frac{2}{3}\pi) \\ M_{bc} &= M_{cb} = M_0 - M_m \cos(2\theta) \\ M_{ca} &= M_{ac} = M_0 - M_m \cos(2\theta + \frac{2}{3}\pi) \end{aligned} \tag{5.3}$$

where M_0 and M_m are the phase mutual inductance initial value and amplitude, respectively. The mathematical models of voltage and flux linkage in three-phase coordinate system are given by

$$\begin{bmatrix} u_a \\ u_b \\ u_c \end{bmatrix} = R_s \begin{bmatrix} i_a \\ i_b \\ i_c \end{bmatrix} + \frac{d}{dt} \begin{bmatrix} \psi_a \\ \psi_b \\ \psi_c \end{bmatrix} \tag{5.4}$$

$$\begin{bmatrix} \psi_a \\ \psi_b \\ \psi_c \end{bmatrix} = \begin{bmatrix} L_a & M_{ab} & M_{ac} \\ M_{ba} & L_b & M_{bc} \\ M_{ca} & M_{cb} & L_c \end{bmatrix} \begin{bmatrix} i_a \\ i_b \\ i_c \end{bmatrix} + \begin{bmatrix} \psi_{pm,a} \\ \psi_{pm,b} \\ \psi_{pm,c} \end{bmatrix} \tag{5.5}$$

By combining (5.4) and (5.5), the equation of phase voltage can be rewritten as

$$\begin{bmatrix} u_a \\ u_b \\ u_c \end{bmatrix} = R_s \begin{bmatrix} i_a \\ i_b \\ i_c \end{bmatrix} + \frac{d}{dt} \left(\begin{bmatrix} L_a & M_{ab} & M_{ac} \\ M_{ba} & L_b & M_{bc} \\ M_{ca} & M_{cb} & L_c \end{bmatrix} \begin{bmatrix} i_a \\ i_b \\ i_c \end{bmatrix} + \begin{bmatrix} \psi_{pm,a} \\ \psi_{pm,b} \\ \psi_{pm,c} \end{bmatrix} \right)$$

$$= R_s \begin{bmatrix} i_a \\ i_b \\ i_c \end{bmatrix} + \begin{bmatrix} L_a & M_{ab} & M_{ac} \\ M_{ba} & L_b & M_{bc} \\ M_{ca} & M_{cb} & L_c \end{bmatrix} \frac{d}{dt} \begin{bmatrix} i_a \\ i_b \\ i_c \end{bmatrix} + \begin{bmatrix} i_a \\ i_b \\ i_c \end{bmatrix} \frac{d}{d\theta} \begin{bmatrix} L_a & M_{ab} & M_{ac} \\ M_{ba} & L_b & M_{bc} \\ M_{ca} & M_{cb} & L_c \end{bmatrix} \omega_e + \frac{d}{d\theta} \begin{bmatrix} \psi_{pm,a} \\ \psi_{pm,b} \\ \psi_{pm,c} \end{bmatrix} \omega_e \tag{5.6}$$

Then, the torque components produced by currents of phases A, B, and C can be expressed as

$$\begin{bmatrix} T_{e,a} \\ T_{e,b} \\ T_{e,c} \end{bmatrix} = \frac{1}{2} \begin{bmatrix} i_a \\ i_b \\ i_c \end{bmatrix}^2 \frac{\partial}{\partial \theta} \begin{bmatrix} L_a & M_{ab} & M_{ac} \\ M_{ba} & L_b & M_{bc} \\ M_{ca} & M_{cb} & L_c \end{bmatrix} + \begin{bmatrix} i_a \\ i_b \\ i_c \end{bmatrix} \frac{\partial}{\partial \theta} \begin{bmatrix} \psi_{pm,a} \\ \psi_{pm,b} \\ \psi_{pm,c} \end{bmatrix} = \begin{bmatrix} T_{r,a} \\ T_{r,b} \\ T_{r,c} \end{bmatrix} + \begin{bmatrix} T_{em,a} \\ T_{em,b} \\ T_{em,c} \end{bmatrix} \tag{5.7}$$

where T_r is the reluctance torque and T_{em} the electromagnetic torque.

In order to estimate the flux linkage accurately in the ALFSPMM, it is necessary to transform the equivalent equations in the 3-phase static frame to the *d-q* synchronous frame. Then, the voltage in the *d-q* axes can be expressed as

$$\begin{aligned} u_d &= R_s i_d + \frac{d\psi_d}{dt} - \psi_q \frac{d\theta}{dt} \\ u_q &= R_s i_q + \frac{d\psi_q}{dt} + \psi_d \frac{d\theta}{dt} \end{aligned} \tag{5.8}$$

The flux linkage in the *d-q* axes can be expressed as

$$\begin{aligned} \psi_d &= L_d i_d + \psi_m \\ \psi_q &= L_q i_q \end{aligned} \tag{5.9}$$

It should be noted that in order to simplify the calculation process, here L_d and L_q are assumed to be constants similar to those of the traditional PMSMs.

The electromagnetic torque can be expressed as

$$T_e = \frac{3}{2} p\left(\psi_d i_q - \psi_q i_d\right) \tag{5.10}$$

5.3 Numerical Simulations

5.3.1 Setup and parameters

In this section, the ALFSPMM is simulated in the environment of MATLAB/Simulink. In the figures below, the conventional DTC, conventional FCS-MPDTC and proposed FCS-MPDTC are abbreviated to DTC, MPDTC-8 and MPDTC-20, respectively. The block diagrams of above control methods are illustrated in Figs. 5.3.1, 5.3.2 and 5.3.3, respectively. The parameters of the motor and control system are listed in Table 5-1. In the fabrication process of proposed motor, we found that it is difficult to wind the wires on the stator poles directly due to the narrow internal space of the motor. The wires are wound on heat-resistant plastic holders which are then mounted on to the stator poles. Since the use of holders reduces the slot filling factor, the wire diameter was reduced in order to maintain the number of turns. As a result, the rated current is dropped to 1.5A and the rated speed is limited to 800r/min in the experimental tests. The system sampling frequencies in all control method are set to 5 kHz.

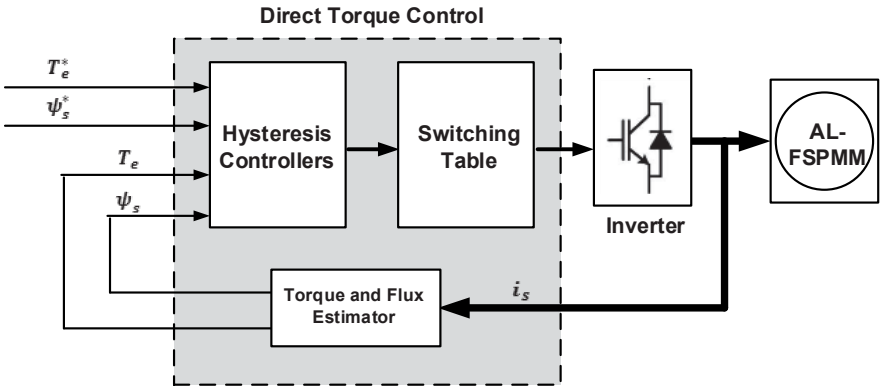

Fig. 5.3.1 Block diagram of DTC drive system

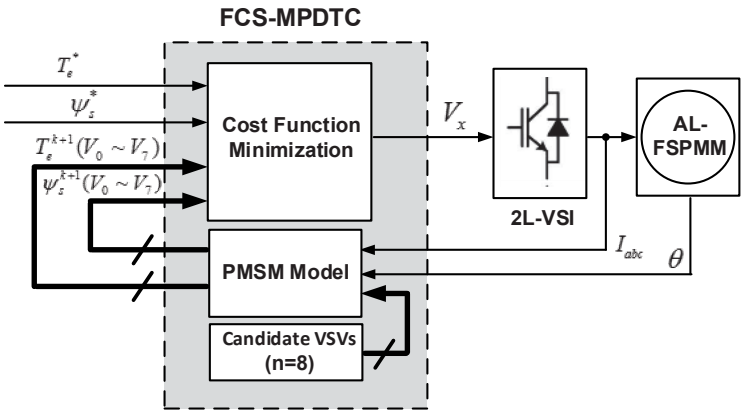

Fig. 5.3.2 Block diagram of conventional FCS-MPDTC drive system

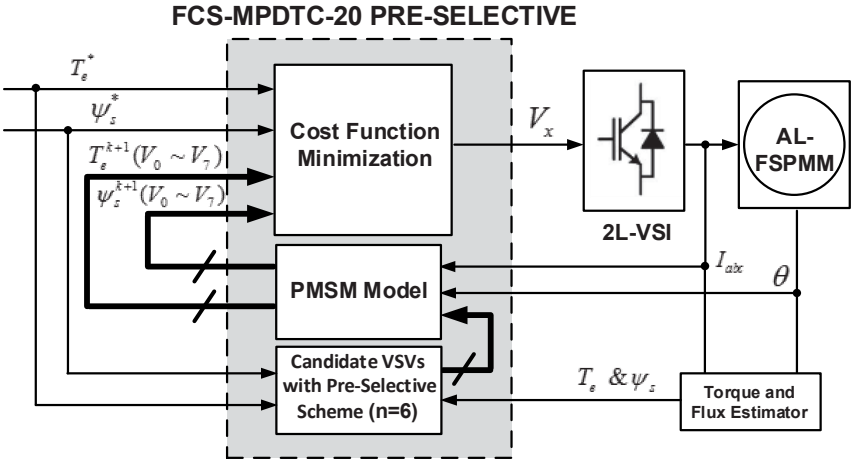

Fig. 5.3.3 Block diagram of proposed FCS-MPDTC drive system

Table 5-1 Machine and Control Parameters

Stator resistance	R_s	3.66 Ω
d-axis inductance	L_d	9.5 mH
q-axis inductance	L_q	10.4 mH
Permanent magnet flux	ψ_f	0.07 Wb
Number of pole pairs	p	7
DC bus voltage	V_{dc}	120 V
Rated torque	T_{rated}	1 Nm
Rated speed	ω_{rated}	800 r/min
Rated stator current	I_{rated}	1.5 A
Weighting factor of flux	k_1	14
Control system sampling frequency	f_{sys}	5000 Hz

5.3.2 Combined load test

This simulation test combines start-up, steady-state and external load tests. The control system sampling frequency is 5 kHz. The motor starts up from 0s with a reference speed (400 rpm or 800 rpm). An external load is applied at 0.15s. A segment (2-3 periods) of the stator current of phase A is used to calculate the total harmonic distortion (THD) and current harmonic spectrum. On the left hand side of each figure, the curves are the stator current, stator flux, torque and motor speed, respectively. On the right hand side, the curves are segment of the stator current, THD and current harmonic spectrum.

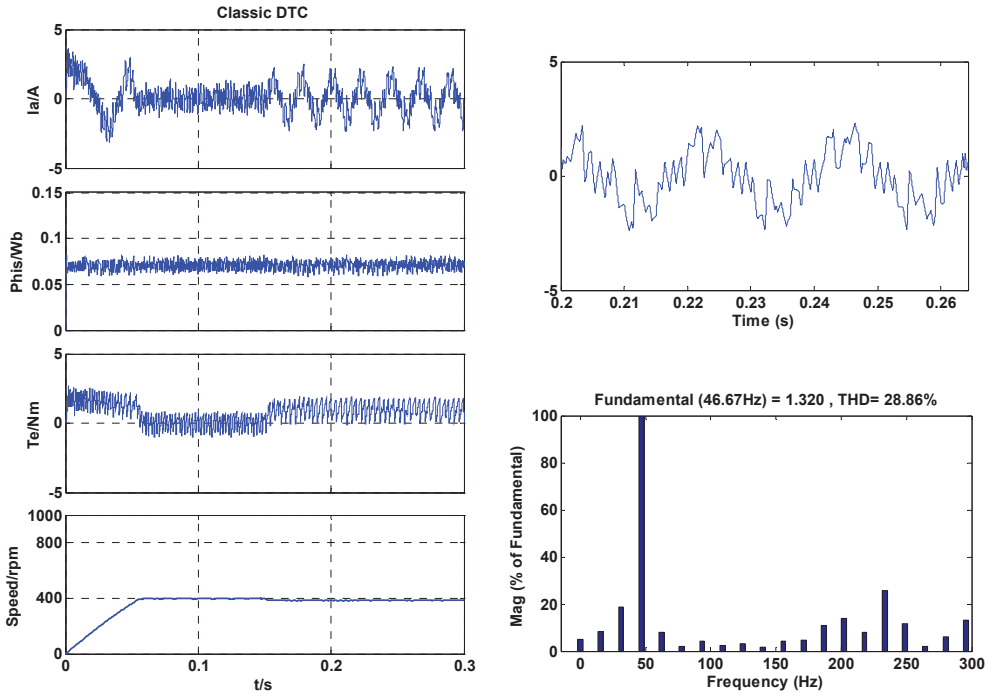

(a)

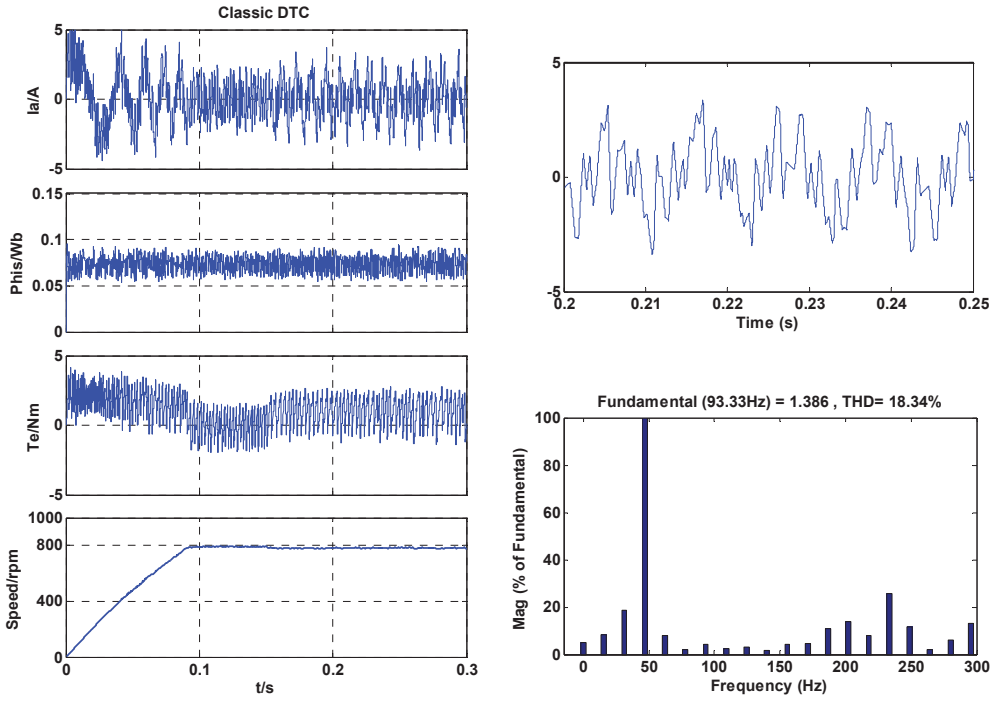

(b)

Fig. 5.3.4 Combined load test of DTC, where (a) at 400 rpm, and (b) at 800 rpm

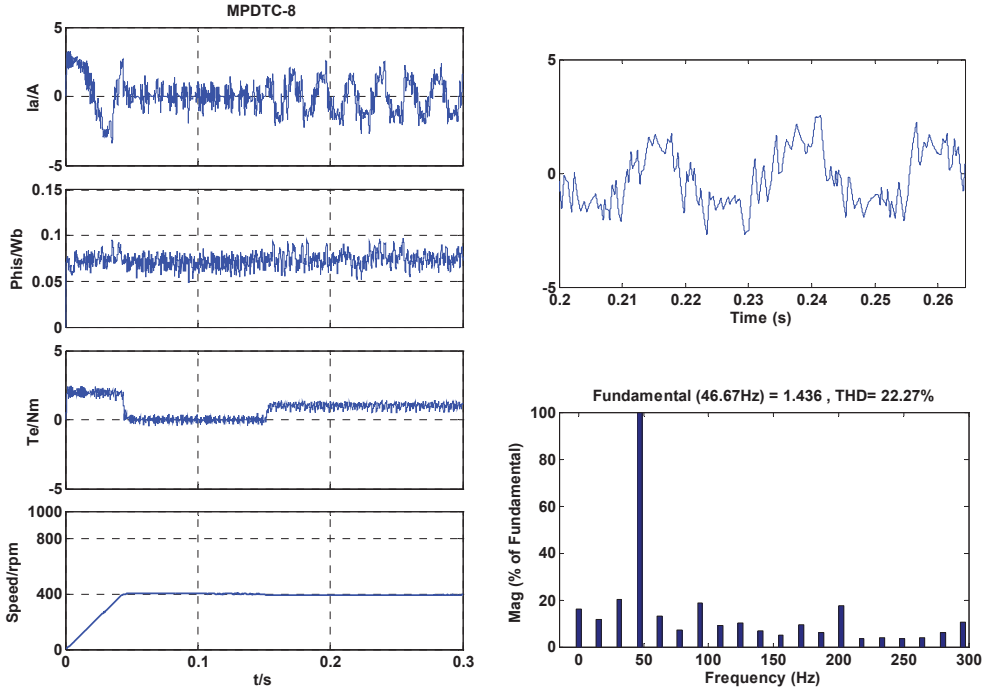

(a)

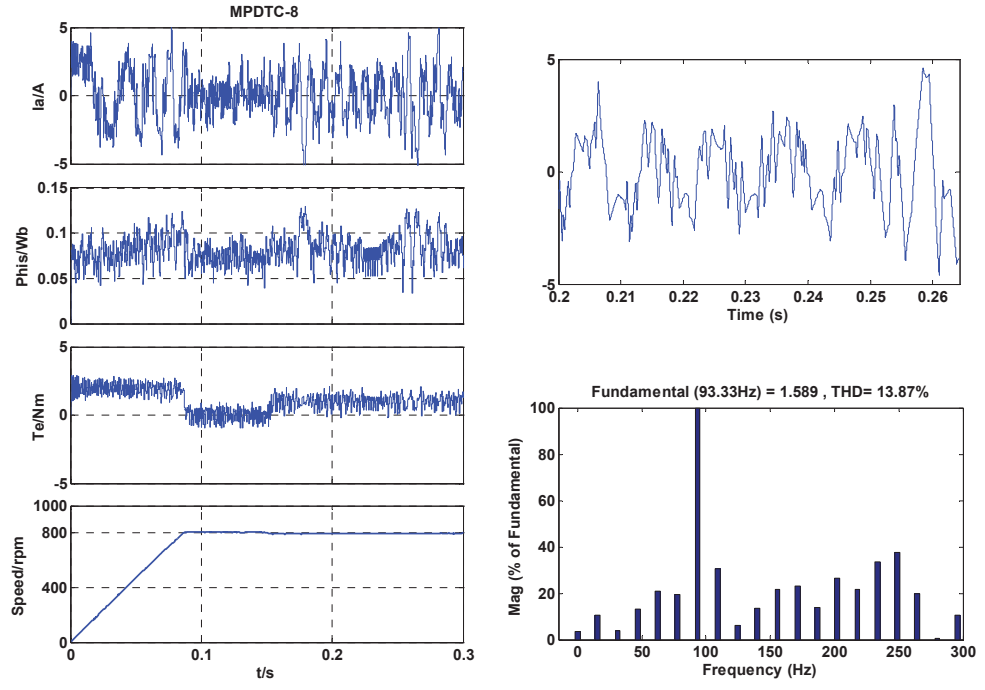

(b)

Fig. 5.3.5 Combined load test of conventional FCS-MPDTC,
where (a) at 400 rpm, and (b) at 800 rpm

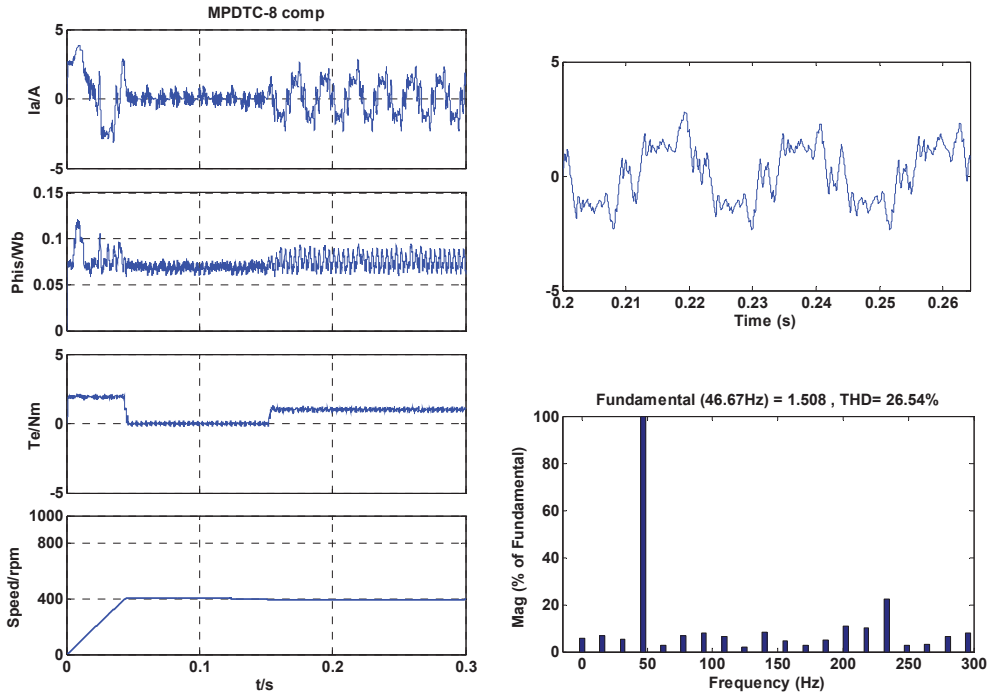

(a)

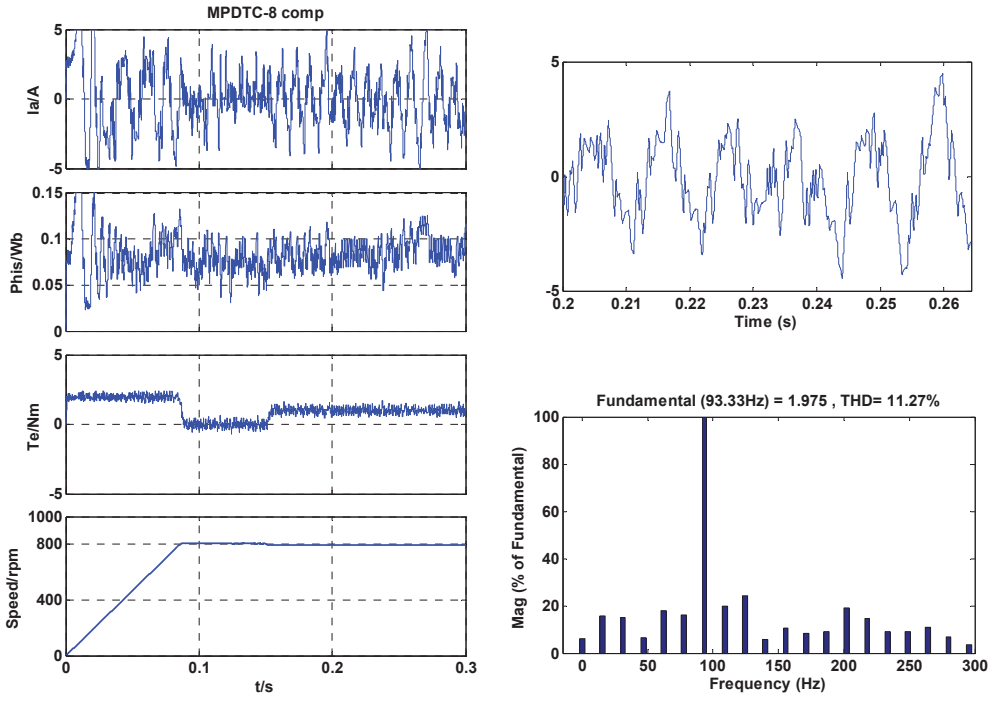

(b)

Fig. 5.3.6 Combined load test of conventional FCS-MPDTC with one-step delay compensation, where (a) at 400 rpm, and (b) at 800 rpm

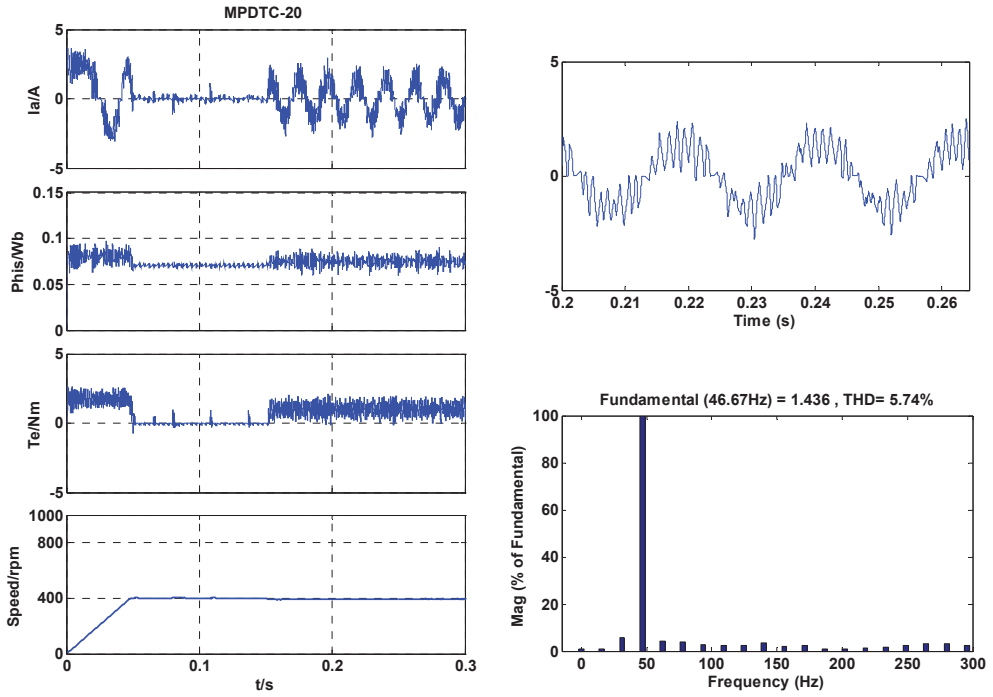

(a)

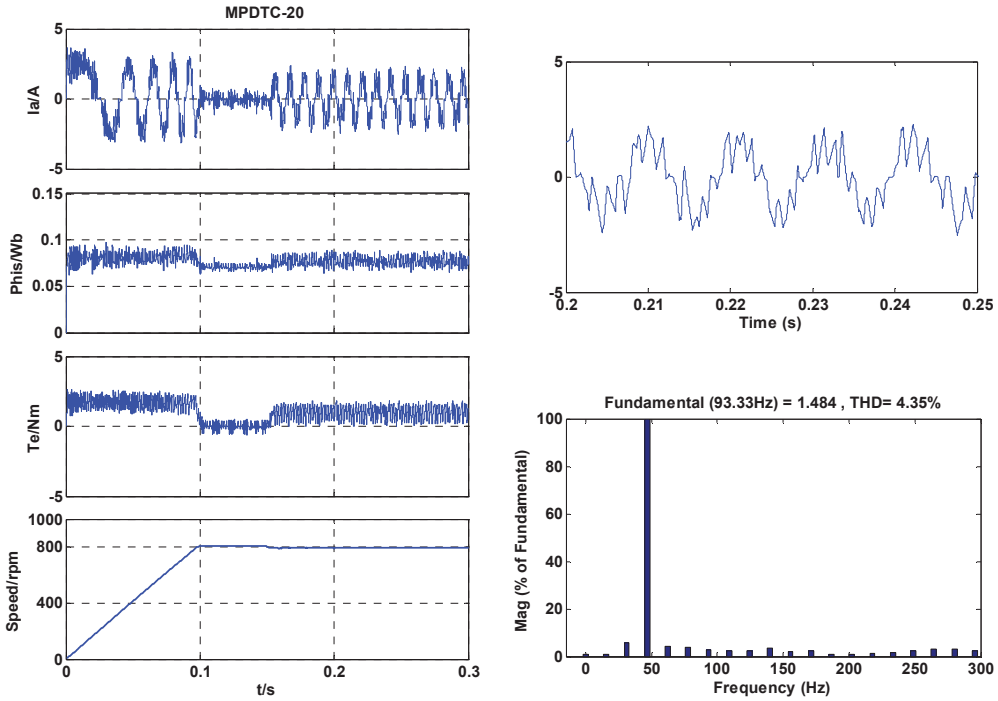

(b)

Fig. 5.3.7 Combined load test of proposed FCS: (a) at 400 rpm, and (b) at 800 rpm

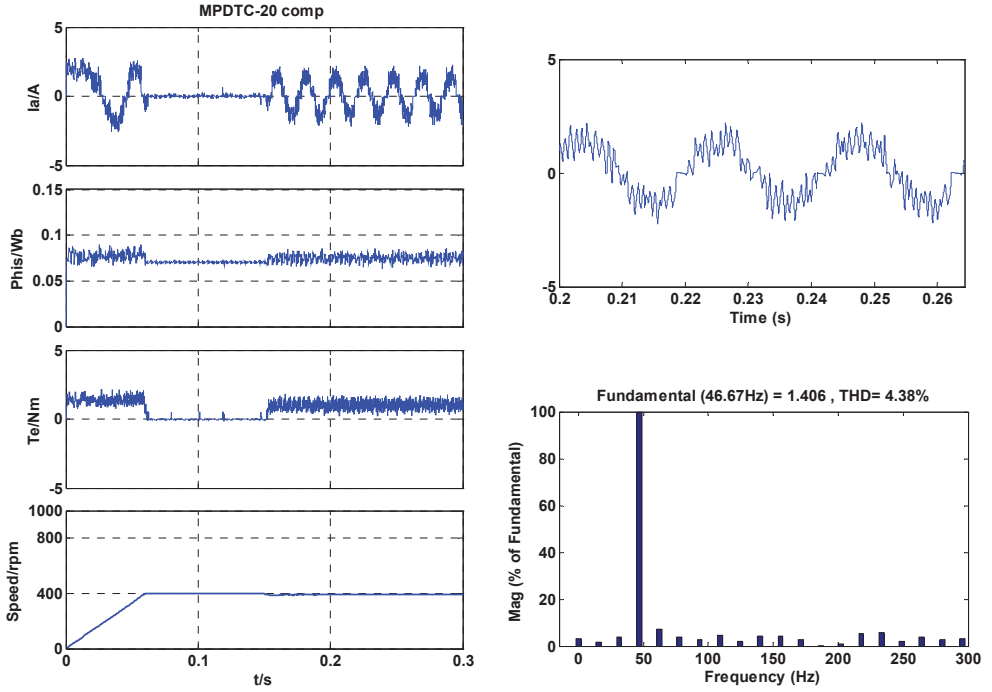

(a)

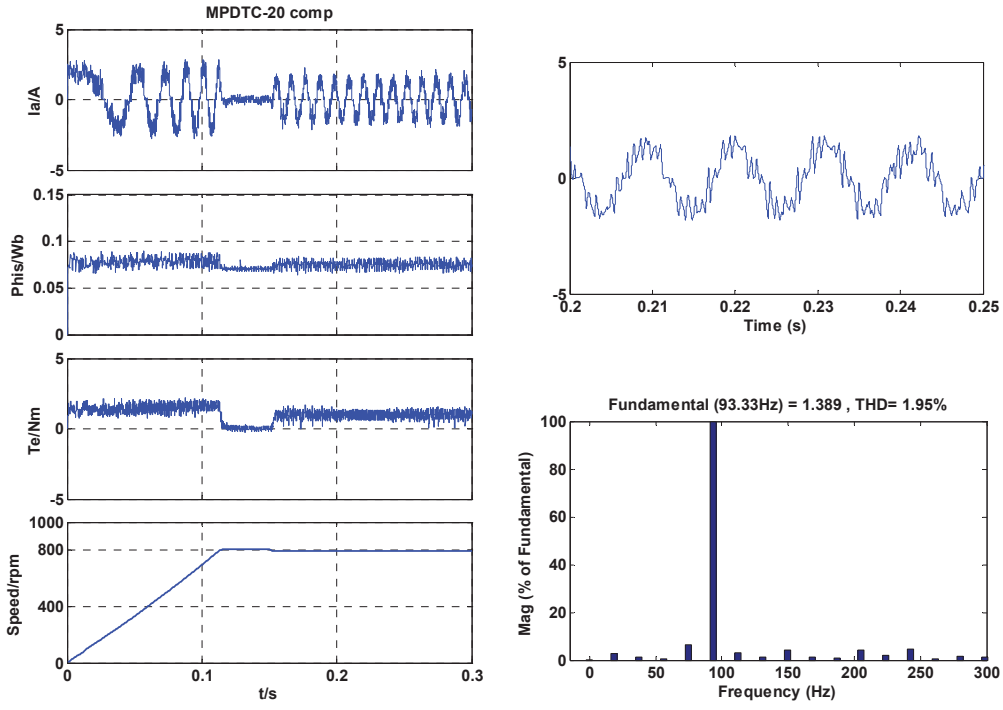

(b)

Fig. 5.3.8 Combined load test of proposed FCS-MPDTC with one-step delay compensation, where (a) at 400 rpm, and (b) at 800 rpm

From above figures, it is shown that the implementation of FCS-MPDTC can improve the performance significantly. The proposed FCS-MPDTC achieves the lowest the stator current THD, torque ripple and flux ripple. With the help of one-step delay compensation algorithm, the torque and flux ripples are further reduced. It can also be seen that the dynamic responses of all control methods are similar, but the steady state performance of the proposed FCS-MPDTC is better than those of DTC and conventional FCS-MPDTC.

5.4 Experimental Tests

5.4.1 Setup of experimental test platform

In addition to the simulation studies, the control methods mentioned above are experimentally tested on a two-level inverter-fed motor drive system as shown in Fig. 5.4.3. The control and motor parameters remain the same as listed in Table 5-1. A dSPACE DS1104 PPC/DSP control board is employed to implement the real-time algorithm coding using the C language. A three-phase intelligent power module equipped with an insulated-gate bipolar transistor (IGBT) is used as an inverter. The gating pulses are generated in the DS1104 board and then sent to the inverter. The load is applied using a programmable dynamo-meter controller DSP6000 as shown in Fig. 5.4.2. A 10000-pulse incremental encoder is equipped to obtain the rotor speed of ALFSPMM as shown in Fig. 5.4.1. All experimental results are recorded by the ControlDesk interfaced with DS1104 and PC at 5 kHz sampling frequency.

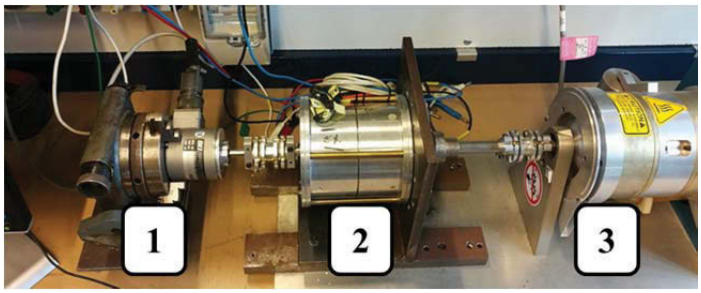

Fig. 5.4.1 Platform setup of experimental test, where (1) encoder, (2) ALFSPMM, and (3) dynamometer.

Fig. 5.4.2 Platform setup of experimental test, where (1) power quality clamp meter, (2) dynamometer controller, and (3) DC power supply.

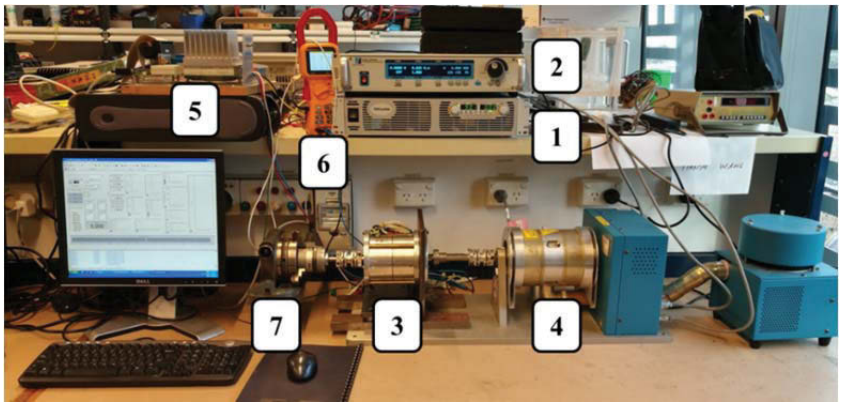

Fig. 5.4.3 Platform setup of experimental test, where (1) DC power supply, (2) dynamometer controller, (3) ALFSPMM, (4) dynamometer, (5) dSPACE control board, (6) power quality clamp meter, and (7) encoder.

5.4.2 Steady state responses (no load and with load)

The measurements of steady-state performance are presented in this section. The tests are repeated at variable speed and under variable load. Only a part of the test results (at the rated and half rated speed and under no load and rated load) are plotted in this section. Figs. 5.4.4- 5.4.7 plots the experimental steady-state performance. From top to bottom, the curves are the torque, stator flux and inverter switching frequency. The torque/flux ripples are defined as the standard deviation of torque/flux values. The average switching frequency is obtained by counting the total switching jumps N of six legs of two-level inverter over a fixed period of 0.05 s.

It can be seen that the torque and flux ripples of proposed FCS-MPDTC are lower than those of the conventional DTC and conventional FCS-MPDTC. The implementation of

one-step delay compensation can further reduce the torque and flux ripples and also an increase of switching frequency can be observed.

The quantitative index of average switching frequency, stator flux ripple and torque ripple for these tests will be summarized in Section 5.5.

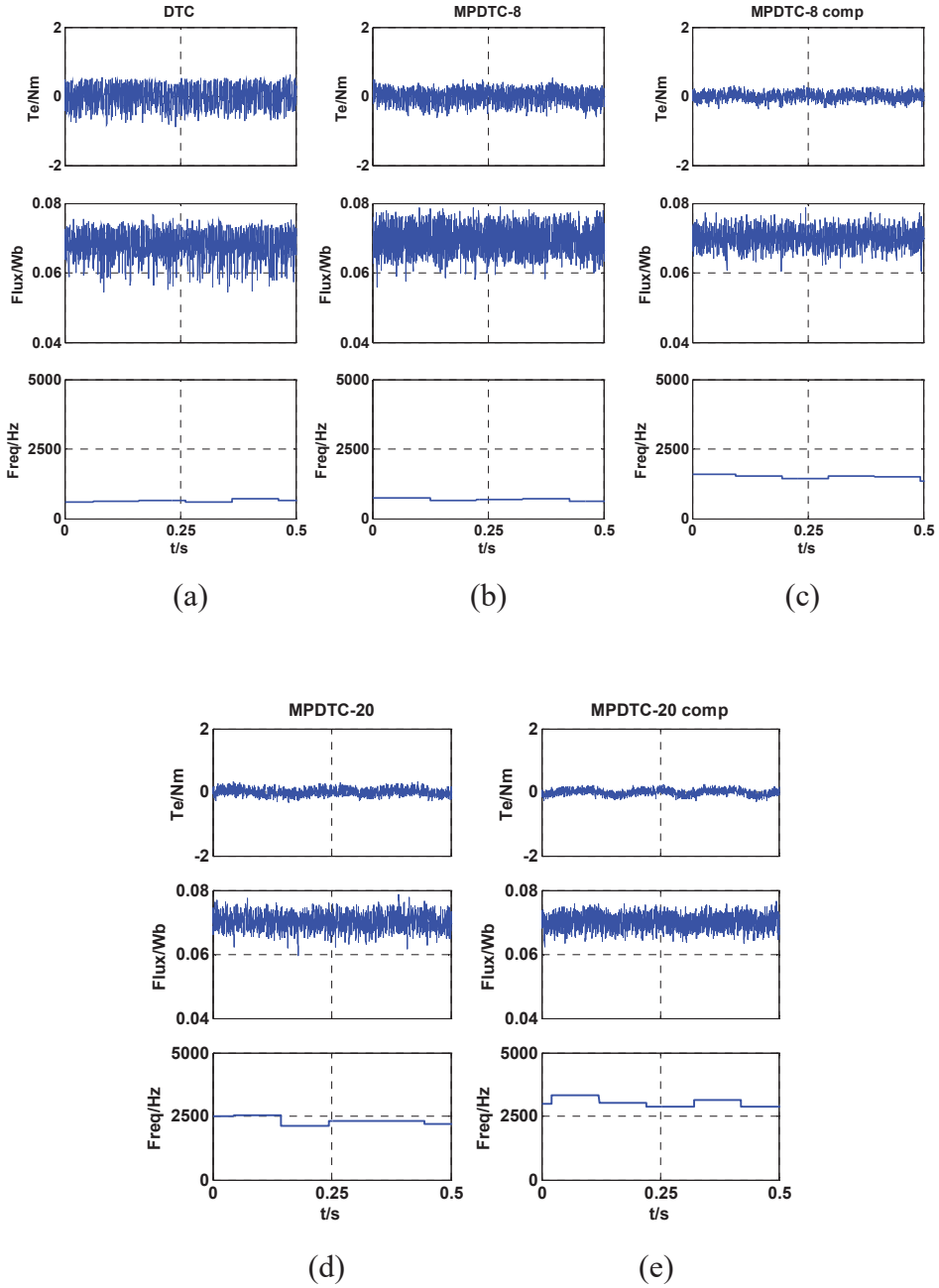

Fig. 5.4.4 Steady-state response at 400 rpm (no load) for (a) DTC, (b) MPDTC-8, (c) MPDTC-8 with one-step delay compensation, (d) MPDTC-20 and (e) MPDTC-20 with one-step delay compensation

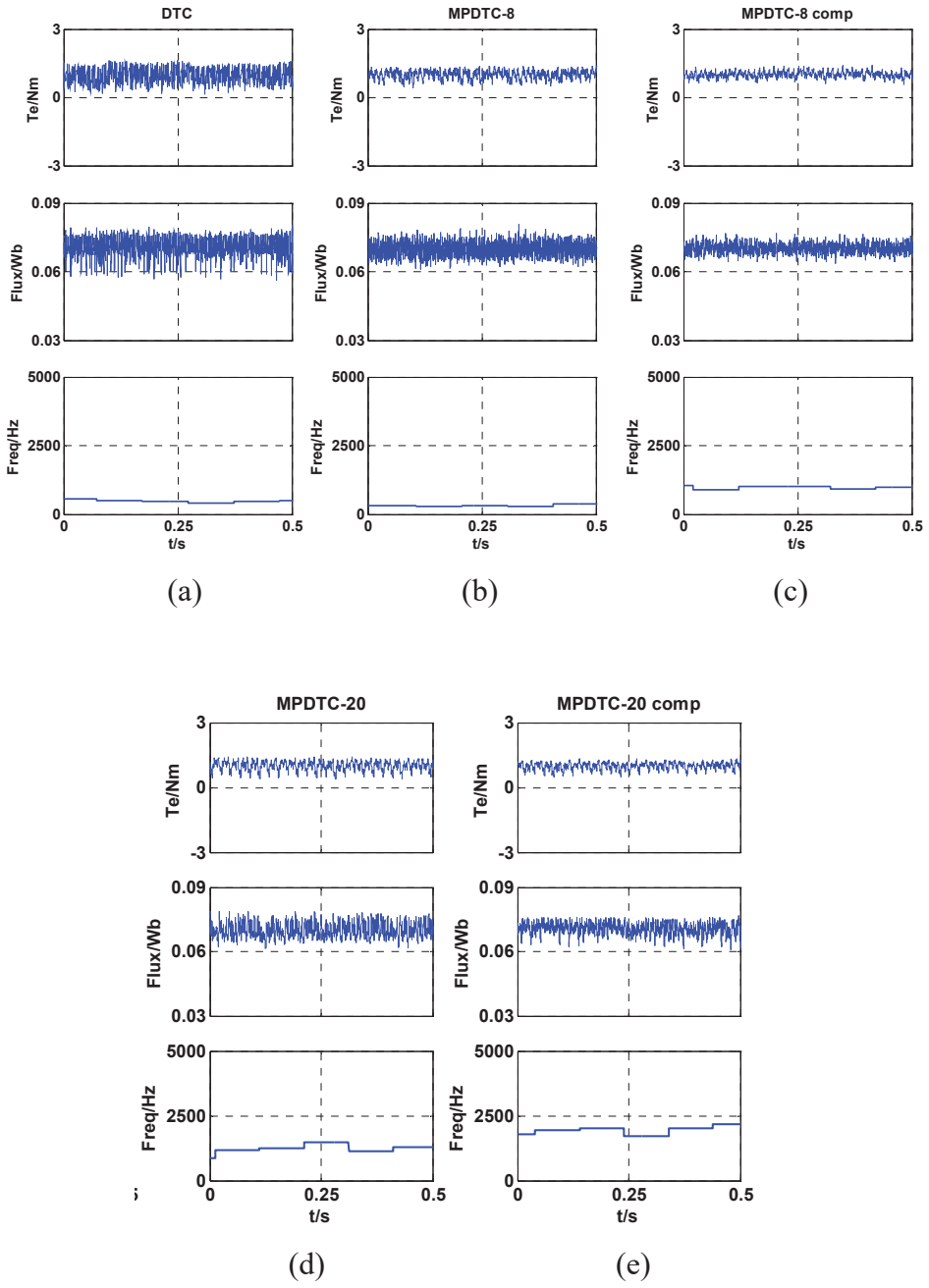

Fig. 5.4.5 Steady-state response at 400 rpm (rated load) for (a) DTC, (b) MPDTC-8, (c) MPDTC-8 with one-step delay compensation, (d) MPDTC-20 and (e) MPDTC-20 with one-step delay compensation

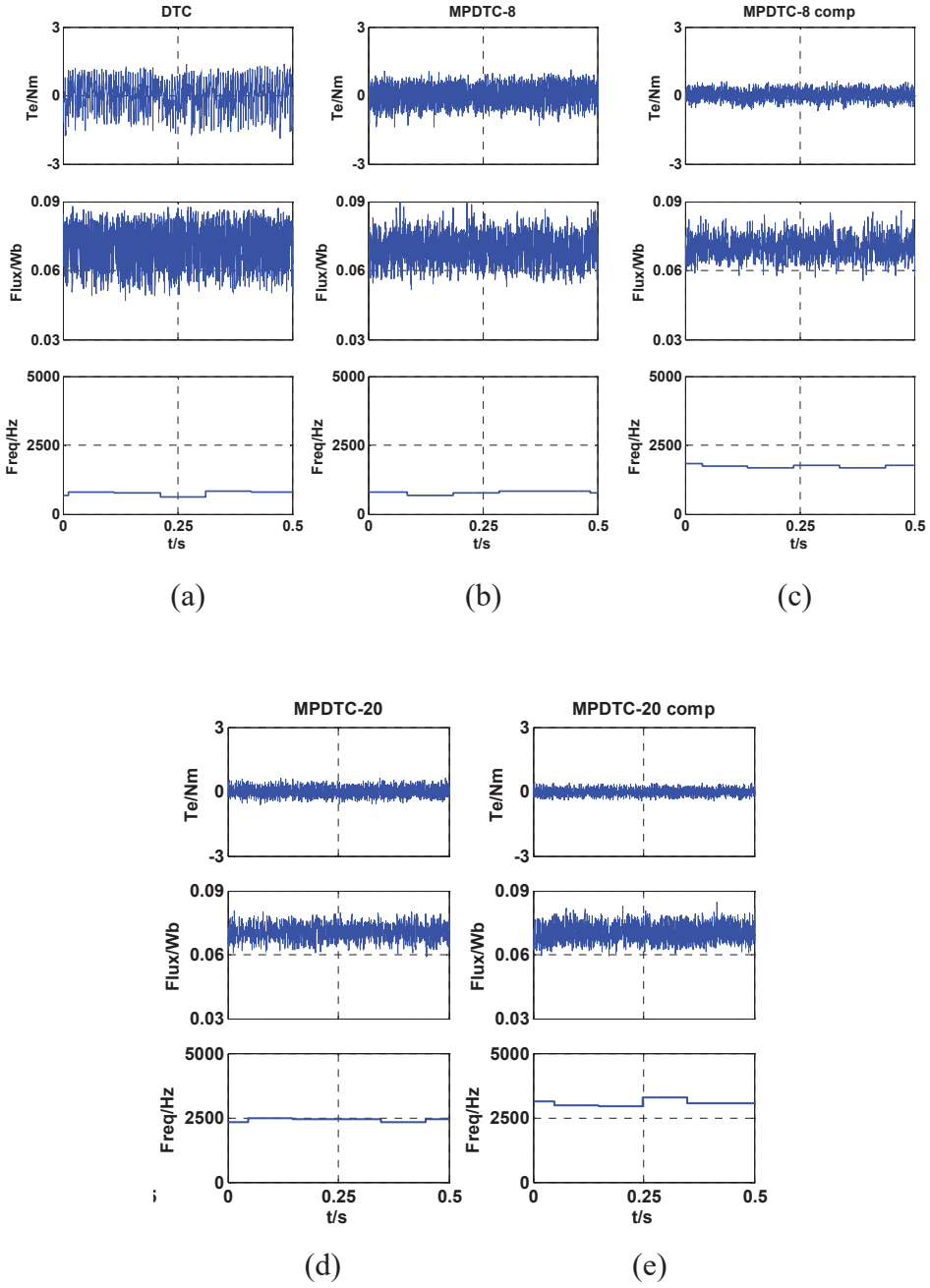

Fig. 5.4.6 Steady-state response at 800 rpm (no load) for (a) DTC, (b) MPDTC-8, (c) MPDTC-8 with one-step delay compensation, (d) MPDTC-20 and (e) MPDTC-20 with one-step delay compensation

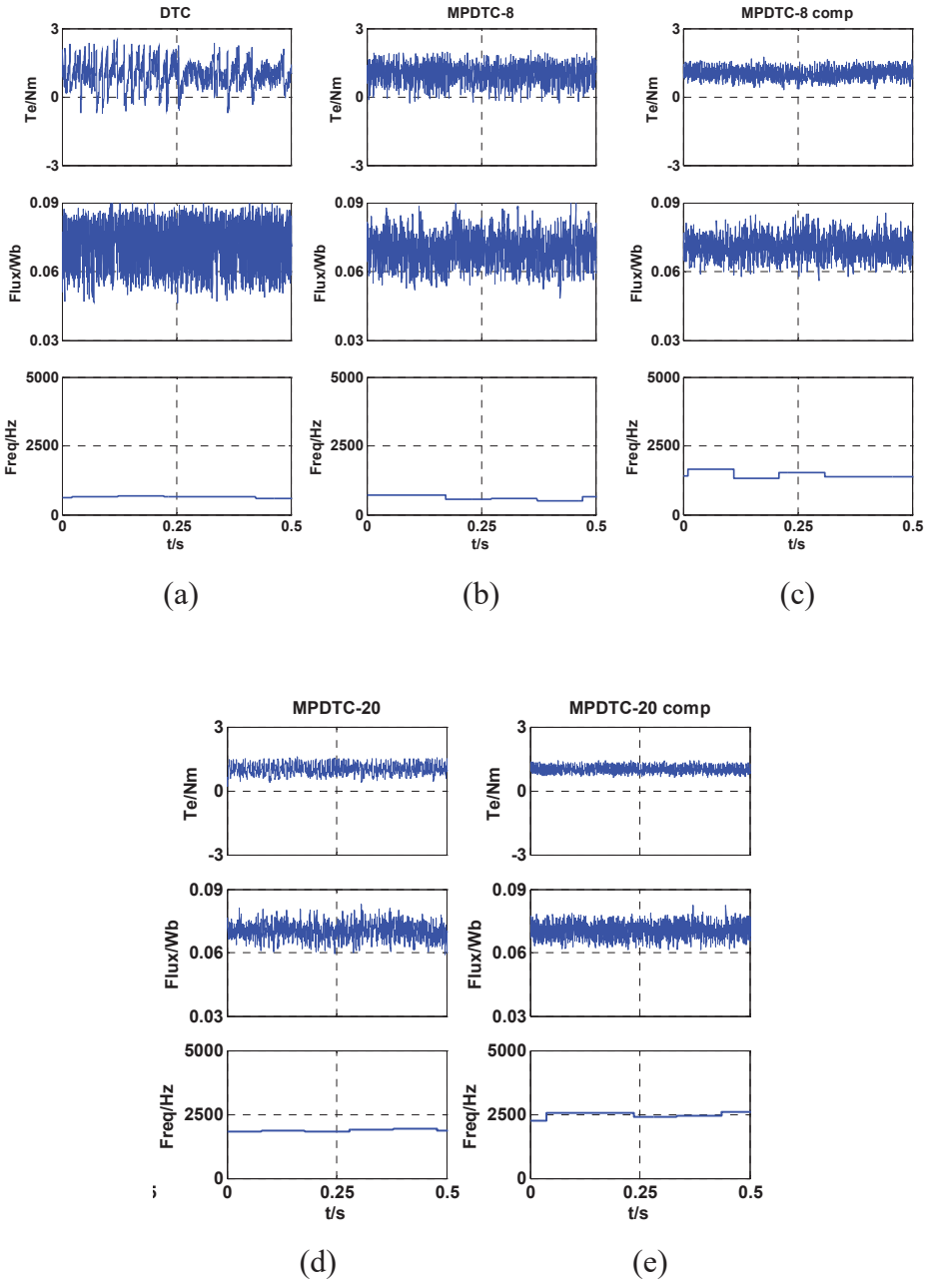

Fig. 5.4.7 Steady-state response at 800 rpm (rated load) for: (a) DTC, (b) MPDTC-8, (c) MPDTC-8 with one-step delay compensation, (d) MPDTC-20 and (e) MPDTC-20 with one-step delay compensation

5.4.3 Start-up tests

In this section, the start-up response is presented. By introducing a ramp-up function in the PI controller, the motor speed accelerates from 0 to 800 rpm steadily with a small overshoot. In Fig. 5.4.8, from top to bottom, the curves shown are the stator current, stator flux, torque and rotor speed. It is observed that whilst the dynamic responses for these methods are similar, the steady state performance of the proposed FCS-MPDTC with one-step delay compensation is the best.

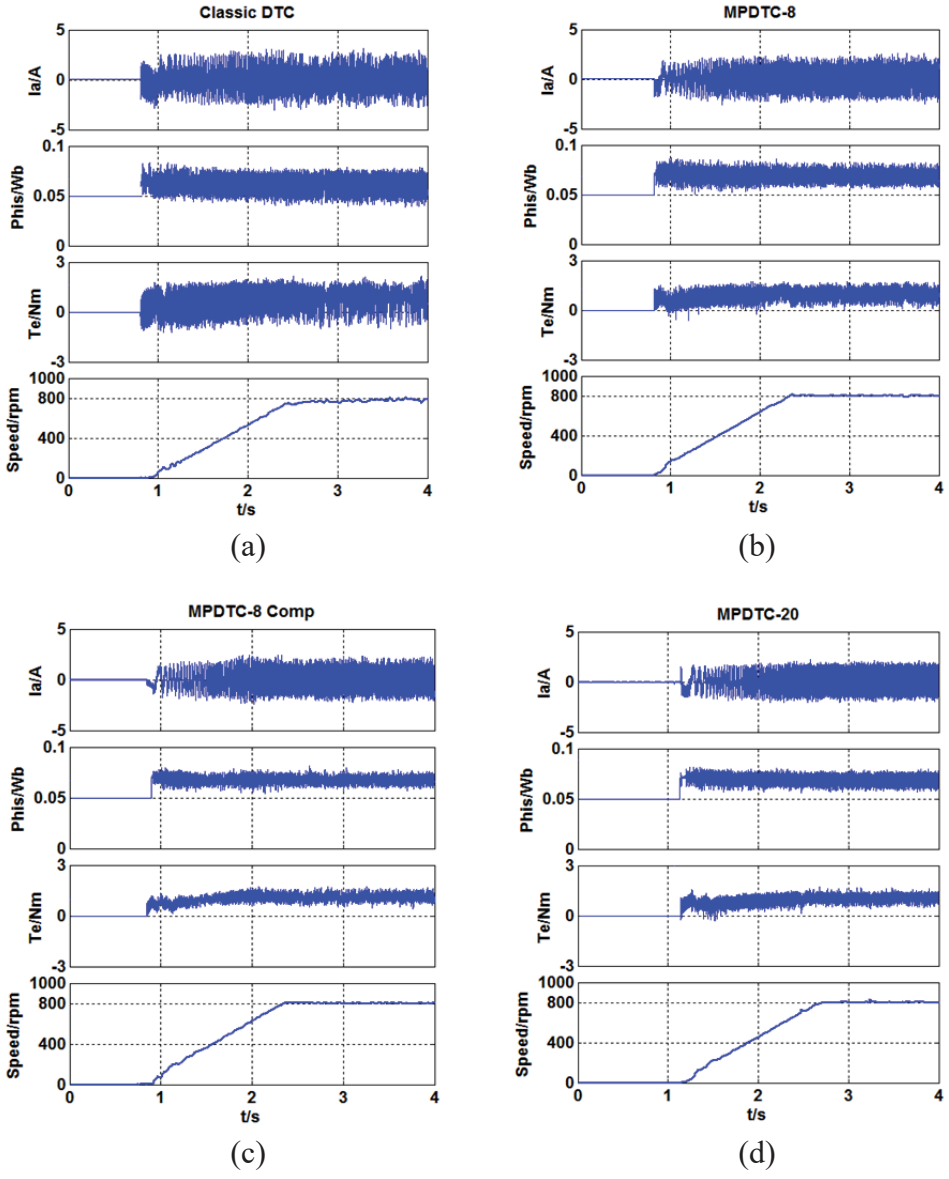

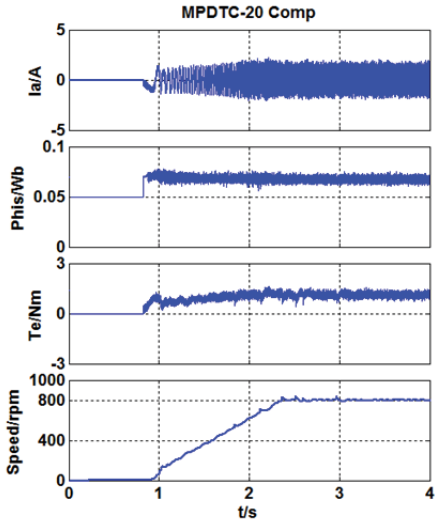

(e)

Fig. 5.4.8 Start-up response from standstill to 800 rpm for (a) DTC, (b) MPDTC-8, (c) MPDTC-8 with one-step delay compensation, (d) MPDTC-20, and (e) MPDTC-20 with one-step delay compensation

5.4.4 Deceleration tests

In this section, the test started with a motor speed of 800 rpm and the reference speed is set to 400 rpm at around 1s. In Fig. 5.4.9, from top to bottom, the curves are stator current, stator flux, torque and motor speed respectively. By introducing a ramp-up function in the PI controller, all these control methods exhibited excellent performance and the motor speed decreased from 800 rpm to 400 rpm smoothly.

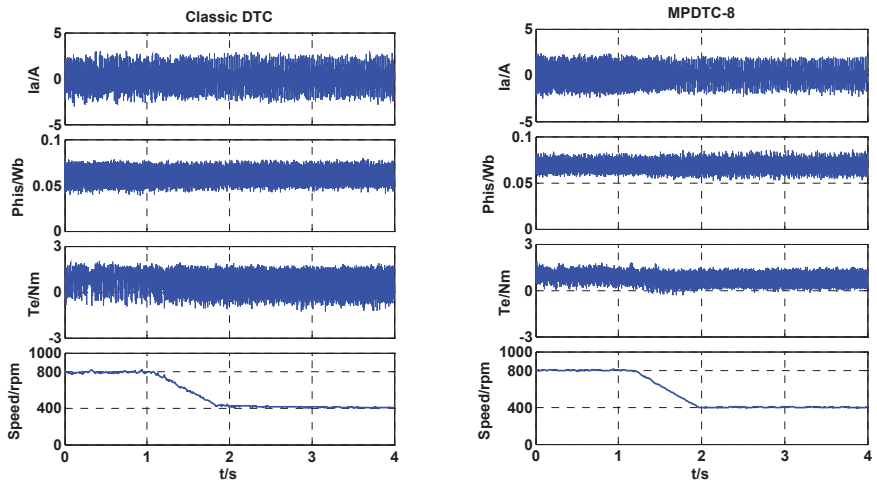

(a) (b)

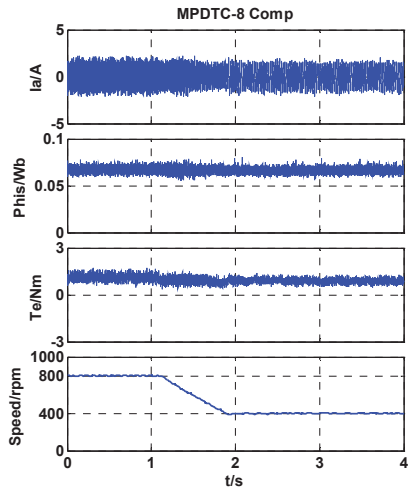

(c)

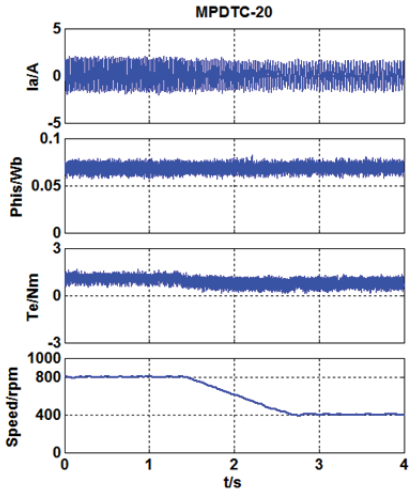

(d)

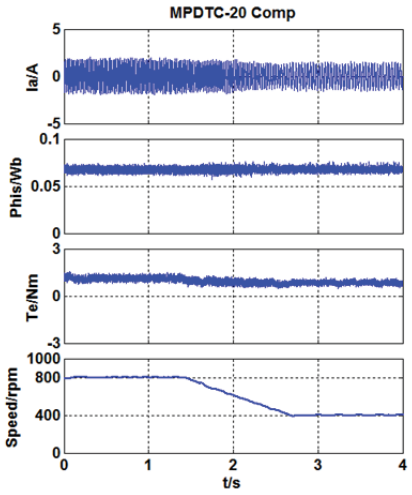

(e)

Fig. 5.4.9 Deceleration test for (a) DTC, (b) MPDTC-8, (c) MPDTC-8 with one-step delay compensation, (d) MPDTC-20, and (e) MPDTC-20 with one-step delay compensation

5.4.5 Load tests

The section presents the response to external load disturbance of these methods. The motor is operated at a steady rate of 800 rpm when a load of 1 Nm is applied on the shaft. As shown in Fig. 5.4. 10, all these control methods presented good dynamic performance and in a very short period, the motor speed returns to its original value due to the fast torque response. It can be found that the classic DTC spend around 1s to recover the original speed. For conventional FCS-MPDTCs and proposed FCS-MPDTCs, the recovery time is approximately 0.5s.

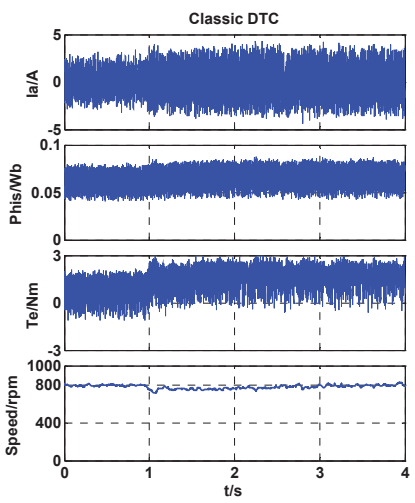

(a)

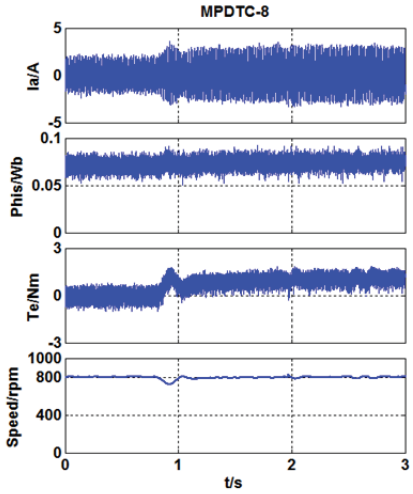

(b)

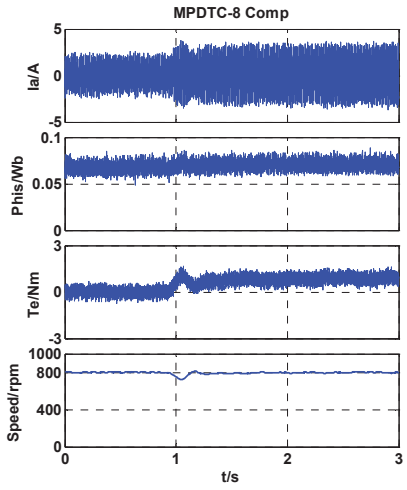

(c)

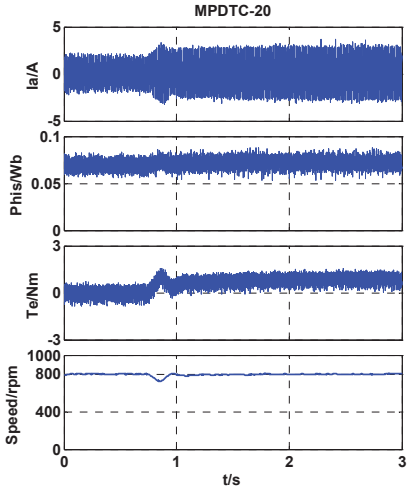

(d)

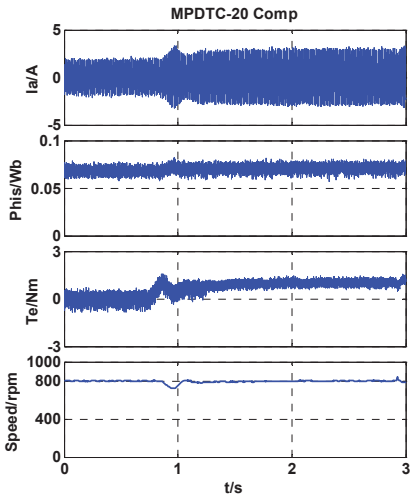

(e)

Fig. 5.4.10 Load test for: (a) DTC, (b) MPDTC-8, (c) MPDTC-8 with one-step delay compensation, (d) MPDTC-20 and (e) MPDTC-20 with one-step delay compensation

5.5 Quantitative Analysis and Comparison of Control Methods

This section summarises the detailed results of steady-state experimental tests. The experimental steady-state tests are repeated at different speeds (from 300 to 800 rev/min) and load settings (from 0 to 1 Nm). In Tables 5-2 to 5-6 below, the bold horizontal columns are the motor speed and the bold vertical columns are the load torque. The torque/flux ripples are defined as the standard deviation of torque/flux values. The average inverter switching frequency is obtained by counting the total switching jumps N of six legs of two-level inverter over a fixed period of 0.05 s.

5.5.1 Conventional DTC

The steady-state experimental tests of conventional DTC are summarized in this section.

Torque ripples

Table 5-2a Steady-state torque ripples of DTC (Unit: Nm)

		Speed (Rev/min)					
		300	**400**	**500**	**600**	**700**	**800**
Torque (Nm)	**0**	0.2635	0.282	0.3471	0.4322	0.5391	0.6071
	0.25	0.2528	0.2933	0.3769	0.4024	0.5443	0.6036
	0.5	0.2316	0.2706	0.351	0.4124	0.5536	0.6128
	0.75	0.2197	0.2831	0.355	0.4065	0.4577	0.6061
	1	0.2075	0.2512	0.321	0.4332	0.4955	0.5712

Flux ripples

Table 5-2b Steady-state flux ripples of DTC (Unit: Wb)

		Speed (Rev/min)					
		300	**400**	**500**	**600**	**700**	**800**
Flux (Wb)	**0**	0.0035	0.0038	0.0045	0.0053	0.0075	0.0089
	0.25	0.0037	0.004	0.0045	0.0062	0.0074	0.0087
	0.5	0.0038	0.0041	0.0044	0.0062	0.0078	0.0095
	0.75	0.004	0.0041	0.005	0.0059	0.0081	0.0094
	1	0.004	0.005	0.00625	0.0074	0.0085	0.0099

Inverter switching frequencies

Table 5-2c Steady-state inverter switching frequencies of DTC (Unit: Hz)

		Speed (Rev/min)					
		300	**400**	**500**	**600**	**700**	**800**
Switching frequency (Hz)	**0**	865.584	635.292	399.728	555.56	654.352	765.64
	0.25	759.6	594.32	592	450	698	757.452
	0.5	669.536	362.24	405.912	440.68	661.16	751.764
	0.75	602	478.712	435.365	389.608	562.448	696.4
	1	463.728	474.147	491.254	503.556	515.488	645.392

5.5.2 Conventional FCS-MPDTC

The steady-state experimental tests of conventional FCS-MPDTC are summarized in this section.

Torque ripples

Table 5-3a Steady-state torque ripples of FCS-MPDTC (Unit: Nm)

		Speed (Rev/min)					
		300	**400**	**500**	**600**	**700**	**800**
Torque (Nm)	**0**	0.1722	0.1997	0.2475	0.2813	0.3536	0.4543
	0.25	0.1664	0.1889	0.2362	0.2794	0.3316	0.4378
	0.5	0.1582	0.1681	0.224	0.2598	0.3207	0.4344
	0.75	0.1459	0.1539	0.2123	0.2068	0.3073	0.4324
	1	0.1324	0.1769	0.2175	0.2177	0.3079	0.4177

Flux ripples

Table 5-3b Steady-state flux ripples of FCS-MPDTC (Unit: Wb)

		Speed (Rev/min)					
		300	**400**	**500**	**600**	**700**	**800**
Flux (Wb)	**0**	0.0034	0.0039	0.0047	0.0052	0.0058	0.0067
	0.25	0.0034	0.004	0.0048	0.005	0.006	0.0064
	0.5	0.0036	0.0039	0.0048	0.0051	0.0062	0.0066
	0.75	0.0033	0.0033	0.0047	0.0052	0.006	0.0068
	1	0.003	0.0033	0.0042	0.005	0.006	0.0069

Inverter switching frequencies

Table 5-3c Steady-state inverter switching frequencies of FCS-MPDTC (Unit: Hz)

		Speed (Rev/min)					
		300	**400**	**500**	**600**	**700**	**800**
Switching frequency (Hz)	**0**	738.496	684.656	721.68	690.172	766.856	779.112
	0.25	763.688	652.848	717.992	614.952	682.056	744.472
	0.5	640.432	533.82	671.032	556.528	618.208	661.808
	0.75	511.848	458.08	584.596	458.576	589.94	668
	1	383.56	325.208	444.172	385.2	500.352	614.664

5.5.3 Conventional FCS-MPDTC with one-step delay compensation

The steady-state experimental tests of conventional FCS-MPDTC with one-step delay compensation are summarized in this section.

Torque ripples

Table 5-4a Steady-state torque ripples of FCS-MPDTC with one-step delay compensation (Unit: Nm)

		Speed (Rev/min)					
		300	**400**	**500**	**600**	**700**	**800**
Torque (Nm)	**0**	0.1054	0.1101	0.1311	0.1506	0.1901	0.2128
	0.25	0.1024	0.1085	0.1299	0.1552	0.1795	0.2139
	0.5	0.0973	0.1078	0.1301	0.1459	0.1841	0.2203
	0.75	0.102	0.1062	0.1323	0.1507	0.1854	0.2258
	1	0.1198	0.1283	0.1368	0.1563	0.1867	0.226

Flux ripples

Table 5-4b Steady-state flux ripples of FCS-MPDTC with one-step delay compensation (Unit: Wb)

		Speed (Rev/min)					
		300	**400**	**500**	**600**	**700**	**800**
Flux (Wb)	**0**	0.002	0.0025	0.0029	0.0032	0.0039	0.0044
	0.25	0.0022	0.0025	0.0029	0.0032	0.0039	0.0044
	0.5	0.0023	0.0025	0.0031	0.0032	0.0038	0.0045
	0.75	0.0022	0.0022	0.0032	0.0032	0.0039	0.0045
	1	0.0018	0.0022	0.0028	0.0026	0.004	0.0046

Inverter switching frequencies

Table 5-4c Steady-state inverter switching frequencies of FCS-MPDTC with one-step delay compensation (Unit: Hz)

		Speed (Rev/min)					
		300	**400**	**500**	**600**	**700**	**800**
Switching frequency (Hz)	**0**	1753.4	1509.4	1636.2	1483.1	1715.1	1733.7
	0.25	1568.8	1469.6	1676	1430.1	1655.2	1685.8
	0.5	1468.5	1386.6	1562.1	1374.2	1530.1	1737.2
	0.75	1279.8	1207.4	1369.5	1200	1424.8	1619.1
	1	1065.1	970.968	1254.5	1104.6	1252.7	1452.4

5.5.4 Proposed FCS-MPDTC

The steady-state experimental tests of proposed FCS-MPDTC are summarized in this section.

Torque ripples

Table 5-5a Steady-state torque ripples of proposed FCS-MPDTC (Unit: Nm)

		Speed (Rev/min)					
		300	**400**	**500**	**600**	**700**	**800**
Torque (Nm)	**0**	0.103	0.1129	0.1343	0.1919	0.1928	0.2333
	0.25	0.1013	0.1069	0.1339	0.167	0.1987	0.2252
	0.5	0.0998	0.1115	0.1367	0.159	0.1859	0.2319
	0.75	0.1045	0.1463	0.134	0.1625	0.188	0.224
	1	0.1744	0.2129	0.1765	0.1827	0.2056	0.2317

Flux ripples

Table 5-5b Steady-state flux ripples of proposed FCS-MPDTC (Unit: Wb)

		Speed (Rev/min)					
		300	**400**	**500**	**600**	**700**	**800**
Flux (Wb)	**0**	0.0021	0.0027	0.003	0.0034	0.0035	0.0036
	0.25	0.0023	0.0031	0.0032	0.0031	0.0034	0.0038
	0.5	0.0028	0.0034	0.0035	0.0034	0.0037	0.0038
	0.75	0.0032	0.0031	0.0033	0.0032	0.0033	0.0038
	1	0.0028	0.0035	0.0029	0.0028	0.0031	0.0037

Inverter switching frequencies

Table 5-5c Steady-state inverter switching frequencies of proposed FCS-MPDTC (Unit: Hz)

		Speed (Rev/min)					
		300	**400**	**500**	**600**	**700**	**800**
Switching frequency (Hz)	**0**	2909.0	2538.2	2331.9	2495.4	2336.0	2227.9
	0.25	2815.4	2437.1	2322.9	2242.3	2275.0	2176.6
	0.5	2593.8	2056.7	2060.3	2144.0	2218.2	2062.7
	0.75	2210.5	2005.4	1920.5	2097.1	1897.4	1927.7
	1	2077.3	1365.3	1765.8	1841.2	1815.4	1653.4

5.5.5 Proposed FCS-MPDTC with one-step delay compensation

The steady-state experimental tests of proposed FCS-MPDTC with one-step delay compensation are summarized in this section.

Torque ripples

Table 5-6a Steady-state torque ripples of proposed FCS-MPDTC with one-step delay compensation (Unit: Nm)

		Speed (Rev/min)					
		300	**400**	**500**	**600**	**700**	**800**
Torque (Nm)	**0**	0.0896	0.0916	0.0945	0.0989	0.1211	0.154
	0.25	0.0859	0.087	0.0922	0.1025	0.1167	0.1434
	0.5	0.0826	0.0862	0.0927	0.1191	0.1248	0.1517
	0.75	0.0889	0.1254	0.118	0.158	0.1343	0.1469
	1	0.1621	0.1563	0.1655	0.2054	0.1698	0.1494

Flux ripples

Table 5-6b Steady-state flux ripples of proposed FCS-MPDTC with one-step delay compensation (Unit: Wb)

		Speed (Rev/min)					
		300	**400**	**500**	**600**	**700**	**800**
Flux (Wb)	**0**	0.0019	0.0025	0.0027	0.003	0.0035	0.0039
	0.25	0.0021	0.0029	0.003	0.003	0.0035	0.0037
	0.5	0.0027	0.003	0.0031	0.0028	0.0033	0.0036
	0.75	0.0032	0.0027	0.003	0.0026	0.0031	0.0035
	1	0.0025	0.0027	0.0027	0.0026	0.0027	0.0033

Inverter switching frequencies

Table 5-6c Steady-state inverter switching frequencies of proposed FCS-MPDTC with one-step delay compensation (Unit: Hz)

		Speed (Rev/min)					
		300	**400**	**500**	**600**	**700**	**800**
Switching frequency (Hz)	**0**	3865.5	3331.1	3222.6	2807.0	2814.8	2861.9
	0.25	3619.0	3084.3	3127.7	2666.5	2642.5	2776.4
	0.5	3193.7	2498.0	2812.1	2345.6	2421.5	2594.4
	0.75	2428.9	2268.1	2204.5	1952.6	2259.6	2422.2
	1	1987.0	2112.7	1908.3	1338.1	1773.2	2189.4

5.5.6 Analysis of torque/flux ripples and inverter switching frequencies

The torque/flux ripples and inverter switching frequencies of different control methods are compared under different load conditions in the following charts.

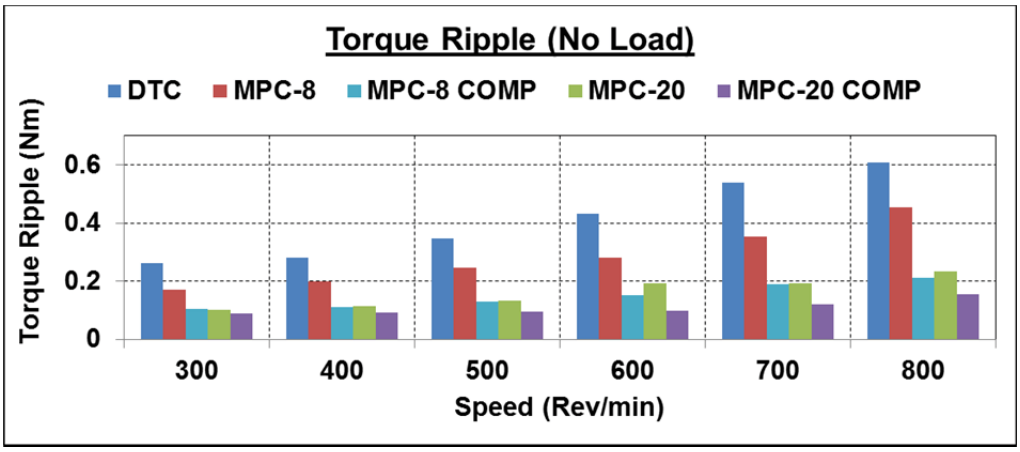

(a)

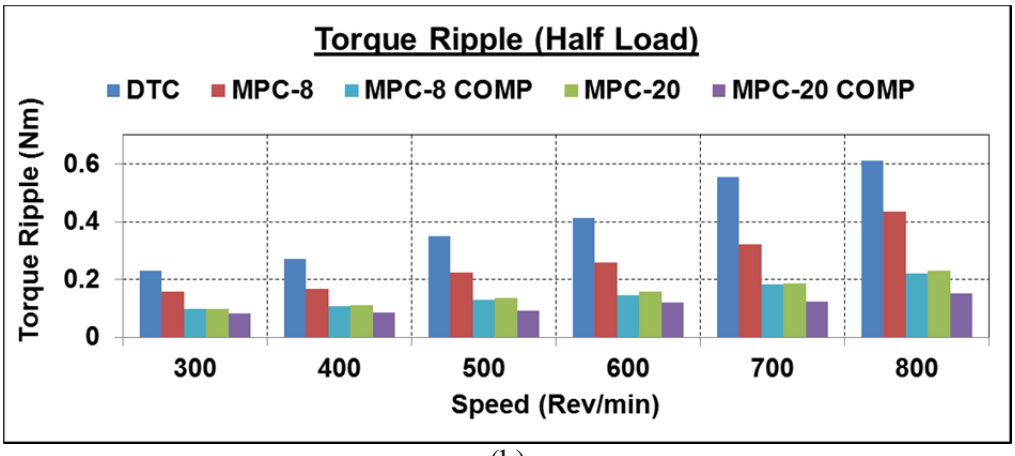

(b)

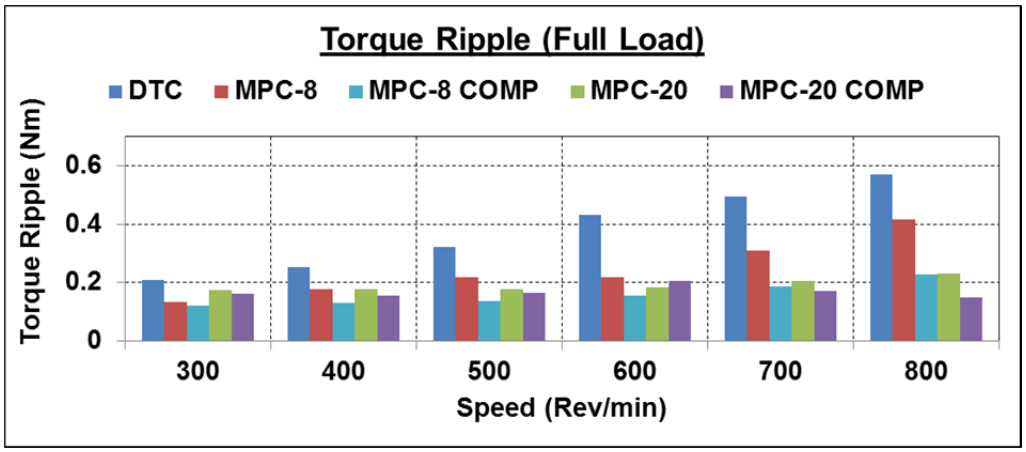

(c)

Fig. 5.5.1 Comparison of torque ripples in different control methods, under (a) no load, (b) half load, and (c) full load conditions

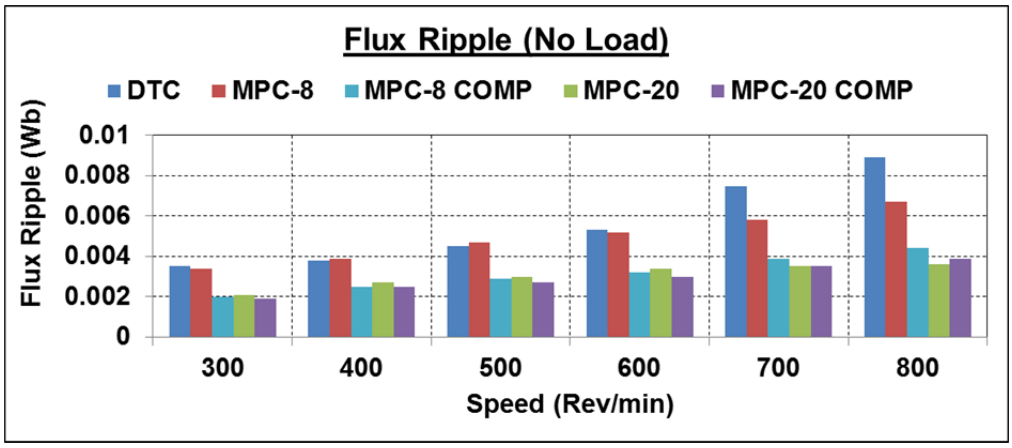

(a)

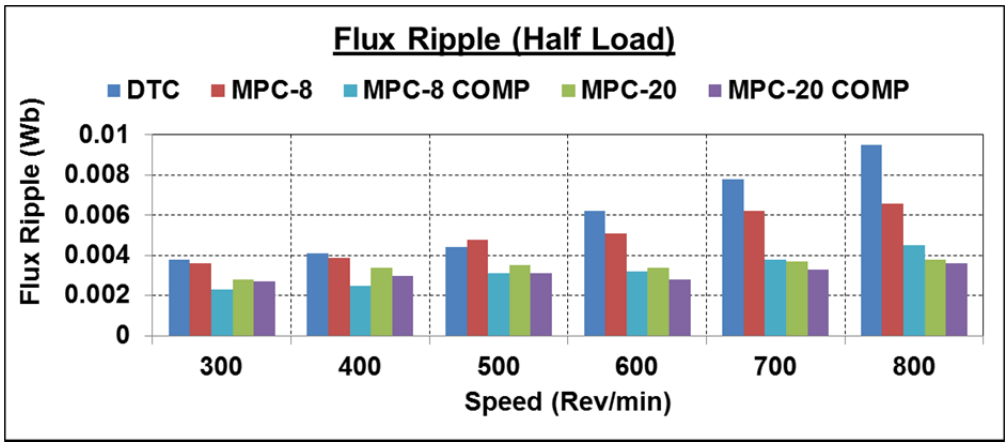

(b)

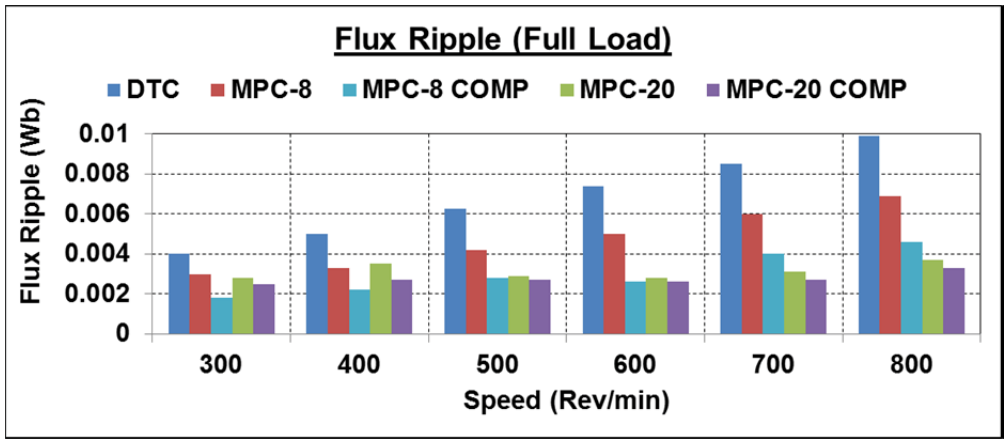

(c)

Fig. 5.5.2 Comparison of flux ripples in different control methods, under (a) no load, (b) half load, and (c) full load conditions

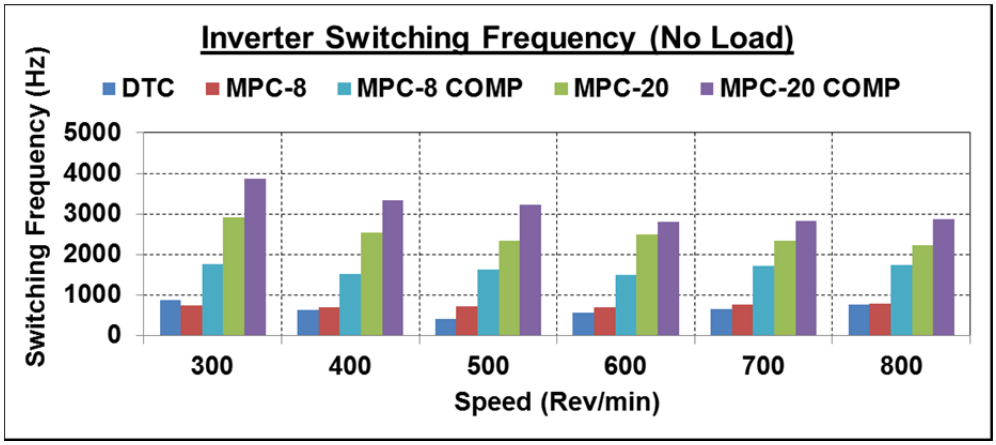

(a)

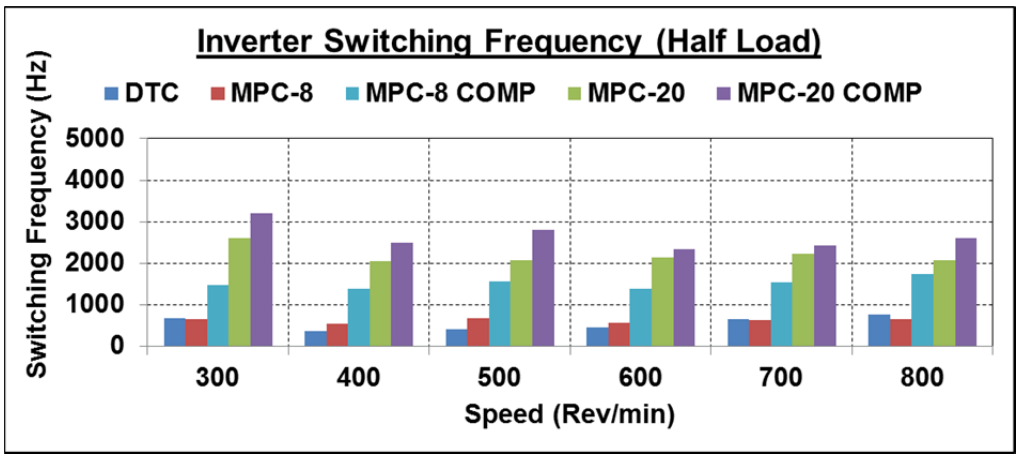

(b)

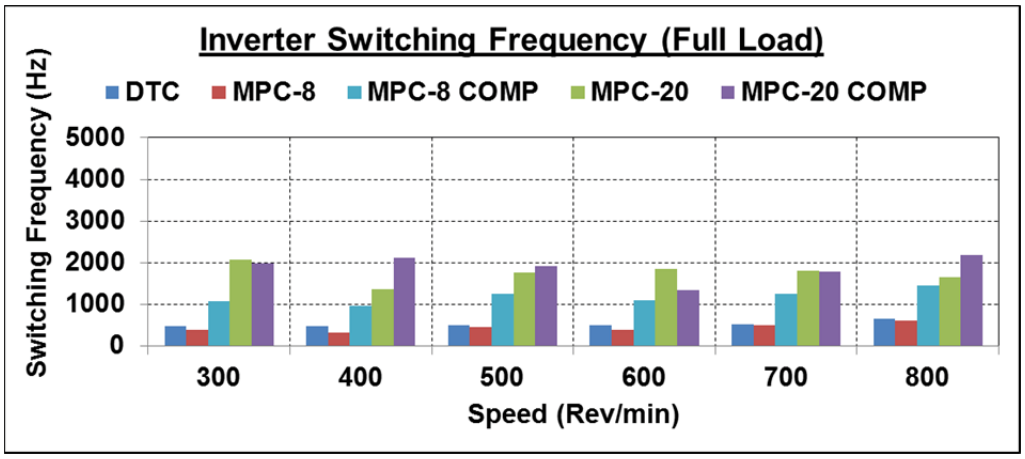

(c)

Fig. 5.5.2 Comparison of inverter switching frequencies in different control methods, under (a) no load, (b) half load, and (c) full load conditions

5.5.7 Drive system efficiency

The drive system efficiency is introduced to evaluate the performance of the algorithms. The drive system efficiency is defined as

$$\eta_{sys} = P_{out} / P_{dc} \tag{5.11}$$

where η_{sys} is the drive system efficiency, P_{out} the output power measured by the dynamo-meter, and P_{dc} the power output of DC power supply. The experimental drive system efficiency contours are presented in Figs. 5.5.3-5.5.7. The speed is varied from 37.5% rated speed to 100% rated speed and the load torque is varied from 0% rated torque to 100% rated torque.

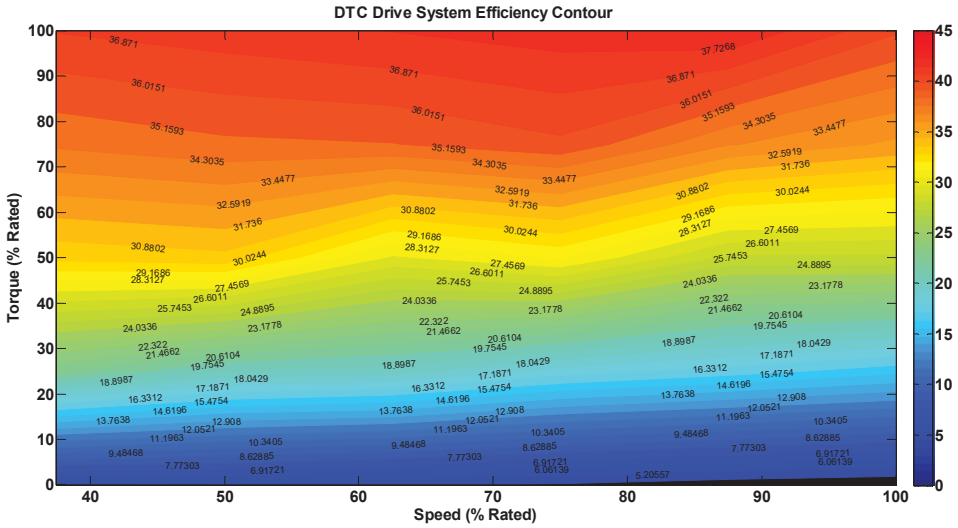

Fig. 5.5.3 Drive system efficiency contour of DTC

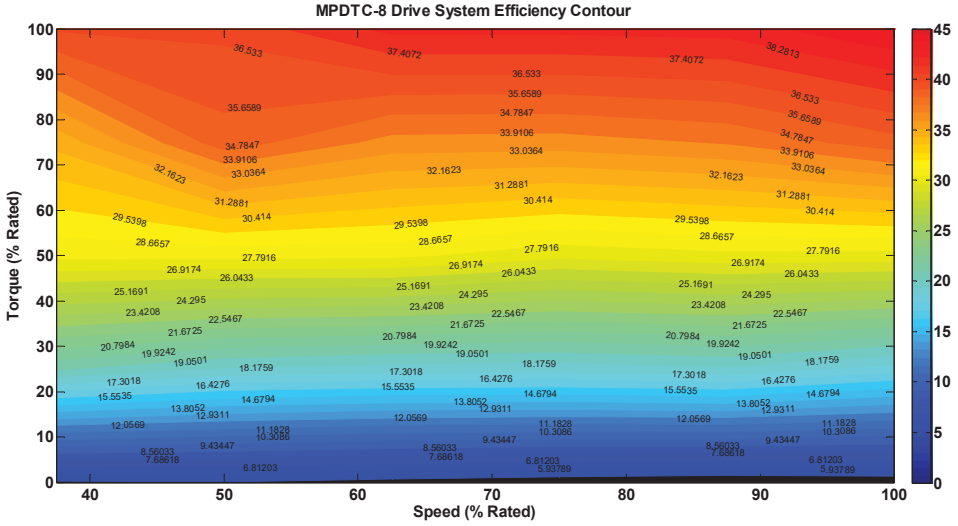

Fig. 5.5.4 Drive system efficiency contour of conventional FCS-MPDTC

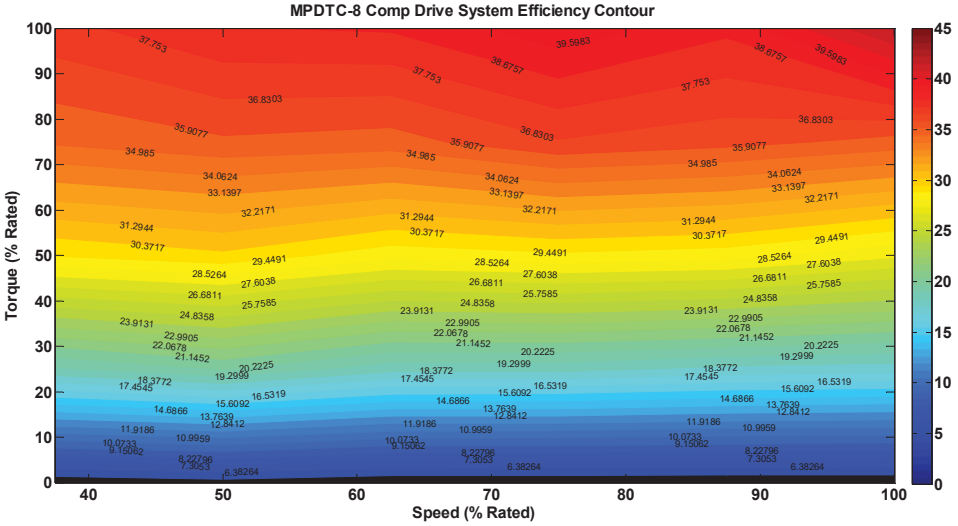

Fig. 5.5.5 Drive system efficiency contour of conventional FCS-MPDTC with one-step delay compensation

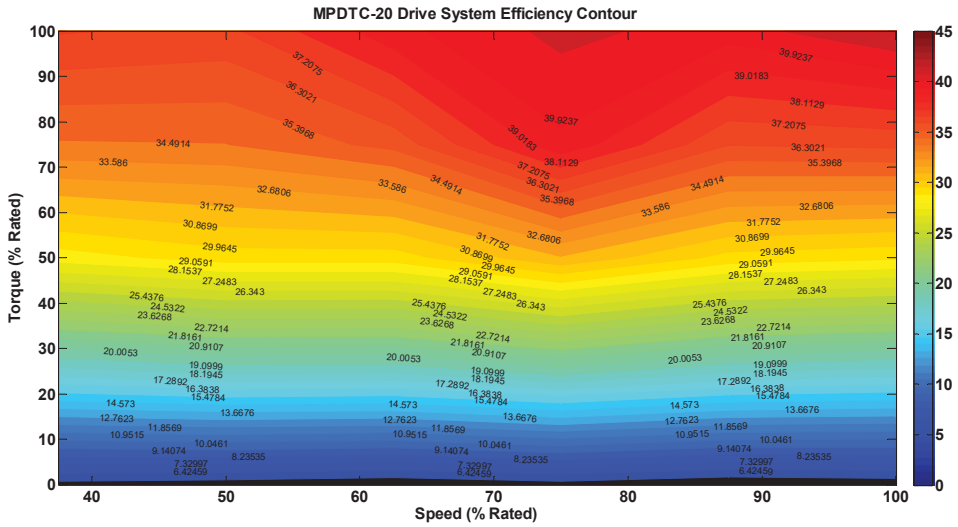

Fig. 5.5.6 Drive system efficiency contour of proposed FCS-MPDTC

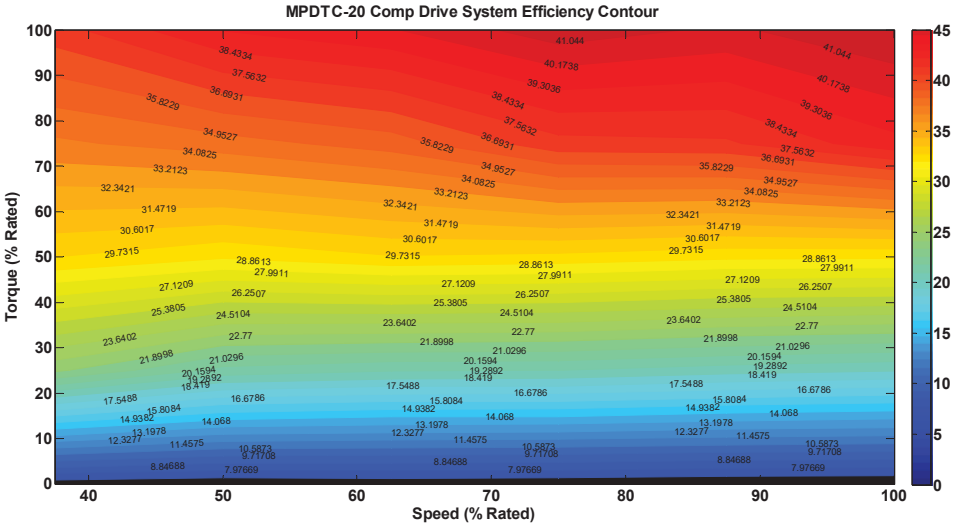

Fig. 5.5.7 Drive system efficiency contour of proposed FCS-MPDTC with one-step delay compensation

5.5.8 Discussion of the test results

The simulation and experimental tests results listed above are discussed below in detail:

Conventional FCS-MPDTC vs. Conventional DTC

From the experimental tests results, it is seen that the implementation of FCS-MPDTC can reduce the flux and torque ripples by -2.63% and 29.18% at 400 rpm under no load,

34.00% and 29.58% at 400 rpm under full load, 24.72% and 25.17% at 800 rpm under no load, and 30.30% and 26.87% at 800 rpm under full load, respectively..

In conclusion, the conventional FCS-MPDTC can achieve lower torque ripple than that of DTC as proven by both the simulation and experimental results. However, its feature in flux ripple reduction is unstable. The highest drive system efficiency of the conventional DTC and conventional FCS-MPDTC are 36.16% and 41.37%, respectively. The conventional FCS-MPDTC presents higher drive system efficiency in all regions and wider high-efficiency range than conventional DTC. A detailed discussion of the drive system efficiency is presented in Section 5.6.

Conventional FCS-MPDTC +comp vs. Conventional FCS-MPDTC

From the experimental tests results, it is seen that the implementation of one-step delay compensation can reduce the flux and torque ripples by 35.90% and 44.87% at 400 rpm under no load, 33.33% and 27.47% at 400 rpm under full load, 34.33% and 53.16% at 800 rpm under no load, and 33.33% and 45.89% at 800 rpm under full load, respectively.

With the help of one-step delay compensation, the steady-state performance of the conventional FCS-MPDTC has been improved significantly. It should be noticed that the switching frequency has been increased by almost 2-3 times in most tests when the one-step delay is compensated. The highest drive system efficiency of the conventional FCS-MPDTC and conventional FCS-MPDTC with one-step delay compensation are 41.37% and 40.03%, respectively. It can be seen that the implementation of one-step delay compensation can increase the efficiency in most of the operational regions. However, a slight decrease of efficiency is noticed at the high-speed high-load region.

Proposed FCS-MPDTC vs. Conventional FCS-MPDTC

From the experimental test results, it is seen that the proposed FCS-MPDTC can reduce the flux and torque ripples by 30.77% and 43.47% at 400 rpm under no load, -6.06% and 0.06% at 400 rpm under full load, 46.27% and 48.65% at 800 rpm under no load, and 46.38% and 44.53% at 800 rpm under full load, respectively.

As shown in the above test analysis, the introduction of proposed method can effectively reduce the torque and flux ripples. A noticeable increase of inverter switching frequency is also observed. The highest drive system efficiency of proposed FCS-MPDTC and conventional FCS-MPDTC are 41.73% and 41.37%, respectively. The proposed FCS-MPDTC presents higher drive system efficiency in all regions and wider high-efficiency range than the conventional FCS-MPDTC.

Proposed FCS-MPDTC +comp vs. Conventional FCS-MPDTC +comp

From the experimental test results, it is seen that the implementation of proposed method can reduce the flux and torque ripples by 0.00% and 16.80% at 400 rpm under no load, -22.73% and -21.82% at 400 rpm under full load, 11.36% and 27.63% at 800 rpm under no load, and 28.26% and 33.89% at 800 rpm under full load, respectively.

The performance of proposed FCS-MPDTC is better than that of the conventional FCS-MPDTC in the high-speed and high-load region. The highest drive system efficiency of the proposed FCS-MPDTC and conventional FCS-MPDTC are 41.91% and 40.03%, respectively. The proposed FCS-MPDTC presents slightly higher drive system efficiency than the conventional FCS-MPDTC in all regions.

Conclusion of the discussion

According to the analysis above, it can be concluded that:

- The conventional FCS-MPDTC can achieve lower torque ripple than that of the conventional DTC whilst maintaining/reducing the switching frequency as proven by both simulation and experimental results. However, the ability of the conventional FCS-MPDTC in flux ripple reduction is insignificant and even unstable.
- The introduction of the proposed method can effectively reduce the torque and flux ripples. A noticeable increase of the inverter switching frequency is also observed. The drive system efficiency of this method is the highest in all regions.
- When the one-step delay is compensated, the steady-state performance of the conventional FCS-MPDTC and proposed FCS-MPDTC in terms of torque and flux

ripple reduction can be improved. It should be noticed that the performance improvement also comes with a switching frequency increase (twice or more).

5.6 Summary

In this chapter, the model of ALFSPMM is derived. The proposed FCS-MPDTC together with the conventional FCS-MPDTC and conventional DTC are investigated by both numerical simulation and experimental tests. It is shown that the proposed FCS-MPDTC can provide better steady state performance, similar dynamic response and higher system efficiency than the other control methods under the condition of same sampling frequency. When the one-step delay is compensated, the performance can be further improved along with the switching frequency increase.

However, it is found that the overall drive system efficiency is low (maximum about 40%). The possible reasons are:

1) Inadequate structural strength of the rotor laminations.

A high frequency scraping sound is noticed when the ALFSPMM is being tested, most likely caused by the grinding between the rotor and stator laminations. The best possible reason is that the rotor or/and stator laminations deform when the motor is spinning, due to the inadequate structural strength of the rotor or/and stator laminations. This should be improved in the next prototype.

2) Limited operating point

The space for stator windings is reduced due to unexpected design issue. To maintain the number of turns of the winding, the diameter of the copper wires is down-sized. As a result, the rated stator current is lower than the expectation and the operating point of ALFSPMM is limited to the low-speed and low-load region, i.e. low efficiency region.

To thoroughly investigate the performance of the proposed FCS-MPDTC, above tests are repeated and expended in a commercially produced PMSM drive system. The results are detailed in Chapter 6.

CHAPTER 6.

NUMERICAL SIMULATION AND EXPERIMENTAL TESTS OF PMSM

6.1 Introduction

In Chapter 5, the proposed FCS-MPDTC together with the conventional FCS-MPDTC and conventional DTC are investigated by both numerical simulation and experimental tests. Due to the inadequate structural strength of the rotor lamination and limited operating point, the overall drive system efficiency is relatively low. To thoroughly investigate the performance of the proposed FCS-MPDTC, the tests in Chapter 5 are expended and repeated in a commercially produced PMSM drive system.

Firstly, the model of PMSM for model predictive control is repeated in Section 6.2. In Section 6.3, the conventional DTC, conventional FCS-MPDTC and proposed FCS-MPDTC are simulated in the environment of Matlab/Simulink. In Section 6.4, above tests are experimentally repeated on the PMSM drive system controlled by a dSPACE. Finally, the quantitative analysis in terms of torque/flux ripples and drive system efficiencies are presented in Section 6.5. To make a fair comparison, the experimental results of these control methods under the similar inverter switching frequency are presented in Section 6.7.

6.2 Model of PMSM

Since the detailed model of PMSM in the *d-q* axes is derived in Chapter 4, only key equations are repeated in this section.

Voltage equations in the *d-q* axes are defined as

$$\begin{aligned} u_d &= R_s i_d + \frac{d\psi_d}{dt} - \psi_q \frac{d\theta}{dt} \\ u_q &= R_s i_q + \frac{d\psi_q}{dt} + \psi_d \frac{d\theta}{dt} \end{aligned} \tag{4.7}$$

Flux linkage equations in the *d*-*q* axes are defined as

$$\begin{aligned} \psi_d &= L_d i_d + \psi_f \\ \psi_q &= L_q i_q \end{aligned} \tag{4.8}$$

where L_d and L_q are the inductance of *d*- and *q*-axes, respectively, and ψ_f is the flux linkage generated by the permanent magnet.

It can be found that the *q*-axis flux linkage is produced by the *q*-axis stator current only. Along the *d*-axis, the flux linkage is produced by both the *d*-axis stator current and the permanent magnet on the rotor. The electrical model in (4.7) can be rewritten as

$$\begin{aligned} u_d &= R_s i_d + L_d \frac{di_d}{dt} - \omega_e L_q i_q \\ u_q &= R_s i_q + L_q \frac{di_q}{dt} + \omega_e L_d i_d + \omega_e \psi_f \end{aligned} \tag{4.9}$$

The electromagnetic torque is expressed as

$$T_e = \frac{3}{2} p \left(\psi_d i_q - \psi_q i_d \right) \tag{4.16}$$

Substituting (4.8) into (4.16), one obtains

$$\begin{aligned} T_e &= \frac{3}{2} p \left[\psi_f i_q + \left(L_d - L_q \right) i_d i_q \right] \\ &= \frac{3p|\psi_s|}{4L_d L_q} \left[2\psi_f L_q \sin\delta + |\psi_s| \left(L_d - L_q \right) \sin 2\delta \right] \end{aligned} \tag{4.17}$$

where δ is the electrical angle between the stator- and rotor-flux vectors.

As shown, the electromagnetic torque is composed of two parts: the permanent-magnet torque and the reluctance torque caused by the rotor saliency.

For a surface-mounted PMSM without saliency, the *d*- and *q*-axis inductances are equal to the synchronous inductance, i.e. $L_d = L_q = L_s$. The torque does not include the reluctance torque and can be simplified as

$$T_e = \frac{3}{2} p \psi_f i_q = \frac{3}{2} p \frac{\psi_f |\psi_s|}{L_s} \sin\delta \tag{4.18}$$

The voltage and stator-flux equations can also be simplified similarly.

In the stationary frame (the components indicated by $\alpha\beta$), they can be expressed using a complex vector as

$$u_s = R_s i_s + \frac{d\psi_s}{dt} \tag{4.19}$$

$$\psi_s = L_s i_s + \psi_r \tag{4.20}$$

where $\psi_r = \psi_f e^{j\theta_r}$.

The torque in the stationary frame can be expressed as

$$T_e = \frac{3}{2} p \psi_s \times i_s = \frac{3}{2} p (\psi_\alpha i_\beta - \psi_\beta i_\alpha) \tag{4.21}$$

6.3 Numerical Simulation

6.3.1 Setup and parameters

In this section, the PMSM is simulated in the environment of MATLAB/Simulink. In the figures below, the conventional DTC, conventional FCS-MPDTC and proposed FCS-MPDTC are abbreviated to DTC, MPDTC-8, and MPDTC-20, respectively. The block diagrams of the above control methods are illustrated in Figs. 6.3.1, 6.3.2 and 6.3.3, respectively. The parameters of motor and control system are listed in Table 6-1. The system sampling frequencies in all control method are set to 5 kHz.

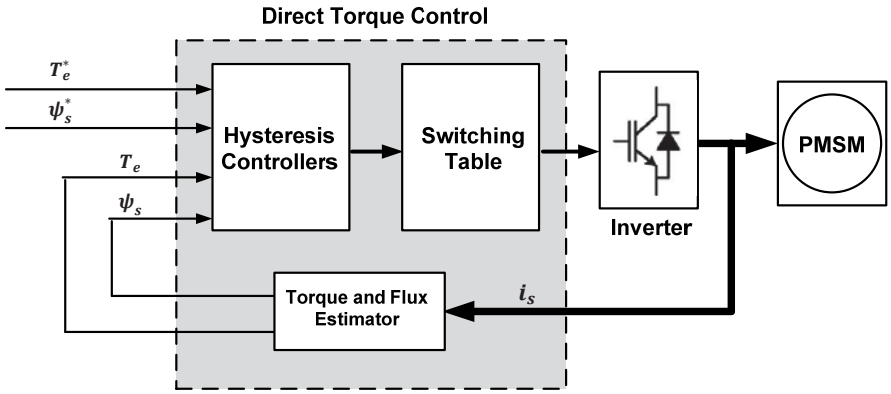

Fig. 6.3.1 Block diagram of DTC drive system

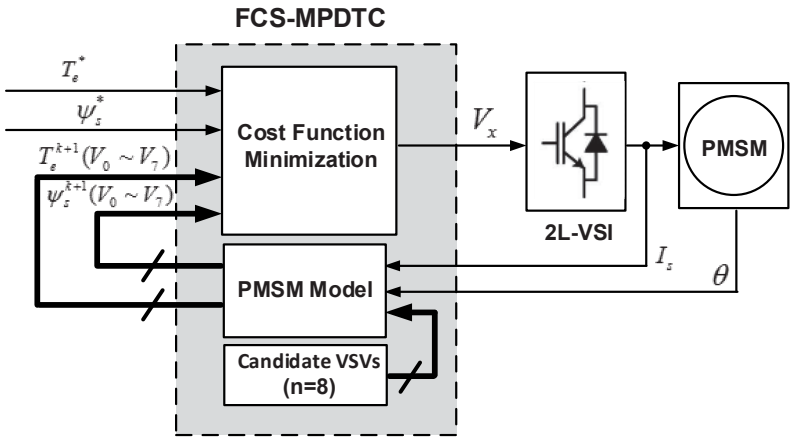

Fig. 6.3.2 Block diagram of conventional FCS-MPDTC drive system

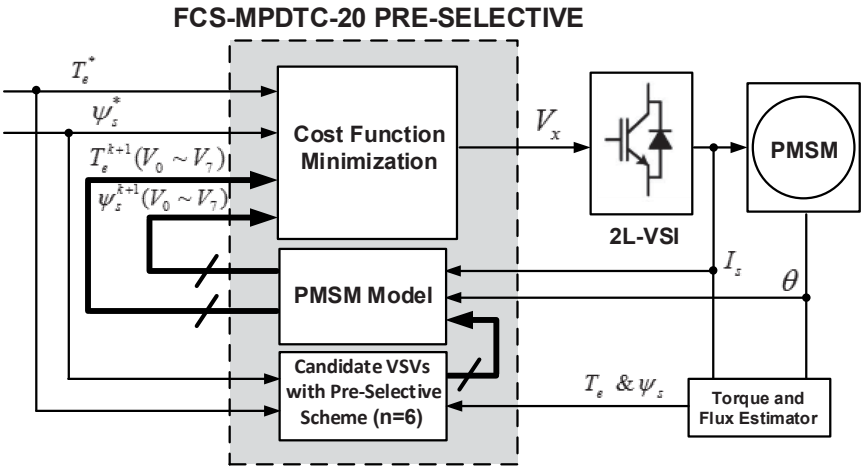

Fig. 6.3.3 Block diagram of proposed FCS-MPDTC drive system

Table 6-1 Machine and Control Parameters

Stator resistance	R_s	0.47 Ω
d-axis inductance	L_d	14.20 mH
q-axis inductance	L_q	15.90 mH
Permanent magnet flux	ψ_f	0.1057 Wb
Number of pole pairs	p	3
DC bus voltage	V_{dc}	200 V
Rated torque	T_{rated}	2 Nm
Rated speed	ω_{rated}	1000 r/min
Weighting factor of flux	k_1	19
Control system sampling frequency	f_{sys}	5 kHz

6.3.2 Combined load test

This simulation test combines start-up, steady-state and external load tests. The control system sampling frequency is 5 kHz. The motor starts up at 0s with a reference speed (400 rpm or 1000 rpm). An external load is applied at 0.15s. A segment (2-3 periods) of the stator current of phase A is used to calculate the total harmonic distortion (THD) and current harmonic spectrum. On the left hand side of each figure below, the curves are the stator current, stator flux, torque and motor speed, respectively. On the right hand side, the curves are segment of the stator current, THD and current harmonic spectrum.

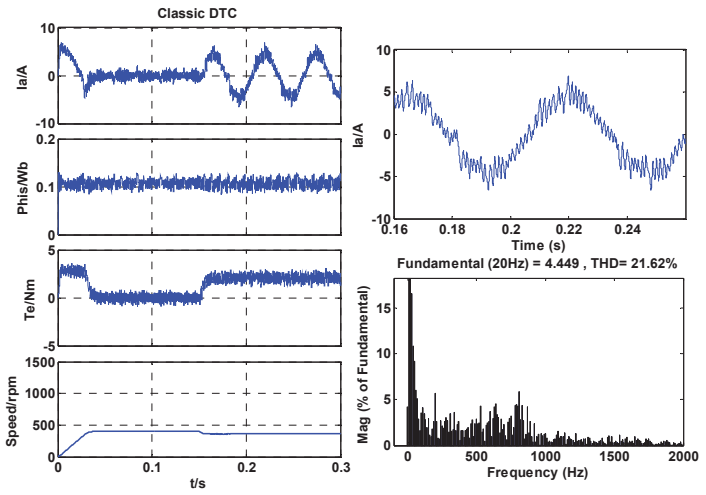

(a)

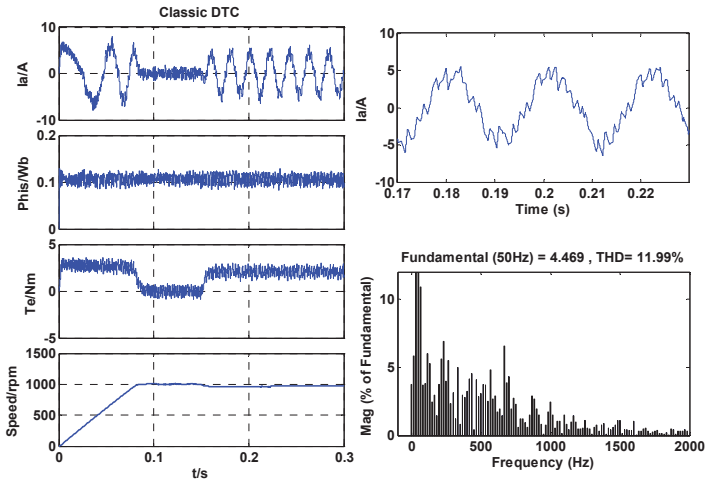

(b)

Fig. 6.3.4 Combined load test of DTC, where (a) at 400 rpm, and (b) at 1000 rpm

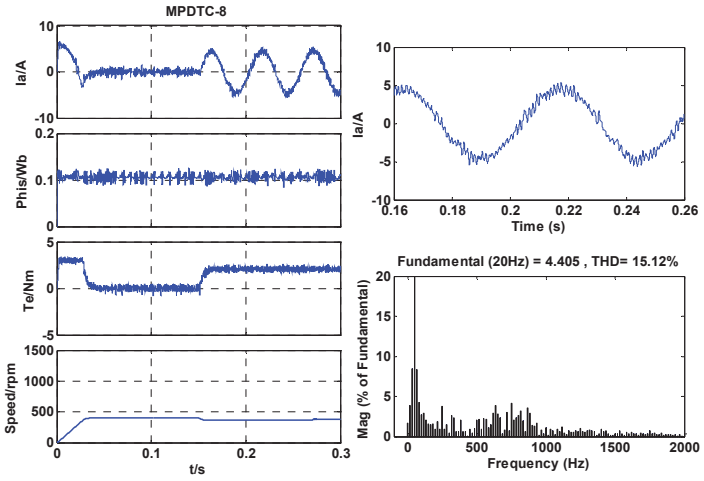

(a)

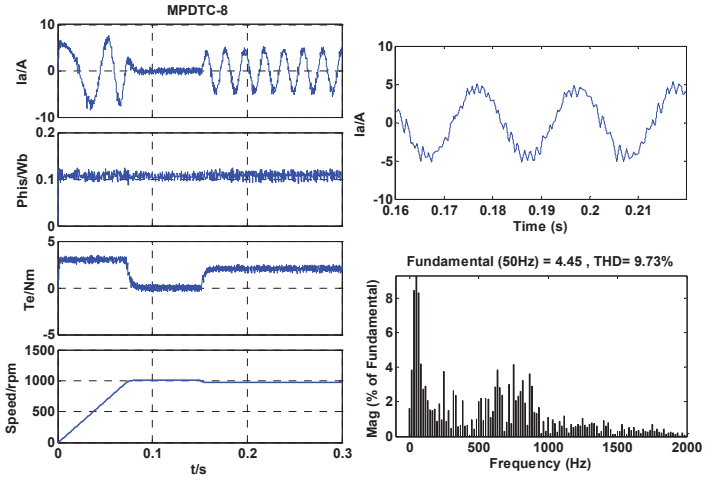

(b)

Fig. 6.3.5 Combined load test of conventional FCS-MPDTC, where (a) at 400 rpm, and (b) at 1000 rpm

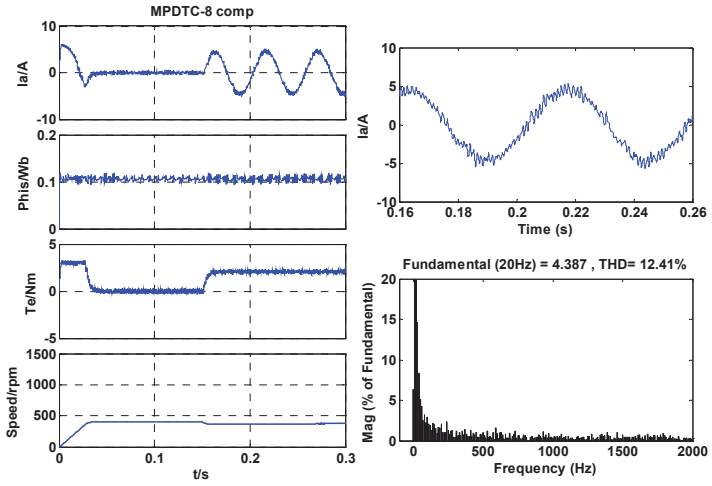

(a)

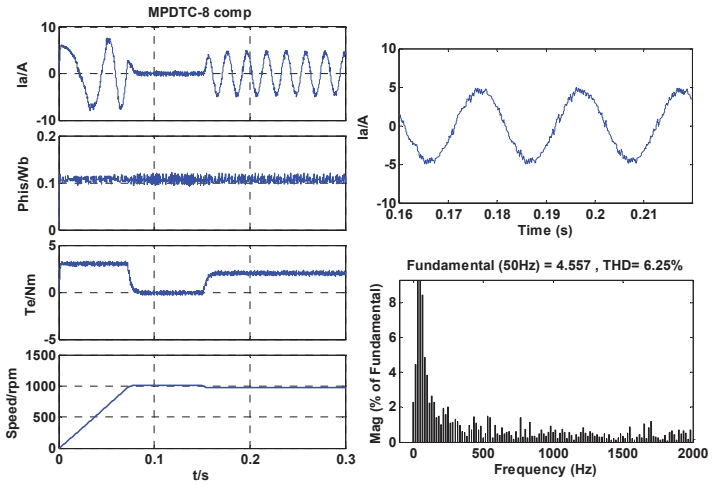

(b)

Fig. 6.3.6 Combined load test of conventional FCS-MPDTC with one-step delay compensation, where (a) at 400 rpm, and (b) at 1000 rpm

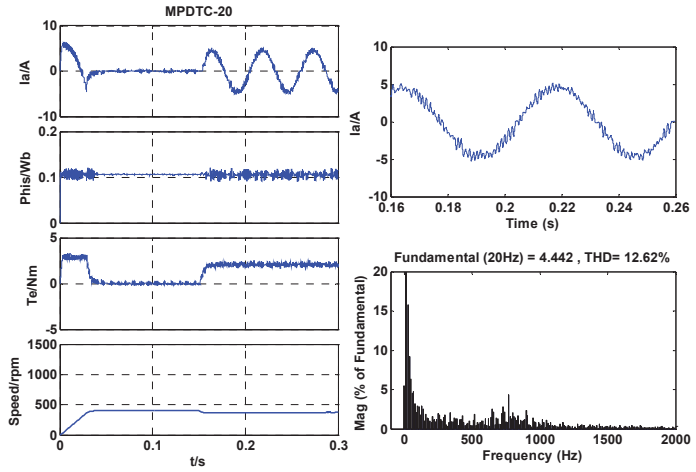

(a)

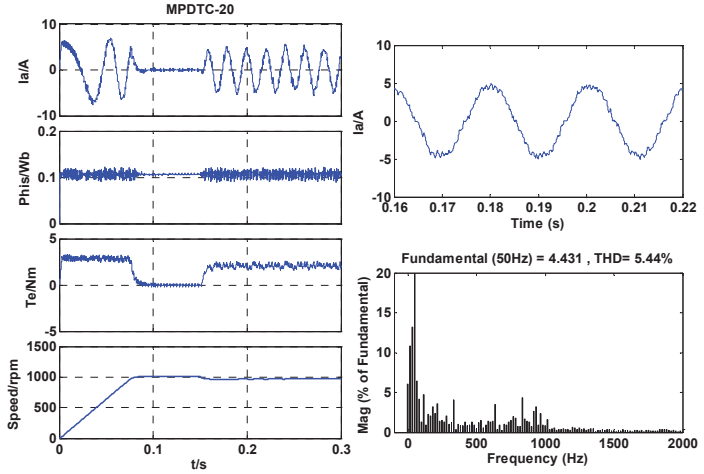

(b)

Fig. 6.3.7 Combined load test of proposed FCS, where (a) at 400 rpm, and (b) at 1000 rpm

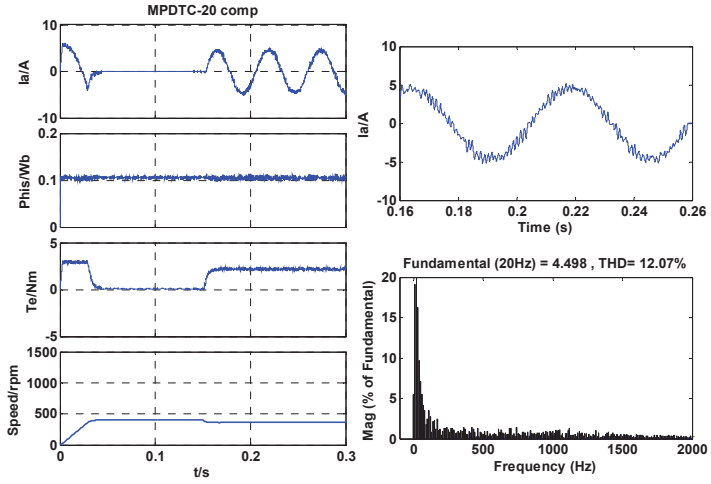

(a)

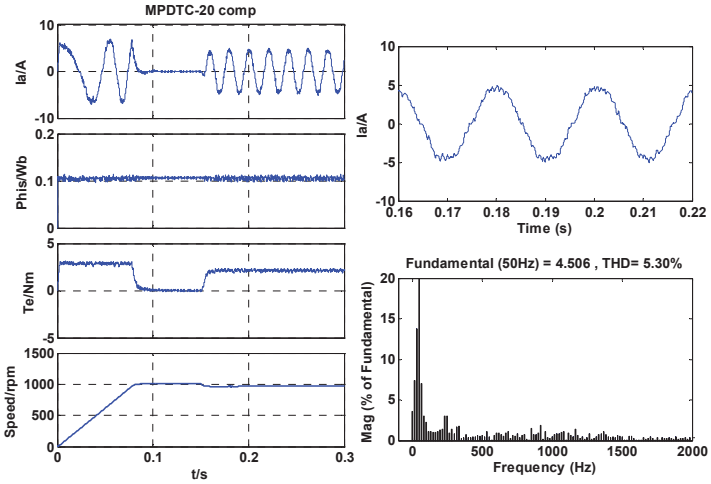

(b)

Fig. 6.3.8 Combined load test of proposed FCS-MPDTC with one-step delay compensation, where (a) at 400 rpm, and (b) at 1000 rpm

From above figures, it is shown that the implementation of FCS-MPDTC can improve the performance significantly. The proposed FCS-MPDTC achieves the lowest the stator current THD, and torque and flux ripples. With the help of the one-step delay compensation algorithm, the torque and flux ripples are further reduced. Although the dynamic responses of all control methods are similar, the steady state performance of the proposed FCS-MPDTC is better than those of DTC and conventional FCS-MPDTC.

6.4 Experimental Tests

6.4.1 Setup of experimental test platform

In addition to the simulation studies, the control methods mentioned above are experimentally tested on a two-level inverter-fed motor drive system as shown in Fig. 6.4.1. The control and motor parameters remain the same as those introduced in Table 6-1. A dSPACE DS1104 PPC/DSP control board is employed to implement the real-time algorithm coding using the C language. A three-phase intelligent power module equipped with an insulated-gate bipolar transistor (IGBT) is used as an inverter. The gating pulses are generated in the DS1104 board and then sent to the inverter. The load is applied using a programmable dynamo-meter controller DSP6000. The motor speed is obtained by an interior 2500-pulse incremental encoder. All experimental results are recorded by the ControlDesk interfaced with DS1104 and PC at 5 kHz sampling frequency.

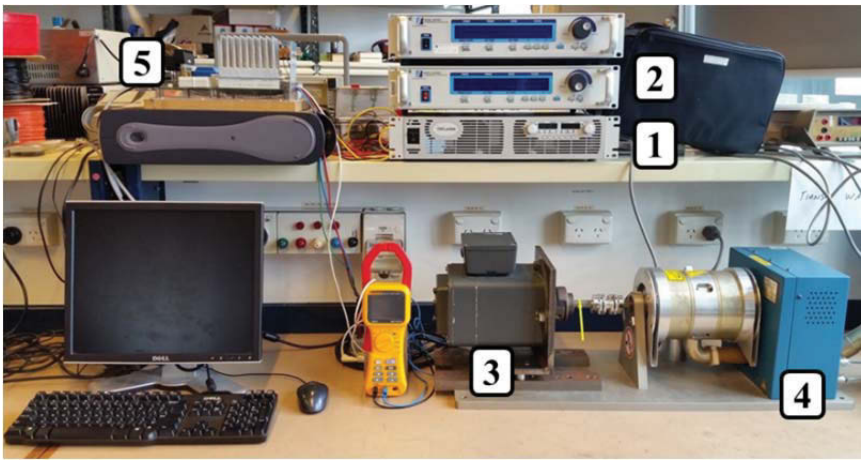

Fig. 6.4.1 Platform setup of experimental test, where (1) DC power supply, (2) dynamometer controller, (3) PMSM, (4) dynamometer and (5) dSPACE control board.

6.4.2 Steady state responses (no load and with load)

The measurements of steady-state performance are presented in this section. In the figures below, from top to bottom, the curves are the torque, stator flux and inverter switching frequency. The torque/flux ripples are defined as the standard deviation of torque/flux values. The average switching frequency is obtained by counting the total switching jumps N of six legs of two-level inverter over a fixed period of 0.05 s.

The tests are repeated under variable speed and variable load. Only a part of the test results (20% rated, 60% rated and 100% rated speed; no load and rated load) are plotted. A comprehensive quantitative analysis of test results is presented at the end of this section.

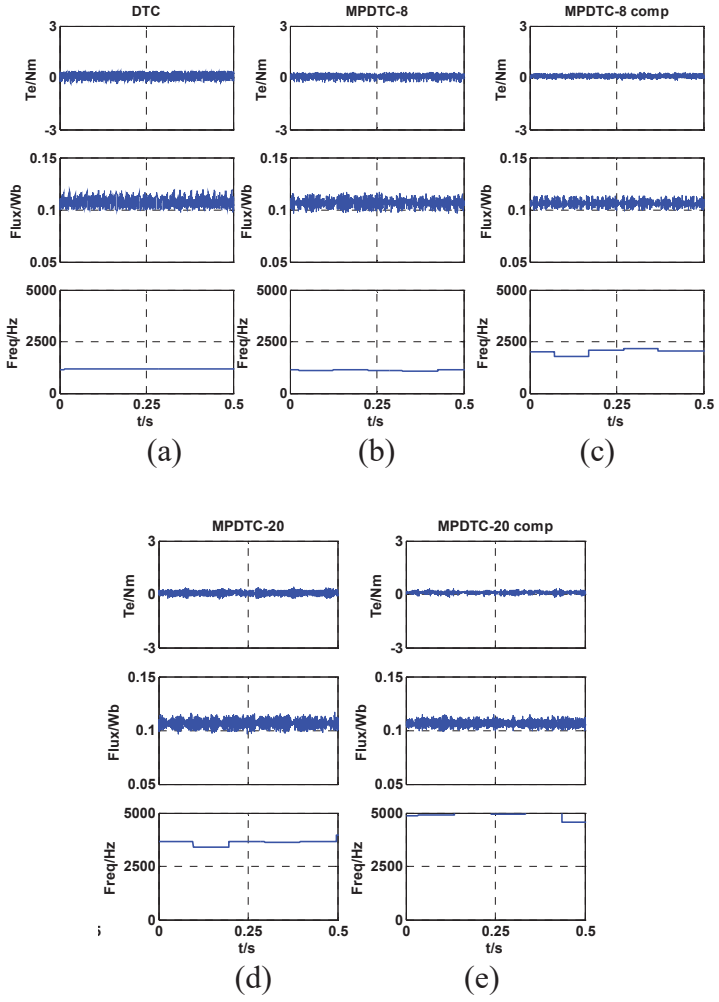

Fig. 6.4.2 Steady-state response at 200 rpm (no load) for (a) DTC, (b) MPDTC-8, (c) MPDTC-8 with one-step delay compensation, (d) MPDTC-20, and (e) MPDTC-20 with one-step delay compensation

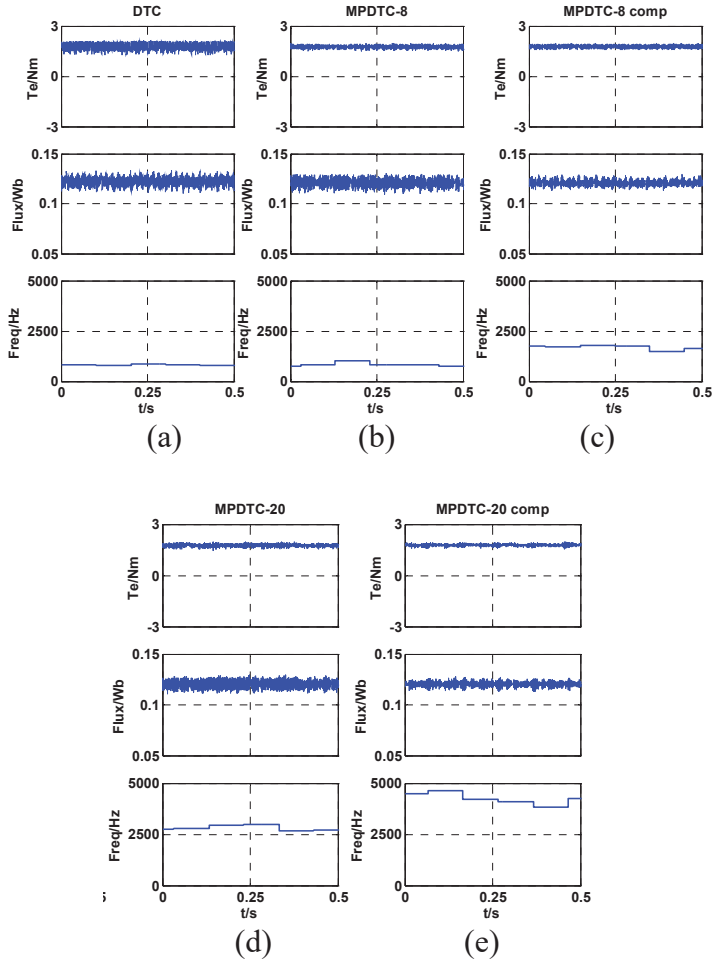

Fig. 6.4.3 Steady-state response at 200 rpm (2 Nm load) for (a) DTC, (b) MPDTC-8, (c) MPDTC-8 with one-step delay compensation, (d) MPDTC-20, and (e) MPDTC-20 with one-step delay compensation

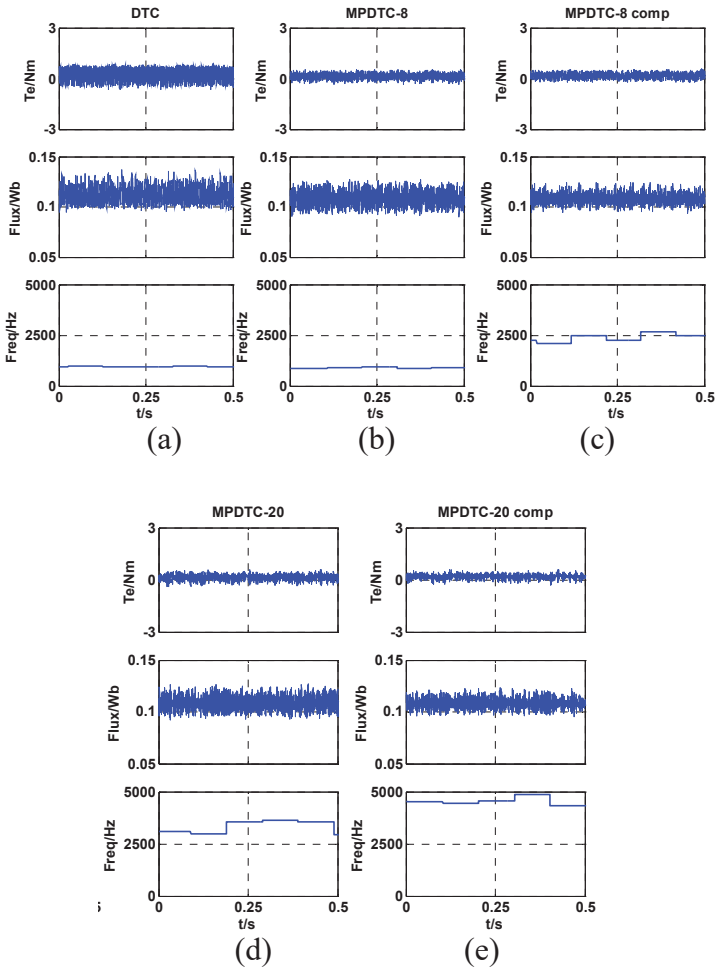

Fig. 6.4.4 Steady-state response at 600 rpm (no load) for (a) DTC, (b) MPDTC-8, (c) MPDTC-8 with one-step delay compensation, (d) MPDTC-20, and (e) MPDTC-20 with one-step delay compensation

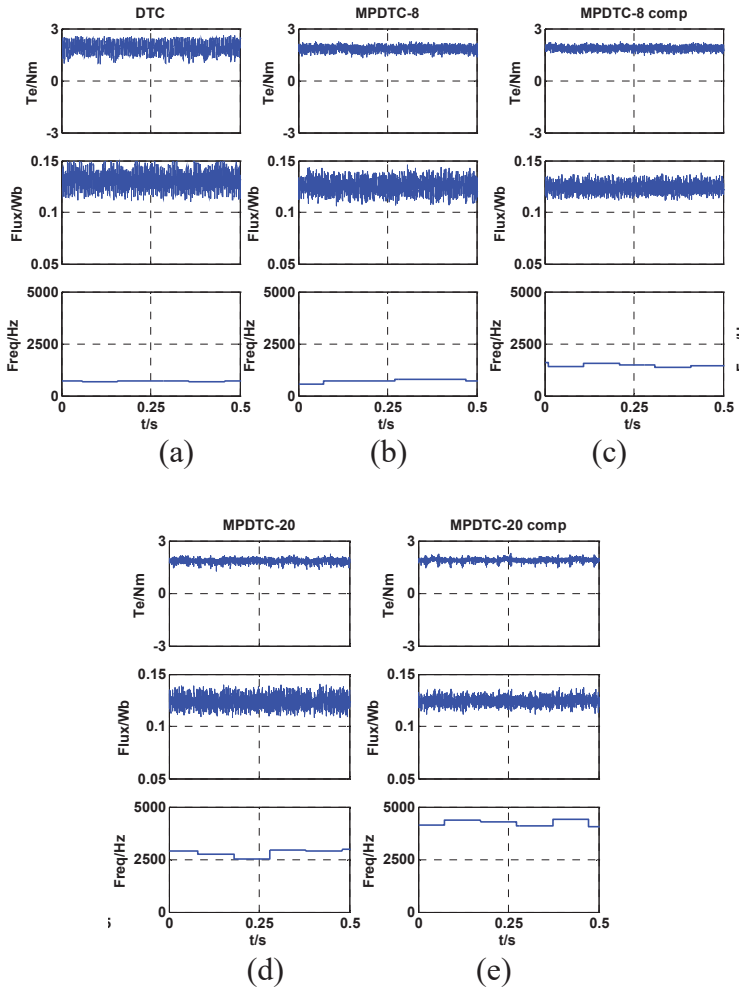

Fig. 6.4.5 Steady-state response at 600 rpm (2 Nm load) for (a) DTC, (b) MPDTC-8, (c) MPDTC-8 with one-step delay compensation, (d) MPDTC-20, and (e) MPDTC-20 with one-step delay compensation

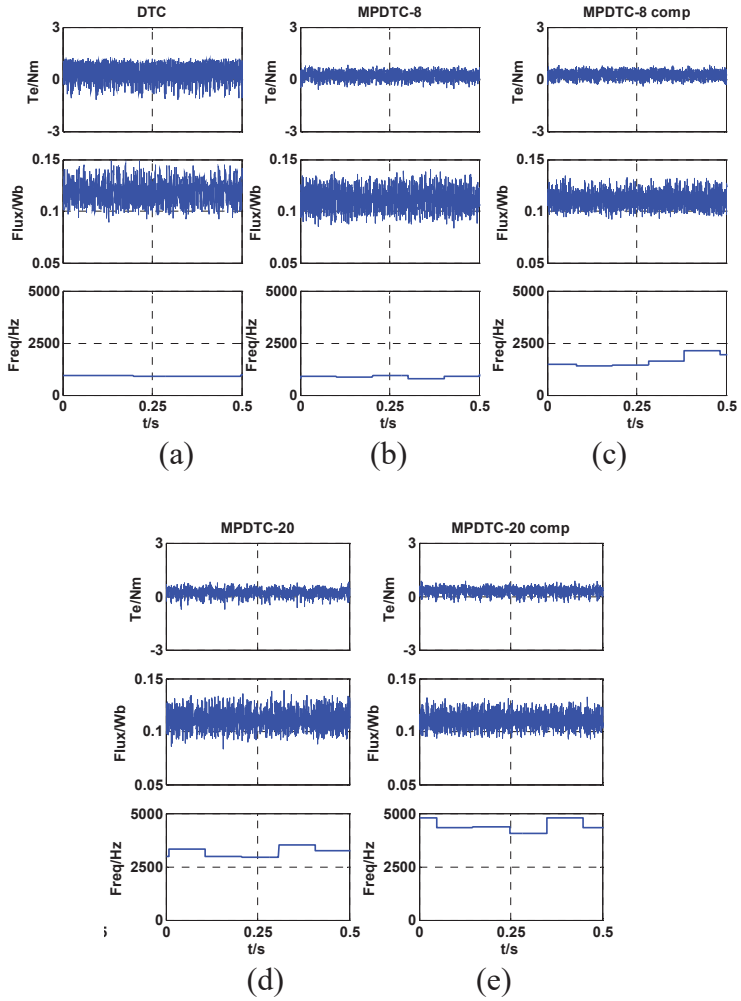

Fig. 6.4.6 Steady-state response at 1000 rpm (no load) for (a) DTC, (b) MPDTC-8, (c) MPDTC-8 with one-step delay compensation, (d) MPDTC-20, and (e) MPDTC-20 with one-step delay compensation

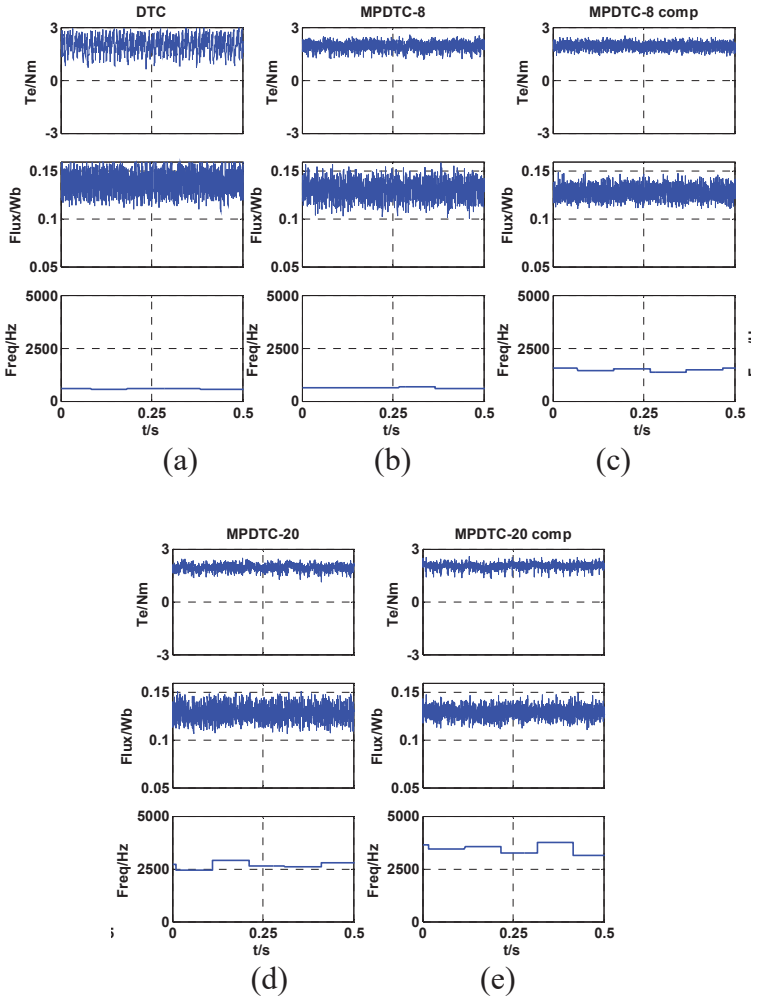

Fig. 6.4.7 Steady-state response at 1000 rpm (2 Nm load) for (a) DTC, (b) MPDTC-8, (c) MPDTC-8 with one-step delay compensation, (d) MPDTC-20, and (e) MPDTC-20 with one-step delay compensation

The experimental steady-state performance is plotted in Figs. 6.4.2- 6.4.7. It can be found that the torque and flux ripples of the proposed FCS-MPDTC are lower than those of the conventional DTC and conventional FCS-MPDTC. The implementation of one-step delay compensation can further reduce the torque and flux ripples and also an increase of switching frequency can be observed.

The quantitative index of average switching frequency, and stator flux and torque ripples for these tests will be summarized in Section 6.5.

6.4.3 Start-up tests

In this section, the start-up response is presented. By introducing a ramp-up function in the PI controller, the motor speed accelerates from 0 to 1000 rpm steadily with a small overshoot. In Fig. 6.4.8, from top to bottom, the curves shown are the stator current, stator flux, torque, and rotor speed. It is observed that whilst the dynamic responses for these methods are similar, the steady state performance of the proposed FCS-MPDTC with one-step delay compensation is the best.

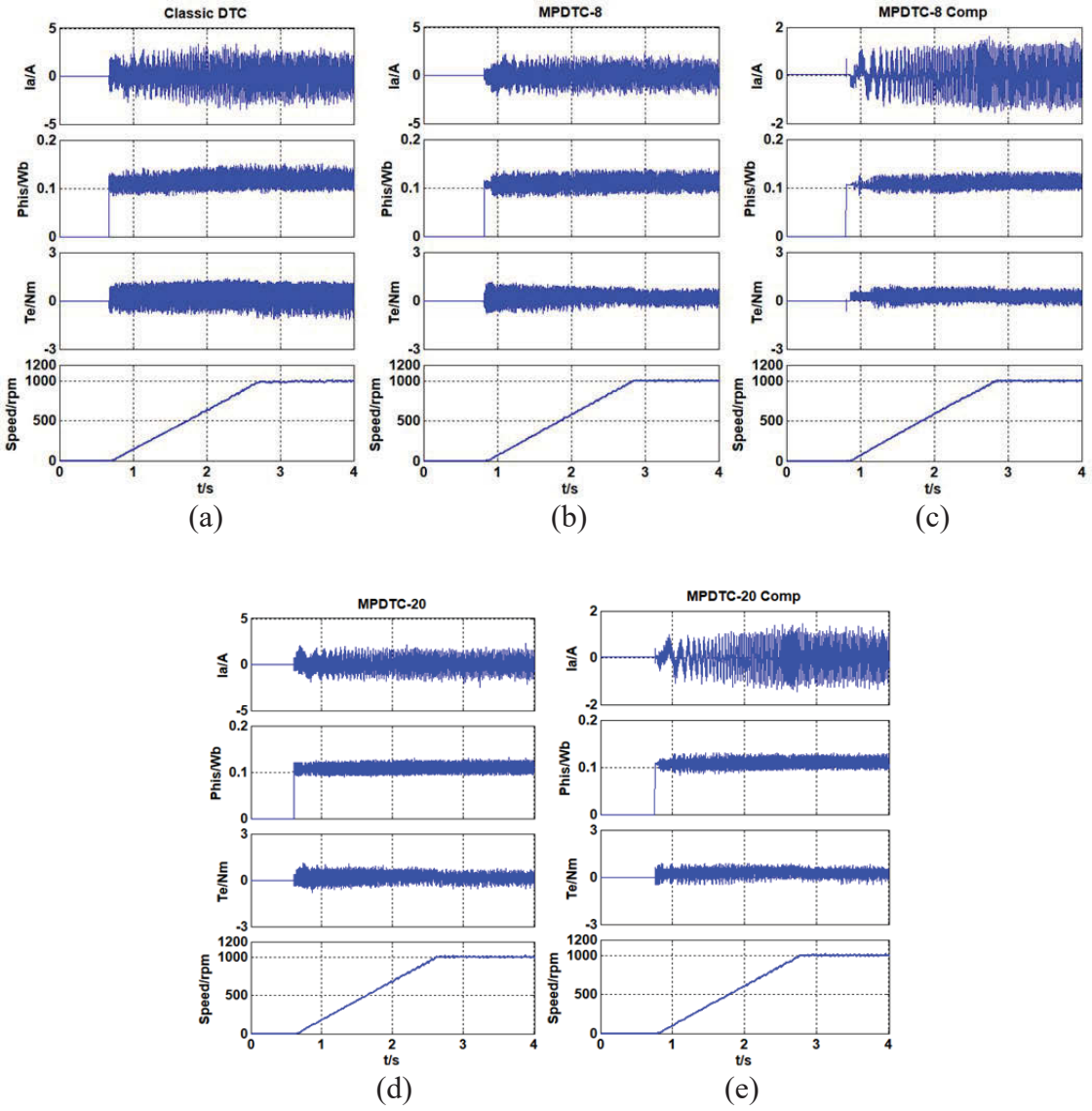

Fig. 6.4.8 Start-up response from standstill to 1000 rpm for (a) DTC, (b) MPDTC-8, (c) MPDTC-8 with one-step delay compensation, (d) MPDTC-20, and (e) MPDTC-20 with one-step delay compensation

6.4.4 Deceleration tests

In this section, the test started with a motor speed of 1000 rpm and the reference speed is set to 200 rpm at around 1s. In Fig. 6.4.7, from top to bottom, the curves are stator current, stator flux, torque and motor speed, respectively. By introducing a ramp-up function in the PI controller, all these control methods exhibited excellent performance and the motor speed decreased from 1000 rpm to 200 rpm smoothly.

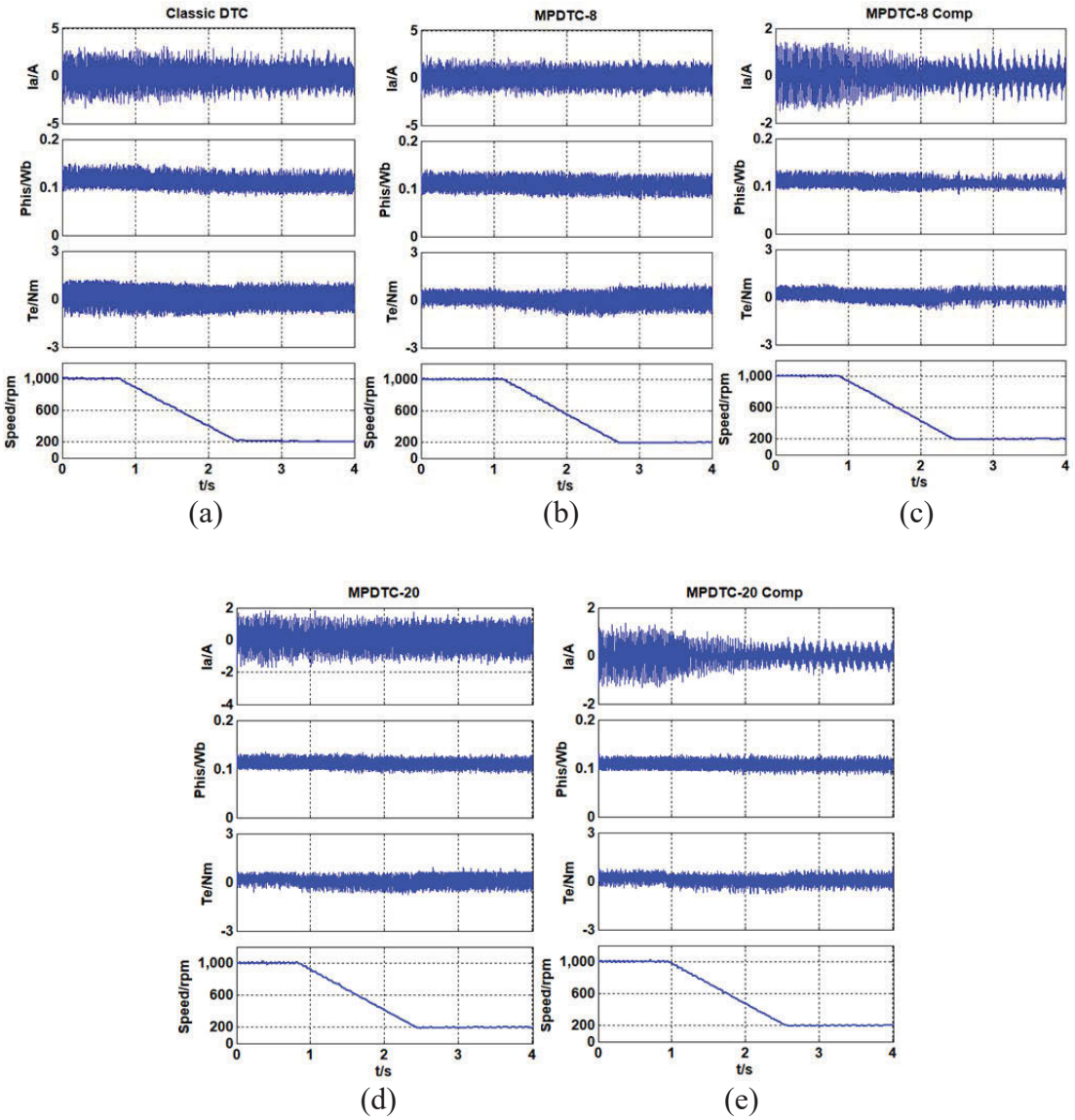

Fig. 6.4.9 Deceleration test for (a) DTC, (b) MPDTC-8, (c) MPDTC-8 with one-step delay compensation, (d) MPDTC-20, and (e) MPDTC-20 with one-step delay compensation

6.4.5 Load tests

The section presents the response to external load disturbance of these methods. The motor operates at a steady rate of 1000 rpm and a 2 Nm load is applied on the shaft. As shown in Fig. 6.4.8, all these control methods presented good dynamic performance and in a very short period, the motor speed returns to its original value due to the fast torque response.

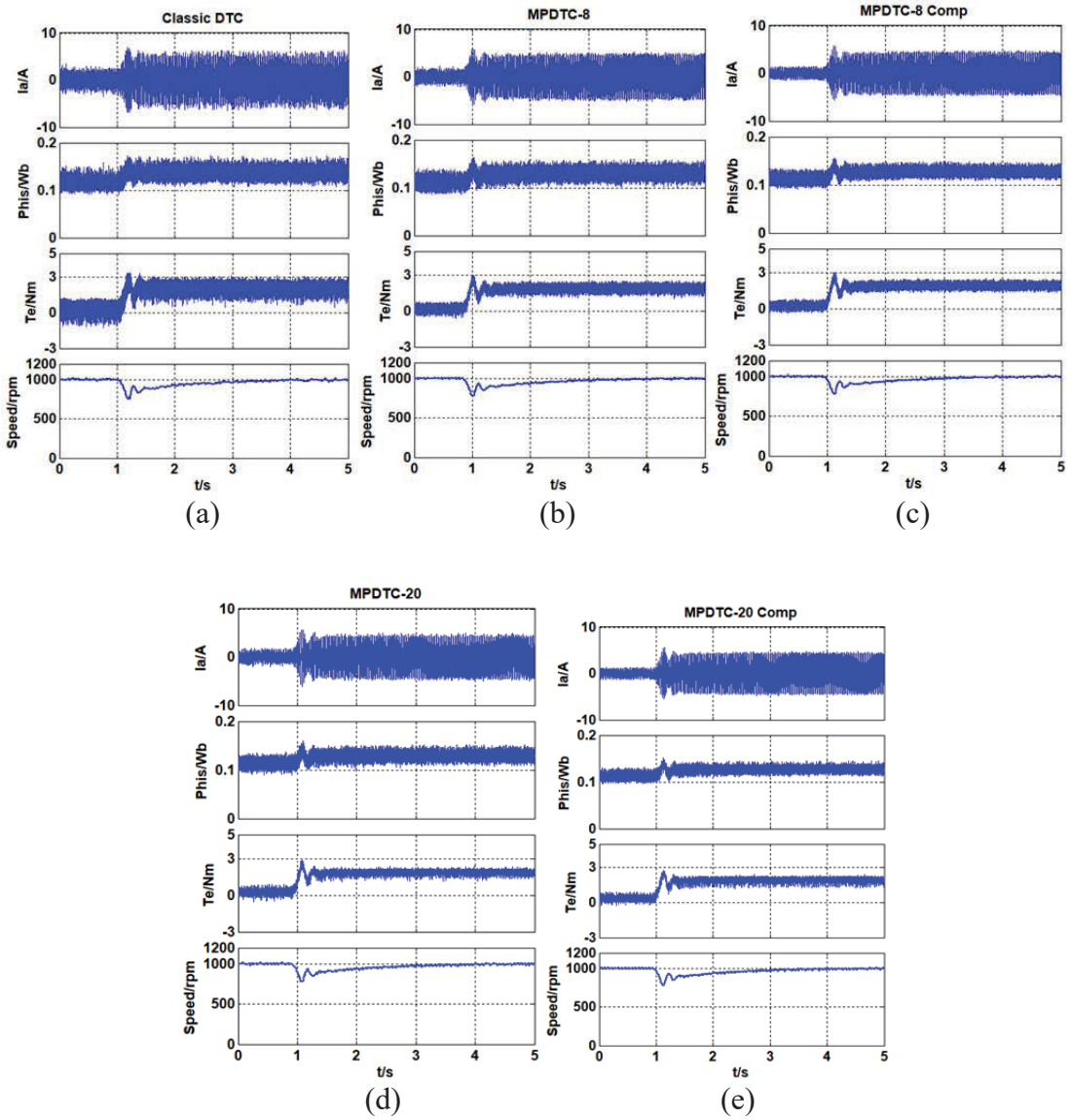

Fig. 6.4.10 Load test for (a) DTC, (b) MPDTC-8, (c) MPDTC-8 with one-step delay compensation, (d) MPDTC-20, and (e) MPDTC-20 with one-step delay compensation

6.5 Quantitative Analysis and Comparison of Control Methods

The experimental steady-state tests are repeated at different speed (from 200 to 1000 rev/min) and load settings (from 0 to 2 Nm). In the tables below, the bold horizontal columns are motor speed and the bold vertical columns are load torque. The torque/flux ripples are defined as the standard deviation of torque/flux values. The average inverter switching frequency is obtained by counting the total switching jumps N of six legs of two-level inverter over a fixed period of 0.05 s. The detailed results of steady-state experimental tests are summarised in this section.

6.5.1 Conventional DTC

The steady-state experimental tests of conventional DTC are summarized in this section.

Torque ripples

Table 6-2a Steady-state torque ripples of DTC (Unit: Nm)

		Speed (Rev/min)				
		200	**400**	**600**	**800**	**1000**
Torque (Nm)	**0**	0.1622	0.2864	0.4291	0.5680	0.7177
	0.25	0.1732	0.3006	0.4031	0.5483	0.7036
	0.5	0.1736	0.2864	0.4005	0.5310	0.6869
	0.75	0.1703	0.2812	0.3947	0.5269	0.6706
	1	0.1762	0.2733	0.3690	0.5233	0.6657
	1.25	0.1748	0.2698	0.3756	0.5148	0.6549
	1.5	0.1668	0.2574	0.3520	0.4948	0.6382
	1.75	0.1626	0.2476	0.3535	0.4910	0.6336
	2	0.1562	0.2478	0.3420	0.4846	0.6789

Flux ripples

Table 6-2b Steady-state flux ripples of DTC (Unit: Wb)

		Speed (Rev/min)				
		200	**400**	**600**	**800**	**1000**
Flux (Wb)	**0**	0.0052	0.0093	0.0129	0.0170	0.0223
	0.25	0.0054	0.0088	0.0125	0.0170	0.0217
	0.5	0.0052	0.0088	0.0120	0.0175	0.0208
	0.75	0.0054	0.0084	0.0120	0.0167	0.0205
	1	0.0052	0.0086	0.0122	0.0159	0.0202
	1.25	0.0050	0.0088	0.0117	0.0151	0.0211
	1.5	0.0052	0.0086	0.0115	0.0154	0.0205
	1.75	0.0052	0.0084	0.0115	0.0165	0.0208
	2	0.0050	0.0082	0.0115	0.0159	0.0222

Inverter switching frequencies

Table 6-2c Steady-state inverter switching frequencies of DTC (Unit: Hz)

		Speed (Rev/min)				
		200	**400**	**600**	**800**	**1000**
Switching frequency (Hz)	**0**	1494.2	1621.1	1511.4	1198.7	843.0
	0.25	1589.3	1452.7	1454.8	1115.0	907.5
	0.5	1638.9	1626.1	1173.1	1081.4	947.5
	0.75	1663.7	1457.3	1197.5	1090.2	938.0
	1	1670.6	1393.5	1142.0	1008.5	805.7
	1.25	1648.1	1266.7	1101.2	909.0	852.3
	1.5	1405.6	1248.3	999.9	901.0	797.0
	1.75	1322.9	1204.9	906.2	900.0	791.9
	2	1251.8	1059.8	917.3	831.3	672.9

6.5.2 Conventional FCS-MPDTC

The steady-state experimental tests of conventional FCS-MPDTC are summarized in this section.

Torque ripples

Table 6-3a Steady-state torque ripples of FCS-MPDTC (Unit: Nm)

		Speed (Rev/min)				
		200	**400**	**600**	**800**	**1000**
Torque (Nm)	**0**	0.1100	0.1825	0.2579	0.3230	0.3872
	0.25	0.1175	0.1916	0.2423	0.3118	0.3796
	0.5	0.1177	0.1825	0.2407	0.3019	0.3706
	0.75	0.1155	0.1792	0.2372	0.2996	0.3618
	1	0.1196	0.1742	0.2218	0.2976	0.3591
	1.25	0.1186	0.1719	0.2257	0.2927	0.3533
	1.5	0.1131	0.1641	0.2115	0.2814	0.3443
	1.75	0.1103	0.1578	0.2125	0.2792	0.3418
	2	0.1060	0.1580	0.2055	0.2755	0.3484

Flux ripples

Table 6-3b Steady-state flux ripples of FCS-MPDTC (Unit: Wb)

		Speed (Rev/min)				
		200	**400**	**600**	**800**	**1000**
Flux (Wb)	**0**	0.0048	0.0084	0.0115	0.0149	0.0192
	0.25	0.0049	0.0080	0.0111	0.0149	0.0187
	0.5	0.0048	0.0080	0.0106	0.0153	0.0179
	0.75	0.0049	0.0076	0.0106	0.0146	0.0177
	1	0.0048	0.0078	0.0109	0.0139	0.0174
	1.25	0.0046	0.0080	0.0104	0.0132	0.0182
	1.5	0.0048	0.0078	0.0102	0.0135	0.0177
	1.75	0.0048	0.0076	0.0102	0.0144	0.0179
	2	0.0046	0.0074	0.0102	0.0139	0.0188

Inverter switching frequencies

Table 6-3c Steady-state inverter switching frequencies of FCS-MPDTC (Unit: Hz)

		Speed (Rev/min)				
		200	**400**	**600**	**800**	**1000**
Switching frequency (Hz)	**0**	1575.4	1728.1	1629.0	1306.6	929.3
	0.25	1675.8	1548.6	1568.1	1215.3	1000.4
	0.5	1728.1	1733.4	1264.5	1178.8	1044.5
	0.75	1754.2	1553.5	1290.8	1188.3	1034.1
	1	1761.5	1485.5	1230.9	1099.2	888.2
	1.25	1737.8	1350.3	1186.9	990.9	939.6
	1.5	1482.1	1330.7	1077.8	982.1	878.6
	1.75	1394.9	1284.4	976.8	981.0	872.9
	2	1319.9	1129.7	988.7	906.1	750.4

6.5.3 Conventional FCS-MPDTC with one-step delay compensation

The steady-state experimental tests of conventional FCS-MPDTC with one-step delay compensation are summarized in this section.

Torque ripples

Table 6-4a Steady-state torque ripples of FCS-MPDTC with one-step delay compensation (Unit: Nm)

		Speed (Rev/min)				
		200	**400**	**600**	**800**	**1000**
Torque (Nm)	**0**	0.0973	0.1577	0.2179	0.2669	0.3132
	0.25	0.1038	0.1655	0.2047	0.2577	0.3071
	0.5	0.1041	0.1577	0.2034	0.2495	0.2998
	0.75	0.1021	0.1549	0.2004	0.2476	0.2927
	1	0.1057	0.1505	0.1874	0.2459	0.2905
	1.25	0.1048	0.1486	0.1907	0.2419	0.2858
	1.5	0.1000	0.1417	0.1787	0.2325	0.2785
	1.75	0.0975	0.1363	0.1795	0.2308	0.2765
	2	0.0937	0.1365	0.1736	0.2277	0.2760

Flux ripples

Table 6-4b Steady-state flux ripples of FCS-MPDTC with one-step delay compensation (Unit: Wb)

		Speed (Rev/min)				
		200	**400**	**600**	**800**	**1000**
Flux (Wb)	**0**	0.0039	0.0066	0.0087	0.0109	0.0136
	0.25	0.0040	0.0063	0.0084	0.0109	0.0133
	0.5	0.0039	0.0063	0.0081	0.0113	0.0127
	0.75	0.0040	0.0060	0.0081	0.0108	0.0126
	1	0.0039	0.0061	0.0083	0.0102	0.0124
	1.25	0.0037	0.0063	0.0079	0.0097	0.0129
	1.5	0.0039	0.0061	0.0078	0.0099	0.0126
	1.75	0.0039	0.0060	0.0078	0.0106	0.0127
	2	0.0037	0.0058	0.0078	0.0102	0.0130

Inverter switching frequencies

Table 6-4c Steady-state inverter switching frequencies of FCS-MPDTC with one-step delay compensation (Unit: Hz)

		Speed (Rev/min)				
		200	**400**	**600**	**800**	**1000**
Switching frequency (Hz)	**0**	2205.4	2629.3	2714.7	2406.4	1912.9
	0.25	2345.9	2356.2	2613.1	2238.3	2059.3
	0.5	2419.1	2637.5	2107.2	2171.0	2150.0
	0.75	2455.7	2363.8	2151.0	2188.5	2128.5
	1	2465.9	2260.2	2051.2	2024.5	1828.3
	1.25	2432.7	2054.5	1977.9	1824.9	1934.0
	1.5	2074.7	2024.8	1796.0	1808.8	1808.5
	1.75	1952.6	1954.3	1627.8	1806.8	1796.8
	2	1847.8	1718.9	1647.6	1668.9	1750.4

6.5.4 Proposed FCS-MPDTC

The steady-state experimental tests of proposed FCS-MPDTC are summarized in this section.

Torque ripples

Table 6-5a Steady-state torque ripples of proposed FCS-MPDTC (Unit: Nm)

		Speed (Rev/min)				
		200	**400**	**600**	**800**	**1000**
Torque (Nm)	**0**	0.0972	0.1073	0.1202	0.1353	0.1408
	0.25	0.0929	0.0981	0.1151	0.1258	0.1373
	0.5	0.0826	0.1013	0.1082	0.1283	0.1315
	0.75	0.0778	0.0935	0.1086	0.1207	0.1267
	1	0.0745	0.0914	0.1072	0.1222	0.1249
	1.25	0.0717	0.0886	0.1039	0.1123	0.1211
	1.5	0.0666	0.0849	0.1014	0.1099	0.1225
	1.75	0.0653	0.0809	0.0990	0.1117	0.1175
	2	0.0624	0.0806	0.0950	0.1104	0.1130

Flux ripples

Table 6-5b Steady-state flux ripples of proposed FCS-MPDTC (Unit: Wb)

		Speed (Rev/min)				
		200	**400**	**600**	**800**	**1000**
Flux (Wb)	**0**	0.0031	0.0041	0.0051	0.0058	0.0061
	0.25	0.0031	0.0040	0.0049	0.0058	0.0061
	0.5	0.0032	0.0040	0.0049	0.0054	0.0059
	0.75	0.0032	0.0042	0.0048	0.0055	0.0059
	1	0.0031	0.0040	0.0049	0.0054	0.0059
	1.25	0.0032	0.0040	0.0049	0.0053	0.0059
	1.5	0.0032	0.0041	0.0048	0.0051	0.0059
	1.75	0.0031	0.0040	0.0046	0.0054	0.0056
	2	0.0031	0.0039	0.0047	0.0051	0.0054

Inverter switching frequencies

Table 6-5c Steady-state inverter switching frequencies of proposed FCS-MPDTC (Unit: Hz)

		Speed (Rev/min)				
		200	**400**	**600**	**800**	**1000**
Switching frequency (Hz)	**0**	3024.0	2736.5	2599.1	2381.8	2275.7
	0.25	2989.6	2776.5	2345.5	2410.6	2393.5
	0.5	3001.1	2638.6	2442.2	2293.3	2244.4
	0.75	2959.8	2611.9	2348.6	2299.4	2123.8
	1	2913.2	2477.4	2524.0	2404.1	2186.7
	1.25	2640.4	2462.9	2308.0	2433.5	2205.3
	1.5	2481.5	2386.9	2278.5	2190.9	2081.4
	1.75	2514.7	2462.5	2214.0	2043.1	2028.3
	2	2369.9	2454.8	2176.4	2079.1	1809.1

6.5.5 Proposed FCS-MPDTC with one-step delay compensation

The steady-state experimental tests of proposed FCS-MPDTC with one-step delay compensation are summarized in this section.

Torque ripples

Table 6-6a Steady-state torque ripples of proposed FCS-MPDTC with one-step delay compensation (Unit: Nm)

		Speed (Rev/min)				
		200	**400**	**600**	**800**	**1000**
Torque (Nm)	**0**	0.0601	0.0800	0.0960	0.1081	0.1287
	0.25	0.0575	0.0749	0.0890	0.1095	0.1283
	0.5	0.0595	0.0713	0.0883	0.1062	0.1234
	0.75	0.0518	0.0714	0.0878	0.1092	0.1213
	1	0.0509	0.0685	0.0908	0.1066	0.1179
	1.25	0.0466	0.0725	0.0872	0.1078	0.1191
	1.5	0.0492	0.0693	0.0867	0.1095	0.1156
	1.75	0.0479	0.0700	0.0856	0.0980	0.1135
	2	0.0479	0.0637	0.0838	0.0961	0.1073

Flux ripples

Table 6-6b Steady-state flux ripples of proposed FCS-MPDTC with one-step delay compensation (Unit: Wb)

		Speed (Rev/min)				
		200	**400**	**600**	**800**	**1000**
Flux (Wb)	**0**	0.0026	0.0037	0.0040	0.0044	0.0051
	0.25	0.0026	0.0034	0.0038	0.0046	0.0052
	0.5	0.0025	0.0033	0.0039	0.0046	0.0048
	0.75	0.0024	0.0033	0.0036	0.0042	0.0047
	1	0.0023	0.0030	0.0037	0.0042	0.0046
	1.25	0.0022	0.0031	0.0035	0.0043	0.0045
	1.5	0.0022	0.0029	0.0034	0.0043	0.0044
	1.75	0.0021	0.0028	0.0033	0.0038	0.0043
	2	0.0021	0.0028	0.0033	0.0038	0.0040

Inverter switching frequencies

Table 6-6c Steady-state inverter switching frequencies of proposed FCS-MPDTC with one-step delay compensation (Unit: Hz)

		Speed (Rev/min)				
		200	**400**	**600**	**800**	**1000**
Switching frequency (Hz)	**0**	4317.4	3756.2	3521.0	3329.1	3138.4
	0.25	3909.0	3865.7	3515.8	3316.1	2969.2
	0.5	3900.8	3949.5	3344.0	3175.9	3153.2
	0.75	4267.9	3709.9	3327.9	3231.9	3126.4
	1	4034.8	3579.5	3361.7	3204.4	3154.2
	1.25	3960.6	3448.2	3205.2	3185.0	2963.3
	1.5	3650.9	3359.4	3290.7	3304.8	2980.7
	1.75	3550.5	3393.5	3313.0	3043.1	2685.6
	2	3549.8	3461.1	3289.3	2886.3	2335.5

6.5.6 Analysis of torque/flux ripples and inverter switching frequencies

The torque/flux ripples and inverter switching frequencies of each control method are compared in following charts.

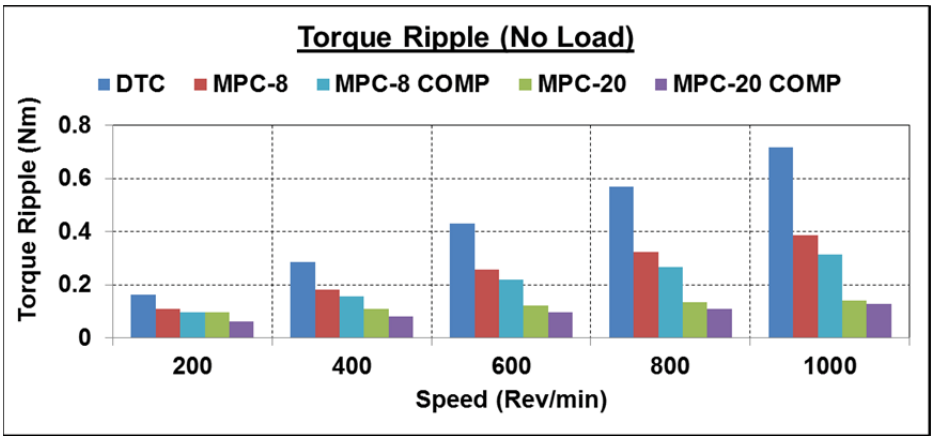

(a)

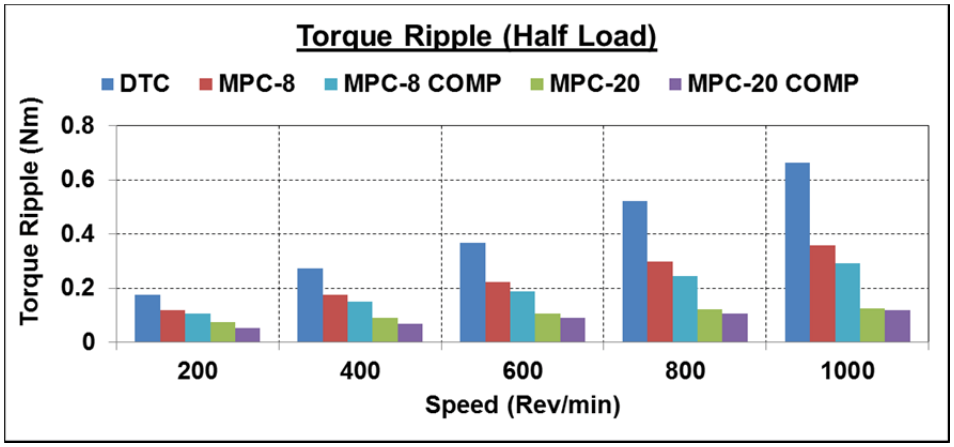

(b)

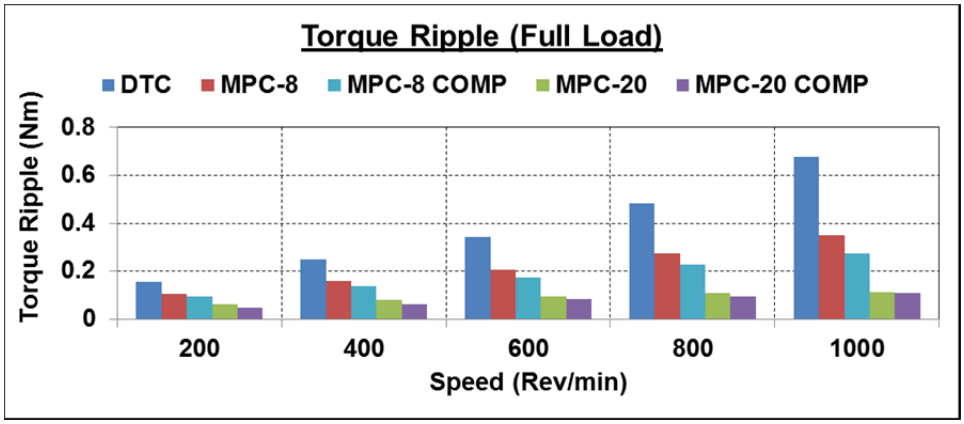

(c)

Fig. 6.5.1 Comparison of torque ripples in different control methods under (a) no load, (b) half load, and (c) full load conditions

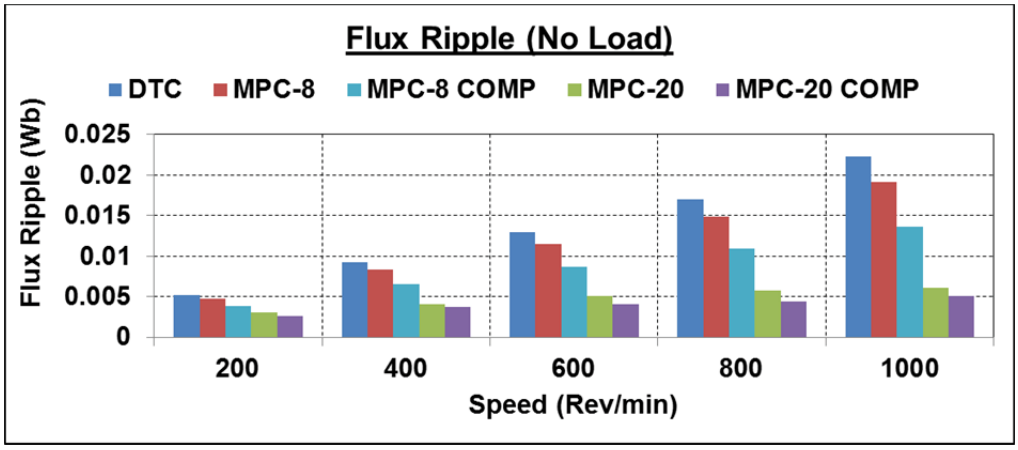

(a)

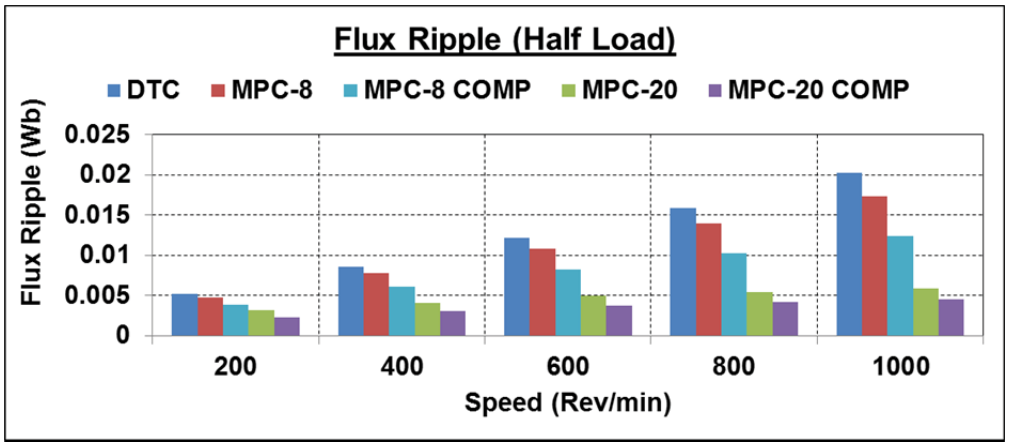

(b)

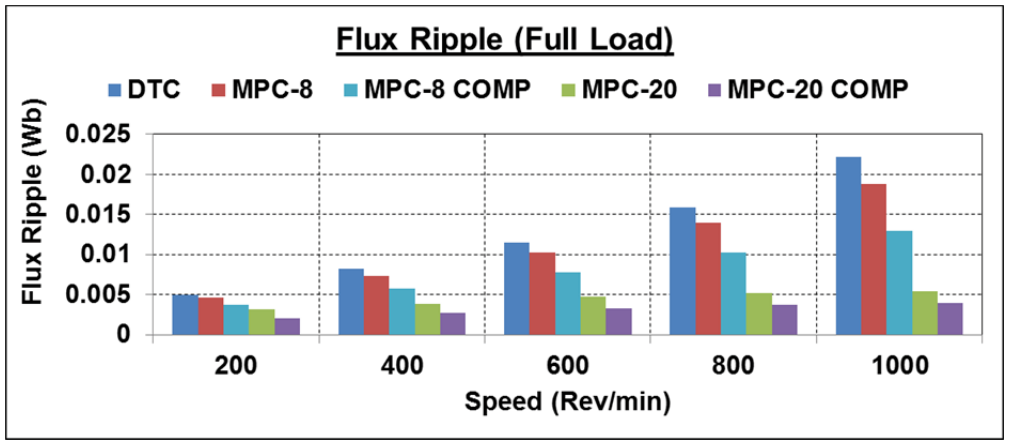

(c)

Fig. 6.5.2 Comparison of flux ripples in different control methods under (a) no load, (b) half load, and (c) full load conditions

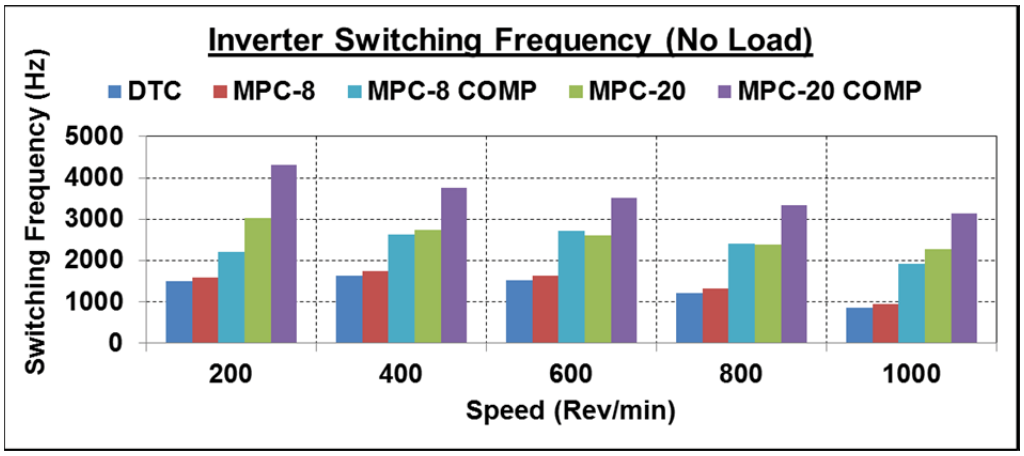

(a)

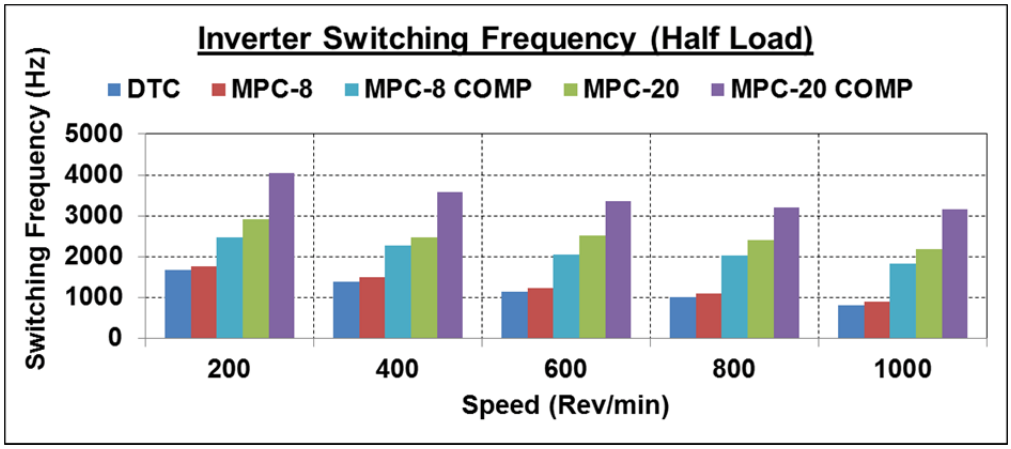

(b)

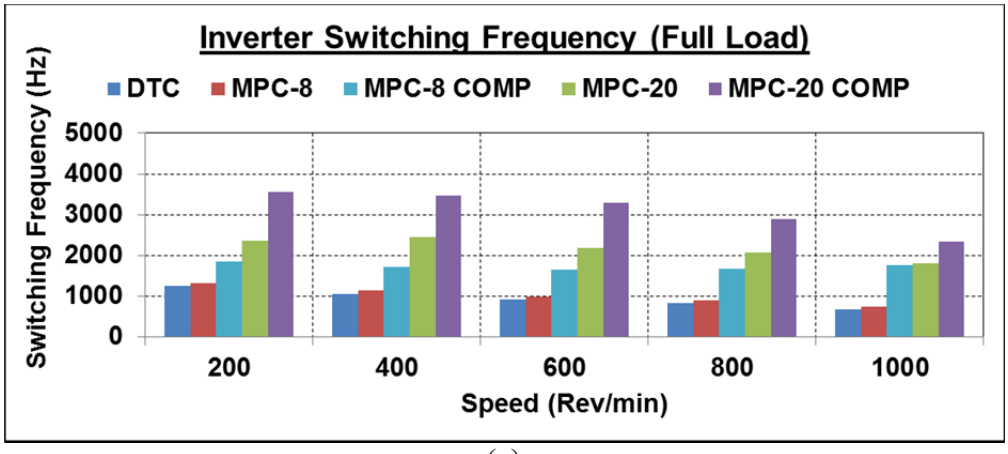

(c)

Fig. 6.5.2 Comparison of inverter switching frequencies in different control methods under (a) no load, (b) half load, and (c) full load conditions

6.5.7 Drive system efficiency

The drive system efficiency is introduced to evaluate the performance of the algorithms. The drive system efficiency is defined as

$$\eta_{sys} = P_{em} / P_{dc} \tag{5.11}$$

where η_{sys} is the drive system efficiency, P_{out} the output power measured by the dynamo-meter, and P_{dc} the power output of DC power supply. The experimental drive system efficiency contours are presented in Figs. 6.5.3-6.5.7. The speed is varied from 20% rated speed to 100% rated speed and the load torque is varied from 0% rated torque to 100% rated torque.

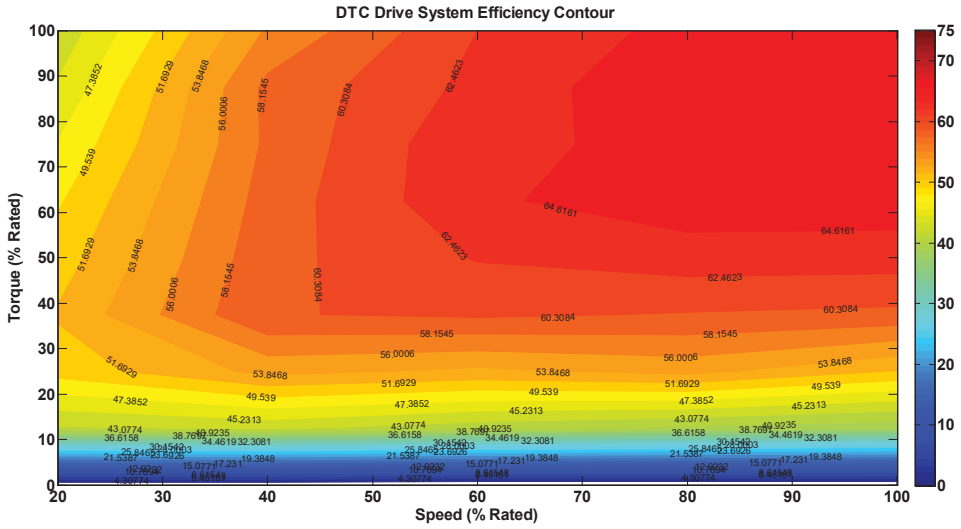

Fig. 6.5.3 Drive system efficiency contour of DTC

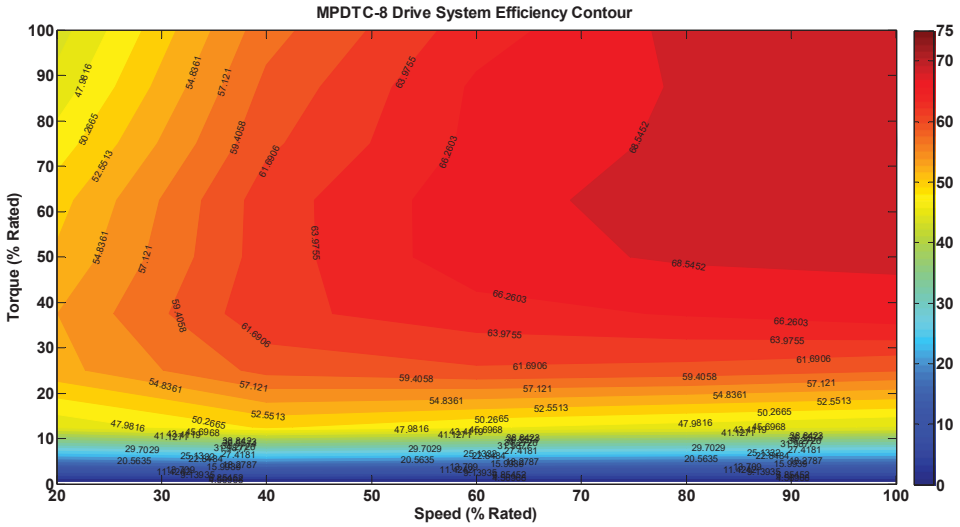

Fig. 6.5.4 Drive system efficiency contour of conventional FCS-MPDTC

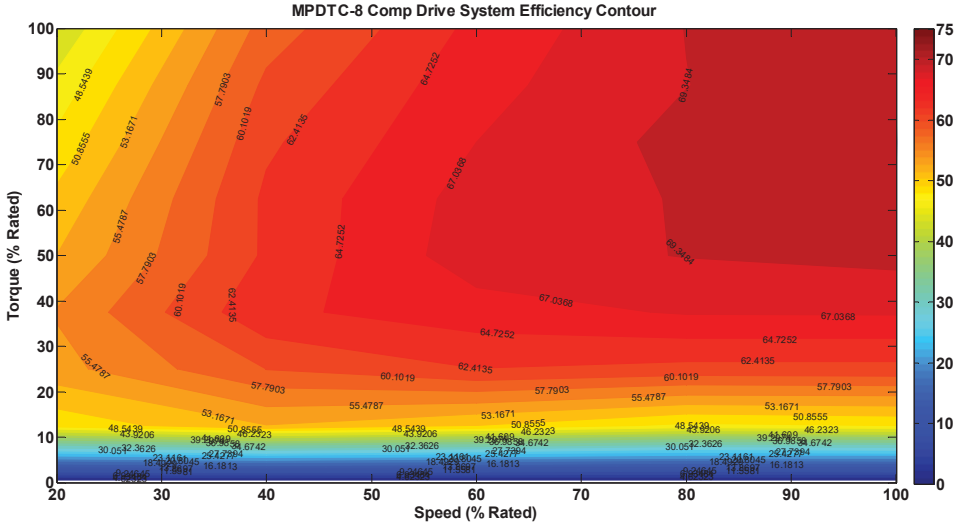

Fig. 6.5.5 Drive system efficiency contour of conventional FCS-MPDTC with one-step delay compensation

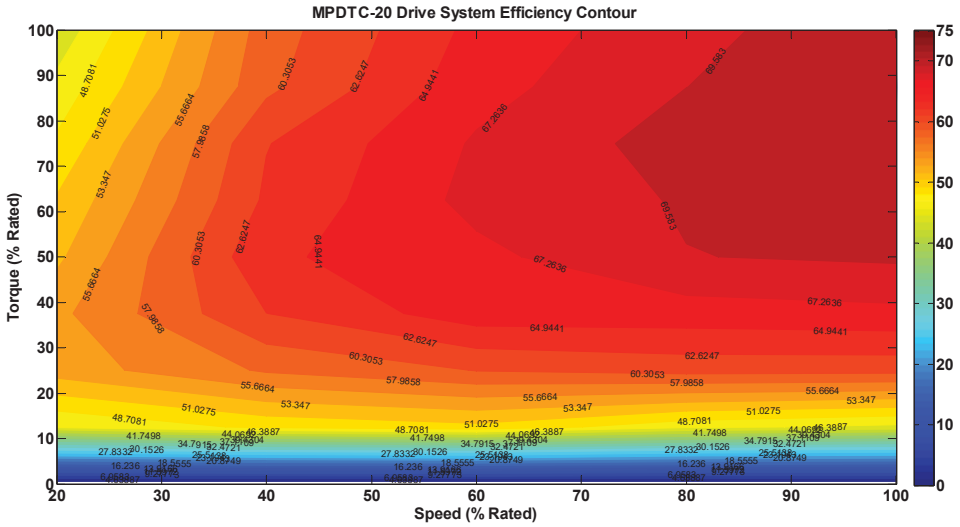

Fig. 6.5.6 Drive system efficiency contour of proposed FCS-MPDTC

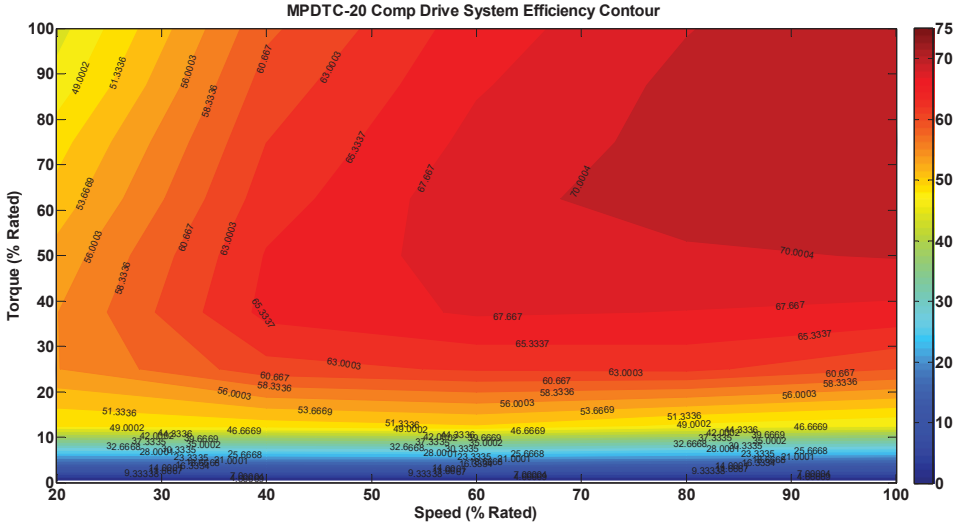

Fig. 6.5.7 Drive system efficiency contour of proposed FCS-MPDTC with one-step delay compensation

6.5.8 Discussion of the test results

The simulation and experimental tests results listed above are discussed below in detail:

- **Conventional FCS-MPDTC vs. Conventional DTC**

From the experimental tests results, it is seen that the implementation of FCS-MPDTC can reduce the flux and torque ripples by 7.69% and 32.18% at 200 rpm under no load, 8.00% and 32.14% at 200 rpm under full load, 10.85% and 39.90% at 600 rpm under no load, 11.30% and 39.91% at 600 rpm under full load, 13.90% and 46.05% at 1000 rpm under no load, and 15.32% and 48.68% at 1000 rpm under full load, respectively.

In conclusion, the conventional FCS-MPDTC can achieve lower torque and flux ripples than that of DTC as proven by both the simulation and experimental results. The highest drive system efficiency of the conventional DTC and conventional FCS-MPDTC are 66.77% and 70.83%, respectively. The conventional FCS-MPDTC presents higher drive system efficiency in all regions and wider high-efficiency range than conventional DTC.

- **Conventional FCS-MPDTC +comp vs. Conventional FCS-MPDTC**

From the experimental test results, it is seen that the implementation of one-step delay compensation can reduce the flux and torque ripples by 18.75% and 11.55% at 200 rpm under no load, 19.56% and 11.60% at 200 rpm under full load, 24.35% and 15.51% at 600 rpm under no load, 23.53% and 15.52% at 600 rpm under full load, 29.17% and 19.11% at 1000 rpm under no load, and 30.85% and 20.78% at 1000 rpm under full load, respectively.

With the help of one-step delay compensation, the steady-state performance of the conventional FCS-MPDTC is improved significantly. It should be noticed that the switching frequency almost increase by 2-3 times in most tests when the one-step delay is compensated. The highest drive system efficiency of the conventional FCS-MPDTC and conventional FCS-MPDTC with one-step delay compensation are 70.83% and 71.66%, respectively. It is seen that the implementation of one-step delay compensation can increase the efficiency in most operational regions. However, a slight decrease of

efficiency is noticed at the high-speed high-load region.

- **Proposed FCS-MPDTC vs. Conventional FCS-MPDTC**

From the experimental test results, it is seen that the proposed FCS-MPDTC can reduce the flux and torque ripples by 35.42% and 11.64% at 200 rpm under no load, 32.61% and 41.13% at 200 rpm under full load, 55.65% and 53.39% at 600 rpm under no load, 53.92% and 53.77% at 600 rpm under full load, 68.23% and 63.64% at 1000 rpm under no load, and 71.28% and 67.57% at 1000 rpm under full load, respectively.

As shown in the above test analysis, the introduction of the proposed method can effectively reduce the torque and flux ripples. A noticeable increase of inverter switching frequency is also observed. The highest drive system efficiency of the proposed FCS-MPDTC and conventional FCS-MPDTC are 71.90% and 70.83%, respectively. The proposed FCS-MPDTC presents higher drive system efficiency in all regions and wider high-efficiency range than the conventional FCS-MPDTC.

- **Proposed FCS-MPDTC +comp vs. Conventional FCS-MPDTC +comp**

From the experimental test results, it is seen that the implementation of the proposed method can reduce the flux and torque ripples by 33.33% and 38.23% at 200 rpm under no load, 43.24% and 48.88% at 200 rpm under full load, 54.02% and 55.94% at 600 rpm under no load, 57.69% and 51.73% at 600 rpm under full load, 62.5% and 58.91% at 1000 rpm under no load, and 69.23% and 61.12% at 1000 rpm under full load, respectively.

The performance of the proposed FCS-MPDTC is better than that of the conventional FCS-MPDTC in the high-speed and high-load region. The highest drive system efficiency of proposed FCS-MPDTC and conventional FCS-MPDTC are 72.33% and 71.66%, respectively. The proposed FCS-MPDTC presents slightly higher drive system efficiency than the conventional FCS-MPDTC in all regions.

6.6 Experimental Tests at Same Switching Frequency

The simulation and experimental tests presented above are all conducted under the same control system sampling frequency (5 kHz). Due to the nature of the DTC algorithm, the inverter switching frequencies of these control methods are varied in a wide range (from several hundred to several thousand Hz). To achieve a fair comparison, the inverter switching frequencies of these control methods should be maintained at a similar level and the control system sampling frequencies of each method need to be adjusted accordingly. From quantitative analysis in Section 6.5.6, it is seen that the inverter switching frequency varies not only with the control methods, but also with the speed and load settings. As a result, it will be extremely difficult and complex to conduct all the tests under the similar inverter switching frequency. To thoroughly investigate the effectiveness of proposed MPC method, only one set of experimental tests (100% rated speed and 100% rated load) are performed under the similar inverter switching frequency.

Based on extensive numerical simulation and experimental tests, the control system sampling frequencies of the conventional DTC, conventional FCS-MPDTC, and proposed FCS-MPDTC are set to 7 kHz, 7 kHz, and 5 kHz, respectively. The one-step delay compensation is applied to all methods and all tests are carried out in the same platform introduced in Fig. 6.4.1.

6.6.1 Steady state responses (no load and with load)

The measurements of steady-state performance at the rated speed and rated load are shown in Fig. 6.6.1. From the top to bottom, the curves are the torque, stator flux, and inverter switching frequency, respectively. A quantitative comparison of these three control methods is shown in Table 6-7. The torque/flux ripples, total harmonic distortion (THD) of phase current and average switching frequency are calculated based on the results from 0.15s to 0.25s. The torque/flux ripples are defined as the standard deviation of torque/flux values. The average switching frequency is obtained by counting the total switching jumps N of six legs of two-level inverter over a fixed period of 0.05 s.

Under the similar average switching frequency, a significant reduction of torque and

flux ripples is observed in the proposed method. Compared with the conventional DTC and conventional FCS-MPDTC, the proposed method presents a torque ripple reduction of 69.2% and 53.5% and a flux ripple reduction of 69.2% and 68.1%, respectively.

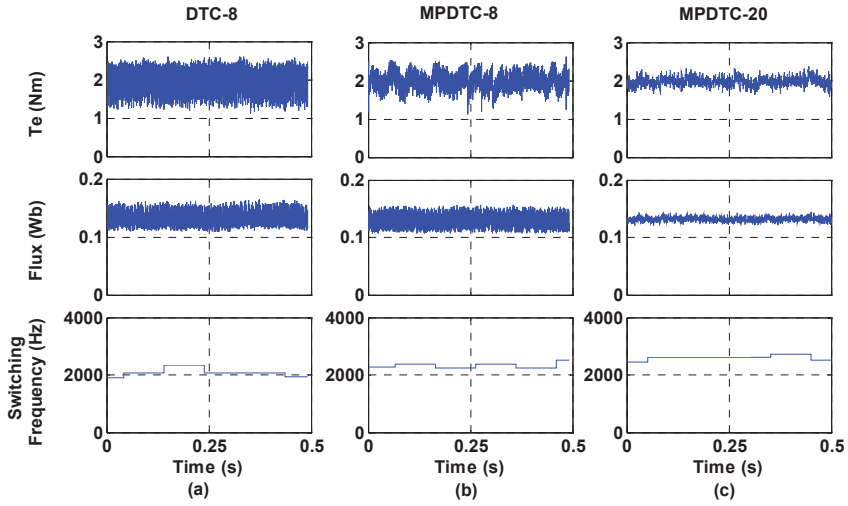

Fig. 6.6.1 Experimental steady-state response at rated speed and load, where (a) conventional DTC, (b) conventional FCS-MPDTC, and (c) proposed FCS-MPDTC

Table 6-7 Quantitative Comparison of Experimental Results

Method	**Torque Ripple T_{rip} (Nm)**	**Flux Ripple ψ_{rip} (Wb)**	**Average Switching Frequency f_{av} (Hz)**
DTC-8 comp	0. 3482	0.0117	2182.1
MPDTC-8 comp	0. 2310	0.0113	2281.8
MPDTC-20 comp	0.1073	0.0040	2335.5

6.6.2 Dynamic performance

The experimental measurements of no-load starting tests, external load tests, and no-load decelerating tests are shown in Fig. 6.6.2, Fig. 6.6.3 and Fig. 6.6.4, respectively. From top to bottom, the horizontal axes are the stator current, stator flux, torque, and motor speed. In the no-load starting and decelerating tests, a ramp-up function is introduced to regulate the variation rate of the reference speed. In Fig. 6.6.2, the motor starts from stand still and then reaches the rated speed. In Fig. 6.6.3, the motor is running at 1000 rpm when a 2 Nm external load is applied to the shaft. In Fig. 6.6.4, the motor speed starts from 1000 rpm and then decreases to 200 rpm. It can be seen that the

dynamic responses of all three methods are similar. However, the flux and torque ripples of the proposed method are smaller than the other two methods.

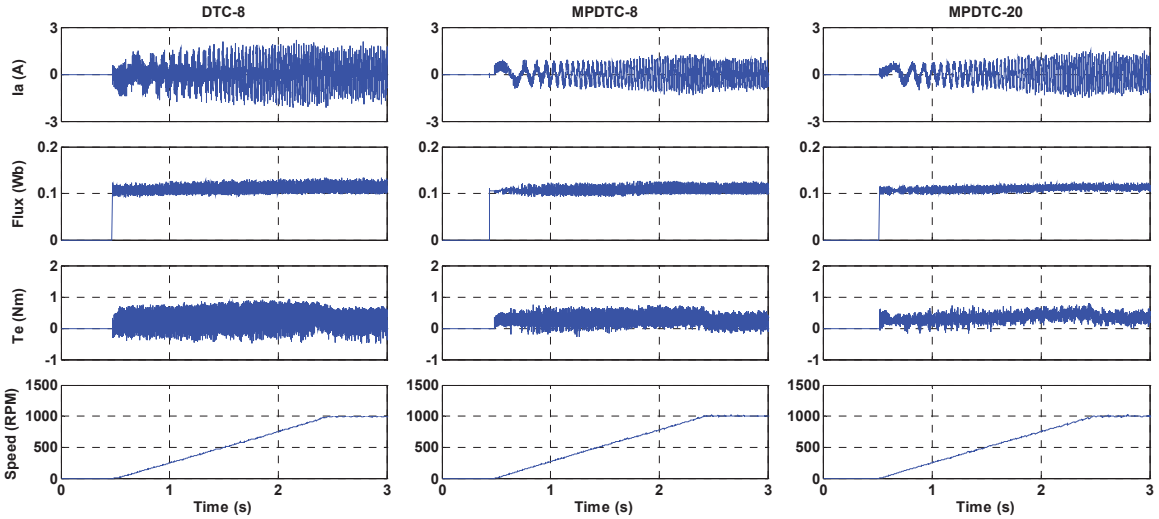

Fig. 6.6.2 Experimental start-up responses with no load from standstill to rated speed, where (a) conventional DTC, (b) conventional FCS-MPDTC and (c) proposed FCS-MPDTC

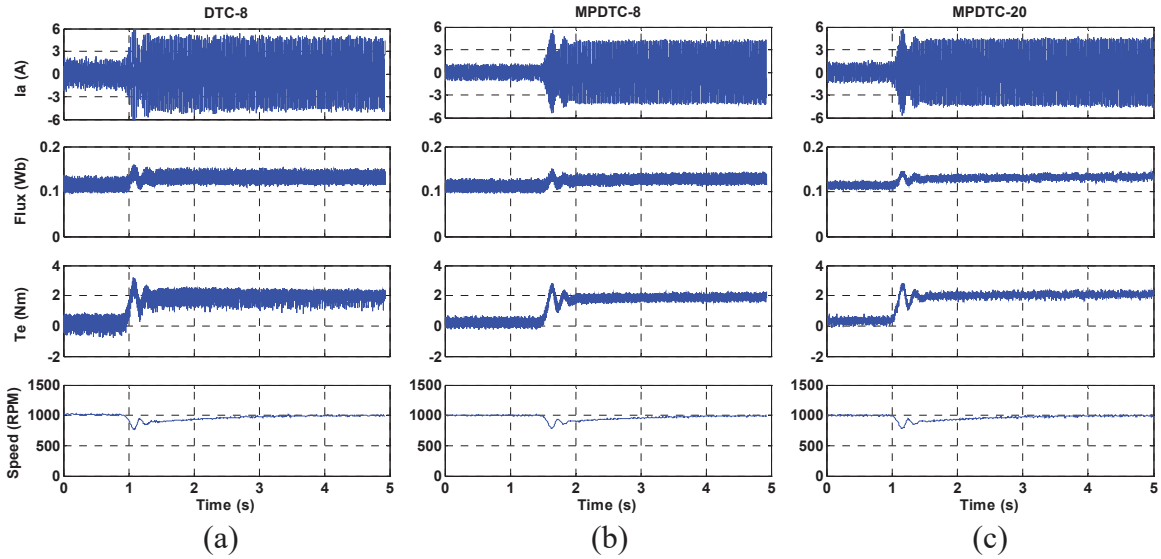

Fig. 6.6.3 Experimental load test, where (a) conventional DTC, (b) conventional FCS-MPDTC, and (c) proposed FCS-MPDTC

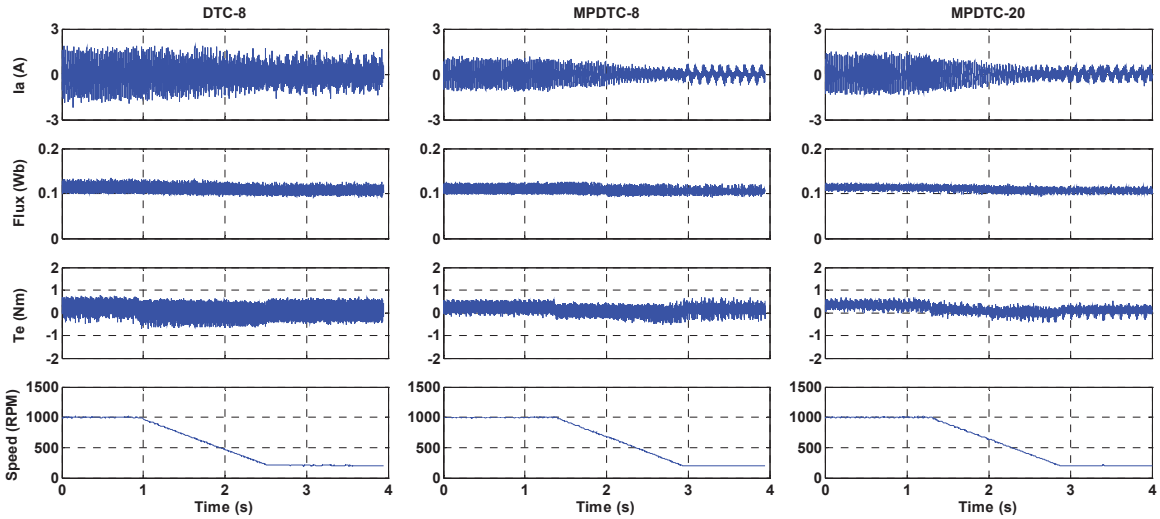

Fig. 6.6.4 Experimental decelerating responses from 1000 rpm to 200 rpm, where (a) conventional DTC, (b) conventional FCS-MPDTC, and (c) proposed FCS-MPDTC

6.6.3 Drive system efficiency

The experimental drive system efficiency contours are presented in Fig. 6.6.5. The speed is varied from 20% rated speed to 100% rated speed and the load torque is varied from 0% rated torque to 100% rated torque. It is noticed that the proposed FCS-MPDTC presents higher drive system efficiency in all regions and remarkably wider high-efficiency range than the other two methods. The highest drive system efficiency of the conventional DTC, conventional FCS-MPDTC, and proposed FCS-MPDTC are 70.8%, 71.2%, and 72.8%, respectively.

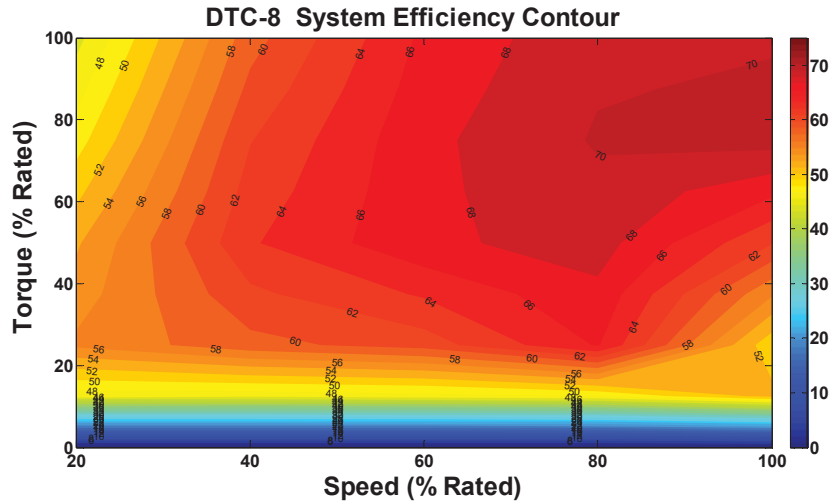

(a)

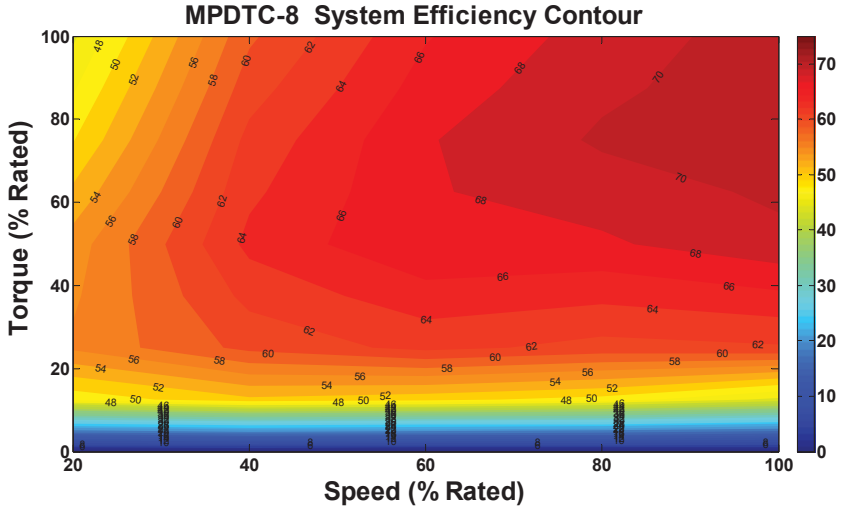

(b)

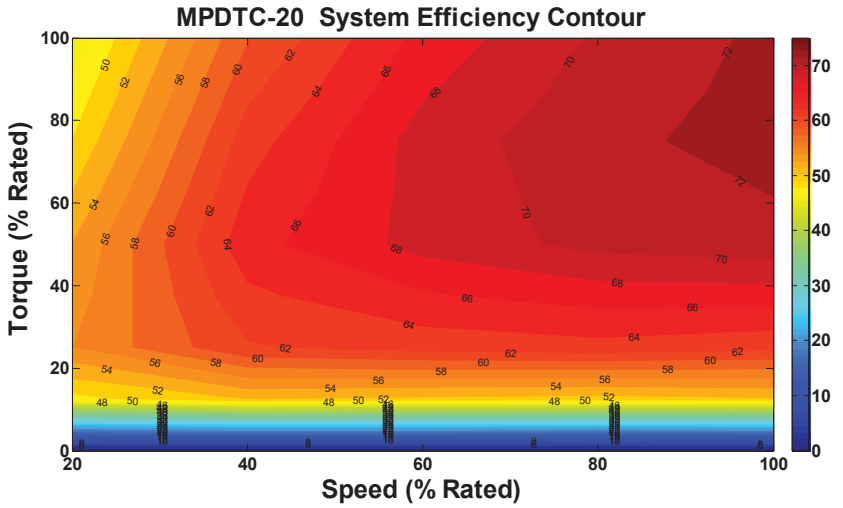

(c)

Fig. 6.6.5 Experimental drive system efficiency contours, where (a) conventional DTC, (b) conventional FCS-MPDTC, and (c) proposed FCS-MPDTC

6.7 Summary

According to the analysis above, it can be concluded that:

- The conventional FCS-MPDTC can achieve lower torque ripple than that of the conventional DTC whilst maintaining/reducing the switching frequency as proven by both simulation and experimental results. However, the conventional FCS-MPDTC's ability in flux ripple reduction is insignificant and even unstable.
- The introduction of the proposed method can effectively reduce the torque and flux ripples. A noticeable increase of inverter switching frequency is also observed. The drive system efficiency of this method is the highest in all regions.
- When the one-step delay is compensated, the steady-state performance of the conventional FCS-MPDTC and proposed FCS-MPDTC in terms of torque and flux ripple reduction is improved. It should be noticed that the performance improvement also comes with a switching frequency increase.
- To make a fair comparison, the experimental results of these control methods under the similar inverter switching frequency are repeated in Section 6.7. The effectiveness of the proposed FCS-MPDTC is confirmed by the test results.

CHAPTER 7

CONCLUSIONS AND FUTURE WORKS

7.1 Conclusions

The main achievements of this thesis are summarized below:

- A comprehensive literature review was presented for the developmental history of EVs, electrical machines, and PMSM machine structural topologies and control strategies for EV drives. The principles, implementations and improvements of various control methods, such as the six-step control, field oriented control (FOC), direct torque control (DTC) and model predictive control (MPC), were discussed in details.
- An axially laminated flux switching permanent magnet machine (ALFSPMM) with high grain oriented (HiB) silicon steel stator and rotor cores is proposed. The detailed fabrication procedures are also presented. The theoretical characteristics of ALFSPMM, such as back-*emf*, self/mutual inductance and cogging torque are calculated by the 2D finite element method (FEM). Experimental measurements of the prototype machine are presented to validate the FEM calculation.
- A simple low-cost method to measure the cogging torque is presented.
- The issues in the motor fabrication are discussed. The influence of misalignment between the stator core and the rotor shaft (a common issue in motor manufacturing) is investigated by FEM.
- A novel FCS-MPDTC with extended control set of twenty modulated voltage space vectors is proposed in this thesis. To mitigate the computational burden caused by the increased number of voltage space vectors, a pre-selective scheme is designed for the proposed FCS-MPDTC to filter out the impractical voltage vectors instead of evaluating all twenty voltage space vectors.
- The drive system performance and efficiency of the conventional direct torque control, conventional FCS-MPDTC, and proposed method are investigated. The theory and simulation are validated by experimental results on the ALFSPMM and a commercially produced PMSM.

7.2 Future Works

The possible future works following this thesis project is listed below:

On the machine side

- To study the performance of the drive system in detail, the efficiency of the motor and the efficiency of the inverter need to be analyzed and measured individually.
- A large scale prototype motor need to be built and tested on the prototype EV.
- To facilitate the industrial manufacturing, the following aspects should be considered in the future: (a) dies should be made of tool steel in order to improve the accuracy and durability, (b) the lengths of the steel sheets in each layer should be individually calculated in order to save the material and reduce the grinding time, and (c) the stator/rotor laminations should be annealed in order to recover the magnetic property deterioration in the bending process.

On the control side

- A flux weakening scheme can be developed for the proposed FCS-MPDTC to extend further the operational speed range for wide speed range applications, e.g. electric vehicles.
- New constrains can be developed for the cost function to further reduce the torque and flux ripples and increase the system efficiency.
- A comparison between the proposed FCS-MPDTC and other duty ratio optimization methods can be investigated.

On the drive system design side

- The idea of system-level design optimisation can be implemented in the development of EV drive system in the future. This could improve the steady and dynamic performances, reliability, and efficiency of the drive system, and also reduce the cost in mass production.

APPENDIX A. LIST OF PUBLICATIONS FROM THIS WORK

Journal papers:

[1] **Tianshi Wang**, Chengcheng Liu, Wei Xu, Gang Lei, Mohammad Jafari, Youguang Guo, Jianguo Zhu, "Fabrication and Experimental Analysis of an Axially Laminated Flux-Switching Permanent-Magnet Machine," *Industrial Electronics, IEEE Transactions on* , vol. 64, no. 2, pp. 1081-1091, Feb. 2017.

[2] **Tianshi Wang**, Chengcheng Liu, Gang Lei, Jianguo Zhu, "Model Predictive Direct Torque Control of Permanent Magnet Synchronous Motors with Extended Set of Voltage Space Vectors", *IET Electric Power Applications (early access)*, Apr. 2017.

[3] Chengcheng Liu, Gang Lei, **Tianshi Wang**, Youguang Guo, Youhua Wang, Jianguo Zhu, "Comparative Study of Small Electrical Machines With Soft Magnetic Composite Cores," *Industrial Electronics, IEEE Transactions on* , vol. 64, no. 2, pp. 1049-1060, Feb. 2017.

[4] Mohammad Jafari, Zahra Malekjamshidi, Gang Lei, **Tianshi Wang**, Glenn Platt, Jianguo Zhu, "Design and Implementation of an Amorphous High-Frequency Transformer Coupling Multiple Converters in a Smart Microgrid," *Industrial Electronics, IEEE Transactions on* , vol. 64, no. 2, pp. 1028-1037, Feb. 2017.

[5] Gang Lei, **Tianshi Wang**, Jianguo Zhu, Youguang Guo, Shuhong Wang, "System-Level Design Optimization Method for Electrical Drive Systems—Robust Approach," *Industrial Electronics, IEEE Transactions on* , vol.62, no.8, pp. 4702-4713, Aug. 2015

[6] Gang Lei, **Tianshi Wang**, Youguang Guo, Jianguo Zhu, Shuhong Wang, "System-Level Design Optimization Methods for Electrical Drive Systems: Deterministic Approach," *Industrial Electronics, IEEE Transactions on* , vol.61, no.12, pp.6591-6602, Dec. 2014

[7] Gang Lei, Yonguang Guo, Jianguo Zhu, **Tianshi Wang**, "System Level Six Sigma Robust Optimization of a Drive System With PM Transverse Flux Machine," *Magnetics, IEEE Transactions on* , vol.48, no.2, pp. 923-926, Feb. 2012

[8] Wei Xu, Gang Lei, **Tianshi Wang**, Xinghuo Yu, Jianguo Zhu, Youguang Guo, "Theoretical Research on New Laminated Structure Flux Switching Permanent Magnet Machine for Novel Topologic Plug-In Hybrid Electrical Vehicle," ," *Magnetics, IEEE Transactions on* , vol. 48, no. 11, pp. 4050-4053, Nov. 2012.

Conference papers:

[1] **Tianshi Wang** , Youguang Guo and Jianguo Zhu, "Finite-Control-Set Model Predictive Direct Torque Control of PMSMs with Virtual Space Vectors," *Industrial Electronics and Applications (ICIEA), 2017 International Conference on,* (Accepted)

[2] **Tianshi Wang**, Yongchang Zhang, Youguang Guo and Jianguo Zhu, "An Assessment of The Influence of Sampling Frequency on Steady-State Performance

of PMSM Drive System", *Australasian Universities Power Engineering Conference (AUPEC), 2012 International Conference on,* pp. 1-4, Sep. 2012

[3] **Tianshi Wang**, Jianguo Zhu and Yongchang Zhang, "Model Predictive Torque Control for PMSM with Duty Ratio Optimization", *Electrical Machines and Systems (ICEMS), 2011 International Conference on* , vol., no., pp. 1-5, 20-23 Aug. 2011

[4] **Tianshi Wang**, Jianguo Zhu, Yongchang Zhang, Youguang Guo and Gang Lei, "Simulation and Experimental Studies of Permanent Magnet Synchronous Motor Control Methods", *Applied Superconductivity and Electromagnetic Devices (ASEMD), 2011 International Conference on,* pp. 252-255, Dec. 2011

[5] Yongchang Zhang, Zhengxi Li, **Tianshi Wang** and Jianguo Zhu, "Predictive direct torque and flux control of doubly fed induction generator with switching frequency reduction for wind energy applications", *Electrical Machines and Systems (ICEMS), 2011 International Conference on* , vol., no., pp. 1-6, 20-23 Aug. 2011

[6] Yongchang Zhang, Zhengxi Li, **Tianshi Wang** and Jianguo Zhu, "Evaluation of a class of improved DTC method applied in DFIG for wind energy applications", *Electrical Machines and Systems (ICEMS), 2011 International Conference on* , vol., no., pp. 1-6, 20-23 Aug. 2011

[7] Wei Xu, Jianguo Zhu, Yongchang Zhang and **Tianshi Wang**, "Electromagnetic design and performance evaluation on 75 kW axially laminated flux switching permanent magnet machine", *Electrical Machines and Systems (ICEMS), 2011 International Conference on* , vol., no., pp. 1-6, 20-23 Aug. 2011